

AD A 041 224

AFAL-TR-76-74 ✓



1.06 MICROMETER AVALANCHE PHOTODIODE DETECTOR

SCIENCE CENTER, ROCKWELL INTERNATIONAL
1049 CAMINO DOS RIOS
THOUSAND OAKS, CALIFORNIA 91360

APRIL 1977

TECHNICAL REPORT AFAL-TR-76-74
FINAL REPORT FOR PERIOD 3 DECEMBER 1973 - 4 AUGUST 1975

Approved for public release; distribution unlimited

RECEIVED
12 APR 1977

AIR FORCE AVIONICS LABORATORY
AIR FORCE WRIGHT AERONAUTICAL LABORATORIES
AIR FORCE SYSTEMS COMMAND
WRIGHT-PATTERSON AIR FORCE BASE, OHIO 45433

WJ. _____
DDC FILE COPY

NOTICE

When Government drawings, specifications, or other data are used for any purpose other than in connection with a definitely related Government procurement operation, the United States Government thereby incurs no responsibility nor any obligation whatsoever; and the fact that the government may have formulated, furnished, or in any way supplied the said drawings, specifications, or other data, is not to be regarded by implication or otherwise as in any manner licensing the holder or any other person or corporation, or conveying any rights or permission to manufacture, use, or sell any patented invention that may in any way be related thereto.

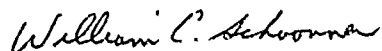
This report has been reviewed by the Information Office (OI) and is releasable to the National Technical Information Service (NTIS). At NTIS, it will be available to the general public, including foreign nations.

This technical report has been reviewed and is approved for publication.



DONALD J. PEACOCK, Project Engineer
Electro-Optic Detectors Group
Electro-Optics Technology Branch

FOR THE COMMANDER



WILLIAM C. SCHCONOVER, Chief
Electro-Optics Technology Branch
Electronic Technology Division

Copies of this report should not be returned unless return is required by security considerations, contractual obligations, or notice on a specific document.

UNCLASSIFIED

SECURITY CLASSIFICATION OF THIS PAGE (When Data Entered)

REPORT DOCUMENTATION PAGE		READ INSTRUCTIONS BEFORE COMPLETING FORM
1. REPORT NUMBER AFAL-TR-76-74	2. GOVT ACCESSION NO.	3. RECIPIENT'S CATALOG NUMBER
4. TITLE (and Subtitle) 1.06 Micrometer Avalanche Photodiode Detector.	5. TYPE OF REPORT & PERIOD COVERED Final Report 12/3/73 - 8/4/75	
6. AUTHOR(s) Richard C. Eden	7. PERFORMING ORG. REPORT NUMBER SC571.16TRF	8. CONTRACT OR GRANT NUMBER(s) F33615-74-C-1030
9. PERFORMING ORGANIZATION NAME AND ADDRESS Science Center, Rockwell International 1049 Camino Dos Rios Thousand Oaks, California 91360	10. PROGRAM ELEMENT, PROJECT, TASK AREA & WORK UNIT NUMBERS Project No. 2001	
11. CONTROLLING OFFICE NAME AND ADDRESS Air Force Avionics Laboratory (DHO-3) Air Force Systems Command Wright-Patterson Air Force Base, Ohio 45433	12. REPORT DATE Apr 77	13. NUMBER OF PAGES 273
14. MONITORING AGENCY NAME & ADDRESS (if different from Controlling Office)	15. SECURITY CLASS. (of this report) UNCLASSIFIED	
15a. DECLASSIFICATION/DOWNGRADING SCHEDULE		
16. DISTRIBUTION STATEMENT (of this Report) Final pgs 3 Dec 73 - 4 Aug 75		
APPROVED FOR PUBLIC RELEASE; DISTRIBUTION UNLIMITED		
17. DISTRIBUTION STATEMENT (of the abstract entered in Block 20, if different from Report)		
18. SUPPLEMENTARY NOTES		
19. KEY WORDS (Continue on reverse side if necessary and identify by block number) 1.06 Micron Gigabit Low Noise Nd-YAG Laser Laser Communications GAASFET Preamp Avalanche Heterojunctions Photodiode III-V Alloy Optical Receiver Microwave Avalanche Photodiode		
20. ABSTRACT (Continue on reverse side if necessary and identify by block number) Satellite laser communications at gigabit data rates based on the Nd-YAG laser are of great interest to the Air Force. In this report, the development of a complete solid state 1.06μ optical receiver which can be used in optical communications at data rates approaching 1.5 Gb/s, or in other applications requiring sensitive, short-pulse detection, is described. This work entailed both the development of a new type of heterojunction III-V semiconductor alloy avalanche photodiode and an extremely charge-sensitive wideband low-noise preamp		

DD FORM 1 JAN 73 1473

EDITION OF NOV 65 IS OBSOLETE

UNCLASSIFIED

SECURITY CLASSIFICATION OF THIS PAGE (When Data Entered)

micrometers

319 1473

$GaAs(1-x)Sb(x)$

UNCLASSIFIED

SECURITY CLASSIFICATION OF THIS PAGE (When Data Entered)

design making use of GaAs Schottky barrier-gate field effect transistors (GAASFET's) operating in the negative-feedback "transimpedance" mode. The inverted homo-heterojunction $GaAs_{1-x}Sb_x$ avalanche photodiodes developed in this program give 1.064 μ quantum efficiencies over 96%, and for typical 3 μ l diameter devices, have bulk leakages of about 300 pA, total leakages of about 3nA at -50 volts bias, and junction capacitances of only $C_j=0.1$ pf. Since all of the light absorption in the 1.0 μ to 1.08 μ spectral width of these APD's is absorbed in the depletion region, for which the transit time is under 50 ps, the intrinsic APD frequency response is of the order of 10 GHz. Peak avalanche gains up to 24dB at 273 MHz have been obtained with these devices. The very low junction capacitance of this new APD makes it possible to realize an extremely charge-sensitive receiver by hybrid integrating the APD with a correspondingly low input capacitance preamp. This ultra-low input capacitance is achieved in the receivers developed under this program by the use of a GAASFET input stage, with the resistor thermal noise minimized by operating the input stage as an "operational amplifier" in the negative feedback or "transimpedance" mode. For closed-loop bandwidths approaching gigahertz, of course, this "op-amp" must be very fast to avoid oscillation. Several preamp designs were tried in this work. In the fastest preamp fabricated, the input capacitance was approximately 0.28 pf (plus 0.1 pf APD capacitance), the open-loop "op-amp" gain was 20 with a gain-bandwidth of 5 GHz, and the closed-loop frequency response with a 5K Ω feedback resistance was $F_{3dB} = 1.6$ MHz. The response of the receiver to a short current impulse gives an output pulsewidth of 1ns (full width at 10% maximum) and a pulse of only $N_0 = 347$ electrons will give a peak output equal to the rms noise output. With appropriate short pulse sampling of the output, this receiver should achieve 10^{-6} bit error rate detection of PGBM modelocked laser data with a difference in signal between a "1" and a "0" of only $N_{ph} = 3440/M$ photons/bit, where M is the avalanche gain (for low M). (Bit error rate measurements in an actual high data rate laser communications system on receivers of this type have given values of required signal level to achieve a given BER in excellent agreement with those calculated from our preamp test data. Even for small avalanche gains, this is the most sensitive 1.06 μ high data rate receiver available anywhere. As the 1.06 μ APD gains are increased, it should be possible to achieve very substantial reductions in power level required for gigabit laser communications.

UNCLASSIFIED

SECURITY CLASSIFICATION OF THIS PAGE (When Data Entered)

SC571.16TRF

FOREWORD

This report was prepared by the Science Center, Rockwell International under contract F33615-74-C-1030. This report covers the period 3 December 1973 through 4 August 1975, and is the Final Report on this contract. The work described herein was carried out by the Science Center, Rockwell International, Thousand Oaks, California

The principal investigator for this project was Dr. Richard C. Eden and the associate principal investigator was Dr. James S. Harris. The principal technical support for this work at the Science Center was provided by Kenichi Nakano, Cheol K. Kim and Ira Deyhimy.

The program manager was Dr. A. S. Joseph.

The Contracting Officer for this project from Wright-Patterson Air Force Base was Donald J. Peacock.

ACCESSION for	
RTIS	White Section <input checked="" type="checkbox"/>
DCB	Buff Section <input type="checkbox"/>
UNANNOUNCED	<input type="checkbox"/>
JUSTIFICATION.....	
BY	
DISTRIBUTION/AVAILABILITY CODES	
Dist.	AVAIL. FOR SPECIAL
A	

D D C
REGISTERED
JUL 6 1975
R

TABLE OF CONTENTS

	<u>Page</u>
1.0 INTRODUCTION AND SUMMARY	1
1.1 Introduction	1
1.2 Summary	9
2.0 SYSTEM REQUIREMENTS AND DESIGN APPROACH FOR THE GIGABIT RECEIVER	13
2.1 Analysis of Detector Requirements in a Modelocked Laser Communications	13
2.1.1 Optical Pulse Detection in the Poisson Limit ...	13
2.1.2 Detection of Modelocked Laser Pulses with an Avalanche Photodiode Receiver	17
2.1.3 Avalanche Photodiode Receiver Performance in the Preamp Noise Limited (Low Avalanche Gain) Region	23
2.1.4 High Avalanche Gain Performance of the APD Receiver	26
2.1.5 Comparison of Various Receiver Approaches for Gigabit Nd-YAG Laser Communication	30
2.1.6 Influence of Modulator Extinction Ratio on Communication Performance with Different Receiver Approaches	32
2.2 III-V Alloy Microwave Avalanche Photodiode Design	37
2.2.1 Device Design of the Inverted Heterojunction Microwave Avalanche Photodiode	38
2.2.2 Device Design of the Inverted Homo-Heterojunction Avalanche Photodiode	43
2.3 Design Approach for the Low Noise Gigabit GAASFET Preamp	48
2.3.1 Requirements for Attaining High Pulse Sensitivity in a Preamp	48

TABLE OF CONTENTS (Con't)

	<u>Page</u>
2.3.2 Model for Signal Response and Noise Output for a Feedback-Mode Preamp	50
2.3.3 Effect of Post-Receiver Amplifier Bandwidth on the Pulse Detection Performance of a Feedback-Mode Preamp	54
2.3.4 Preliminary, Lower Bandwidth, GAASFET Preamp Designs	55
2.3.4.1 Basic Design of the Mark IA Two-GAASFET Preamp .	56
2.3.4.2 Mark II Three-GAASFET Preamp Design	60
2.3.5 Basic Design of the Gigabit Mark III Three-GAASFET Preamp	62
2.3.6 GAASFET Voltage Gain Characteristics	65
3.0 TECHNICAL APPROACH	70
3.1 III-V Alloy Materials Technology	70
3.1.1 Materials Selection	70
3.1.2 Materials Growth and Evaluation	72
3.2 Fabrication of the III-V Alloy Avalanche Photodiode Devices	81
3.3 Measurement Techniques	90
3.3.1 Measurement Techniques Utilized in this Work but Described Elsewhere (with References)	90
3.3.2 Electrical Measurements on Chip or Wafer Devices	92
3.3.3 High-Frequency Drain Resistance Measurements on GAASFET Chips	94
3.3.4 Scanning Laser Microscope	96
3.3.5 UHF Avalanche Gain Measurements with the Scanning Laser Microscope	107
3.3.6 Precision Current-Protected Avalanche Photodiode Power Supply	110
3.3.7 Digital Processing Oscilloscope System	112
3.3.8 Application of the DPO System for Gigabit Preamp Noise Measurements	117
3.3.8.1 Noise Histogram Analysis for Predicting Receiver BER	118

TABLE OF CONTENTS (Con't)

	<u>Page</u>
3.3.8.2 Use of the DPO System for 1/f Noise Character- ization	123
3.3.9 Absolute Noise Spectral Density Measurements Using the Tektronix 7L13 Spectrum Analyzer	124
3.3.10 Use of the DPO System for Measuring the Current Impulse Response and $(V/Q)_p$ to Determine Preamp N_o	129
3.3.11 Techniques for Applying the DPO System to Preamp Evaluation	136
4.0 AVALANCHE PHOTODIODE AND GIGABIT RECEIVER PERFOR- MANCE RESULTS	140
4.1 Inverted Homo-Heterojunction $\text{GaAs}_{1-x}\text{Sb}_x$ Avalanche Photodiode Results	140
4.1.1 Active Layer Doping Profile	
4.1.2 APD Junction Capacitance	142
4.1.3 Response Time of Delivered 50Ω - Packaged Devices	142
4.1.4 APD Reverse Dark Current	144
4.1.5 Spectral Dependence of Photoresponse and Absolute Quantum Efficiency	147
4.1.6 High-Frequency Avalanche Gain	150
4.1.7 Spatial Uniformity of Quantum Efficiency and Avalanche Gain	152
4.2 Performance Results for the Preliminary, Lower Bandwidth, Preamp Designs	157
4.2.1 Results for Mark IA GAASFET Preamps	157
4.2.1.1 Circuit Description for GAASFET Preamps #4 and #5	157
4.2.1.2 Performance Results for GAASFET Preamp #5	163
4.2.1.3 Performance Results for GAASFET Preamp #4	169
4.2.2 Results for Mark II GAASFET Preamp	173
4.2.2.1 Circuit Description for GAASFET Preamp #7	173
4.2.2.2 Performance Results for GAASFET Preamp #7	178

TABLE OF CONTENTS (Con't)

	<u>Page</u>
4.2.2.3 Performance of Mark II GAASFET Preamp #7 in a 400 Mb/s PGBM 1.064 μ Optical Communications System	
4.3 Performance Results for the Gigabit Mark III GAASFET Preamps	190
4.3.1 Circuit Description for the Mark III Preamps ...	191
4.3.2 Performance Results for GAASFET Preamp #8	203
4.3.3 Performance Results for AF Delivered GAASFET Preamp #6 (As Originally Delivered - Before Modification	215
5.0 CONSLUSIONS	224
6.0 REFERENCES	

LIST OF ILLUSTRATIONS

<u>Figure</u>		<u>Page</u>
1.1	Photograph of GAASFET Pream #8 shown with a signal-averaged oscilloscope trace showing the subnanosecond response of #8 (measured through cascaded B&H preamps) to a current impulse input of 4125 electrons (25mV/cm vertical, 1nS/cm horizontal).	2
2.1	Example of Optical Detection in the Poisson (counting statistics) Limit. For $\bar{n}_1 = 50$, $\bar{n}_0 = 5$, optimum decision level is to call $n \geq 20$ a "1" and $n \leq 19$ a "0", for which we obtain an average probability of error per bit of $BER = 4.12 \times 10^{-7}$.	15
2.2	Schematic of Avalanche Photodiode Receiver Defining Response Parameters.	19
2.3	Comparison of the calculated Performance of Various 1.06μ Detectors as 400 Mb/s PGBM Mode-locked Laser Communications Receivers. Plotted is the number of photons per bit required for 10^{-6} bit error rate data reception as a function of internal detector gain. $N_0 = 175$ electrons assumed for lowest curve GAASFET preamp as a goal; best performance achieved to date is $N_0 = 347$ electrons for preamp #8, the curve for which would lie a factor of 2 above this for low M.	31
2.4	Calculated Signal Level to Achieve a 10^{-6} B.E.R. Versus Modulator Zero Bandthrough or Extinction Ratio for Photomultipliers (or Other Poisson Statistics Receivers as Compared to a Preamp-Noise-Limited Receiver (APD Receiver at Low M).	35

LIST OF ILLUSTRATIONS (Con't)

<u>Figure</u>		<u>Page</u>
2.5	Original Inverted Heterojunction III-V Alloy Microwave Avalanche Photodiode Design. Note that the peak electric field (high avalanche gain) region is at the p^+ (transparent buffer layer) - n^- (absorbing active layer) heterojunction interface.	39
2.6	Example of Spectral Photoresponse Which Can Be Obtained in Either Inverted Heterojunction or (Fully Depleted) Inverted Homo-Heterojunction Avalanche Photodiode. While this illustrates narrowband photoresponse which can be obtained, experimental devices are made with wider response peaks and near 100% quantum efficiencies.	41
2.7	Device Structure for an Inverted Homo-Heterojunction $\text{GaAs}_{1-x}\text{Sb}_x$ Avalanche Photodiode. Note that as opposed to the earlier structure of Fig. 2.5, the peak electric field is at a p-n homojunction produced during continuous growth of the n^- active (absorbing) layer by adding a small amount of p-type dopant to the melt. The device is normally operated with the n^- layer completely depleted.	45
2.8	Signal and Noise Models for Feedback-Mode (Trans-impedance-Type) Preamp. a) General case of feedback element with (Frequency-dependent) noise voltage e_2 . b) Usual case of feedback element a resistor paralleled by a capacitance where we transform the resistor noise to a frequency-independent input noise current, i_{nj} .	51
2.9	Simplified Circuit Diagram for the Mark IA GAASFET Preamps Design. (Complete circuit diagram is shown in Fig. 4.9.)	57

LIST OF ILLUSTRATIONS (Con't)

<u>Figure</u>		<u>Page</u>
2.10	AC Equivalent Circuit of the First Stage of Mark IA or Mark II Preamps Including Parasitic Impedances. This circuit is analyzed using the TEK BASIC program listed in Appendix A.5.	59
2.11	Simplified Circuit Diagram for the Mark II GAASFET Preamp Design. (Complete circuit diagram for Preamp #7 is shown in Fig. 4.16.)	61
2.12	Simplified Circuit Diagram of the Mark III GAASFET Preamp Design. (Complete circuit diagram for GAASFET Preamp #8 is shown in Fig. 4.24.)	64
2.13	Circuit Model for Cascode FET Arrangement Illustrating the Greatly Increased Voltage Gain of a Dual-Gate GAASFET Compared to a Single-Gate. a) Cascode equivalent circuit for a dual gate GAASFET. b) Low-frequency (omitting capacitances) model for a). c) Equivalent circuit for b) defining the equivalent drain resistance and equivalent transconductance for the dual-gate FET or cascode arrangement. Note that $(R_D)_{CAS} \gg R_D$.	67
3.1	Energy bandgap vs. lattice constant for all of the binary and ternary alloy semiconductors of Al, Ga or In with P, As or Sb. The solid lines are for direct bandgap materials and the dashed lines for indirect bandgap materials.	71
3.2	Ga rich region of the GaAsSb phase diagram. The Solid lines are liquidus isotherms while the dashed lines are $GaAs_xSb_{(1-x)}$ isocomposition lines.	73

LIST OF ILLUSTRATIONS (Con't)

<u>Figure</u>		<u>Page</u>
3.3	Experimental and calculated Sb distribution curves for GaAsSb solid.	75
3.4	Energy bandgap vs. composition for the GaAs _(1-x) Sb _x alloy system. The region 0.4 < x < 0.65 is inaccessible because of a miscibility gap in the alloy.	76
3.5	Sb profile obtained from X-ray emission on SEM for two GaAsSb layers grown on a GaAs substrate. The melt composition for each epitaxial layer was identical but growth conditions at the time the second melt was brought over the substrate caused the Sb concentration to dip at the interface.	78
3.6	Graphite slider boat used for "doping drop" growths. Top slider (small insert with holes) is where the dopant is placed and the quartz push rod is used to push this slider back to where the sets of holes line up and the dopant drops through into the melt to change the doping.	80
3.7	Normarski phase contrast photomicrographs of the surface details of an APD structure. Note the alignment of surface features along <110> directions.	82
3.8	Interference phase contrast photomicrograph of the surface of an APD structure. These surface features are between 1 and 2 fringes which corresponds to a height of 2700 to 5400Å.	83

LIST OF ILLUSTRATIONS (Con't)

<u>Figure</u>		<u>Page</u>
3.9	Device Fabrication Procedure for the Inverted Homo-Heterojunction Avalanche Photodiode (starting with the 3-layer epitaxial growth structure and ending with the APD chips ready for mounting or packaging).	84& 85
3.10	a) Reflection photograph of a diode where the dark circular dot is the mesa outline and the metal contact in the center. b) Transmission photograph of a diode is taken by the infrared microscope from the layer side. The dark square area is the metal contact on the substrate side. The large bright circle is the window on the substrate side. The dark circular dot is the outline of the mesa and metal contact to the contact layer.	87
3.11	New Compact 50 Ω Microwave Mount for Inverted Heterojunction Microwave Avalanche Photodiodes. Internal LC filter attenuates RFI on APD bias power supply. Note that the front sample mounting and cover plate floats at the APD substrate bias, so exposed metal should be covered with a suitable insulation if danger of accidental contact exists. Fig. 4.3 shows a photograph of this mount with an APD pulse response.	88
3.12	Precision Micropositioner Probe Station Fabricated for Working With Small Geometry Devices.	93

LIST OF ILLUSTRATIONS (Con't)

<u>Figure</u>		<u>Page</u>
3.13	Circuit Diagram For Active Probe Test Setup for Measuring Open-Circuit Gain of GAASFET's. The hybrid IC chip, 0.200" square, is mounted near the end of the probe so that the drain is supplied from a high impedance, low capacitance current source.	95
3.14	Diagram of the optical table layout used for this work, including the 1.06 μ (modelocked), 1.152 μ , and 6328Å lasers and the scanning light microscope.	97
3.15	Block-Diagram of the Scanning Laser Microscope System.	99
3.16	a) Photograph of the Scanner Unit of the Scanning Laser Microscope taken along the direction of the exit beam. Beam enters the GC0401 spatial filter from the right.	100
	b) Another view of the Scanner Unit of the Scanning Laser Microscope with the 40X 0.5NA Catadioptric Mirror Objective at the right.	101
3.17	Scanning light microscope micrographs of response of a Si photodiode at 6328Å. (a) and (b) intensity modulated display for diode at 0 and 20 volts bias respectively. The dark ring indicating no response is the Ohmic contact to the diode. (c) and (d) are a combined intensity modulation and contour mapping display of the same diode at 0 and 20 volts bias respectively.	106
3.18	Circuit Diagram for the Precision \pm 200 volt Floating APD Supply.	111
3.19	Regulated \pm 120 Vdc Power Supply for Use in the APD Supply of Fig. 3.18.	113

LIST OF ILLUSTRATIONS (Con't)

<u>Figure</u>		<u>Page</u>
3.20	Measurement Equipment Routinely Used For GAASFET Preamp Evaluation, including the Tektronix Digital Processing Oscilloscope.	115
3.21	10^6 Sample Noise Histogram Measured for Mark III GAASFET Pream #6 at $V_{APD} = 80$ volts Through Cascaded B&H's. Histogram (lower curve, zero at bottom) displayed at 2500 counts/cm vertical. Horizontal for all curves in 25 mV/cm, positive to right, zero center. The log of the experimental distribution and the calculated log curve ($K_0 = 9.628$, $\sigma = 12.96\text{mV}$) are displayed at $e^{1.535}$ per cm., or 1.5 divisions vertical equals 1 decade.	122
3.22	Measurement Approach for Determining Current Pulse Response and (V_p/Q_p) for a Preamplifier.	131
3.23	Block Diagram of a Mark I or Mark III GAASFET Preamp Showing the C_c Measurement Procedure for $(V/Q)_\delta$.	134
4.1	Carrier Concentration versus Depth, $N(x)$, measured on two different 5 mil diameter diodes on the K-9 epitaxial growth used for these homo-heterojunction APD's (structure of Fig. 2.7).	141
4.2	Capacitance-Voltage Relationship for a 5 mil diameter K-9 APD. Capacitances for a 3 mil APD are about one third of this.	143
4.3	Response of Two 3 mil M8-1 Inverted Heterojunction Microwave Avalanche Photodiodes to Modelocked Nd-YAG Laser Pulses. Upper curve (inverted) is from older mount (Ref. 1) shown on left into S-4 sampler, whereas lower (upward-going) curve is for similar APD in the new compact 50Ω mount shown at the upper right and Fig. 3.11 into an S-6 sampler. Both curves at 200pS/cm. Note the clean fall and return to baseline between the two laser pulses for the new diode mount.	145

LIST OF ILLUSTRATIONS (Con't)

<u>Figure</u>		<u>PAGE</u>
4.4	Total Reverse (Dark) Current for 3 mil (lower curve) and 5 mil (upper curve) diameter K-9 Homo-Heterojunction APD's. Note that the bulk leakage at low biases scales with area while surface current, dominant at higher biases, scales with perimeter.	146
4.5	Spectral Photoresponse for a 5 mil Diameter K-9 APD for Biases from $V_{APD} = 2$ volts to $V_{APD} = 99.07$ volts. Ordinate is quantum efficiency (quantum efficiency-gain product for $V_{APD} > 70$ volts) versus wavelength. More typical K-9 APD's as used in the GAASFET receivers have 15% to 20% higher V_B 's and 0.01μ to 0.02μ longer wavelength response than this particular device.	148
4.6	High-Frequency Avalanche Gain versus APD Reverse Bias for the 5 mil diameter K-9 $GaAs_{1-x}Sb_x$ APD in GAASFET Preamp #7 (a). Complete curve, including noise, for the final delivered GAASFET Preamp #7 is shown in Fig. 4.21.	151
4.7	Scanning (Modelocked) Laser Microscope intensity-modulated pictures of the 273 MHz photoresponse of Mark IA Preamp #4. Scale is 1 mil/div, 10X 0.17 NA objective.	153
4.8	K-9 5 mil Diameter APD in GAASFET Preamp #5.	155
4.9	Circuit Diagram for Mark IA Preamp Design with specific values for GAASFET Preamp #5.	158
4.10	Circuit Diagram for the Power Supply-Monitor Unit for the Mark IA GAASFET Preamps (#4 and #5). Note that Power Suplly units are <u>not</u> interchangeable between preamps.	159

LIST OF ILLUSTRATIONS (Con't)

<u>Figure</u>		Page
4.11	Block Diagram of the Mark IA Preamps, with specific values and performance parameters for GAASFET Preamps #5.	160
4.12	Current Impulse Response for Mark IA GAASFET Preamp #5 for a current impulse input of $N_e = 8154$ electrons (output through cascaded B&H 50 Ω preamps). Current impulse response displayed at 10 mV/cm (zero 3 div below center), 1nS/cm. Also shown are the integral response, displayed at 10 pVs/cm (zero at bottom), and the frequency response obtained from the FFT of the current impulse response, displayed at 500 μ V/cm vertical (zero at bottom) and 256 MHz/cm horizontal ($f = 0$ at left edge).	164
4.13	Noise output spectra from GAASFET Preamp #5 through cascaded B&H's.	166
4.14	Current Impulse Response for Mark IA GAASFET Preamp #4 Measured Through Cascaded B&H's. Input pulse was $N_e = 8005$ electrons. Current impulse response displayed at 20 mV/cm vertical (zero 3 div below center), 1nS/cm horizontal, with integral at 20 pVS/cm. Also shown is the FFT-derived frequency response, displayed at 250 μ V/cm vertical (zero at bottom), 204.8 MHz/cm horizontal (zero at left edge).	170
4.15	Noise output spectra from GAASFET Preamp #4 through cascaded B&H's.	172
4.16	Circuit Diagram for Mark II GAASFET Preamp #7.	175
4.17	Circuit Diagram for the Power Supply-Monitor Unit for Mark II GAASFET Preamp #7.	176

LIST OF ILLUSTRATIONS (Con't)

<u>Figure</u>		<u>Page</u>
4.18	Functional Block Diagram for the Mark II GAASFET Preamp Design with specific values and performance parameters for Preamp #7.	177
4.19	Current Impulse Response for Mark II GAASFET Preamp #7 Measured With Output Directly into S-6 Sampler. Input pulse was $N_e = 53,000$ electrons. The current impulse response is displayed directly (zero at 2 div above center) and digitally smoothed (zero at top), both at 10 mV/cm, 1nS/cm, with the integral response at 10 pVS/cm. Also shown is the FFT-derived frequency response displayed at 500 μ V/cm vertical (zero at bottom), 256 MHz/cm horizontal (zero at left edge). Note that the bandwidth of the Q_2 internal gain stage is about 500 MHz.	179
4.20	Noise output spectra from Mark III GAASFET Preamp #7.	182
4.21	Variation of 273 MHz Signal Output and Illuminated and Dark Noise Outputs for Mark II GAASFET Preamp #7 (b) with final delivered APD. Noise curves are measured by detuning spectrum analyzer off of modelocked laser frequency.	184
4.22	Scanning light microscope pictures of the 273 MHz photoresponse of Mark II GAASFET Preamp #7. Scale is 1 mil/div.	186
4.23	Comparison of Calculated Average Power Required to Achieve a Given BER for GAASFET Preamp #7 (Mark II) With Experimental Points from McDonnell Douglas measurements.	189

LIST OF ILLUSTRATIONS (Con't)

<u>Figure</u>		<u>Page</u>
4.24	Circuit Diagram of the Mark III GAASFET Preamp Design with specific values for Preamp #8.	192
4.25	Power Supply-Monitor Unit for Mark III GAASFET Preamp #8.	193
4.26	Function Block Diagram for the Mark III Preamp Design, with specific values and performance parameters for GAASFET Preamp #8.	194
4.27	I_D vs. V_{DS} curves for GaAs MESFETS in Preamp #8.	196
4.28	Output time domain reflectometry traces for GAASFET Preamp #8 and a precision 50Ω reference termination (upper trace is right), 50mV/cm vertical, 1nS horizontal, 30 ps time resolution.	197
4.29	Noise Output Spectra from the output stage Preamp #8 with the gate of Q_3 terminated 25Ω to ground. Measured through cascaded B&H preamps.	199
4.30	Open-Loop dc Transfer characteristic of the Q_1 - Q_2 "op-amp" in Preamp #8. Horizontal is V_{g1} (1 V/cm, zero at right) and vertical is V_F , the op-amp dc output voltage (0.5V/cm, zero 2 cm from top). Normal feedback operation point is at $V_F = V_{D1} = -1.65V$. V_{DS} of $Q_1 \cong V_F + 6.2$ volts.	201
4.31	100 MHz Open-Loop Gain of Mark III GAASFET Preamp #8. Vertical is linear display of 100 MHz output, -30 dBm full scale, Horizontal is V_F , 0.5 volts/cm (zero at right). Measured gain at balance is $A_{12} A_3 = 17.5$ db.	201
4.32	Open-Loop Gain and noise, GAASFET Preamp #8, 0 to 1820 MHz frequency range. Preamp output straight into 7L13. Discrete frequency lines are inputs at frequencies of 20, 42, 50, 100, 150, 200, 250, 300, 350, 400, 450 and 480 MHz.	201

LIST OF ILLUSTRATIONS (Con't)

<u>Figure</u>		<u>Page</u>
4.33	Open-Loop Noise Output Spectrum from GAASFET Preamp #8. Q_1 in balance, $V_F = -1.65$ Vdc, gate of A_1 terminated 25Ω to ground. Measured through cascaded B&H preamps.	204
4.34	Current impulse response of GAASFET Preamp #8 (with $V_{APD} = 100$ volts) to a 4125 -electron current impulse (receiver output amplified thru cascaded B&H wideband 50Ω amplifiers). Upper curve output directly as seen on sampling oscilloscope (12.15 mV rms voltage noise). Lower curve is a 1024 waveform signal average of output. Both curves at 50 mV/cm, 1 ns/cm.	205
4.35	Current impulse response of Mark III GAASFET Preamp #8 (signal-averaged result from Fig. 4.34) displayed at 25 mV/cm vertical, 1 ns/cm and (light trace) 200 ps/cm horizontal.	207
4.36	Current impulse response of GAASFET Preamp #8 with $V_{APD} = 100$ V measured directly into S-6 (without B&H preamps). Input Step; $V_{STEP} = 0.2442$ volts through internal C_C . Current impulse at 5 mV/cm, 1 ns/cm, zero 3 cm below center. Integral at 2 pVs/cm, 1 ns, zero at bottom (-4 cm). FFT at 150 V/cm, 256 MHz/cm horizontal, with $f=0$ at left edge (vertical zero at bottom).	208
4.37	Closed-Loop ($R_F = 5K\Omega$) Noise Output Spectra from GAASFET Preamp #8 through cascaded B&H's.	210
4.38	Spectral Dependence of Noise Output Voltage (Open-Loop and Closed-Loop) for Mark III GAASFET Preamp #8.	212

LIST OF ILLUSTRATIONS (Con't)

<u>Figure</u>		<u>Page</u>
4.39	Response of GAASFET Preamp #8 with 5 mil APD to 400 Mb/s 1.06 μ PGBM modelocked laser data stream. Measured on McDonnell-Douglas Test Communications System. 10mV/cm vert. (through B&H DC 3002 preamp). $(I_p)_{AVE}=1\mu A$.	214
4.40	Output time-domain reflectometry traces for GAASFET Preamp #6 with power on (upper trace) and power off lower trace at right (Q_3 "saturated").	216
4.41	Output response of GAASFET preamp #6, measured through cascaded B&H preamps ($A=77.2$), to a current impulse of $N_e = 20,760$ electrons (75mV/cm, 1nS/cm, zero 2 cm below center). Also shown are the integral response (50pVS/cm, 1nS/cm, zero 3 cm below center) and FET - derived frequency response (2mV/cm vertical, zero 4 cm below center, 256 MHz/cm horizontal, $f = 0$ at left edge).	218
4.42	Frequency dependence of the voltage noise output (per root hertz) from Mark III GAASFET preamp #6. In addition to the normal closed-loop output noise spectrum, the open-loop and the Q_3 output stage [only] (plus B&H preamp) noise spectra are shown, along with the theoretical Johnson noise for $R_F = 2.5K\Omega$.	221

1.0 INTRODUCTION AND SUMMARY

1.1 Introduction

Gigabit data rate communications between synchronous satellites would require prohibitive amounts of power at microwave frequencies because of the large antenna beam divergences. At optical wavelengths, beam divergences of a few microradians can be obtained with modest optics, so that more reasonable fractions of laser transmitter power are intercepted by the receiver optics. This makes it possible, at least in principle, to achieve gigabit data rate of optical communication between satellites with practical laser power levels at the transmitter. The 1.06μ Nd-YAG laser is attractive for this application because of the good CW pump power to laser output power conversion efficiency possible with this material and the fact that its wide gain line makes it possible to obtain short (< 200 ps FWTM) optical pulsewidths in modelocked operation. In laser communications, concentrating all of the optical energy into short pulses with high peak power improves both the efficiency of modulation (no optical energy is wasted while the modulator is making transitions between states) and the detection sensitivity (because the peak received power is higher relative to the background light level or equivalent detector noise) relative to simple CW transmission.

The implementation of a gigabit satellite laser communications system of this type requires, along with the modelocked laser, optics, tracking system, etc., both a modulator and a receiver with very wide bandwidth capability. For example, in the Air Force 405B laser communications system a double modulator arrangement is used at the output of a polarized 500 Mpps modelocked Nd-YAG laser such that a pulse may be transmitted either in its original polarization or at 90° in either its original "time slot" or delayed by 1ns. In this PQM system, the second modulator must make a 90° rotation — no rotation transition in 1ns, which requires a modulator with bandwidth well in excess of 1 GHz if good extinction ratio is to be obtained. Similarly, it is necessary to have

SC571.16TRF

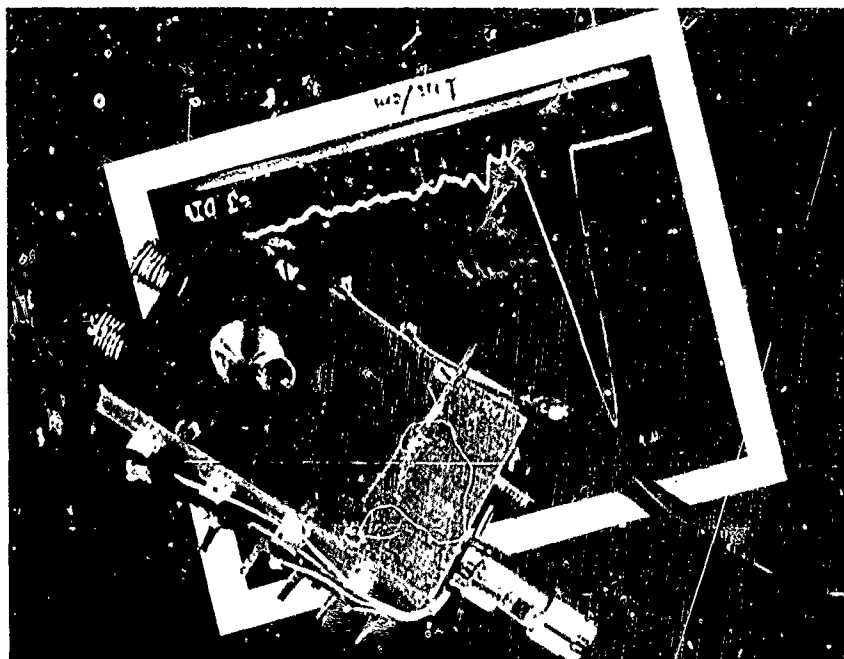


Fig. 1.1 Photograph of GAASFET preamp #8 shown with a signal-averaged oscilloscope trace showing the subnanosecond response of #8 (measured through cascaded B&H preamps) to a current impulse input of 4125 electrons (25 mV/cm vertical, 1nS/cm horizontal).

an optical receiver with transient response to the short modelocked laser pulses of 1ns or less (rise or fall from peak to baseline). While it is principally this wide bandwidth which pushes the state of the art in the optical modulator, in the receiver, it is necessary to have not only wide signal bandwidth, but in addition, extreme sensitivity in order to achieve acceptably low error rates in data detection with the very low signal power levels available at the receiver.

In the Air Force 405B gigabit laser communications system, as is often the case in systems work, the direction that the system development takes depends upon the availability (or non-availability) of certain key components. In this case one of the key factors giving rise to the present orientation of the 405B system is the lack of a suitable high quantum efficiency photocathode at the 1.064μ Nd-YAG laser line. If a high gain, high quantum efficiency photomultiplier for 1.06μ were available with the required speed, reliability and low noise count characteristics, they would represent a very attractive solution to the 1.06μ receiver problem. Of course, in a photomultiplier (or other shot-noise-limited) receiver approach, the modulator must have high extinction ratio for reasonable system performance. Because the electro-optic coefficients for most common modulator materials are considerably higher in the visible wavelength range than they are at 1.06μ , it is more difficult to fabricate a high-speed modulator at 1.06μ than it is at 0.53μ , for example, assuming the same materials are used. Of course, it should be possible to develop optimized 1.06μ modulator materials with some research effort, but at least from a close to "off the shelf" standpoint of the key devices (the modulator and receiver), the 1.06μ approach looks difficult (or at least did at the time of brassboard approach was committed).

Fortunately, while high quantum efficiency 1.06μ photomultipliers and high extinction ratio gigabit 1.06μ modulators were not available, another approach to laser communication using the Nd-YAG laser was -

doubling to 0.53μ . At 0.53μ , reasonably good quantum efficiency photocathodes ($\eta_{0.53\mu} \sim 20\%$ to 25%) are available. Consequently, a high-speed photomultiplier should, at least in principle, provide a reasonably sensitive low noise receiver at this wavelength. For example, assuming an ideal photomultiplier with no excess gain noise or spurious noise mechanisms, the photoelectron counting limit to distinguish a "1" from a "0" with an error probability of 10^{-6} when the sum of modulator zero feedthru, background photocurrent and photocathode dark current is 10% of the signal amplitude is 47 photoelectrons/bit (on a transmitted "1"). Hence, assuming a photocathode quantum efficiency of about $\eta_{0.53\mu} = 45\%$ a signal level of about 200 green photons on a received "1" would be required for the 10^{-6} BER.

While the 0.53μ frequency-doubled approach has the advantage of a higher state of modulator development and much higher quantum efficiency photomultipliers than are available at 1.06μ , there are significant disadvantages as well. For one thing, 0.53μ photons are much more "expensive" in terms of laser input power than 1.06μ photons. Even in an ideal doubler it would take two 1.06μ photons to make one 0.53μ photon; in practical systems a reasonable estimate is that 0.53μ photons are about three times as "expensive" as 1.06μ photons. Further, the frequency doubler itself is a somewhat "touchy" device. Certainly, given a reasonable 1.06μ modulator and sensitive 1.06μ detector, the 1.06μ approach would have to be given serious consideration. (The fact that the Rayleigh scattering for 1.06μ light is only one sixteenth that for 0.53μ light could be of some significance for satellite to ground links as well.)

These considerations, however, do not constitute a full system analysis since other factors and details need to be considered. For example, with a given optics size, the diffraction spreading for 1.06μ is twice as great as for 0.53μ .

An attractive solution to the 1.06μ receiver problem would be a stable, reliable all solid-state receiver using an avalanche photodiode detector. Unfortunately, the material from which the highest gain avalanche photodiodes have been fabricated, silicon, is virtually useless for this gigabit 1.06μ application. The problem is that silicon, an indirect bandgap semiconductor, has an optical absorption coefficient of only $\alpha_L = 10 \text{ cm}^{-1}$ at 1.064μ , which means that any device which has a depletion width large enough to have reasonable quantum efficiency at 1.06μ will have a transit time far too long for gigabit data rate use (the 1.06μ quantum efficiency-gain product will be $f_{3dB}\eta_{1.06\mu} < 40 \text{ MHz}$ for Si devices). For example, good high gain silicon APD's are available with 1.06μ quantum efficiencies of 15% or so, but their frequency response is barely 200 MHz. A silicon device could be fabricated with narrower depletion region to give adequate bandwidth for gigabit data rate use, but its 1.06μ quantum efficiency would be too low to be useful in the communications system. (On the other hand, a silicon APD of this type could make a good 0.53μ detector, since $\alpha_L \approx 10^4 \text{ cm}^{-1}$ for silicon at 0.53μ .)

What is required for a good high quantum efficiency, high speed, low noise 1.06μ avalanche photodiode is a direct bandgap semiconductor with an energy gap of about 1.1 eV and an optical absorption coefficient of about 10^4 cm^{-1} at 1.064μ . The ternary III-V semiconductor alloys can meet these requirements. In the work described here, we have fabricated $\text{GaAs}_{1-x}\text{Sb}_x$ avalanche photodiodes with 1.06μ quantum efficiencies of the order of 96%, junction capacitances of $C_j \sim 0.1 \text{ pf}$ and depletion region transit times of under 50 ps (under 20 ps in some devices). Since the bulk leakage currents of these devices are only about 300 pA, the photon-counting limit of such a detector (not considering excess avalanche gain noise or preamp noise) would be well under 100 photons/bit for a 10^{-6} BER. This would represent over a factor of 10 reduction in transmitter power relative to the 0.53μ approach.

Of course, in a real APD receiver, both the preamp noise and the excess avalanche gain noise are important, the former dominating for small APD gains ($M < 10$) and the latter at very high APD gains ($M > 200$; see Fig. 2.3). It is handy in an APD detector to have high avalanche gain so that one does not have to be particularly careful about the preamp noise, although operation with lower APD gain with a quieter preamp will always give better performance under the same conditions than using higher APD gain with a noisier preamp. Unfortunately, in the III-V alloy APD detectors, this is somewhat academic, as no one (either in our laboratory or elsewhere) has succeeded in repeatably attaining 1.06μ avalanche gains in the hundreds in ternary alloy APD's. In this work, the peak APD gains were of the order of 20-25 dB, which means that considerable care is required to limit preamp noise if high receiver sensitivity is to be attained. For this reason the contractual effort was shared between improving the heterojunction III-V alloy avalanche photodiode developed under previous contracts (Refs. 1 and 2) and developing an extremely low noise preamp to go with the APD. The goal of this research program was to develop a 1.06μ optical receiver capable of detecting a gigabit data rate binary-modulated modulated laser data stream with a $<10^{-6}$ bit error rate with a signal level of 1000 photons/bit for a received "1". (Such a receiver would have performance, in terms of required transmitter power, roughly equivalent to what could be accomplished with the 0.53μ frequency-doubled approach.)

The approach to this gigabit 1.06μ receiver development is to hybrid integrate the $\eta_{1.06\mu} = 96\%$ $\text{GaAs}_{1-x}\text{Sb}_x$ heterojunction avalanche photodiode with an extremely charge sensitive wideband preamp utilizing GaAs Schottky barrier field effect transistors (GAASFET's). The remarkable charge sensitivities attained in these receivers (as low as $N_0 = 347$ electrons in an input current pulse for a peak output equal to the rms noise output) are made possible by the exceptionally low APD junction capacitances (~ 0.1 pf) and GAASFET input capacitances (0.28 pf), combined with the reduced Johnson noise current attained by operating the

preamp in the negative feedback (transimpedance) mode. A picture of one of these receivers is shown in Fig. 1.1. Development of such a radical new preamplifier approach is an undertaking of considerable magnitude and was supported, along with this Air Force contract, by two NASA (GSFC) contracts (NAS5-23134 and NAS5-23333) for lower data rate 1.06 μ receivers. Because these contracts share with this Air Force work a common base of technology, the results for these NASA-delivered preamps is included in this report as an important background for understanding the Air Force gigabit receiver results. An important side benefit of this associated work was a NASA-funded comparison between available 1.06 μ detectors in terms of their performance in a 400 Mb/s 1.06 μ PGBM optical communications system at McDonnell Douglas Astronautics, St. Louis. The results of measurements on one of our GaAs_{1-x}Sb_x APD-GAASFET receivers which was optimized for use with this 400 Mb/s system gave bit error rate versus signal power performance in these system measurements in excellent agreement (Fig. 4.23) that calculated from our test data on the preamp. Biased for no detector avalanche gain at all, the receiver achieved a 10⁻⁶ BER with a lower signal level than the best Varian III-V alloy cathode PMT required at optimum gain. Operated at an avalanche gain of only M = 2, this receiver was more sensitive than two silicon avalanche photodiodes operated optically in series and electrically in parallel operated at a gain of M = 100. (Of course the speed of this silicon APD arrangement is far too low for gigabit use.) The receivers developed under this program have demonstrated that they are most sensitive wideband 1.06 μ optical receivers demonstrated anywhere.

The important question for the Air Force with regard to this receiver program is how does this 1.06 μ receiver impact the future of the 405B gigabit optical communication system program. How does our present performance compare with the system requirements and what can reasonably be expected in the future? The most sensitive GAASFET preamp

developed in this program has a maximum bit rate of nearly 1.5 Gb/s and requires a signal level difference between a "1" and a "0" of about $N_{ph} = 3440/M$ photons/bit (where M is the avalanche gain) to detect a 1.064μ modelocked laser pulse with a 10^{-6} error probability. While the peak avalanche gains obtained with these $GaAs_{1-x}Sb_x$ APD's are above $M = 10$ (20 dB), the average gains over the detector area are more of the order of 10 dB. Using this lower value for M , we see that we would require a bit over 1000 1.064μ photons/bit for 10^{-6} BER communications.

It should be noted that at these lower levels of avalanche gain, the required signal level is not a strong function of modulator extinction ratio (as it is with a PMT detector), so that the 1.06μ modulator problem is not so severe with this detector approach (see Fig. 2.4). As discussed in Section 4.1, the mechanisms limiting the avalanche gain in our current APD's are believed to be fairly well understood, so that there is every reason to expect to achieve much higher average avalanche gains with additional effort. Note that with the present receiver parameters with an average detector gain of 30 or more, the laser power required at the receiver would be only 10% to 20% of that required in the 0.53μ frequency-doubled approach. From the standpoint of the present level of performance and the improvements possible with further developmental effort, this heterojunction $III-V$ alloy APD-GASFET receiver work could have considerable impact on the future directions of the Air Force 405B gigabit satellite laser communication system.

1.2 Summary

The central effort in this program has been to develop a high quantum efficiency, low capacitance APD and an extremely charge-sensitive preamp to be hybrid integrated with the APD to make a very

low-noise, gigabit data rate receiver for 1.06 μ laser communications. This work has necessitated a number of corollary efforts including the development of special analytical tools such as a scanning laser microscope for the avalanche photodiode development, an analysis of the laser communication detection problem with special attention to the preamp noise-limited case, and the development of detailed signal and noise models for the integrated GAASFET preamps, along with special measurement techniques using a Tektronix Digital Processing Oscilloscope for experimentally determining the parameters of these models.

Many different analytical techniques are used in the GaAs_{1-x}Sb_x APD development work, varying all the way from specialized applications of the scanning electron microscope in microscopic compositional analysis of III-V alloy epitaxial layers to the use of our scanning laser microscope for studying the UHF avalanche gain uniformity of completed detectors. Some of these analytical techniques are described in detail in Section 3, but most are only briefly mentioned with references to more complete descriptions (Section 3.3.1). Because the Digital Processing Oscilloscope represents a new tool for electronic measurements, the application of which will not be familiar to most readers, this system is described in Section 3.3.7 and the methods of applying this system to the particular preamp measurement problems incurred in this work are discussed in Section 3.3.8. Appendix A contains the computer programs developed for the DPO to do everything from the measurement of noise histograms on preamps in order to be able to accurately predict their low bit error rate performance, to calculating preamp performance from circuit models. Also described in Section 3 are techniques for doing absolute noise measurements with Tektronix 7L13 spectrum analyzer. It should be commented that the rapid progress made in the integrated GAASFET preamp development (as seen in

Table 5.1 for example) is a consequence of the application of such sophisticated analytical tools as the DPO to gain an understanding of the problems encountered at each stage of the work in order to overcome them.

To develop an optical receiver optimized for a specific system application, it is first necessary to understand in detail the system so that the appropriate parameters are optimized. In Section 2.1, the detection process in an optical communications system based on on-off modulation of short modelocked laser pulses is analyzed. Special consideration here is given to the case where the preamplifier noise is dominant, as applies for low avalanche gains in these APD receivers. As is shown in Section 2.1.3, in preamp-noise-limited detections, the difference in the number of photons per bit between a "1" and a "0" required for optical communications at a given bit error rate (BER) is proportional to a factor depending on the BER (given in Table 2.1), inversely proportional to the quantum efficiency-gain product of the APD, and proportional to the "minimum detectable current pulse", N_0 for the preamp. This N_0 , which is the number of electrons in a current impulse into the preamp required to give an output pulse with a peak height equal to the rms output noise, is the key parameter to be optimized in the integrated GAASFET preamp. (Techniques for measuring N_0 directly are described in Section 3.3.10.) In the general case of both preamp and APD noise (appropriate for higher avalanche gains), discussed in Section 2.1.4 through 2.1.6, it is shown that as gain is increased, the most important parameters of the APD are quantum efficiency, quantum efficiency-gain product, dark leakage current and excess multiplication noise factor, in more or less that order. In general, the most sensitive receiver will be the one with the highest quantum efficiency and the lowest preamp noise (N_0), using just sufficient avalanche gain to raise the signal shot noise above the preamp (and the lower are the APD dark current and excess noise factors, the closer will be the results to those of an ideal receiver).

The design approach for attaining a high quantum efficiency 1.06μ avalanche photodiode are discussed in Section 2.2. The inverted homo-hetero-junction design brings the light directly into the depletion region through transparent GaAs substrate and $\text{GaAs}_{1-x}\text{Sb}_x$ buffer layers, giving high quantum efficiency, while the peak-field, high gain portion of the depletion region is at a p-n homojunction formed in uninterrupted liquid epitaxial growth by dropping a small amount of p-type dopant into the n^- active layer growth melt. Keeping the gain region away from either a heterojunction or epitaxial growth interface greatly reduces problems due to defect-produced microplasmas limiting gain. The results obtained with these $\text{GaAs}_{1-x}\text{Sb}_x$ homo-heterojunction APD's are discussed in Section 4.1. The "K-9" growth devices used in the integrated preamps have $\eta_{1.064\mu} \geq 96\%$ and for a 3-mil diameter device have a bulk leakage current of $I_b \approx 300$ pA, surface leakage current of about 3nA at a 50 volt bias increasing to ~ 100 nA near V_B (~ 120 volts), a junction capacitance of $C_j \approx 0.1$ pf and a spectral response width of about 1000\AA . The peak high frequency avalanche gains seen with these devices are up to 24 db in small areas, but the gains are nonuniform at the higher gain levels with only a few areas exceeding gains of 15 db or so. The average gains seen in normal defocused beam operation are typically 6-10 db. The principal limitations on the gains achieved with these devices are fluctuations in the active layer thickness due to surface morphology features in the liquid epitaxial growth and to the fact that the wrong complementary device type was used (see Section 2.2.2). The fact that the low-gain carrier was being used to provide the avalanche gain greatly exaggerates the gain nonuniformities which arise because of the fluctuations in the depletion region thickness. Future work will be directed toward correcting these problems and attaining more uniform gains.

The basic approach toward developing highly charge-sensitive (low N_0) gigabit preamps is discussed in Section 2.3. To obtain low N_0 , one must reduce the input capacitance of the preamp and the resistor thermal (Johnson) noise. The capacitance reduction is made possible by using a GaAs Schottky barrier field effect transistor (GAASFET) input. For example,

GAASFET preamp #8 has an input capacitance of about $C_{IM} \approx 0.28$ pf (plus $C_J = 0.1$ pf for the APD), much lower than could be obtained with a silicon bipolar transistor input. The low Johnson noise is obtained by going to a negative feedback type of first stage. In this approach, the first stage is used as an operational amplifier in the "transimpedance" mode with the feedback resistance, R_f , connected between the output and the (inverting) input. In this mode, R_f may be larger than a corresponding load resistance (to give the same bandwidth) by a factor approximately equal to the "op-amp" gain. Of course, for stable closed loop operation at frequencies approaching a gigahertz as desired here, the "op-amp" must have very low phase shift. The "op-amp" in GAASFET preamp #8 has an open-loop gain of about 20 with a gain-bandwidth product of about 5 GHz, enabling a closed-loop receiver f_{3db} of 620 MHz with a feedback resistance of $R_f = 5000\Omega$. The impulse response time for this receiver, shown in Fig. 1.1, is $\ln 5$ full width at 10% maximum and the peak to 5% fall time (665ps) would allow pulsed data reception to data rates on the order of 1.5 GHz before the onset of serious intersymbol interference. The minimum detectable current pulse for this preamp is $N_0 = 347$ electrons, about an order of magnitude better than typical 50Ω silicon bipolar wideband preamps for comparable pulsewidths. The characteristics of each of the preamps fabricated in either this Air Force work or the associated NASA contracts are described in Sections 4.2 through 4.4 and summarized in Table 5.1.

The conclusions from this work are discussed in Section 5 and will not be reiterated here. We have at the present the most sensitive optical receiver for detecting short 1.06μ modelocked laser pulses available. With further improvements in the avalanche gain characteristics in the $\text{GaAs}_{1-x}\text{Sb}_x$ detectors, we could achieve sensitivities perhaps an order of magnitude better than what we have now - a very exciting prospect indeed, both for the Air Force 405B laser communications system, and for other systems applications of 1.06μ receivers.

2.0 SYSTEM REQUIREMENTS AND DESIGN APPROACH FOR THE GIGABIT RECEIVER

The purpose of this work is to develop a gigabit bandwidth 1.06μ optical receiver suitable for use as the data receiver in the Air Force 405B gigabit data rate satellite optical communications system based on a modelocked Nd-YAG laser. Because these systems require, along with very high speed, exceptionally high receiver sensitivity (because of the low signal levels available over the long path lengths), the use of conventional low quantum efficiency 1.06μ detectors is precluded. The approach adopted for this solid state receiver is to combine a near-unity quantum efficiency 1.06μ photodiode of very low capacitance (for high charge pulse sensitivity) with a very low current noise, high charge sensitivity wideband preamp, with sufficient avalanche gain in the photodiode to attain the required performance. Since the performance requirements on the avalanche photodiode (APD) and preamp are dictated by the optical communication system application, it is relevant to begin with an analysis of the detector requirements in an optical communications system based on a modelocked laser.

2.1 Analysis of Detector Requirements in a Modelocked Laser Communications System

2.1.1 Optical Pulse Detection in the Poisson Limit

Consider an optical communications system effectively consisting of a modelocked laser putting out short light pulses (of width ΔT) at a repetition frequency (data rate) R or period (bit time) $T = 1/R$ (where $T \gg \Delta T$), followed by an optical modulator synchronized to the modelocked pulse stream. For our purposes, let us consider simple pulse-gate binary modulated (PGBM) operation in which pulses are either passed or "deleted," rather than the more complex PQM operation in which the "zero's" are not discarded, since the reduction of signal level by going to PQM from PGBM will be essentially the same for all detectors. The modelocked laser-modulator is followed by transmitting optics and a long path length to the receiving optics. While the number of transmitted photons per bit for each "1" (where a "1" is taken as a pulse passing with minimum attenuation through the modulator and a "0" is with maximum attenuation)

is relatively constant, the fact that over the long path lengths considered only a tiny fraction of the transmitted photons are collected by the receiver optics makes the received photon flux statistical in nature. (Both the optical absorption processes in media and the optics diffraction losses are statistically random processes, making the received signal pulses random when the received level is much less than the transmitted level.)

This statistically random nature of the received signal itself sets a limit to the performance which can be attained in an optical communications system. In concept, the very best performance that a receiver could attain would be to count all the photons arriving from the transmitter through to the receiver optics during each "bit time." (We assume throughout that the clock has been accurately extracted from the received data stream so that the bit interval is precisely known.) The statistically random nature of the received photons means that, for example, if when the transmitter is sending a "1" we receive an average number of photons \bar{n}_1 each bit time, then the probability for measuring n photons (n is of course a positive integer) in a bit time is given by the Poisson distribution as

$$P_1(n) = \frac{e^{-\bar{n}_1} \bar{n}_1^n}{n!} \quad (2.1)$$

An example of the application of Eq. 2.1 to ideal photon counting detection is shown in Fig. 2.1. Here we consider the case when an average of $\bar{n}_1 = 50$ photons/bit is received on a transmitted "1" and 10% of this or $\bar{n}_0 = 5$ photons/bit is received on a transmitted zero (either because of limited modulator extinction, background light or a combination of both). The probability distributions $P_1(n)$ for $\bar{n}_1 = 50$ and $p_0(n)$ for $\bar{n}_0 = 5$ are shown in Fig. 2.1 by circles and x's respectively (the lines connecting the points in some areas are for visualization purposes only; the Poisson distributions are defined only at integral values of n). Optimum communication is achieved by putting the "decision level" near the crossover points

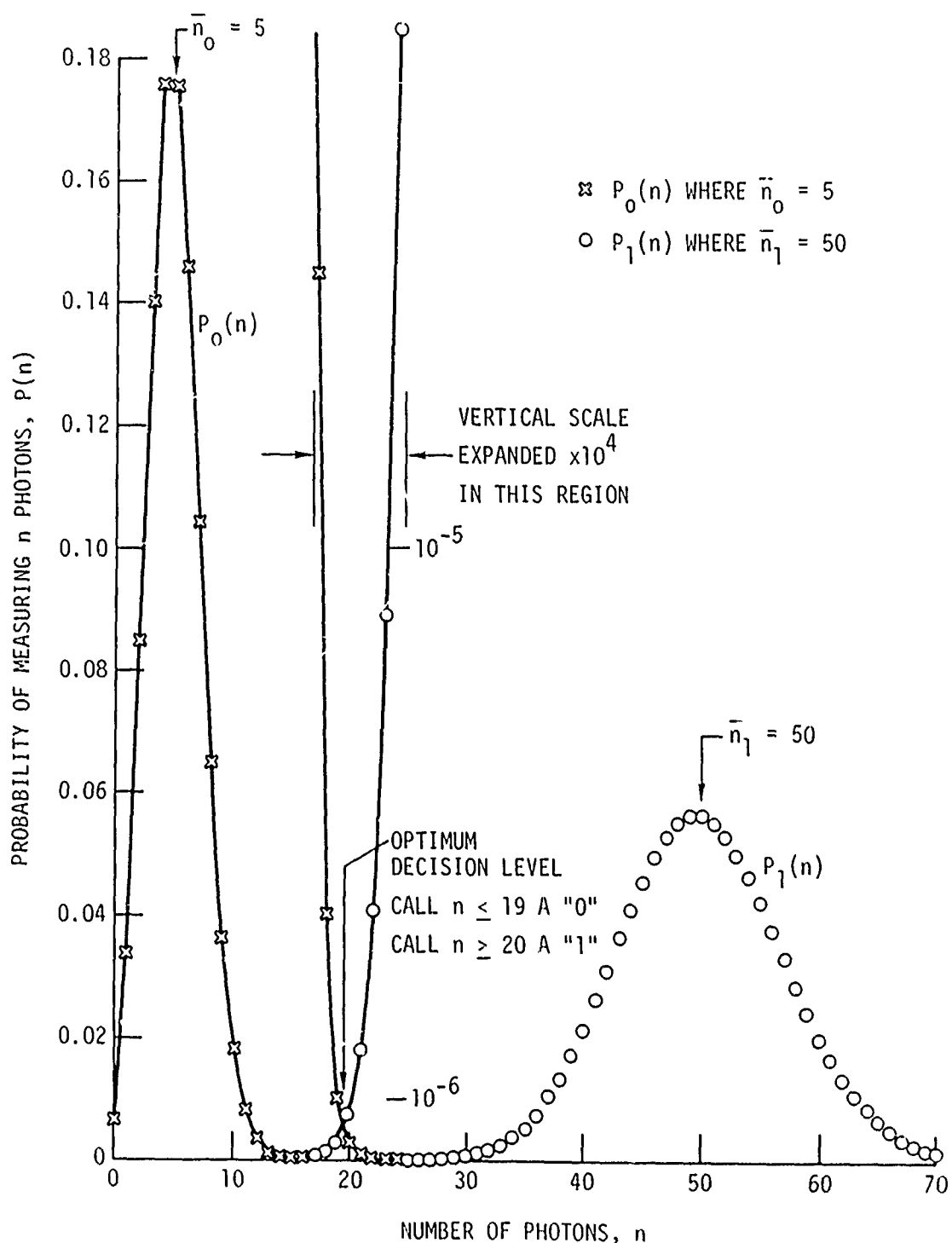


Fig. 2.1 Example of optical detection in the poisson (counting statistics) limit. For $\bar{n}_1 = 50$, $\bar{n}_0 = 5$, optimum decision level is to call $n \leq 19$ a "0" and $n \geq 20$ a "1", for which we obtain an average probability of error per bit of BER $4.12 \cdot 10^{-7}$.

of the probability distributions. In Fig. 2.1 for example, if we guess that any time we count 20 or more photons, then a "1" was transmitted and any time we count 19 or fewer photons a "0" was transmitted, we will minimize the percentage of time our guess is wrong (the bit error rate). Assuming equal numbers of "1's" and "0's" are transmitted, then the bit error rate (B.E.R.) will be given by

$$\text{B.E.R.} = \frac{1}{2} [\text{P.E. (1)} + \text{P.E. (0)}] \quad (2.2)$$

or

$$\text{B.E.R.} = \frac{1}{2} \left[\sum_{n=0}^{19} P_1(n) + \sum_{n=20}^{\infty} P_0(n) \right] \quad (2.3)$$

In Fig. 2.1, $\text{P.E. (1)} = 4.79 \times 10^{-7}$ and $\text{P.E. (0)} = 3.45 \times 10^{-7}$, so $\text{B.E.R.} = 4.12 \times 10^{-7}$ for this $\bar{n}_1 = 50$, $\bar{n}_0 = 5$ case ($S = \bar{n}_0/\bar{n}_1 = 0.1$). If we reduce the signal level slightly, the B.E.R. will increase; for example, for $\bar{n}_1 = 46.95$ photons/bit, $S = 0.1$ we have $\text{B.E.R.} = 10^{-6}$ (i.e., one error in one million received bits).

In fact, there is no such perfect "photon counter" detector which will give the performance described above. An electron multiplier, however, can in principal come quite close to achieving photo-electron counting. Hence in a photomultiplier with a cathode of quantum efficiency η electrons/photon, it should be possible to receive $S = 0.1$ data with $\bar{n}_{e1} = 47$ photoelectrons/bit or $\bar{n}_1 = n_{ph} = 47/\eta$ photons/bit. (Unfortunately, "real life" photomultipliers often do not achieve this because of other extraneous noise sources). Other detector approaches such as the avalanche photodiode receiver depart even further from this simple Poisson statistics-photon (or photoelectron) counting model. Here the preamplifier noise (Johnson noise), dark current shot noise, and excess avalanche gain noise

on the signal and dark currents must be considered over and above the counting statistics noise (shot noise) of the signal itself. While APD receivers do indeed have extra noise sources, it should be noted that their high quantum efficiencies can make it possible for the APD receiver to go to lower signal levels for the same B.E.R. than a low quantum efficiency "ideal" photomultiplier. To demonstrate this we must redo the simple Poisson statistics analysis including preamplifier noise-which means treating the Gaussian statistics case.

2.1.2 Detection of Modelocked Laser Pulses with an Avalanche Photodiode Receiver

In an avalanche photodiode receiver, there exist both signal-independent noise sources such as the preamplifier noise and signal-dependent noise (i.e., the multiplied shot noise on the received signal). In general we can treat this mixed noise case by using Gaussian statistics which describe the preamp noise exactly and even give quite a good approximation to the signal level results for the purely shot-noise-limited case treated in Section 2.1.1 using Poisson statistics. When signal-independent noise sources are present (such as preamp Johnson noise or shot noise on leakage current or background light flux), the width of the received modelocked laser pulses and the bandwidth or impulse response of the receiver become very important. In the following analysis, we first describe the general pulse detection process in the presence of certain levels of Gaussian noise on a transmitted "1" and a transmitted "0". We then consider the limit of signal-independent noise only (preamp noise dominant) before going on to the general case of both signal dependent and signal independent noise.

Let us specifically consider the case in which the optical communications data is transmitted as a binary modulation of modelocked laser pulses, where the pulse width, ΔT , is much less than the repetition period, T ($T = 1/R$, where R is the data rate). We wish to calculate the number of photons per bit, N_{ph} , required to transmit data at some specified bit error rate (B.E.R.) where N_{ph} photons are on the average received at the detector during a transmitted "1", and SN_{ph} (where $S < 1$)

is the mean number of photons received for a transmitted "0" (if we ignore any background light, S is the modulator "zero feedthru" or reciprocal of the modulator extinction ration [E.R.]). For purposes of our discussion the system is specified by S , ΔT and B.E.R., and the detector performance is to be evaluated on the signal level, N_{ph} , required to give that bit error rate (B.E.R.).

Figure 2.2. is a generalized description of the avalanche photodiode receiver portion of the system. Here the avalanche photodiode is indicated by a current source, $i_p(t)$, in parallel with some shunt conductance, G_{IN} (G_{IN} is typically a small capacitance). For short transit times in the APD, the photocurrent, $i_p(t)$, will be a replica of the light pulse; that is

$$i_p(t) = \eta M I_{ph} \quad (\text{for } T_{TR} \ll \Delta T). \quad (2.4)$$

Here, η is the quantum efficiency, M the avalanche gain, and I_{ph} is the "photon current" or q (the electronic charge, 1.602×10^{-19} coul) times the number of photons per second. Whether or not this "quasi steady state" condition of the transit time T_{TR} being much less than the pulsewidth is satisfied, the integrated charge in the current pulse, Q_p , will be given by

$$Q_p = \int_0^1 i_p(t) dt = q \eta M N_{ph} \quad (2.5)$$

where N_{ph} is the number of photons per bit arriving at the detector.

For our purposes only two characteristics of the preamplifier are of import; the output voltage pulse response to the input current pulse $i_p(t)$ and the output voltage noise. Both of these must be specified under the condition where the input is shunted by the APD shunt conductance, G_{IN} . In general, the exact current pulseshape, $i_p(t)$ must be used in determining the amplifier response $V_o(t)$, but when the current pulse is

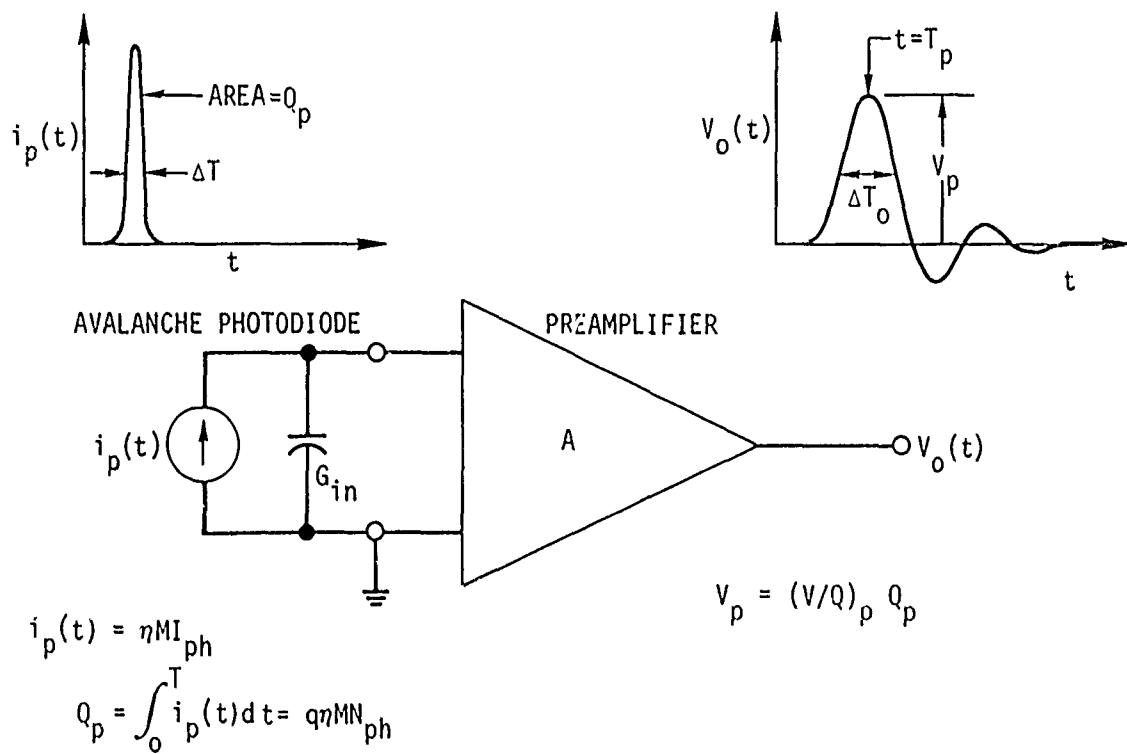


Fig. 2.2 Schematic of avalanche photodiode receiver defining response parameters.

considerably faster than the amplifier pulse response, as shown in Fig. 2.2, $V_o(t)$ becomes essentially the δ -function current pulse response, with $V_o(t)$ proportional to the charge in the current pulse, Q_p . In general, if we have the output response to a current impulse $[i_p(t) = Q_p \delta(t-t_o)]$, which we will refer to as $V_\delta(t)$, then we can obtain the response to any real input $i_p(t)$ by convolving $V_\delta(t)$ with $i_p(t)$. For acceptable application in communications, the transient response $V_o(t)$ must have declined to some very small fraction of the peak response (V_p) within one bit time of the peak response. (To the extent to which this is not satisfied, succeeding pulses will overlap, causing the judgement of whether a received bit is a "zero" or a "one" to be influenced by whether the preceding pulse was a "zero" or a "one"; this condition degrades the accuracy of the decision process, making it necessary to increase N_{ph} in order to achieve a given B.E.R. in much the same way as the modulator "zero feedthru", S , increases N_{ph} . We assume here that $V_o(T_p+T)/V_p \ll S$ or V_{no} so that this "bit tailing" will have no significant effect.)

Attaining the lowest possible error rate from the output of this optical receiver requires using an extracted clock to effectively sample the output when the signal-to-noise ratio is at its highest (i.e., at time T_p in Fig. 2.2.) Hence, the critical parameters of the preamplifier are the peak output voltage (V_p in Fig. 2.2), and the rms output voltage noise, v_{no} . Since V_p is proportional to Q_p , we can express this as

$$(V/Q)_p = V_p/Q_p. \quad (2.6)$$

For an impulse current input $i_p(t) = Q_p \delta(t)$, this quantity will be referred to as $(V/Q)_\delta$. In general, for input current pulse widths, ΔT , short with respect to the output pulsewidth, $(V/Q)_p \simeq (V/Q)_\delta$; otherwise, $(V/Q)_p$ is somewhat less than $(V/Q)_\delta$ by factor determined by convolving $i_p(t)$ and $V_\delta(t)$ as described previously.

In order to calculate the error probability, let us assume the preamplifier output noise is Gaussian with a standard deviation equal to the rms noise voltage, v_n . We also assume we have an ideal sampler and level detector (comparator) following the preamplifier such that if the peak output voltage at the sample time (T_p in Fig. 2.2) exceeds a threshold level V_D , then the received bit is called a "1", and if $V_o(T_p)$ is less than V_D , the bit is identified as a "0". The probability of error on a transmitted "1" is just the probability that the instantaneous signal plus noise when the sample is taken will be below V_D (where, of course, V_D is between the mean signal for a received "1", V_{p1} and the mean signal for a received "0", V_{p0}). In analogy to Eqs. 2.2 and 2.3 for the discrete case, this can be expressed in terms of the integral over the "tail" of the Gaussian probability density, $P_1(V)$, extending beyond V_D as

$$P.E.(1) = \int_{-\infty}^{V_D} P_1(V) dV = Q \left(\frac{V_{p1} - V_D}{v_{n1}} \right) \quad (2.7)$$

where the Q function is the Gaussian "tail" integral

$$Q(x) = \frac{1}{\sigma\sqrt{2\pi}} \int_x^{\infty} e^{-\frac{t^2}{2\sigma^2}} dt \quad (2.8)$$

which may be obtained in standard statistical tables⁽³⁾, and we have taken $\sigma = v_{n1}$, the total output noise when a "1" is received. Similarly, we have the error probability on a zero given by

$$P.E.(0) = \int_{V_D}^{\infty} P_0(V) dV = Q \left(\frac{V_D - V_{p0}}{v_{n0}} \right) \quad (2.9)$$

If we have equal numbers of transmitted "0's" and "1's", then we can very nearly optimize the decision level V_D for minimum total error rate by letting $P.E.(0) = P.E.(1)$. (This equates the probability integrals; for exact optimization we should equate the probability

densities , but this approximation is extremely accurate for the cases of interest here and leads to considerably simpler equations for the results.) Equating equations 2.7 and 2.9, we have

$$\frac{V_{P1} - V_D}{V_{n1}} = \frac{V_D - V_{P0}}{V_{n0}} \quad \text{or} \quad V_D = \frac{V_{n0}V_{P1} + V_{n1}V_{P0}}{V_{n1} + V_{n0}} \quad (2.10)$$

Substituting V_D back into the error expressions, we have

$$\text{B.E.R.} = \text{P.E.}(1) = \text{P.E.}(0) = Q\left(\frac{V_{P1} - V_{P0}}{V_{n1} + V_{n0}}\right) \quad (2.11)$$

The expression in parenthesis is in effect a "signal to noise ratio" and will be designated by

$$\text{S.T.N.} \equiv \frac{V_{P1} - V_{P0}}{V_{n1} + V_{n0}} \quad (2.12)$$

and in terms of this, the bit error rate is given by

$$\text{B.E.R.} = Q(\text{S.T.N.}) \quad (2.13)$$

for example, for $\text{S.T.N.} = 4.75342$, the error rate is $\text{B.E.R.} = 10^{-6}$, the nominal bit error rate specification for the APD receiver under this contract. The relationship between B.E.R. and S.T.N. is given for decade B.E.R. values in Table 2-1 (taken from Ref. 3).

TABLE 2.1

<u>B.E.R.</u>	<u>S.T.N.</u>	<u>B.E.R.</u>	<u>S.T.N.</u>
10^{-1}	1.28155	10^{-8}	5.61200
10^{-2}	2.32635	10^{-9}	5.99781
10^{-3}	3.09023	10^{-10}	6.36134
10^{-4}	3.71902	10^{-11}	6.70602
10^{-5}	4.26489	10^{-12}	7.03448
10^{-6}	4.75342	10^{-13}	7.34880
10^{-7}	5.19934	10^{-14}	7.65063

Table 2.1 Required values of "signal-to-noise ratio",

$$\text{S.T.N.} = \frac{V_{p1} - V_{p0}}{V_{n1} + V_{n0}} \text{ to give the given values of received bit error rate.}$$

2.1.3 Avalanche Photodiode Receiver Performance in the Preamp Noise Limited (Low Avalanche Gain) Region

Of particular interest for this work is the low APD gain limit of signal-independent noise which leads to a simple closed form solution for the required signal level to achieve a specified B.E.R. and identifies the crucial preamp performance parameter for modelocked pulse optical communication. For the specific case of preamplifier noise dominated operation being considered here, we have the output noise independent of the input signal level, i.e., $v_{n1} = v_{n0}$, with both these just equal to the preamplifier rms output noise voltage which we have previously referred to as v_{no} (i.e., $v_{n1} = v_{n0} = v_{no}$). Also, we assume that since $N_{ph}(0) = SN_{ph}$ where N_{ph} is the mean number of photons received at the detector for a transmitted "1" and S is the modulator "zero feedthru" (typically S is of the order of 0.1), from Eq. 2.5 we have $Q_p(0) = SQ_p(1)$ and hence from Eq. 2.6, $V_p(0) = SV_p(1) = SV_p$. Rewriting Eq. 2.12 for this case we have

$$\text{S.T.N.} = \frac{V_p (1-S)}{2 v_{no}} \quad (\text{for } v_{n1}=v_{n0}=v_{no}, V_p(0)=SV_p). \quad (2.14)$$

If we specify the value of S.T.N. to be the minimum acceptable to give the desired B.E.R., then Eq. 2.14 can be used to determine the minimum acceptable mean output pulse height for a received "1", V_p , as

$$V_p = \frac{2 v_{no} (\text{S.T.N.})}{1-S} \quad (2.15)$$

Substituting Eq. 2.6 gives the expression for the minimum acceptable mean charge in the photocurrent pulse for a received "1", Q_p as

$$Q_p = \frac{2 v_{no} (\text{S.T.N.})}{(V/Q)_p (1-S)} \quad (2.16)$$

where $(V/Q)_p$ is the preamplifier current pulse peak response parameter (Fig. 2.2 and Eq. 2.6). Using Eq. 2.5, we obtain the key system performance parameter N_{ph} , the minimum (average) number of photons/bit arriving at the detector to obtain the desired bit error rate, as

$$N_{ph} = \frac{2 v_{no} (\text{S.T.N.})}{q\eta M (V/Q)_p (1-S)} \quad (2.17)$$

It is instructive to rearrange Eq. 2.17 in terms of the system, avalanche photodiode, and preamplifier parameters as

$$N_{ph} = \underbrace{\left(\frac{2(\text{S.T.N.})}{q(1-S)} \right)}_{\text{SYSTEM}} \underbrace{\left(\frac{1}{\eta M} \right)}_{\text{APD}} \underbrace{\left(\frac{v_{no}}{(V/Q)_o} \right)}_{\text{PREAMP}} \quad (2.18)$$

Here the system is characterized by the modulator "zero feedthru" S and the required "signal-to-noise ratio", S.T.N. (where $Q(\text{S.T.N.}) = \text{B.E.R.}$ as given in Table 2.1); the avalanche photodiode is characterized by its quantum efficiency-gain product, ηM ; and the preamp is characterized by its peak current pulse response, $(V/Q)_p$ (see Eq. 2.6) and its rms output noise, v_{no} . The preamp which we shall call the "minimum detectable current pulse" of the preamp, N_o , where N_o is given by

$$N_o = \frac{v_{no}}{q(V/Q)_p} \quad (\text{electrons}). \quad (2.19)$$

N_o is just the number of electrons in the current pulse (Fig. 2.2) required to produce an output voltage pulse of peak amplitude (V_p) equal to the rms output noise voltage[†]. Expressing the preamp response in terms of N_o , Eq. 2.18 factors into three convenient dimensionless quantities (actually, the units of N_o for the preamp is electrons and the units of ηM for the APD is electrons per photon giving the units of N_{ph} as photons):

$$N_{ph} = \underbrace{\left(\frac{2(\text{S.T.N.})}{(1-S)} \right)}_{\text{SYSTEM}} \underbrace{\left(\frac{1}{\eta M} \right)}_{\text{APD}} \underbrace{N_o}_{\text{PREAMP}} \quad (2.20)$$

[†] Actually the term N_o in Eqs. 2.19 and 2.20 might better be referred to as N_{op} since it in general depends upon the input pulse shape, reserving the term N_o for the δ -function response case; $N_o = v_{no}/q(V/Q)_\delta$. However, for most of the cases of interest the light pulse is considerably shorter than the response pulse so $(V/Q)_p \approx (V/Q)_\delta$ and with the light pulse as described previously.

We see from Eq. 2.20 that in this low APD gain (low M) limit of operation in which the preamplifier noise is dominant, the required signal level is dependent on the system parameters of bit error rate and (weakly) the modulator extinction ratio (through S.T.N. and S), the quantum efficiency-gain product of the APD, ηM , and the minimum detectable current pulse of the preamp, N_0 . Our approach to obtaining a high sensitivity avalanche photodiode optical receiver is to combine an APD of sufficient ηM product with a preamp of very low N_0 (high charge-pulse sensitivity) in order to obtain a high photon pulse sensitivity. This charge pulse sensitivity figure of merit for the preamp, N_0 , can be directly measured for a given discrete or hybrid preamp by using the methods described in sections 3.3.8 through 3.3.11 of this report.

2.1.4 High Avalanche Gain Performance of the APD Receiver

The general signal-dependent noise case (including both multiplied shot noise and preamp noise) cannot be solved in closed form for the required number of photons/bit as in Eq. 2.20, but it can rather easily be iteratively solved on a digital computer for given parameter values. Recalling that the Gaussian noise analysis of Eqs. 2.4 through 2.13 apply to the general case of signal dependent noise, i.e., $V_{n1} > V_{n0}$ (as opposed to Eqs. 2.14 through 2.20 which apply only to $V_{n0} = V_{n1} = V_{no}$), what is required is to find the value of signal level which will solve Eq. 2.12 for the given parameter values. Writing Eq. 2.12 in terms of equivalent input currents instead of output voltages[†] will make the various signal and noise terms clearer and more familiar. In terms of equivalent input currents to the preamp, we must raise the signal level into the preamp sufficiently so that we have an adequate value of "signal to noise

[†] In general there will be some overall transimpedance for the preamplifier, (V/I) , which will relate steady state output voltages to the input currents; $V_{no} = (V/I)i_{no}$, $V_{p1} = (V/I)I_1$, etc.

ratio", S.T.N. to give the required bit error rate (Eq. 2.13 and Table 2.1), where S.T.N. is given by

$$\text{S.T.N.} = \frac{I_1 - I_0}{i_{n0} + i_{n1}} \quad (2.21)$$

Here I_1 and I_0 are the peak equivalent input currents from the APD into the preamp for a received "1" and "0" respectively, while i_{n0} and i_{n1} are the equivalent input noise currents during received "0's" and "1's". If N_{ph} photons/bit are received on a transmitted "1" and the output pulsewidth is ΔT_0 in Fig. 2.2, then the equivalent average input "photon current" over the pulse, I_{ph} will be

$$(I_{ph})_1 = \frac{q N_{ph}}{\Delta T_0} \quad (2.22)$$

or the average signal current from the APD will be (Eq. 2.4)

$$I_1 = \frac{q\eta M N_{ph}}{\Delta T_0} \quad (2.23)$$

for a transmitted "1", while $I_0 = SI_1$ (where S is the modulator "zero feedthru". The total equivalent input noise current for the preamp, including both multiplied shot noise and preamp noise will be given for a transmitted "1" by

$$i_{n1} = \sqrt{2q\Delta FM^{2+x_n} \left(\frac{q\eta N_{ph}}{\Delta T_0} + I_B \right) + (NF) \frac{4kT\Delta F}{R_L}} \quad (2.24)$$

(i_{n0} is the same except for replacing N_{ph} by SN_{ph}). The right hand term in Eq. 2.24 is just the preamplifier noise contribution (squared), written

in the form of the Johnson noise on a load or feedback resistance R_L ($4kT = 1.62904 \times 10^{-20} \text{ J}$ at 295°K) times a noise factor accounting for the excess noise of the preamp over and above the Johnson noise ($\text{NF} = 10$ (Noise Figure in db)/10). The lefthand term is the multiplied shot noise on the photocurrent plus bulk leakage current term in parenthesis. Here the quantity χ_n is the excess avalanche gain noise term for the APD, a factor which depends on the APD device structure and the relative ionization coefficient between holes and electrons (α_n and α_p). If $\chi_n = 0$, the signal-to-noise ratio (ratio of I_1 to i_{n1} in 2.23 and 2.24) would be independent of M in the shot noise limited region where the preamp term in 2.24 is negligible; the magnitude of χ_n is a measure of what the use of avalanche gain is "costing" in terms of enhanced shot noise. (χ_n is about 0.3 for well-designed silicon APD's where $\alpha_n > \alpha_p$ and $\chi_n \sim 1$ for germanium APD's.) I_B in Eq. 2.24 is the bulk or multiplied leakage; surface or unmultiplied leakage in the APD produces little noise since it is not multiplied by $M^{2+\chi_n}$ as are I_B and the photocurrent.

The only term in Eq. 2.24 which is "not obvious" is what to take as the noise measurement bandwidth, ΔF . We know, of course, that it will be reciprocally related to the output pulsewidth, ΔT_0 , but it is important to have the correct proportionality constant or the magnitude of the shot noise will come out wrong. We can simply obtain the correct relationship between ΔF and ΔT_0 by considering an ideal photodiode ($\eta = 1$, $M = 1$, $I_B = 0$ and no preamp noise) detecting a "square" pulse of N_{ph} photons of width ΔT_0 . From Eq. 2.23 and 2.24, we have as the "signal-to-noise ratio",

$$\frac{S}{N} = \frac{I_1}{i_{n1}} = \frac{\frac{q N_{ph}}{\Delta T_0}}{\sqrt{2q\Delta F \left(\frac{q N_{ph}}{\Delta T_0} \right)}} \quad (2.25)$$

We can obtain the correct value for S/N by applying Gaussian statistics to the photon counting process, itself. For example, in Fig. 2.1, the $\bar{n}_1 = 50$ Poisson distribution curve is quite accurately approximated by a Gaussian distribution with a standard deviation (rms noise) of $\sigma_1 = \sqrt{\bar{n}_1} = \sqrt{50}$ electrons (a consequence of the general theorem that the variance is given as the square root of the mean). Hence, we have the correct shot noise limited signal to rms noise ratio for counting N_{ph} photons as

$$S/N = \frac{N_{ph}}{\sqrt{N_{ph}}} = \sqrt{N_{ph}} \quad (2.26)$$

Equating S/N expressions in Eqs. 2.25 and 2.26 allows us to solve for ΔF :

$$\Delta F = \frac{1}{2\Delta T_0} \quad (2.27)$$

as the correct relationship between the noise bandwidth in Eq. 2.24 and the output pulsewidth, ΔT_0 to give the correct shot noise limit.[†]

The procedure for obtaining the required signal level for PGBM optical communication with a given bit error rate (S.T.N. value from Table 2.1) is to pick a value for N_{ph} , calculate I_1 , I_0 , i_{n1} and i_{no} using the N_{ph} value in Eqs. 2.23 and 2.24 along with the other receiver parameters and solving for S.T.N. in Eq. 2.21. If the trial S.T.N. is less than the

[†] That this is a reasonable result can be noted by considering a pulse of the form of one cycle (0 to 2π) of $V(t) = 1 - \cos 2\pi\Delta Ft$. The 50% points of the pulse would be at $t = 1/4\Delta F$ and $t = 3/4\Delta F$, or $\Delta T_0 = 1/2\Delta F$ as in Eq. 2.27.

required S.T.N. for the specified B.E.R., the N_{ph} value is increased and the process repeated to obtain the minimum N_{ph} which will give the required S.T.N. value. A listing is given in Appendix A.1 for a computer program written in the APL language to carry out this iterative solution for N_{ph} . The iterative process converges rapidly and takes little computer time. The parameter identification in the program is the same as that used above except that for the quantity "R" in the program, use $1/\Delta T_0$ and ignore the identification of R as the data rate (the program was originally written for the special case of non-pulsed data transmission where $1/\Delta T_0 = R$). Actually, the definition of ΔT_0 from Fig. 2.2 is not precise, and the best way to insure that the preamp noise contribution is accurately accounted for is to use Eq. 2.20 to determine the value of N_{ph} for $M = 1$, then run the computer program with $M = 1$ and adjusting $1/\Delta T_0$ ("R" in the program listing) to give exact agreement with the result from Eq. 2.20. If the correct value of current noise spectral density for the preamp has been taken ($[NF] 4kT/R_L$) then the value of T_0 should be close to the half width of the output pulse. A check on this preamp noise term is that the total preamp equivalent input noise should be $i_{np} = [NF]2kT/\Delta T_0 R_L$. This correctly adjusted $1/\Delta T_0$ (or "R") value not only determines the correct preamp noise limit, but also determines the influence of the detector leakage (or background photocurrent), I_B . Further details on this calculation including the effects of some of the major parameters are shown in Appendix I of Ref. 2.

2.1.5 Comparison of Various Receiver Approaches for Gigabit Nd-YAG Laser Communication

The results of a calculation of the required signal level, N_{ph} (photons/bit) for 10^{-6} bit error rate modelocked laser PGBM communication system as is shown in Fig. 2.3 a function of the internal detector gain, M, for several 1.06 μ receiver approaches. The "ideal photomultiplier" curves in Fig. 2.3 at high M values approach the photon counting limit of $N_{ph} = 47/\eta$ photons/bit described in connection with Eq. 2.3 (and Fig. 2.1) and hence in Fig. 2.3 a selected S-1 photocathode PMT with $\eta_{1.06\mu} = 0.1\%$

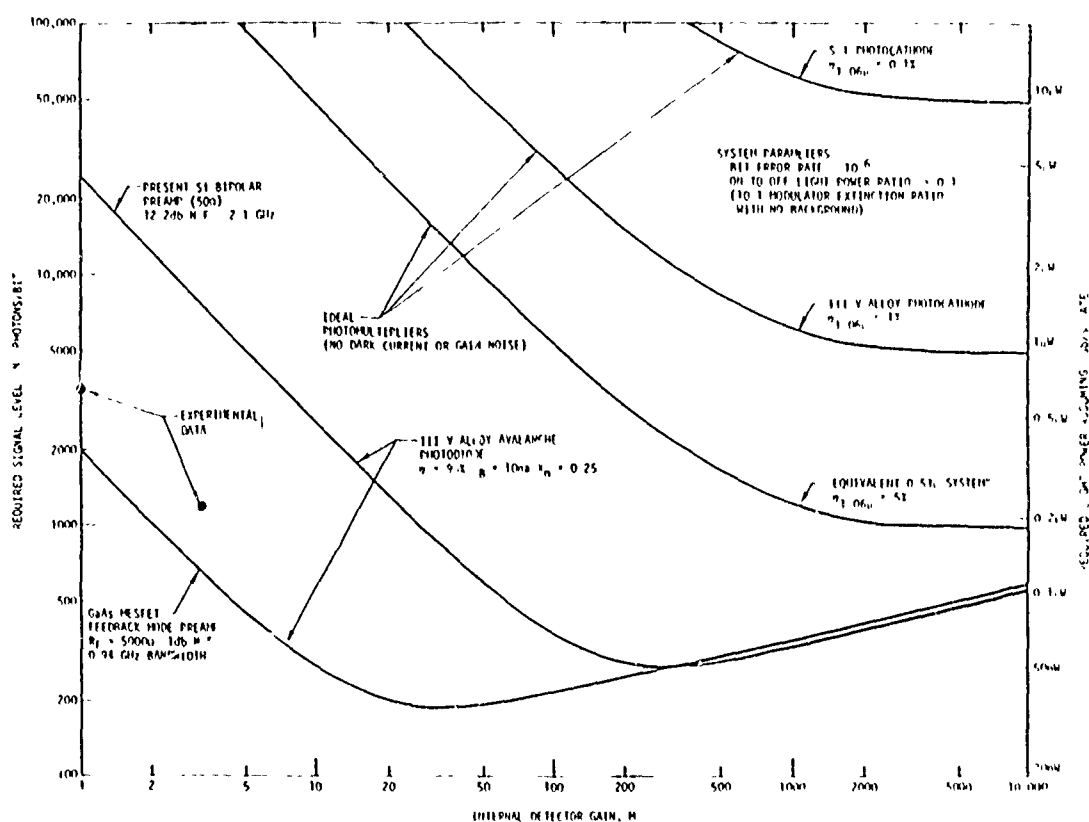


Fig. 2.3 Comparison of the calculated performance of various 1.06 detectors as 400 Mb/s PGBM modelocked laser communications receivers. Plotted is the number of photons per bit required for 10^{-6} bit error rate data reception as a function of internal detector gain. $N_0=175$ electrons assumed for lowest curve GAASFET preamp as a goal; best performance achieved to date is $N_0=347$ electrons for preamp #8, the curve for which would lie a factor of 2 above this for low M .

could reach $N_{ph} = 47,000$ photons/bit, while a III-V alloy cathode with $\eta_{1.06\mu} = 1\%$ should be able to reach 4700 photons/bit. (In fact actual PMT tubes often don't do this well because of extraneous noise sources, but in principal they should be able to achieve this performance. Compared with these PM tube approaches in Fig. 2.3 are two avalanche photodiode receivers, one using a conventional silicon bipolar transistor preamp ($N_o \sim 2250$ electrons assumed) and the other using a much more charge-sensitive GAASFET feedback mode preamp ($N_o = 175$ electrons assumed as a possibly attainable value; we have to date achieved twice this). We have taken $\eta_{1.06\mu} = 95\%$ and $I_B = 10nA$ as representative of our $GaAs_{1-x}Sb_x$ APD's (actually our devices are usually better than this) and we assume an x_n value of 0.25. We see in Fig. 2.3 that the high Johnson noise 50Ω preamp would require large amounts of avalanche gain ($M > 25$) to achieve $N_{ph} \leq 1000$ photons/bit operation. With a very charge-sensitive preamp, however, gains of only $M > 2$ would be sufficient to achieve this performance. The optimum gain for the latter case (which depends strongly on the x_n and I_B values assumed) is lower ($M_{opt} \sim 30$) and the ultimate performance considerably better than could ever be attained with a 50Ω preamp even if the $M_{opt} \sim 300$ gain values required could be attained. It is for this reason that our gigabit 1.06μ receiver effort is directed both toward attaining a high quantum efficiency APD with reasonably high gain and toward developing an extremely charge sensitive wideband preamp for the APD.

2.1.6 Influence of Modulator Extinction Ratio on Communication Performance with Different Receiver Approaches

From discussions with various people, it appears that there is a widespread misunderstanding regarding the significance of modulator

extinction ratio on 1.06 μ laser communications. The point of confusion centers on the reasoning that 1) we know that in the 0.53 μ approach it is essential to have a high modulator extinction ratio for acceptable system performance and 2) we know that in current technology the performance of 1.06 μ modulators is not as good as at 0.53 μ making such high extinction ratios unattainable at present; hence 3) we must conclude that the 1.06 μ approach to laser communications is impractical even if a satisfactory high quantum efficiency avalanche photodiode receiver is available. This reasoning is in gross error and the conclusion totally invalid.

The source of the confusion stems from drawing an invalid analogy between the 0.53 μ (frequency doubled transmitter-photomultiplier detector) approach, which represents an almost ideal shot noise limited system, and the 1.06 μ (direct laser-avalanche photodiode receiver) approach which is typically a preamp (Johnson) noise limited system in which high sensitivity is attained by virtue of the high detector quantum efficiency. In a shot noise limited system, Eqs. 2.12 or 2.21 can be rewritten in terms of the mean number of photoelectrons in a detected modelocked laser pulse, n , in the Gaussian approximation as

$$S.T.N. = \frac{\bar{n}_1 - \bar{n}_0}{\sigma_1 + \sigma_0} = \frac{\bar{n}_1 - \bar{n}_0}{\sqrt{\bar{n}_1} + \sqrt{\bar{n}_0}} \quad (2.28)$$

Using $\bar{n}_0 = S \bar{n}_1$, where S is the "modulator zero feedthru" or reciprocal of the extinction ration, and calling $N_{ph} \equiv \bar{n}_1$, we have

$$S.T.N. = \sqrt{N_{ph}} \left(\frac{1 - S}{1 + \sqrt{S}} \right) \quad (2.29)$$

or, the required signal level for a given S.T.N. (as obtained from B.E.R. from Table 2.1) will be

$$N_{ph} = (S.T.N.)^2 \left(\frac{1 + \sqrt{S}}{1 - S} \right)^2 \quad (2.30)$$

Equation 2.30 is, of course, only an approximation since Gaussian statistics have been assumed rather than the correct discrete Poisson statistics appropriate for the photon counting mode of operation assumed here. Even so, Eq. 2.30 is fairly accurate, particularly for higher values of S , as is shown in Fig. 2.4 where Eq. 2.30 is plotted ("Gaussian Approximation") for $S.T.N. = 4.75342 (10^{-6} \text{ B.E.R.})$ along with the results from Poisson statistics for a 10^{-6} bit error rate (calculated using Eqs. 2.1 to 2.3 as in Fig. 2.1). The number of photo-electrons is indicated on the scale on the right, while the number of photons incident on the detector, N_{ph} is shown on the left assuming a 5% effective 1.06μ quantum efficiency. The important thing to note from Eq. 2.30 and these photomultiplier curves of Fig. 2.4 is the strong dependence of the required number of photons/bit on the modulator "zero feedthru", S , or extinction ratio (scale at top of Fig. 2.4). With an extinction ratio of 200:1 ($S=0.005$) the $\eta = 5\%$ photomultiplier requires 454 photons/bit, while at $E.R. = 10:1 (S=0.1)$ the signal level must be increased a factor of 2 to 939 photons/bit. If the zero feedthru, $S=0.2 (E.R.=5)$, the signal level would have to be 1454 photons/bit, over triple that for the 200:1 case.

Hence, we conclude that for this photomultiplier case (1.06μ or 0.53μ) with zero background light, it is indeed extremely important to make the extinction ratio very high. However, this discussion and conclusion regarding the 0.53μ approach have virtually no relevance to the 1.06μ approach using an avalanche photodiode detector.

For the A.P.D. receiver with integrated GAASFET preamp operating with relatively low avalanche gain (in the $N_{ph} \propto 1/M$ region in Fig. 2.3; $M < 10$), we can obtain N_{ph} from Eq. 2.20. For 10^{-6} B.E.R. ($S.T.N. = 4.7534$)

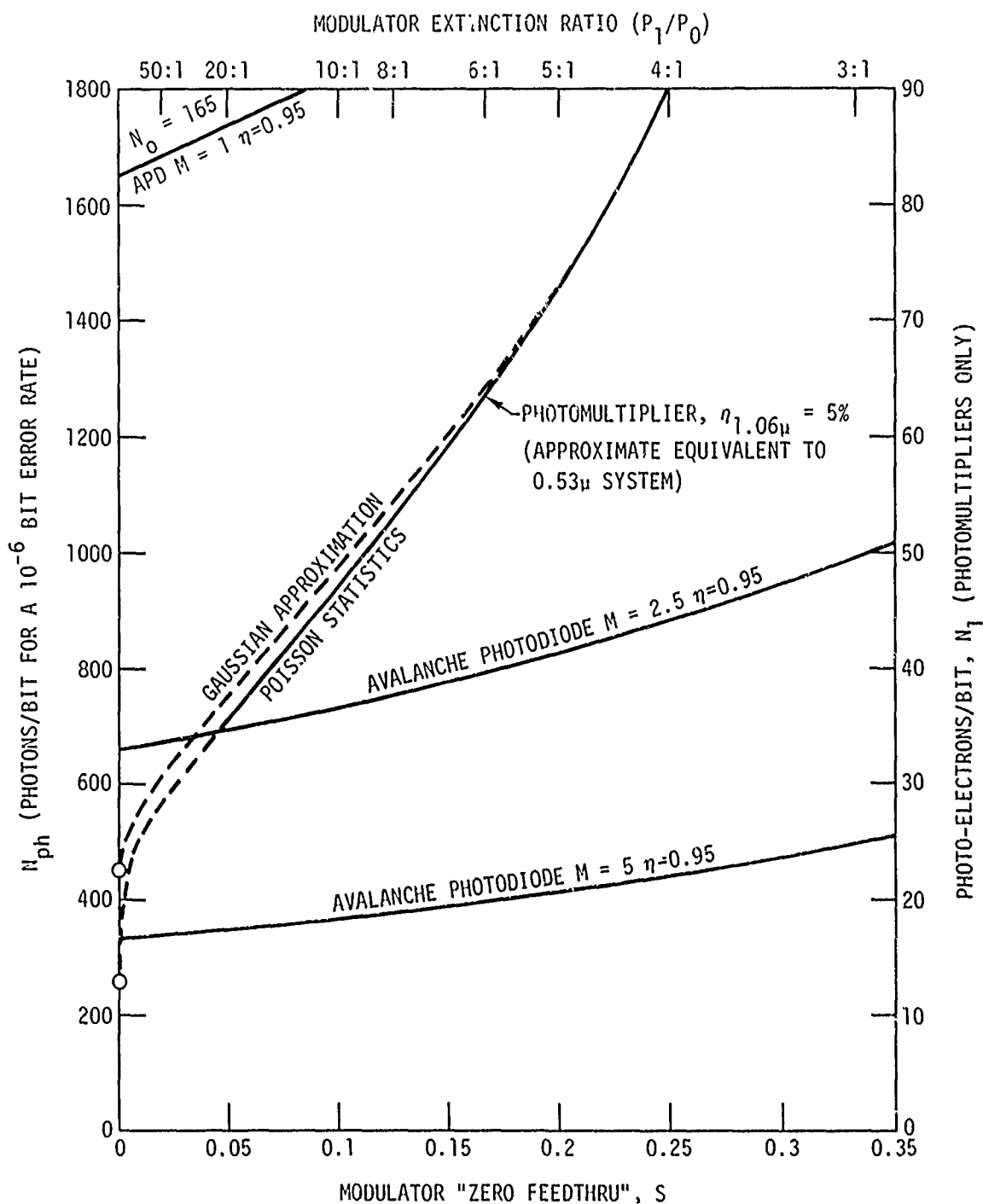


Fig. 2.4 Calculated signal level to achieve a 10^{-6} B.E.R. versus modulator zero feedthru or extinction ratio for photomultipliers (or other poisson statistics receivers as compared to a preamp-noise-limited receiver (APD receiver at low M).

and taking $\eta = 95\%$, and assuming as in Fig. 2.3 $N_0 = 175$ electrons for the preamp, we would have $N_{ph} = 1751/(1-S)M$ photons/bit. This is graphed in Fig. 2.4 for values of gain of $M = 1, 2.5$ and 5 for comparison with the photomultiplier results.

The important thing to note in Fig. 2.4 is the fact that, as opposed to the shot noise limited photomultiplier case, the required signal level for the preamp (Johnson) noise limited avalanche photodiode receiver is only slightly dependent on the modulator extinction ratio (E.R.) or "zero feedthru" (S). The fact that the APD receiver, even at very modest gain levels of 2.5 or 5 , shows a higher sensitivity (considerably lower required signal level, N_{ph} , for the specified 10^{-6} B.E.R.) than the photomultiplier is a consequence of the fact that the quantum efficiency of the APD (taken as 95%) is much higher than the quantum efficiency of the photomultiplier (taken as $\eta_{1.06\mu} = 5\%$). (It should be noted that in fact no stable cross-field photomultipliers with 1.06μ quantum efficiencies of 5% have been developed or seem in the offing; this figure of 5% is taken as an approximate equivalent 1.06μ quantum efficiency for the frequency doubled 0.53μ system.)

This relative insensitivity of the low- M APD receiver to modulator "zero feedthru" (S) also applies to its sensitivity to background light. The analogue to Fig. 2.4 for background radiation would have S being the fraction of the signal flux, N_{ph} , received during one pulse response width, ΔT_0 at the detector due to background light. In this case the APD receiver at the lower gain levels would show no dependence of N_{ph} with S , while the photomultiplier would show only slightly less slope than shown in Fig. 2.4. This requirement for low background light on photomultiplier detectors (particularly when operated in a high extinction ratio modulator system) can make it necessary to utilize a narrowband filter in front of the detector, further reducing its quantum efficiency. Typically, the modest narrowband response characteristics of the III-V alloy avalanche photodiodes are already sufficient to adequately limit background light so that the full quantum efficiency of the detector can be utilized.

2.2 III-V Alloy Microwave Avalanche Photodiode Design

As was pointed out in Section 2.1.5 (and is obvious from Fig. 2.3), the ultimate in gigabit receiver performance will be attained by combining a highly charge-sensitive preamp with an avalanche photodiode (APD) having extremely low capacitance (for high charge sensitivity), high quantum efficiency (near 100%), low leakage, low series resistance and sufficient avalanche gain to raise the signal level above the preamp noise. The first question to be addressed in the APD design is the choice of semiconductor material. Because the optical absorption coefficient in silicon (an indirect bandgap semiconductor at 1.064μ is only 10 cm^{-1} , silicon photodiodes at this wavelength have a serious transit time-quantum efficiency tradeoff ($\eta_{1.06\mu} f_{3\text{db}} \approx 40\text{ MHz}$), which makes it impossible to achieve acceptably high quantum efficiencies with silicon avalanche photodiodes (APD's) that are fast enough for gigabit data rate applications. Direct-bandgap III-V alloys, on the other hand, exhibit optical absorption coefficients on the order of 10^4 cm^{-1} for photon energies just above their energy gaps, so that photodiodes fabricated from these materials can simultaneously exhibit high quantum efficiencies and short transit times. The next question to be resolved is the selection of a device structure. After examining the design goals outlined in the RFP, we concluded that it was unlikely that these goals could be met, even using ternary III-V alloys, by "conventional" avalanche photodiode structures such as Schottky barrier or diffused or implanted p-n diodes. The problems in these conventional homostructures involve high series resistance, low quantum efficiency, difficulty in contacting and guard ringing for avalanche gain, and as a result, excessive capacitance and poor speed of response. Because of these problems, we developed a radically different approach to the avalanche photodiode design which, in addition to being the structure most likely to be able to meet all of the design goals for the system application, has the added advantages of making a very convenient mounting configuration and providing a narrowband optical response characteristic which makes the detector sensitive only to the laser

radiation. Our initial work on these APD's used a device structure referred to as the inverted heterojunction 1.06μ microwave avalanche photodiode - described in Section 2.2.1. Our later work has involved a refinement of this original approach designed for improved avalanche gain characteristics referred to as the inverted homo-heterojunction APD. This structure, described in Section 2.2.2, is used for the APD in the delivered integrated GAASFET receiver.

2.2.1 Device Design of the Inverted Heterojunction Microwave Avalanche Photodiode

In the device approach to the avalanche photodiode detector described here, sophisticated heteroepitaxial fabrication techniques using III-V compound and alloy semiconductors are used in order to circumvent the design tradeoffs (such as between speed and quantum efficiency, etc.) usually entailed in photodiode design. The inverted heterojunction microwave avalanche photodiode structure introduces the light through the transparent substrate into the three-layer III-V alloy (principally $\text{GaAs}_{1-x}\text{Sb}_x$ alloys have been used) detector structure. The use of substrate and alloys with $E_g > h\nu$ as transparent, very low resistance contacts and optical filters makes possible a device with very low series resistance, high quantum efficiency and controllable narrowband optical response. These factors, along with the mesa device structure, give a device with extremely wide signal bandwidth capability, low noise (dark current) and the capability for avalanche gain.

Figure 2.5 shows a drawing of the 1.06μ microwave avalanche photodiode structure. The device structure shown starts with a p^+ GaAs substrate and has alloy compositions selected for 1.06μ peak response. We have also fabricated devices of the complimentary type (i.e., starting with n-type GaAs substrate material) and with alloy compositions giving peak responses in the 0.9 to 1.15μ range (with wider ranges possible). The substrate in this structure serves as a transparent low resistance contact to the device, as well as the physical mounting base and hermetically sealing optical window to the "outside". The light entrance window portion of the substrate is anti-reflection coated to minimize

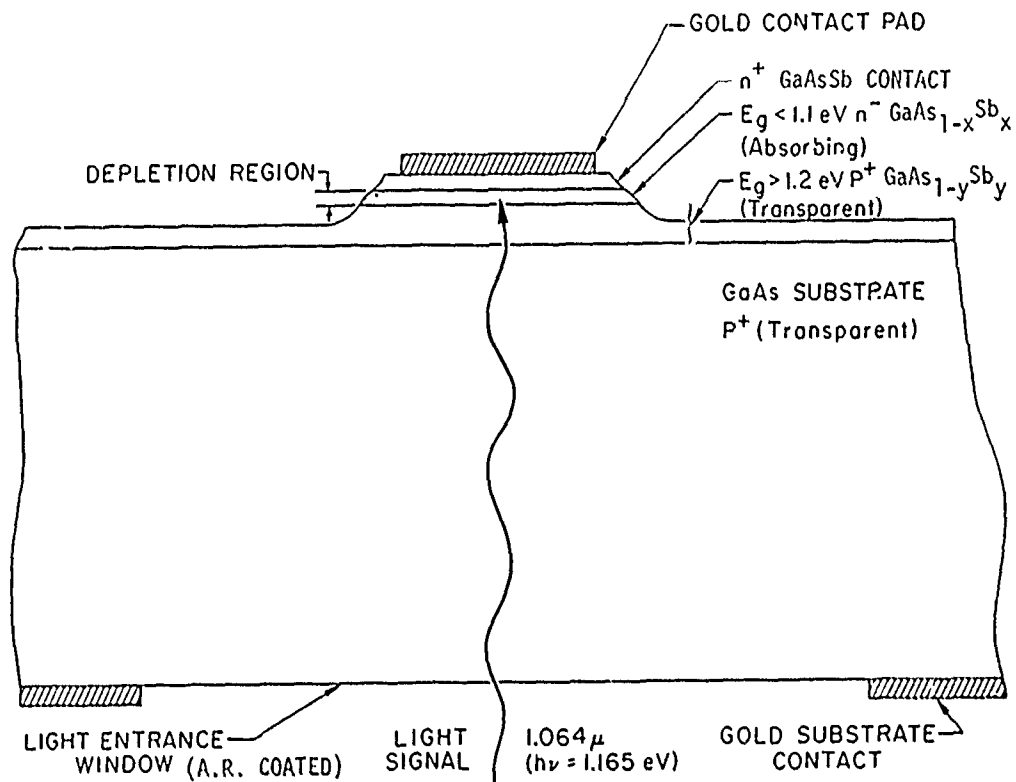
1.06 μ HETEROJUNCTION III-V ALLOY MESA PHOTODIODE

Fig. 2.5 Original Inverted Heterojunction III-V Alloy Microwave Avalanche Photodiode Design. Note that the peak electric field (high avalanche gain) region is at the p^+ (transparent buffer layer) - n^- (absorbing active layer) heterojunction interface.

reflective light loss. The substrate doping is sufficiently high to give low resistance, but not so high as to cause significant free carrier absorption of the light.

The p^+ alloy buffer layer grown on the GaAs substrate is a direct bandgap III-V alloy with composition such that its energy gap is slightly larger than the photon energy of interest (1.165 eV for 1.064 μ wavelength). This means that this layer is transparent at the desired wavelength (hence acting as a transparent low resistance contact to the junction) but, because of the sharp absorption edge of the material, acts as a cutoff filter defining the short wavelength (high $h\nu$) cutoff of the photodiode spectral response. This buffer layer also serves to minimize the lattice mismatch with the n^- active (absorbing) layer over what it would be if it were a GaAs substrate ($E_g = 1.4$ eV) to n^- alloy ($E_g = 1.1$ eV) interface.

On top of the buffer layer is heteroepitaxially grown the n^- alloy "active" layer with energy gap somewhat less than the photon energy ($E_g < h\nu$), such that the material has a very high absorption coefficient ($\alpha \sim 10^4 \text{ cm}^{-1}$) for the light of the wavelength of interest. It is the absorption edge of this layer which defines the long-wavelength cutoff of the spectral photoresponse of the photodiode, i.e., the layer becomes transparent for $h\nu < E_g$. This combined buffer layer-active layer cutoff action in producing a narrowband photoresponse characteristic is illustrated in Fig. 2.6. Here actual transmission curves for a typical GaAs substrate (T_{GaAs}) and a 10 μ thick epitaxial $\text{Ga}_{1-x}\text{In}_x\text{As}$ alloy film (T_{buffer}) are shown (corrected for reflection). For purposes of illustration, the absorption curve for the active layer, $A_{\text{active}} = 1 - T_{\text{active}}$, is taken as $1 - T_{\text{buffer}}$, only shifted to longer wavelength slightly (since the active layer has a smaller energy gap). The quantum efficiency versus wavelength for this structure is given by the product of the transmission of the device up to the depletion region ($T_{\text{GaAs}} T_{\text{buffer}}$) times the absorption in the depletion region (A_{active} ; assuming the whole

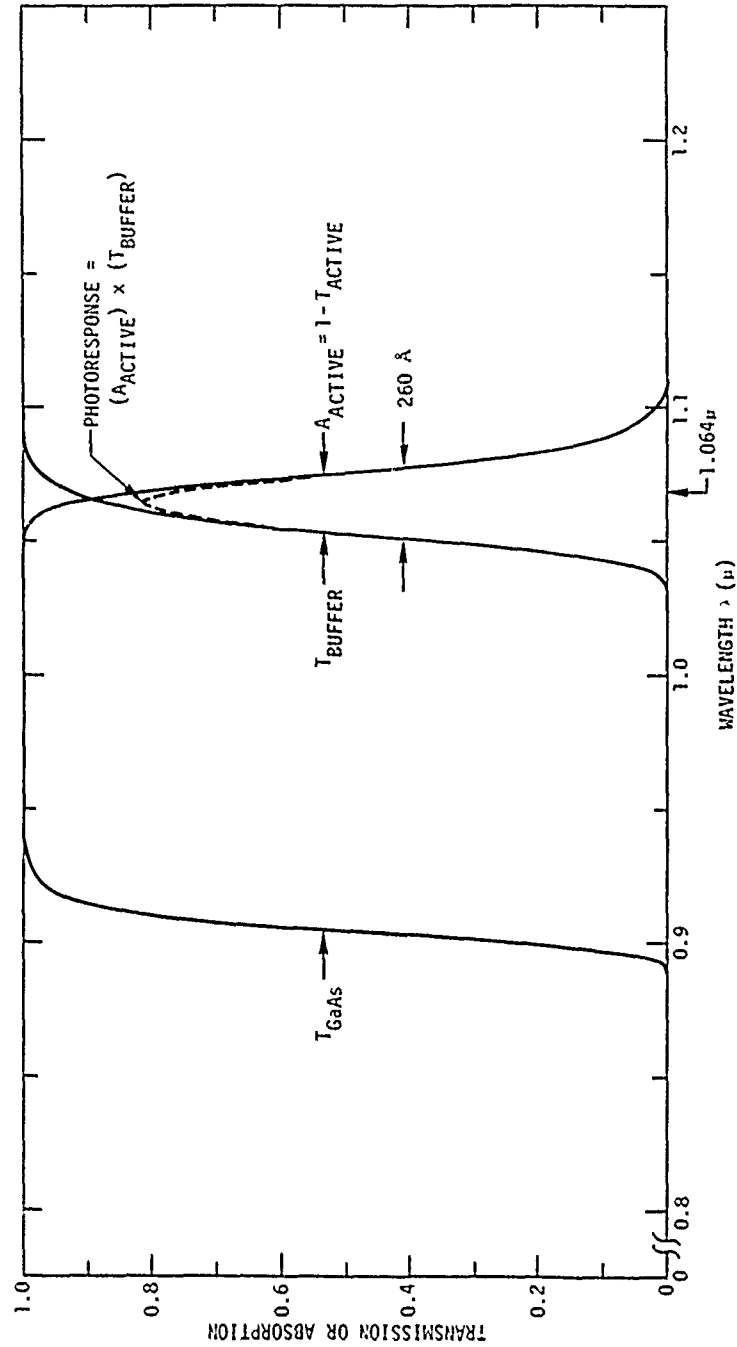


Fig. 2.6 Example of spectral photoresponse which can be obtained in either inverted heterojunction of (fully depleted) inverted homo-heterojunction avalanche photodiode. While this illustrates narrowband photoresponse which can be obtained, usual experimental devices are made with wider response peaks and near 100% quantum effectiveness.

active layer is depleted). This product photoresponse curve, as shown in Fig. 2.6 can be quite narrow (260Å full width at half height) yet have high peak quantum efficiency (about 82% near 1.064μ in the example).

This n^- active layer is depleted from the p-n junction near the interface with the buffer layer well into the layer. The width of the depletion region is determined by the bias voltage and donor concentration in the n^- layer. Typical values for W for $N_d \approx 10^{16} \text{ cm}^{-3}$ are about 3.2μ with a breakdown voltage ~ 70 volts applied (avalanche gain operation). In certain circumstances it may be desirable to deplete all of the way through this n^- active layer to the n^+ alloy contact layer, whereas in other cases depletion only part way through the layer may be preferable (both types have been fabricated). These various conditions of depletion layer width and electric field distribution are obtained by varying the donor concentration and thickness for this n^- alloy active layer.

The final heteroepitaxial layer in the structure is the n^+ alloy contact layer. This layer is heavily doped to provide an ohmic contact for the n^- active layer. In cases where the active layer is completely depleted it also defines the edge of the depletion region. The alloy content is adjusted to give the same (or slightly larger) energy gap as the n^- active layer so that optical transmission measurements may be used to monitor the active layer energy gap as a process control.

Because of the heavy doping of the p^+ substrate and n^+ contact layer, it is easy to alloy metallic ohmic contacts to these regions and to plate the contacts with thick gold for convenience in making contact to the devices.

The device structure is defined by photolithography and etching of the mesa to the required shape and side contours as described in Section 3.2. The angled sides of the mesa at the depletion layer are an essential part of the device structure. The peak electric field in the depletion region occurs at the p-n junction toward the substrate side of the depletion region. If no special precautions were taken at the

surface, concentration of electric field at the edges of the junction would be expected to lead to surface breakdown before the center of the junction area began to give significant avalanche gain. By sloping the junction edges, as shown in Fig. 2.5 by careful etching, the electric field at the edges of the junction is reduced significantly below the values toward the center of the device and hence the device may be used for avalanche operation. The surface may be operated exposed, or covered with a suitable passivation layer.

2.2.2 Device Design of the Inverted Homo-Heterojunction Avalanche Photodiode

In the initial work on these III-V alloy 1.06μ detectors (Ref. 1), inverted heterojunction $\text{GaAs}_{1-x}\text{Sb}_x$ photodiodes of the type just described were developed which had 1.064μ quantum efficiencies over 95%, low leakage currents, and low capacitances and transit times (bandwidths up to dc to 15 GHz into a 50Ω load). In addition to single detectors, of the type shown in Fig. 2.5, two dimensional arrays were fabricated with this structure (Ref. 2). The principal limitation in these earlier devices was that the high frequency avalanche gain attainable was very limited and the gain uniformity was poor because of microplasmas caused by heterojunction interface defects at the peak electric field point in the depletion region. Such problems might reasonably be expected in the structure of Fig. 2.5 because of the fact that at this p^+ buffer- n^- active layer interface there will necessarily be both heterojunction lattice-mismatch defects (because the increased antimony composition in the active layer gives it a larger lattice constant than the buffer) and growth-nucleation non-uniformities caused by the interruption buffer layer melt is removed and the active layer melt is rolled on to the growth surface. Because of the strong dependence of avalanche gain on local electric field or ionizable defects, any such non-uniformities or defects lead to local areas in the junction with reduced breakdown voltages. Such areas will undergo local microplasma breakdown, limiting the useful (low noise) APD reverse bias range to voltage below those required to achieve high avalanche gains over the bulk of the device.

Figure 2.7 shows the device structure for an inverted homo-heterojunction $\text{GaAs}_{1-x}\text{Sb}_x$ 1.06 μ avalanche photodiode designed to circumvent the gain limitations inherent in the earlier inverted heterojunction design. The device is fabricated by growing three liquid epitaxial layers of GaAsSb on a GaAs substrate. The light is brought into the device through the n^+ GaAs substrate, which is, of course, transparent at 1.064 μ ($h\nu = 1.165$ eV) since the photon energy is less than the energy gap ($E_g = 1.4$ eV) and the n^+ doping is not so high as to cause significant "free carrier" (intraband-transition) absorption. The n^+ $\text{GaAs}_{1-y}\text{Sb}_y$ ($y \sim 0.12$) "buffer" layer ($E_g \sim 1.2$ eV) is also transparent at 1.06 μ , but it does serve to define the short wavelength cutoff of the detector, as well as to minimize the lattice mismatch at the buffer-active heterojunction. The active (absorbing) layer of $\text{GaAs}_{1-x}\text{Sb}_x$ ($x \sim 0.17$) is the unique feature of the homo-heterojunction device structure. Because its energy gap (~ 1.1 eV) is less than $h\nu$, the 1.06 μ light is strongly absorbed in this layer, with most of the light absorbed within 1 or 2 microns of the active-buffer interface. The active layer is started in the liquid-epitaxial growth process as an n^- layer ($N_D \sim 1.5 \times 10^{15} \text{ cm}^{-3}$), but after about 3 to 5 microns of growth, p-type dopant is added to the melt so that a p-n homojunction is grown in this active layer. This means that the peak field region of the depletion region occurs at a grown homojunction free from either interlayer growth, interface defects or heterojunction (lattice mismatch or other) interface defects. In the particular devices used in the delivered receivers, the depletion region punches through the n^- active layer to the n^+ buffer at a bias voltage of about 60 volts so that at normal operating biases ($V_R \geq 80$ volts) all of the light is absorbed in the depletion region. This means that the quantum efficiency will be nearly 100% with good antireflection coating of the GaAs light entrance window (we have obtained 1.06 μ reflectances under 0.1% using $\lambda/4$ coatings of Si_3N_4). The quantum efficiency is relatively constant for wavelengths between 1.0 μ and 1.08 μ for these particular detectors.

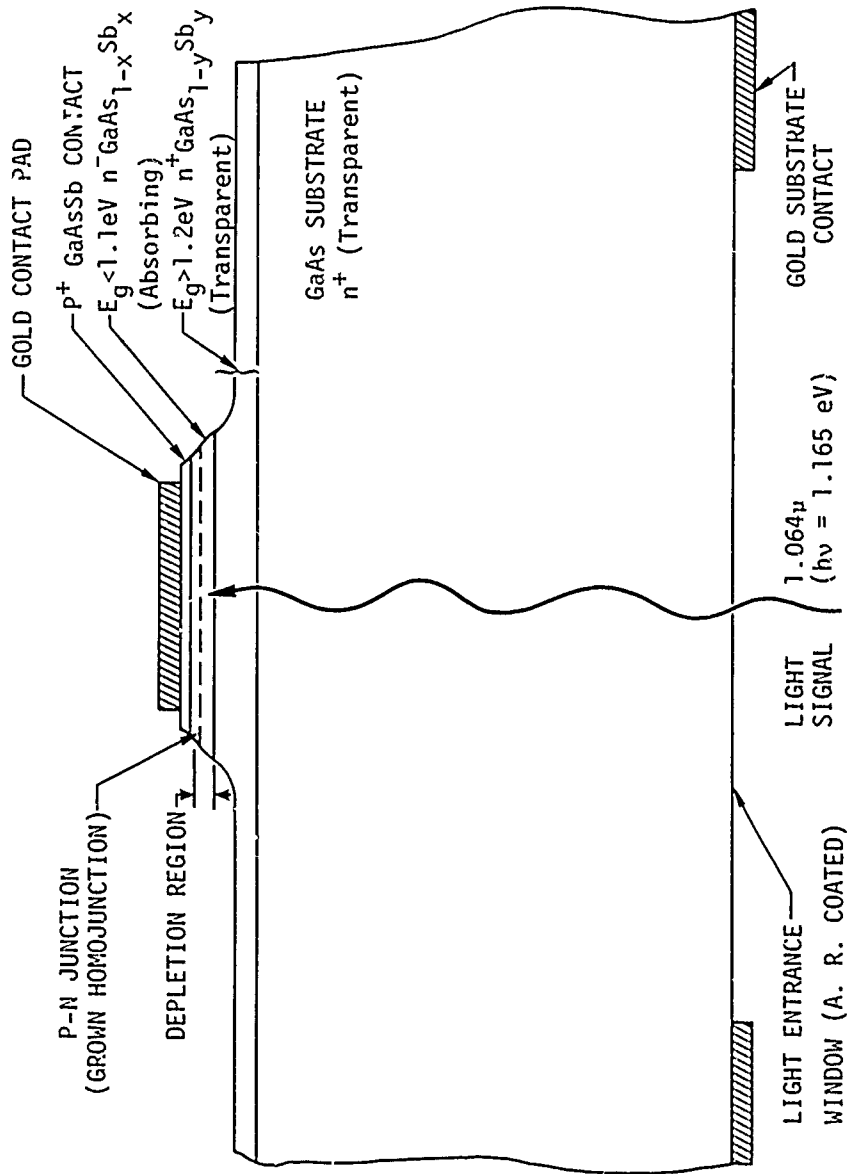


Fig. 2.7

Device Structure for an Inverted Homo-Heterojunction $\text{GaAs}_{1-x}\text{Sb}_x$ Avalanche Photodiode. Note that as opposed to the earlier structure of Fig. 2.5, the peak electric field is at a p-n homojunction produced during continuous growth of the n^- active (absorbing) layer by adding a small amount of p-type dopant to the melt. The device is normally operated with the n^- layer completely depleted.

The principal advantage of this device structure (Fig. 2.7) over that of Fig. 2.5 is that the p-n junction (the peak electric field point or highest avalanche gain region) occurs at a point in the grown epitaxial layer where there is neither any change in lattice constant nor any disturbance in the growth process from changing growth melts. The junction is produced in the process of continuous growth of the n^- layer by adding a tiny amount of p-type dopant to the liquid epitaxial growth melt during growth. The thickness of the n^- layer is established by carefully timing the dopant drop. In addition to giving a relatively defect-free p-n junction region, this structure has the added advantage of absorbing the light in a low-field region of the junction (near the n^+ buffer layer) and drifting one carrier through the high-gain region (somewhat like the silicon "reach-through" APD structure), which can give lower excess noise factor for the APD.

There are a couple of disadvantages for the type of structure shown in Fig. 2.7. One is that in punch-through operation (i.e., the depletion region extending all of the way from the p-n junction through the n^- layer to the n^+ buffer layer), the depletion width, W , is established by the physical distance between the p-n junction and the buffer layer. If there are local variations in W due to growth rate fluctuation over the device, then for a given bias voltage there will be corresponding fluctuations in electric field strength. Since avalanche gain is a very strong function of electric field strength, this can cause sizeable gain non-uniformities across the device. Another disadvantage of fully depleted operation is that there will be fairly high electric fields (though not as high as at the p-n junction) at the n^+ buffer- n^- active layer heterojunction. This could lead to defect ionization problems. Both of these sources of problems could be taken care of by altering the n^- layer doping level and distance from the p-n homojunction to n^- - n^+ heterojunction distance so that the depletion region almost - but not quite - reaches the heterojunction. This would require some minority carrier diffusion to reach the depletion region, of course, but if the thickness of undepleted absorbing material were small enough ($\sim 1\mu$), this should not significantly degrade

quantum efficiency or response time.

An interesting point about the structure of Fig. 2.7 is that one would expect from the location of the p-n junction at the surface side of the n^- layer that with the slope of the mesa edges shown, there would be field concentration near the p-n junction at the device perimeter and hence surface (rather than bulk) breakdown. In fact, considerable effort at the beginning of this work was extended toward developing "upside down" mesas to avoid this problem. However, it was found that if surface passivations are used which tend to induce a p-type surface channel on the $\text{GaAs}_{1-x}\text{Sb}_x$ surface of the n^- layer, the channel effect works opposite to the geometrical field concentration effect so that devices of the type in Fig. 2.7 can be fabricated without giving surface breakdown problems.

The performance obtained with these inverted homo-heterojunction APD's is discussed in Section 4.1. While the performance of these detectors is quite good, (we have obtained peak high frequency gains over 23 db in delivered receivers), as it turns out, the complimentary detector structure should give much better avalanche gain performance. The structure of Fig. 2.7 was adopted on the basis of GaAs ionization data which indicates that hole ionization rates are larger than electron ionization rates. Hence, in this structure the light is absorbed near the n^+ buffer- n^- active layer interface and the photogenerated holes are drifted through the high field region (near the p-n junction) for avalanche gain. However, recent measurements on these $\text{GaAs}_{1-x}\text{Sb}_x$ alloys (Ref. 4.) indicate that in the x range of interest, the electron ionization rate is considerably larger than the hole ionization rate ($\alpha_n \gg \alpha_p$). Measurements of gain versus wavelength on our experimental diodes of the type shown in Fig. 2.7 support this conclusion. In this structure, if (as originally assumed) holes had the higher ionization rate, then the shorter the wavelength, the higher would be the optical absorption coefficient for the light, the closer to the n^+ buffer- n^- active layer heterojunction the carriers would be generated and the more electric field the holes would get to pass through in transiting the junction. Hence,

for $x_p \gg x_n$, we would expect the highest avalanche gain at the short wavelength side of the photoresponse curve. In fact, just the opposite is observed (Fig. 4.5). As the reverse bias on the diodes is increased, the gain increases much sooner toward the long wavelength side of the response, causing, in fact, the response peak at higher biases to shift out to a wavelength which would have been on the long wavelength edge at lower biases. Hence we conclude that the original assumption of $\alpha_p \gg \alpha_n$ must be wrong for this alloy composition and in fact $\alpha_n \gg \alpha_p$. This means that the complimentary APD structure (as Fig. 2.7 but with all doping types reversed) should give much higher, more uniform gains than were observed in the experimentally fabricated APD's reported here.

2.3 Design Approach for the Low Noise Gigabit GAASFET Preamp

As was discussed in Section 2.1.5 (see Fig. 2.3), in order to attain the maximum possible receiver sensitivity, it is essential to combine a very high quantum efficiency APD with a highly charge-sensitive preamp so that minimum avalanche gain (to reduce excess gain noise) can be used in the APD and still bring the signal shot-noise level above the preamp noise. With avalanche photodiodes of the type described here in which the gains have been marginal for attaining this end, it is even more important to have an extremely charge-sensitive preamp (Eq. 2.20). The general approach to attaining this is described in Section 2.3.1, with the specific preamp designs employed in this work described in subsequent sections.

2.3.1 Requirements for Attaining High Pulse Sensitivity in a Preamp

Two fundamental limitations to the sensitivity of a preamp for detecting photocurrent pulses exist: 1) the voltage noise - input capacitance limit and 2) the Johnson or thermal noise current in the load or feedback resistance (Ref. 5). If a photodiode with junction capacitance C_J is connected to a preamp with input capacitance C_{IN} , then a charge pulse Q_p from the photodiode will produce a voltage change $\Delta V \leq Q_p / (C_J + C_{IN})$ (where the \leq is used since there may in general be other shunt conductances).

If the preamp has a total rms input voltage noise e_n , then the minimum detectable charge pulse (amount of charge required to make $\Delta V = e_n$) will be $Q_{\text{MIN}} \geq e_n (C_J + C_{\text{IN}})$, or in terms of the number of electrons,

$$N_0 \geq e_n (C_J + C_{\text{IN}})/q \quad (2.31)$$

where N_0 is the "minimum detectable current pulse" or number of electrons in a current impulse required to make the voltage change equal the rms noise ($q = 1.602 \times 10^{-19}$ coul).

From Eq. 2.31 we see that in order to attain high pulse sensitivity in a preamp for a receiver (that is, low N_0) we must have a preamp with low input voltage noise combined with a total input capacitance (preamp plus photodiode) that is extremely small. In practice, the input voltage noises for wideband amplifying devices of high quality are not widely different, so that the principal way to reduce N_0 is to reduce the capacitance ($C_J + C_{\text{IN}}$). Here we have an excellent start because a 3 mil GaAs_{1-x}Sb_x detector of the type described earlier has only $C_J = 0.1$ pf, and has negligible series resistance so that there is no thermal noise contribution to e_n in the APD. In order to maintain this capacitance advantage, we use a GaAs Schottky barrier field effect transistor (GAASFET) preamplifier, since the input capacitance of a 1 μ gate length GAASFET is typically of the order of 0.2 pf. (Needless to say, in order to keep stray capacitances down to this <0.1pf level, the APD must be hybrid integrated with the preamp.) In comparison with the GAASFET, a silicon bipolar transistor would have similar e_n and typically 5 pf input capacitance, so that N_0 would be over an order of magnitude larger.

To improve the preamp sensitivity (reduce N_0), we must also reduce the Johnson noise current in the load resistor, $i_{\text{nj}} = \sqrt{4KT\Delta F/R}$. The increase in R allowed, for the same bandwidth, by reducing ($C_J + C_{\text{IN}}$) helps, but is insufficient to achieve the two order of magnitude increase

in R required to achieve a one order of magnitude reduction in i_{nj} . In a feedback mode, or transimpedance-type of amplifier with open-loop gain A , the 3db bandwidth is given by $f_{3db} = A/2\pi R_F(C_J + C_{IN})$, as compared with $f_{3db} = 1/2\pi R_L(C_J + C_{IN})$ for a simple load resistor configuration. Hence, by going to a feedback mode GAASFET preamp with $A = 10$ having an order of magnitude lower $(C_J + C_{IN})$ than a simple bipolar transistor preamp, we can increase R by two orders of magnitude and obtain at least an order of magnitude of reduction in i_{nj} and N_o .

2.3.2 Model for Signal Response and Noise Output for a Feedback-Mode Preamp

The detailed role of the input capacitance, input voltage noise, feedback resistance, etc., in the overall signal and noise performance of a negative feedback "transimpedance-type" preamp is shown in Fig. 2.8. Here we consider an ideal (zero noise, zero output impedance, infinite input impedance) operational amplifier with frequency-dependent gain $A(\omega)$ in the triangular block with the relevant departures from non-ideality, a finite input conductance (usually a capacitance), G_{IN} , and a finite input voltage noise, e_1 . Since we are considering a frequency-dependent noise analysis, e_1 is a noise spectral density measured in volts/ \sqrt{Hz} , as is the noise associated with the feedback resistor R_F . The APD in Fig. 2.8 a) is represented by a signal current generator, i_p , in parallel with a conductance (virtually pure capacitance), G_{APD} . Because the series resistance of the $GaAs_{1-x}Sb_x$ APD's we are considering here are so small (a few ohms typically) we can ignore its resistance and its associated voltage noise for our case. The solution for V_{OUT} in terms of i_p and the noise generators e_1 and e_2 is

$$V_{OUT} = \left(\frac{1}{G_F} \right) \frac{i_p + e_2 G_F + e_1 (G_F + G_I)}{1 + 1/A(1 + G_I/G_F)} \quad 2.32$$

where, of course, A , G_F and $G_I = G_{APD} + G_{IN}$ are complex frequency-dependent values, and e_1 and e_2 are in general frequency-dependent.

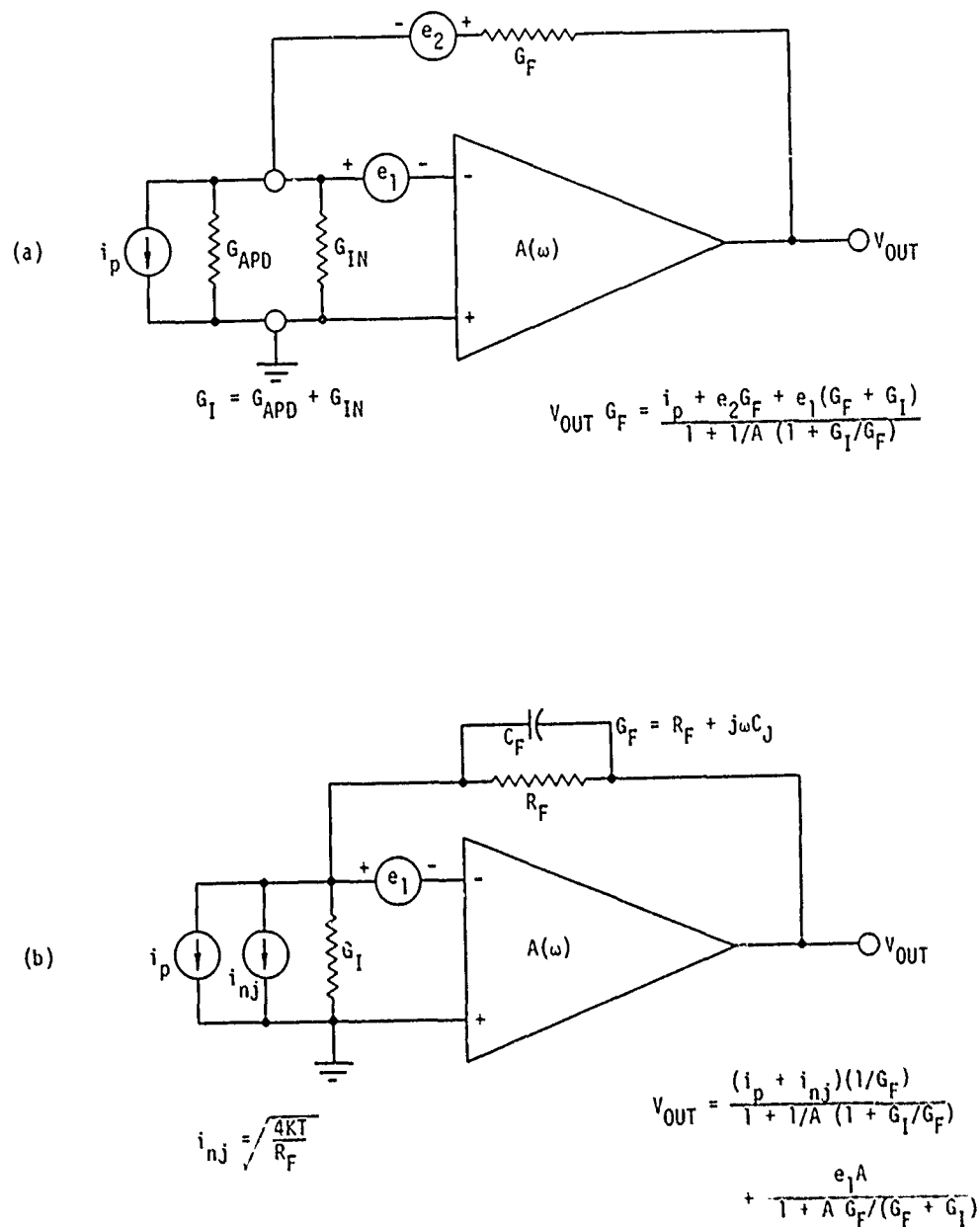


Fig. 2.8 Signal and Noise Models for Feedback-Mode (Trans-impedance-Type) Preamps. a) General case of feedback element with (Frequency-dependent) noise voltage e_2 . b) Usual case of feedback element a resistor paralleled by a capacitance where we transform the resistor noise to a frequency-independent input noise current, i_{nj} .

Figure 2.8 b) shows a slightly simpler version of 2.8 a) more specifically adapted to the preamp case. Here a specific form is taken for G_F in terms of a feedback resistance in parallel with a small capacitance. The e_2 noise voltage source has been replaced by the Johnson noise current source, i_{nj} which is frequency independent (white noise) and is in parallel with the signal source, i_p . (Of course it is understood that i_p includes all of the relevant multiplied shot noise terms from Eq. 2.24, but here we are concerned about the preamp contribution to the noise.) For this case, we have

$$V_{OUT} = \frac{(i_p + i_{nj}) (1/G_F)}{1 + 1/A (1 + G_I/G_F)} + \frac{e_1 (G_F + G_I)}{G_F + 1/A (G_F + G_I)} \quad (2.33)$$

where

$$i_{nj} = \sqrt{4kT/R_F} \quad (2.34)$$

is the Johnson noise current spectral density. While the signal term (Eq. 2.33 with $e_1 = i_{nj} = 0$) in 2.33 may be evaluated at any frequency directly, to obtain the total noise output, we must integrate the square ($V_{OUT} V_{OUT}^*$) of Eq. 2.33 (with $i_p = 0$) over the measurement bandwidth range and then take the square root of the result to get the total noise output in the measurement bandwidth range. We note in Eq. 2.33 that the response to the Johnson (white thermal resistor noise) is exactly the same as the response to the photocurrent signal or signal shot noise, with the signal output at lower frequencies, i.e., approximately

$$V_{OUT} \approx \frac{i_p R_F}{1 + 1/A} \equiv R_o i_p \quad (2.35)$$

The response to the input voltage noise term e_1 (which itself is a function of ω , particularly in the "1/f noise" region for the preamp input device),

on the other hand, is strongly frequency dependent because it is proportional to G_I ($G_I = j\omega C_I = j\omega (C_{IN} + C_{APD})$) in the usual case. In the low to mid frequency range, increasing R_F (reducing G_F) increases the magnitude of the signal term relative to the e_1 term. At high frequencies, G_I must be kept to a minimum (low $C_{IN} + C_{APD}$) to reduce the e_2 contribution. (Of course selecting an input device with low voltage noise, e_1 , helps as well.)

Because the various parameter terms in Eq. 2.33 are complex, it is difficult to learn much more by just examining the response equation. To model a preamp it is necessary to "put in the numbers" and compare with experiment to determine the correct parameter values (e_1 , etc.). A computer program written for the Tektronix Digital Processing Oscilloscope (DPO) in the TEK BASIC language is shown in Appendix A.2. This program was written for the specific case of Fig. 2.8 b) with $G_I = j\omega C_I$ ($C_I = C_{APD} + C_{IN}$) and $A(F) = A_0 / (1 + jF/F_A)$. The low frequency open-loop gain, A_0 , F_A , C_I , R_F and a white-noise voltage source e_1 (called EN in the program) volts/ $\sqrt{\text{Hz}}$ are the input parameters. Lines 1100 to 1147 calculate the real and imaginary parts of the signal term (V_{OUT}/i_p with $e_1 = i_{nj} = 0$ in Eq. 2.33) into arrays C and D and the magnitude squared of the last term (V_{OUT}/e_1 with $i_p = i_{nj} = 0$ in 2.33) in array B. These 512 element arrays cover the frequency range -255 DF to +255 DF or up to 2.55 GHz f_{01} $\Delta F = 10$ MHz. Positive and negative frequency values are used so that the impulse response can be obtained using the inverse Fourier transform (IFT) of C and D (line 1146, includes normalization) with the result into array A. The peak value of A is $(V/Q)_\delta$ from Eq. 2.6 or Fig. 2.2. All we need to know to get the minimum detectable current pulse for the preamp, N_0 (in Eq. 2.19) is the rms output voltage noise with no signal ($i_p = 0$). Having already obtained the pulse response through the IFT, we do not need the real and imaginary parts of signal response any longer, but rather the magnitude of V/I vs. frequency and the magnitude squared for the Johnson noise (lines 1156 and 1158). The rest of the program (to line 1186) is used to carry out the noise voltage (squared) versus frequency, integrate to

get v_{no}^2 and take the square root to get v_{no} and N_o as used in Eq. 2.19 and elsewhere. The outputs from this program include frequency response (including F_{3db} and F_{NOISE} , where $F_{NOISE} = (V_{OUT}/i_p)_{f=0} \int_0^\infty (V_{OUT}/i_p)^2 df$), the impulse response (including $(V/Q)_\delta$), the noise output spectral density, the total output noise voltage and the minimum detectable current pulse, N_o .

2.3.3 Effect of Post-Receiver Amplifier Bandwidth on the Pulse Detection Performance of a Feedback-Mode Preamp

The program modelling for the feedback-mode preamps described above (listing in Appendix A.2) assumes a measurement bandwidth of 2.55 GHz [for $DF = 10$ MHz per calculated point] following the receiver. Because the response of the preamp to the resistor Johnson noise (i_{nj} in Eq. 2.33) and the signal photocurrent, i_p is the same, increasing the bandwidth increases the signal peak height more rapidly than it increases the total Johnson noise (white noise power is proportional to ΔF ; $i_n \propto \Delta F^{1/2}$), so that N_o is improved (reduced) with increased bandwidth. However, the e_1 voltage noise term in Eq. 2.33 is frequency dependent, leading to a high-frequency peak in the noise spectral density. If a reduced post-receiver bandwidth is used it may be possible to actually improve N_o by reducing the output bandwidth somewhat to some optimum (i.e., while reducing bandwidth will cut $(V/Q)_p$ somewhat, it may cut v_{no} more rapidly for a while).

The TEK BASIC program listed in Appendix A.3 calculates (lines 8000-8192) starting with the noise spectral density (from the A.2 program), the noise spectral density and total output noise if the output is passed through a Gaussian filter with impulse response time, T_1 (or standard deviation frequency $GW = 1/2\pi T_1$). A Gaussian filter is taken there for the non-ringing transient response characteristic. Also, because the Fourier transform of a Gaussian frequency response is a Gaussian pulse, sampling the output data stream with a finite-width Gaussian sampling pulse (i.e., sampling with a time weighting $\exp[-(t-T_p)^2/2T_1^2]$ instead of the $\delta(t-T_p)$ sampling assumed in Eq. 2.7 and Fig. 2.2) has the same effect as the Gaussian frequency response filtering on the output noise or signal pulse. The result of the program is a modified noise voltage

spectral density curve (displayed on the DPO in array B ["waveform B"]), and a total voltage noise output.

The effect of the Gaussian filtering on the output pulse height (from the program in A.2) is calculated by means of convolution with the Gaussian filter impulse response in the program in Appendix A.4 (lines 8300 to 8380). The result of this program is the reduced $(V/Q)_\delta$ peak height with the Gaussian filter. This, taken with the results of the A.3 program, allows the N_0 with the bandwidth-limiting output filter to be determined. This program can also be used for determining $(V/Q)_p$, or the peak output when the input light pulse is not a δ -function, but rather a Gaussian pulse with standard deviation T_1 . (The short program, lines 8200-8260 is used to x2 expand and interpolate quadratically the 5ns/div pulse response calculated from the IFT in the program in A.2 to give-in two runs-the 1.25ns/div time scale chosen for this A.4 program.)

Hence, these two programs can be used with the feedback preamp model program to determine the influence of either finite sampling pulse-width or limited post-receiver bandwidth (of Gaussian response shape) on the optical pulse detection capability of the receiver. In cases when the voltage noise (e_1) contribution is not large, there is little influence on N_0 as long as the bandwidth past the preamp is well above the receiver bandwidth. On the other hand, when the e_1 contribution is larger, there may be a significant reduction in N_0 possible by choosing an optimum output amplifier bandwidth (of perhaps 1.5 times the receiver 3 db bandwidth) as compared to wider output bandwidths.

2.3.4 Preliminary, Lower Bandwidth, GAASFET Preamp Designs

The feedback preamplifier model indicates that it is absolutely essential to have very low input capacitance to the preamp (and APD capacitance) in order to achieve high pulse sensitivity. Further, in order that the feedback amplifier be stable, the phase shift in the amplifier must be kept small. (Over most of the frequency range of interest there is 90° phase shift due to $R_F - C_1$ and the total open-loop phase shift

may not exceed 180° when the loop gain is greater than or equal to unity.) This requires an amplifying device of great gain-bandwidth capability. Fortunately the gallium arsenide Schottky barrier field effect trans (GAASFET) has the very low input capacitance and very high gain-bandwidth product as required for this application. Three different preamplifier designs of the transimpedance type using GAASFETs have been developed. The first two designs (Mark IA and Mark II) represent important developments in the GAASFET receiver technology, but do not have bandwidth sufficient for gigabit data rate reception. These are discussed in the section. The successful $>1\text{Gb/s}$ data rate Mark III design is discussed in section 2.3.5. The basic approach to these designs with simplified schematics are given here; the full schematic diagrams are included in the performance results in Section 4.

2.3.4.1 Basic Design of the Mark IA Two-GAASFET Preamp

The first successful GAASFET feedback mode preamps were of the "Mark IA" design shown (in very simplified form) in Fig. 2.9. This two-GAASFET design is the simplest of the optical receiver designs and was used in preamps #4 and #5 (Serial Numbers 004 and 005). The "operational amplifier" here is a single GAASFET, Q_1 with a voltage level shifter zener diode (shown as battery V_Z in Fig. 2.9) to allow for the dc offset between the Q_1 drain (typically $+4\text{Vdc}$) and the Q_1 gate (typically -2Vdc). The gain of this "op-amp" will be of the order of $g_m R_L$, where g_m is the transconductance of Q_1 at the operating bias. In order to obtain sizeable voltage gains ($A_o \sim 5$ to 10) with reasonable Q_1 transconductances ($g_m \sim 10$ to 20 mmhos), it is necessary to have impedance levels at the Q_1 drain of the order of 500 ohms to $1\text{K}\Omega$ (R_L in parallel with the drain resistance, R_D). The purpose of Q_2 is to serve as a low capacitance buffer between the high impedance at the Q_1 drain and the required 50Ω output impedance. To Q_1 , Q_2 looks like a capacitive load (often referred to as C_L) and C_L must be kept small in order that an acceptable bandwidth be maintained in the "op-amp" (Q_1) stage. For this reason a GAASFET is used for Q_2 as well as Q_1 .

The reason for using a single voltage gain stage for the "op-amp" in the feedback preamp is to avoid instability due to accumulated phase shift in several active device stages. Of course, Q_1 in Fig. 2.9 does not represent an "op-amp" at all in the sense of Fig. 2.8 because

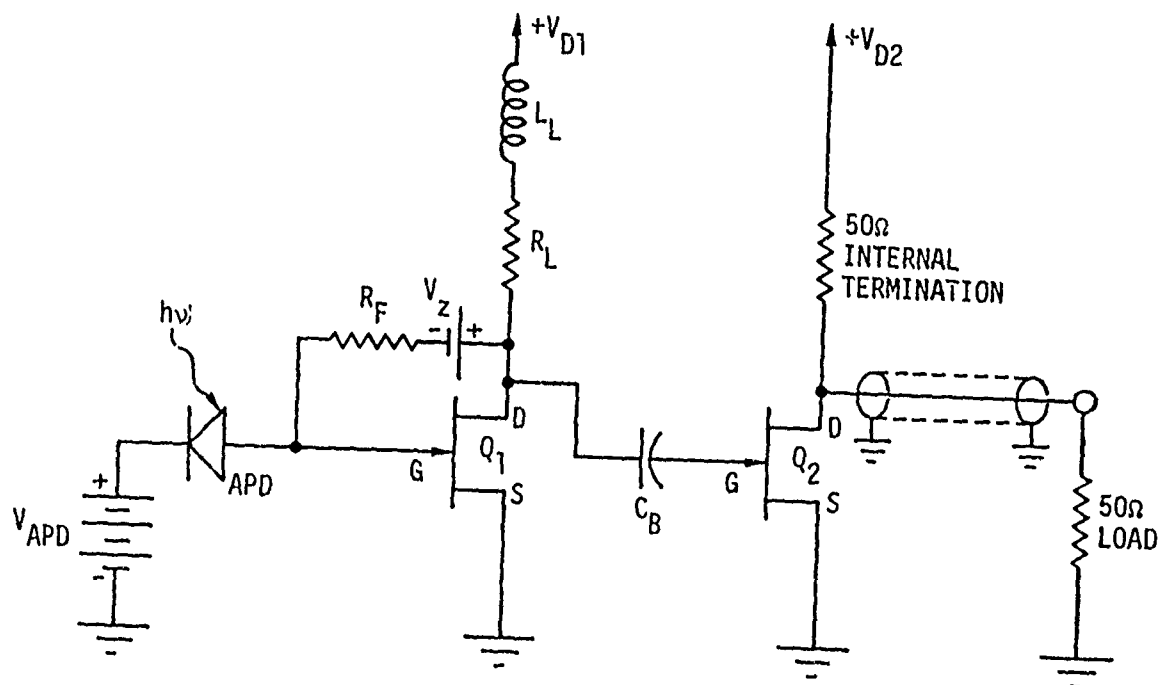
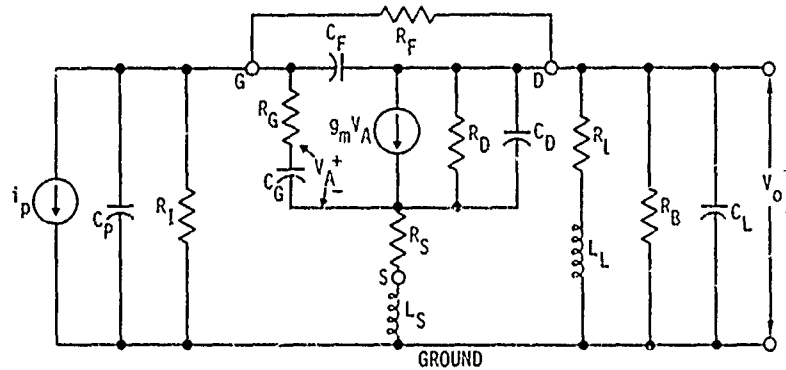


Fig. 2.9 Simplified Circuit Diagram for the Mark IA GAASFET Preamps Design. (Complete circuit diagram is shown in Fig. 4.9.)

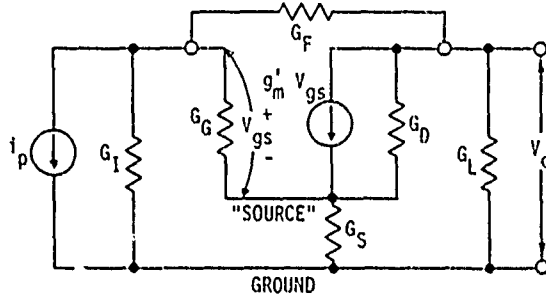
its output impedance is not low. However, since the only loading to the stage is C_L and R_F , if we define $A(\omega)$ in Fig. 2.8 in terms of the voltage gain of Q_1 with C_L and R_F as loads, we can still use the formalism of Section 2.3.2 to describe the preamps and their noise characteristics.

One of the major problems incurred in the earlier portions of this work was that the hybrid-integrated GAASFET receivers proved to be better UHF or microwave oscillators than amplifiers. This is hardly suprising in that this work represents the first effort to push negative feedback "transimpedance amplifier" concepts to the near-gigahertz frequency range. In this frequency range it is possible for any stray lead inductance, etc., in experimental preamps to serve as a feedback element and push the already none-too-generous phase margin of the ideal current-mode feedback configuration beyond the Nyquist limit into oscillation. In order to deal with these problems, a detailed circuit analysis of the Mark IA preamp first stage, including some parasitic elements, was carried out on a digital computer.

Figure 2.10 shows the ac equivalent circuit of the first stage of the GAASFET preamp with parasitic source impedance considered (R_S is internal to the chip, while L_S would represent stray source lead inductance in the circuit or bonding wires). Here an elaborate MESFET model, (Ref. 6) is used. The values quoted for the 2μ gate Fairchild FMX 950 transistor for this model are $R_G = 10\Omega$, $C_G = 0.4\text{pf}$, $R_S = 15\Omega$, $R_D = 625\Omega$, $C_D = 0.05\text{pf}$ and $C_{dg} = 0.01\text{pf}$ ($C_F = C_{dg} + \text{stray}$ would be $\sim 0.02\text{pf}$). The transconductance, g_m , would be about 20 mmho at $I_D \sim 50 \text{ mA}$ for a good device, but $g_m \sim 12 \text{ mmho}$ at the $I_D \sim 10 \text{ mA}$ bias used here. Note in this model that g_m does not amplify V_{gs} , but rather V_a , the voltage across C_g . In the reduced ac equivalent circuit of Fig. 2.10 this problem is avoided by replacing g_m by g_m' , a complex quantity taking into account the R_G - C_G voltage divider action, so that the output current generator is $g_m' V_{gs}$.



a) AC Equivalent Circuit for 3-NODE Analysis.



b) Reduced AC Equivalent Circuit, where

$$\begin{aligned} G_I &= 1/R_I + j\omega C_p & G_G &= (R_G - j/\omega C_G)^{-1} \\ G_F &= 1/R_F + j\omega C_F & G_S &= (R_S + j\omega L_S)^{-1} \\ G_D &= 1/R_D + j\omega C_D & G_L &= R_B^{-1} + j\omega C_L + (R_L + j\omega L_L)^{-1} \end{aligned}$$

$$g'_m = \frac{g_m}{1 + j\omega R_G C_G}$$

The Solution for V_o/i_p is:

$$\frac{V_o}{i_p} = \frac{g'_m - G_F - (1/G_S)[G_F(G_D + G_G + g'_m) + G_D G_G]}{(G_D + G_L)(G_G + G_I) + G_F(G_D + G_L + G_G + G_I + g'_m) + (1/G_S)\{[G_L + G_I][G_F(G_D + G_G + g'_m) + G_D G_G] + G_I[G_L(G_D + G_G) + G_G g'_m]\}}$$

Fig. 2.10 AC Equivalent Circuit of the First Stage of Mark IA or Mark II Preamps Including Parasitic Impedances. This circuit is analyzed using the TEK BASIC program listed in Appendix A.5.

The model of Fig. 2.10 has three independent nodes; the source, the gate, and the drain (output) nodes, with three independent equations to solve simultaneously to give V_o/i_p in terms of the seven complex parameters (G_I , G_F , G_D , G_G , G_S , G_L and g_m). The solution for V_o/i_p is given by

$$\begin{aligned} \frac{V_o}{i_p} = & \frac{g_m' - G_F - (1/G_S)[G_F(G_D + G_G + g_m') + G_D G_G]}{(G_D + G_L)(G_G + G_I) + G_F(G_D + G_L + G_G + G_I + g_m')} \quad (2.36) \\ & + (1/G_S) \left\{ (G_L + G_I)[G_F(G_D + G_G + g_m') + G_D G_G] + G_I[G_L(G_D + G_G) + G_G g_m'] \right\} \end{aligned}$$

Eq. 2.36 is arranged to focus attention on the difference between the parasitic contribution (arising from finite G_S) and the desired 2-node characteristics which would exist with the source grounded (G_S infinite or $1/G_S = 0$). Appendix A.5 contains the listing for a TEK BASIC language computer program to perform this circuit analysis on the D.P.O., along with an explanation of the program. The program is somewhat similar in concept, but much more elaborate than the program described in Section 2.3.2 for Eq. 2.33. In addition to the source lead parasitic impedance shown in Fig. 2.10, the program can treat similar drain lead stray inductances (and with minor modification, other effects). The use of this program made it possible for us to understand the circuit and constructional difficulties which caused the oscillation in the early "Mark I" preamps and to attain stable operation with good performance in the modified "Mark IA" design. The best bandwidths attained with these Mark IA preamps, ~ 400 MHz, are not quite high enough for gigabit communication, however.

2.3.4.2 Mark II Three-GAASFET Preamp Design

In early evaluation work on GAASFET preamps of the "Mark IA" design in a laboratory PGBM 400Mb/s 1.06 μ communication system at

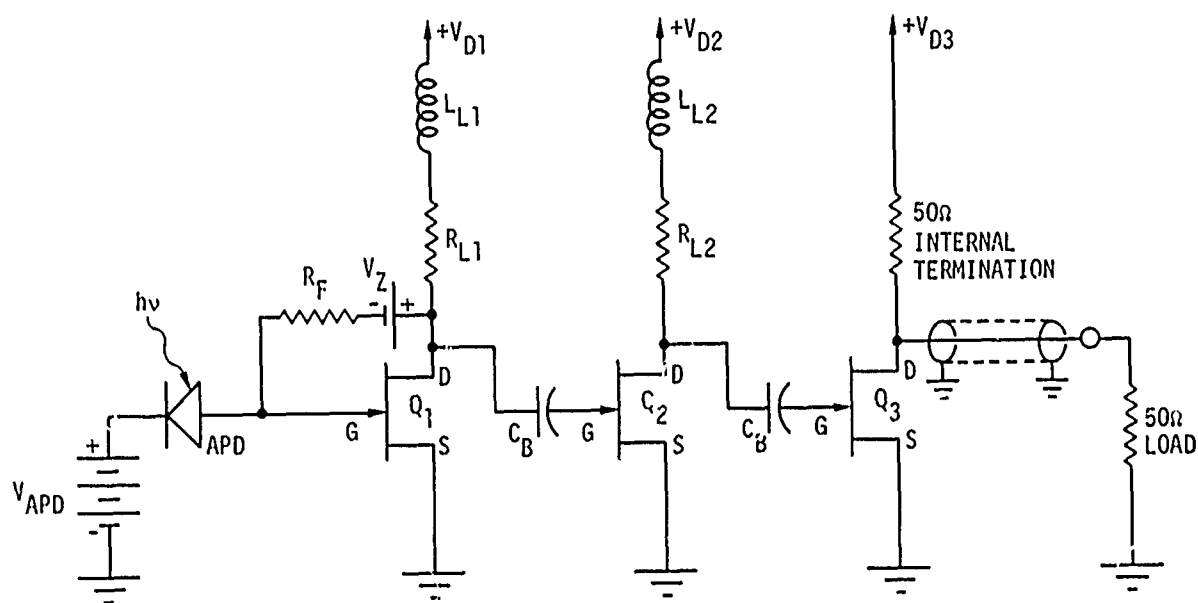


Fig. 2.11 Simplified Circuit Diagram for the Mark II GAASFET Preamp Design. (Complete circuit diagram for preamp #7 is shown in Fig. 4.16.)

McDonnell Douglas, St. Louis (by Dr. Samuel Green), it became clear that the "EMI" environment present in the evaluation facility could cause sufficient cable ground pick-up, power supply injected interference, etc., to cause degraded B.E.R. results. The "Mark II" design was developed as a simple extension of the "Mark IA" design only incorporating an additional gain stage in the preamp itself to help raise the signal level above the interference noise level.

This "Mark II" GAASFET preamp design is shown in simplified schematic form in Fig. 2.11. The functioning of the "op-amp" stage, Q_1 , is exactly the same as in the "Mark IA" design in Fig. 2.9. The only change in design noted in Fig. 2.11 is the addition of the Q_2 gain stage. (Actually, the Mark II preamp is considerably more complicated than the Mark IA, with 5 silicon bipolar transistors and numerous other components added, internal to the preamp for automatic output dc balance, bias generation, etc.; functions not shown in Fig. 2.11.) Q_2 is a simple voltage amplifier stage with approximate gain $g_{m2} (R_{L2} || R_{D2})$ or 13dB in GAASFET preamp #7. As in the Q_1 "op-amp" gain stage, L_{L2} is used to "tweek" the high frequency response slightly to obtain a wider 3dB bandwidth and faster transient response (i.e., to go from a slow simple single pole rolloff to a response with quadratic poles). The value of L_L is selected (in relation to $R_L || R_D$ and C_L) to give a crisp transient response without undesired oscillatory behavior. Because the Q_2 gain stage has a limited bandwidth (~ 500 MHz in #7), the resulting overall bandwidth (~ 300 MHz) is less than for a Mark IA preamp and certainly inadequate for gigabit data rate use.

2.3.5 Basic Design of the Gigabit Mark III Three-GAASFET Preamp

The "Mark IA" and "Mark II" preamp designs are not useable for gigabit data rate communications because of their limited closed-loop bandwidths (of the order of 300-400 MHz in the experimental preamps with R_F values of 3K Ω -4K Ω). For gigabit data rate communications reception of binary-modulated modelocked laser pulses, we must have a receiver bandwidth of >500 MHz (specifically with a peak to near-baseline fall time under 1ns). For greater sensitivity we would like to be able to obtain these wider bandwidths with larger values of feedback resistance, R_F . Detailed analysis of the experimental Mark IA (#4 and #5) and Mark II (#7) preamps indicated that the principal problem was that the loading capacitance on Q_1 , C_L (representing the

combined input capacitance of Q_2 and stray capacitance to ground from the level-shifting circuitry, V_Z , and dc-block, C_B , in Figs. 2.9 and 2.11) was too large. If a large value of $R_{L1} \parallel R_{D1}$ is obtained, then A_O , the open-loop "op-amp" low frequency gain, is high but the 3db rolloff frequency, F_A , drops accordingly, increasing the high frequency phase shift. In fact, the gain-bandwidth product of this "op-amp" will be of the order of $g_{m1}/2\pi C_L$, so that if C_L is too large, there is no way we can obtain higher-frequency performance.

This problem with the earlier designs stems from the fact that Q_1 does not represent a true operational amplifier (as indicated in Fig. 2.8), because it does not have low output impedance. Hence the loading effect of C_L degrades the "op-amp" gain bandwidth. The "Mark III" preamp design was developed as an extension to the Mark IA design concept, making the input stage a two-GAASFET true operational amplifier with low output impedance. The simplified schematic diagram of the "Mark III" preamp design is shown in Fig. 2.12. Here we see that the "op-amp" voltage gain stage is a cascade arrangement with grounded-source Q_1 driving a source follower Q_2 . The level-shifted (V_Z) output from Q_2 is the output feedback point to the input (through R_F), so that now we require that the sum of the phase shifts in Q_1 , Q_2 and the R_F - C_I feedback network be less than 180° , while the open loop gain exceeds 1. This makes it important to use very careful circuit layout as the combined power gain of Q_1 and Q_2 can be very large (circuit oscillations at X-band frequencies have been obtained with experimental Mark III preamps when spurious feedback coupling was allowed to exist). With the appropriate precautions taken with circuit fabrication, we have obtained excellent stable results with the Mark III preamps (#6 and #8).

The open loop gain at lower frequencies, A_O , will be given in the circuit of Fig. 2.12 by

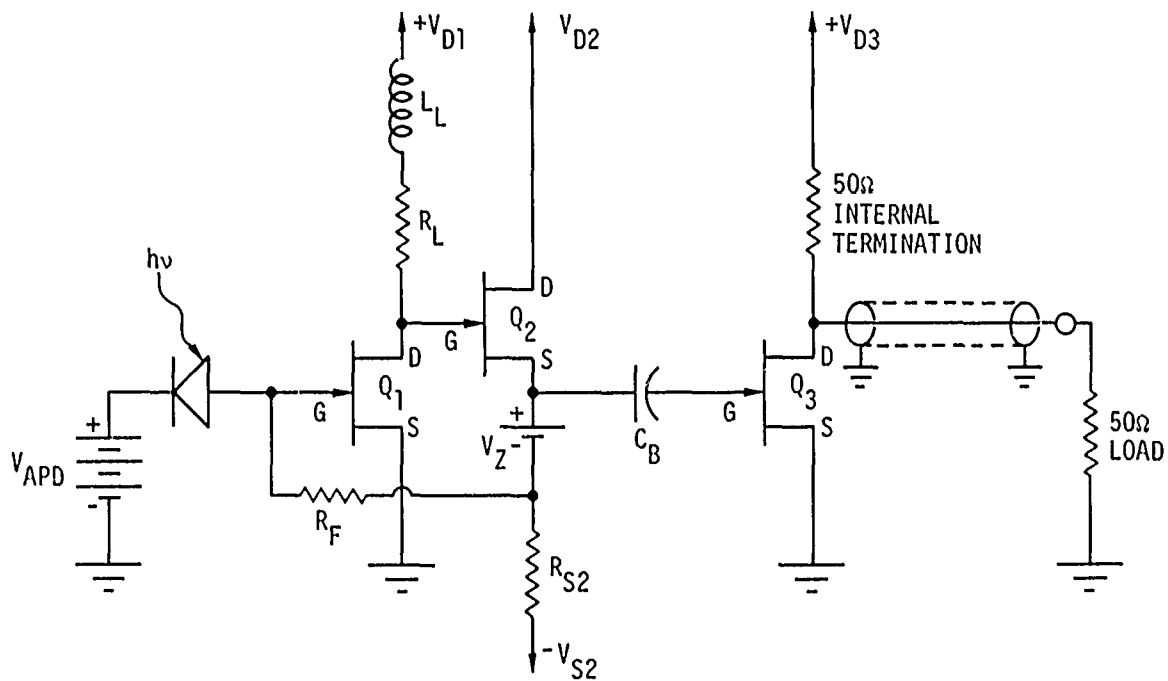


Fig. 2.12 Simplified Circuit Diagram of the Mark III GAASFET Preamp Design. (Complete circuit diagram for GAASFET preamp #8 is shown in Fig. 4.24.)

$$A_o \approx \frac{g_{m1}(R_L \parallel R_{D1})}{1 + 1/g_{m2}(R_{S2} \parallel R_{D2})} \quad (2.37)$$

(where $R_L \parallel R_{D1} \equiv 1/(1/R_L + 1/R_{D1})$, etc.) and the output impedance of the gain stage will be approximately

$$Z_{OUT} \approx 1/(g_{m2} + 1/R_{S2} + 1/R_{D2}) \quad (2.38)$$

For $g_{m2} \approx 12$ mmho, Z_{OUT} will typically be about 75 ohms so that there will be virtually no loading effect from fractional pf load capacitances. Hence, by increasing R_L we can obtain higher gains without destroying the bandwidth (F_A) due to C_L loading. The principal capacitive loading effect of concern is C_D of Q_1 , C_{GD} of Q_2 , and the stray capacitance from the drain of Q_1 (R_L , etc.) to ground. Gain-bandwidth products of the order of 5 GHz have been obtained for the "op-amp" (Q_1 - Q_2) section of "Mark III" GAASFET preamps. This makes it possible to obtain subnanosecond preamp response times with $R_F = 5000\Omega$ feedback resistance values, with corresponding low noise and >1Gb/s data rate capability.

2.3.6 GAASFET Voltage Gain Characteristics

The most important properties of the "op-amp" or input voltage gain stage of the GAASFET preamps is their open-loop voltage gain, A , and their input capacitance. One of the vexing problems encountered in the early part of this work was that it was found that the voltage gains in available GAASFET devices was disconcertingly low. The voltage gain of Q_1 in the Mark IA or Mark II preamps at low or mod frequencies should be of the order of

$$A_o \approx \frac{g_m}{1/R_L + 1/R_D} \equiv g_m(R_L \parallel R_D). \quad (2.39)$$

Measuring g_m from the spacing of the I_D vs. V_{DS} (with V_{gs} as the stepped parameter) curves for typical GAASFET's might give $g_m \approx 0.012$ mhos, $R_D > 5K\Omega$. Hence we would expect for $R_L = 1K\Omega$, for example, $A_o \approx 10$. Experimentally, typical 1μ gate GAASFET's were found to give $A_o \approx 2.5$ to 3 . (Needless to say, an open loop gain of 2.5 does not make a very effective "op-amp".) The problem was found to be that R_D , the drain resistance of the GAASFET, was much lower at high frequencies (above 10^4 or 10^5 Hz) than measured from the "near dc" curves. R_D values of 250 to 400 ohms were found typical for 1μ gate devices (both Science Center - fabricated devices and those obtained from outside vendors), while 2μ gate FMX 950 devices gave somewhat higher values (600Ω - 800Ω with an occasional sample higher).

This low output resistance of the GAASFET's is not, in fact, a spurious effect (it is the high output resistance measured in the low-frequency curves that is the spurious effect-thought to be associated with trapping states at the n^+ GaAs-semi insulating GaAs interface). In fact, in a GAASFET with a very narrow gate, there will be significant coupling between the drain potential and the semiconductor potential under the source side of the gate, just as there is in a triode vacuum tube between the plate potential and the space charge region between the grid and the cathode. Just as in the triode vacuum tube where this leads to a finite plate resistance, in the GAASFET this leads to a finite drain resistance. The narrower the gate region is, the larger will be this drain potential coupling and the lower R_D .

One solution to this problem might be seen, then, in using wider-gate GAASFET's. This is completely unacceptable for our application, however, because the input capacitance (C_{gs} or C_{IN}) increases with gate width and we must have low input capacitance for sensitive charge pulse response. A better result that would work is to use a cascode GAASFET pair for Q_1 as shown in Fig. 2.13 a). Here GAASFET #1 is used in the grounded-source configuration while #2 is used as a grounded-gate amplifier

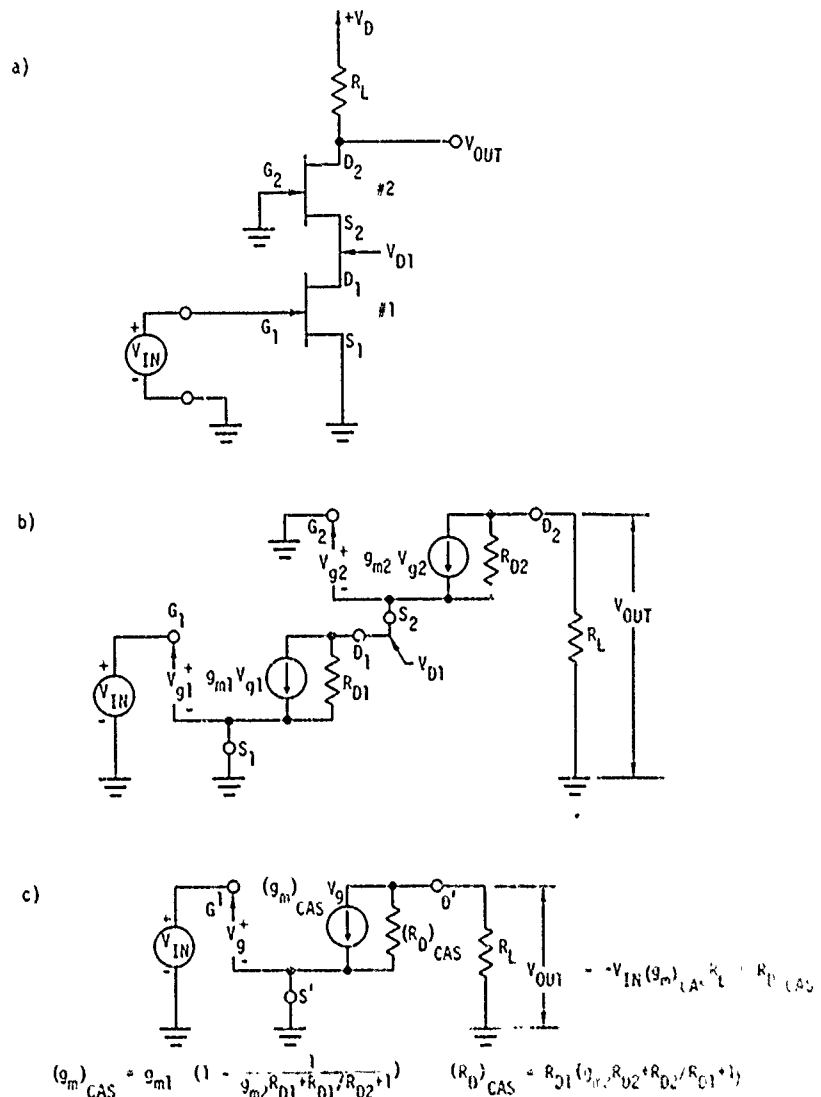


Fig. 2.13 Circuit model for cascode FET arrangement illustrating the greatly increased voltage gain of a dual-gate GAASFET compared to a single-gate. a) Cascode equivalent circuit for a dual gate GAASFET. b) Low-frequency (omitting capacitances) model for a). c) Equivalent circuit for b) defining the equivalent drain resistance and equivalent transconductance for the dual-gate FET or cascode arrangement. Note that $(R_D)_{CAS} \approx R_D$.

to raise the output impedance. The low-frequency (ignoring capacitances) equivalent circuit of this cascode GAASFET voltage gain stage is shown in Fig. 2.13 b). Solving for the gain, V_{OUT}/V_{IN} , we obtain

$$A_o = \frac{-V_{OUT}}{V_{IN}} = \frac{g_{m1} R_L R_{D1} (g_{m2} R_{D2} + 1)}{R_{D1} (g_{m2} R_{D2} + 1) + R_{D2} + R_L} \quad (2.40)$$

The effect of the cascode arrangement is more clearly illustrated by the "equivalent FET" shown in Fig. 2.13 c), where the two GAASFET's in Figs. 2.13 a) and b) are replaced by a single cascode-equivalent GAASFET having transconductance $(g_m)_{CAS}$ and drain resistance $(R_D)_{CAS}$. In terms of these parameters, the gain will be

$$A_o = \frac{-V_{OUT}}{V_{IN}} = \frac{(g_m)_{CAS}}{1/R_L + 1/(R_D)_{CAS}} \equiv (g_m)_{CAS} (R_L \parallel (R_D)_{CAS}) \quad (2.41)$$

(in analogy with Eq. 2.39). From the analysis of Fig. 2.13 b), we obtain for the cascode equivalent transconductance

$$(g_m)_{CAS} = g_{m1} \left[1 - 1/(g_{m2} R_{D1} + R_1/R_2 + 1) \right] \quad (2.42)$$

and for the cascode output (drain) resistance

$$(R_D)_{CAS} = R_{D1} (g_{m2} R_{D2} + R_{D2}/R_{D1} + 1) \quad (2.43)$$

We note that since $g_{m2} R_{D1}$ is considerably greater than unity, in general $(g_m)_{CAS}$ will be only slightly smaller than g_{m1} , while the output resistance, $(R_D)_{CAS}$ will be much larger than R_{D1} which means that the available voltage

gains will be much higher. For example if we take for typical 1μ gate GAASFETs, $g_{m1} = g_{m2} = 0.015$ mho and $R_{D1} = R_{D2} = 300\Omega$ we would have for a cascode arrangement $(g_m)_{CAS} = 0.0127$ mho and $(R_D)_{CAS} = 1950$ ohms. Hence the open-circuit voltage gain ($R_L = \infty$) of the cascode arrangement would be $(g_m)_{CAS} (R_D)_{CAS} = 24.75$ as opposed to $g_{m1} R_{D1} = 4.5$ with a simple grounded emitter stage (a 15db improvement in open-circuit gain).

While the use of a cascode (grounded source-grounded gate) GAASFET pair in place of Q_1 in all of the preamp designs would be called for, in fact it is not necessary to bond up two discrete devices for the pair. A "dual gate" GAASFET operated with the second gate grounded is an operational equivalent to the cascode arrangement of single-gate GAASFETs shown in Fig. 2.13. (This dual-gate GAASFET bears the same relationship to a single-gate unit as a tetrode or pentode vacuum tube bears to a triode.) Measurements on the dual-gate GAASFET chips indicate that the output drain resistances are of the order of the $2K\Omega$ values predicted by Eq. 2.43 and their performance in the gigabit Mark III preamps, particularly #8, has been excellent. It should be noted that from a functional standpoint, the "op-amp" in a Mark III preamp (Fig. 2.12) with a dual-gate GAASFET as Q_1 is effectively a three-GAASFET cascode-cascade amplifier (grounded source-grounded gate-grounded drain [source follower]). The low-frequency open-loop gain obtained in GAASFET preamp #8 is approximately 20.

3.0 TECHNICAL APPROACH

3.1 III-V Alloy Materials Technology3.1.1 Materials Selection

The desired low leakage, high quantum efficiency and wide band-width requirements for this avalanche photodiode place extremely stringent limitations on the materials which can be used. The most important requirement is that the semiconductor must have a direct bandgap with $E_g \sim 1.16$ eV so that the photons are all absorbed within a small distance ($2-3\mu$). There are no elemental or binary compound semiconductors which can satisfy this requirement, thus one is forced to use a III-V ternary alloy. A diagram of energy band gap vs. lattice constant is useful for this selection because it shows the useful alloys, the potential substrate materials and the degree of lattice mismatch between them. Such a diagram is shown in Fig. 3.1. All of the potential III-V alloy combinations are found by following a line of constant energy gap of $E_g = 1.16$ eV across the intersection with each ternary alloy in Fig. 3.1. The possible choices are as follows: $\text{Ga}_x\text{In}_{1-x}\text{As}$, $\text{GaAs}_x\text{Sb}_{1-x}$, $\text{InAs}_x\text{P}_{1-x}$, $\text{In}_x\text{Al}_{1-x}\text{As}$, $\text{GaP}_x\text{Sb}_{1-x}$, $\text{InP}_x\text{Sb}_{1-x}$, $\text{Ga}_x\text{Al}_{1-x}\text{Sb}$ and $\text{In}_x\text{Al}_{1-x}\text{Sb}$. The requirement of a substrate which is transparent at 1.06μ and a reasonable lattice match between substrate and epitaxial layer eliminates all but the first three choices. At the start of this program, InP was not grown domestically, and that which was available was of very low quality, thus it was eliminated in favor of GaAs as the choice for substrate material. Of the above three alloys, only $\text{Ga}_x\text{In}_{1-x}\text{As}$ and $\text{GaAs}_x\text{Sb}_{1-x}$ will grow on GaAs. Both of these ternaries have been grown successfully on GaAs and the choice between these two alloys reduces to the one which has fewer interface problems, better chemical homogeneity and fewer device fabrication problems. Since actual device fabrication and performance are the best measure of these quantities, epitaxial layers of both $\text{Ga}_x\text{In}_{1-x}\text{As}$ and $\text{GaAs}_x\text{Sb}_{1-x}$ were grown and devices fabricated from both. The $\text{GaAs}_x\text{Sb}_{1-x}$ system proved to be the better system for our devices because of our device design. With the

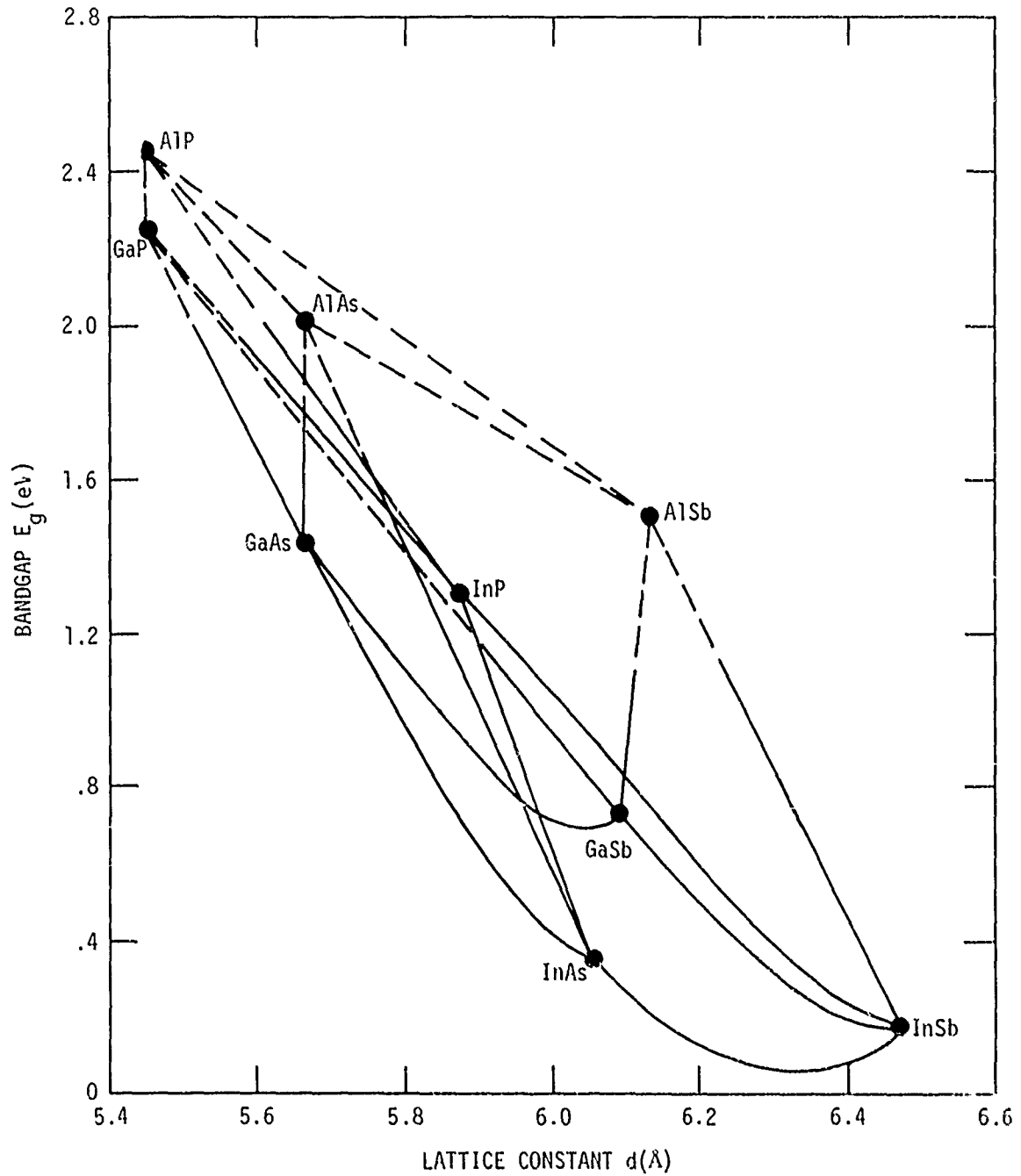


Fig. 3.1 Energy bandgap vs. lattice constant for all of the binary and ternary alloy semiconductors of Al, Ga or In with P, As or Sb. The solid lines are for direct bandgap materials and the dashed lines for indirect bandgap materials

inverted mesa structure described in Section 2.2, the mesa must etch uniformly with no sharp etch pits or surface breakdown will occur before any bulk avalanche gain is achieved. The orientation dependence of growth for ternary alloys on binary substrates was the determining factor in our choice. The best growth face for $\text{Ga}_x\text{In}_{1-x}\text{As}$ on GaAs is the $\langle 111 \rangle_A$ face while that for $\text{GaAs}_x\text{Sb}_{1-x}$ is the $\langle 100 \rangle$. The $\langle 111 \rangle_A$ face is the surface most commonly used for etch pit and dislocation studies because the pits are delineated better than on any other surface, thus the mesa etch proved to be an almost insurmountable problem for the $\text{Ga}_x\text{In}_{1-x}\text{As}$ layers and tipped the balance in favor of the $\text{GaAs}_x\text{Sb}_{1-x}$ system.

3.1.2 Materials Growth and Evaluation

The phase diagram for $\text{GaAs}_x\text{Sb}_{1-x}$ has been reported by Antypas, et al⁽¹¹⁾ and Panish and Illegems.⁽¹²⁾ A computer program was written to solve the equations describing the ternary system. The approach was identical to that of Panish and Illegems⁽¹²⁾ in which both the liquid and solid are treated as simple solutions. This phase diagram formulation is well described by these authors and there is no need to restate the equations here. The values of the parameters used to find the ternary diagram were as follows:

TABLE 3.1

	GaAs	GaSb	Units
T^F	1238	710	$^{\circ}\text{C}$
ΔS^F	16.64	15.8	e.u./mole
α	5160-9.16T	4700-6.0T	cal/mole
$\alpha_{\text{As-Sb}} = 750$	$\beta_{\text{GaAs-GaSb}} = 2700$		cal/mole

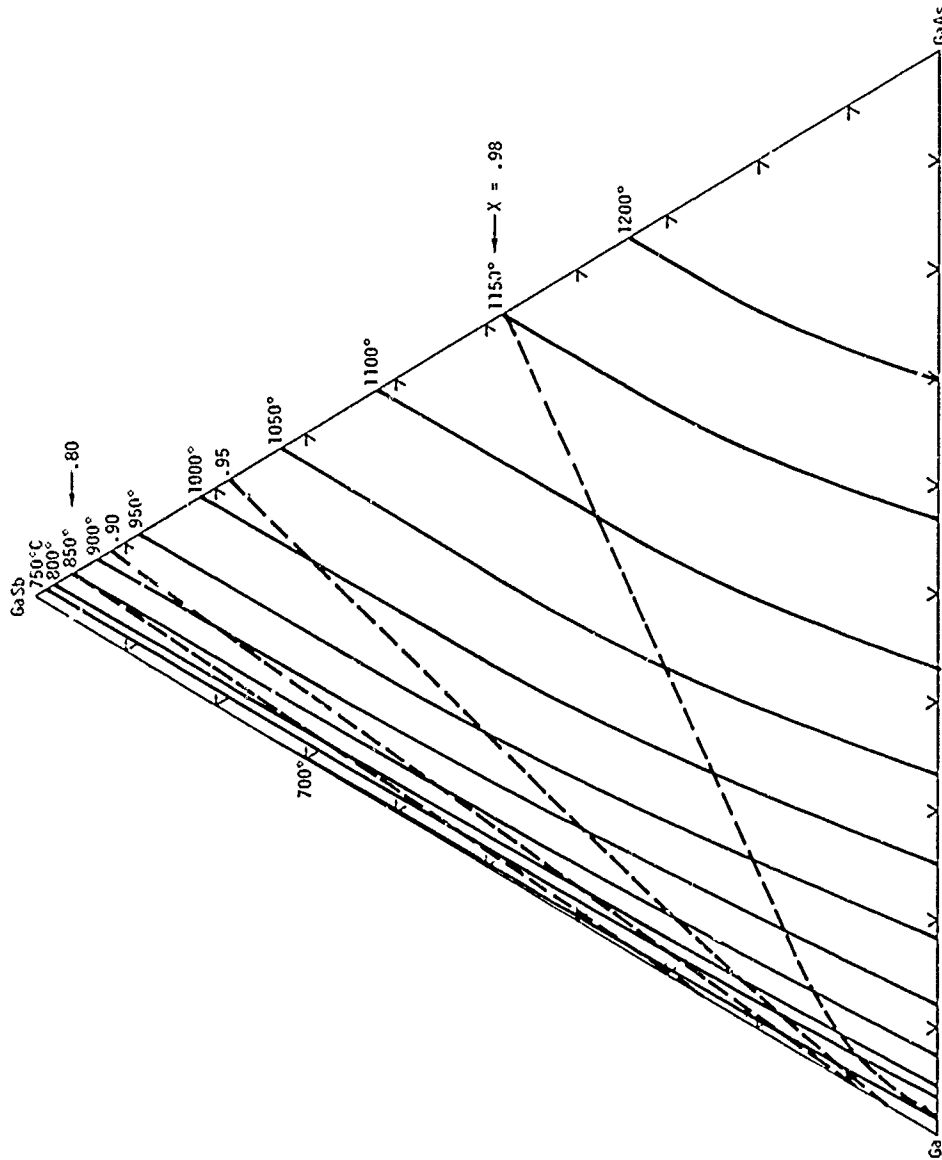


Fig. 3.2 Ga rich region of the GaAsSb phase diagram. The solid lines are liquidus isotherms while the dashed lines are $\text{GaAs}_x\text{Sb}_{(1-x)}$ iso-composition lines.

The calculated liquidus lines for the Ga rich corner are shown in Fig. 3.2 and calculated and experimental points for the coefficient of GaSb vs. Sb mole fraction in the melt with temperature as a parameter is shown in Fig. 3.3. This calculated phase diagram is in reasonable agreement with our experimental data on the composition of epitaxial layers and it has proven to be very useful to determine the melt composition and growth temperature to achieve the desired solid alloy compositions for the multiple layers in the APD.

From the data on the energy bandgap vs. composition for $\text{GaAs}_x\text{Sb}_{1-x}$ (11,13) in Fig. 3.4, a composition of $\sim 16\%$ GaSb (i.e. $x = .84$) is required for the active layer of the avalanche photodiode. In order to avoid Sb build up and compositional changes during growth it is desirable to grow the ternary in a region where the Sb mole fraction in the solid does not change rapidly with temperature. From Fig. 3.3, one observes that temperatures of 750°C or higher are required. We have elected to grow at 775°C with a ΔT of $\sim 5^\circ\text{C}$ during growth of the epitaxial layers. The increasing GaSb fraction with decreasing temperature is a desirable feature in our particular device structure because the buffer layer will tend to be graded to more closely match the active layer and reduce the number of edge dislocations at the interface. Since both p^+-n-n^+ and n^+-p-p^+ structures are required to study the electron and hole avalanche multiplication coefficients, both p^+ and n^+ GaAs substrates are required as well as either p or n doping for each of the three epitaxial layers. For p-type doping Zn, Ge and Si have been used and for n-type Sn and Te have been used. Ge, Si and Sn are particularly useful dopants if more than one epitaxial layer is grown at a time because they all have low vapor pressures and cause a minimum of cross contamination between the melts. These are the only dopants used in the APD structure because a lightly doped region with a moderately high breakdown voltage is always required and the high vapor pressure dopants would preclude the growth of this layer. As noted above, both n^+-p-p^+ and p^+-n-n^+ structures have been grown, however, for simplicity, further descriptions of the growth will refer only to the p^+-n-n^+ structure. For this structure, the buffer layer is Sn doped while both the active and

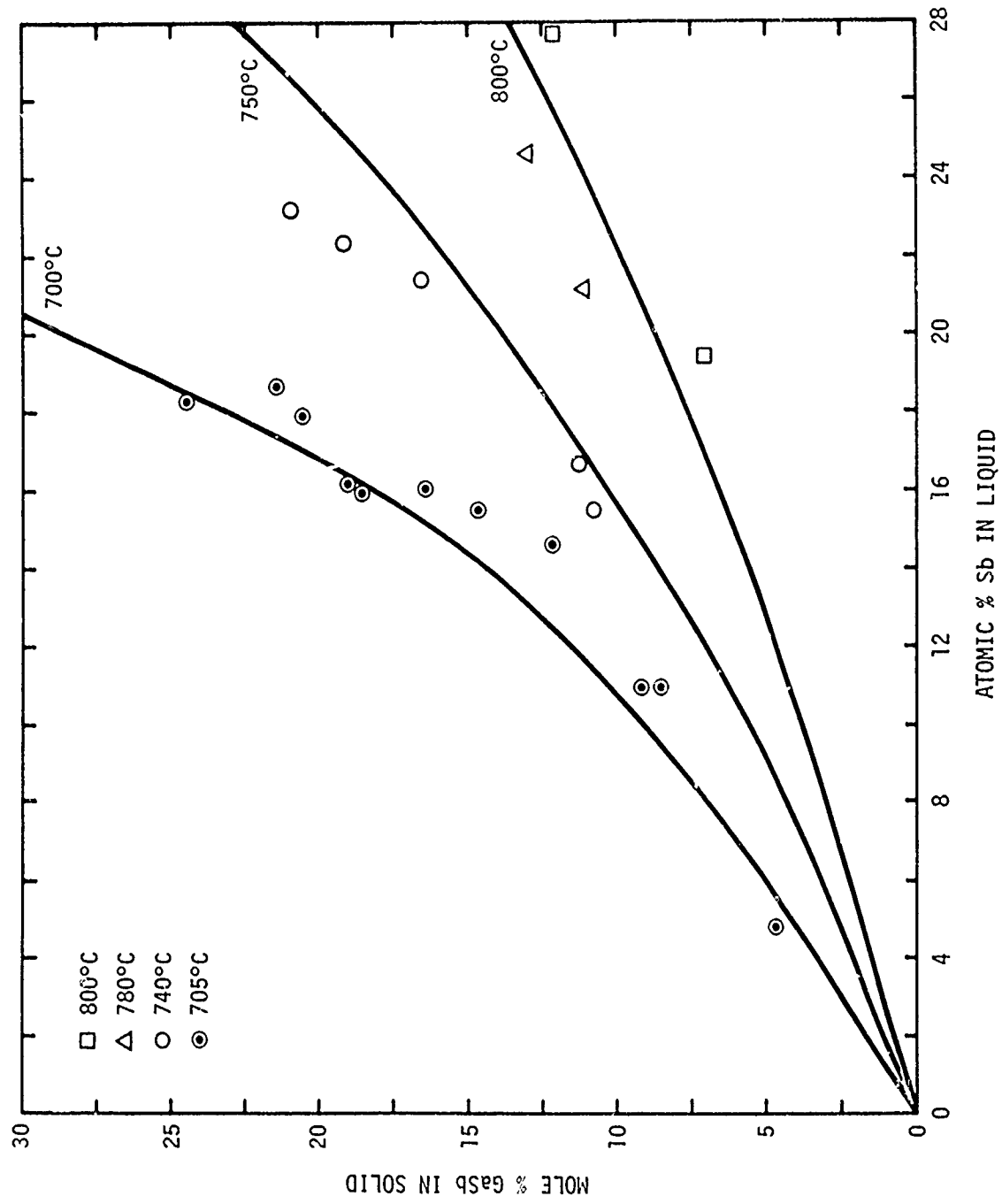


Fig. 3.3 Experimental and calculated Sb distribution curves for GaAsSb solid.

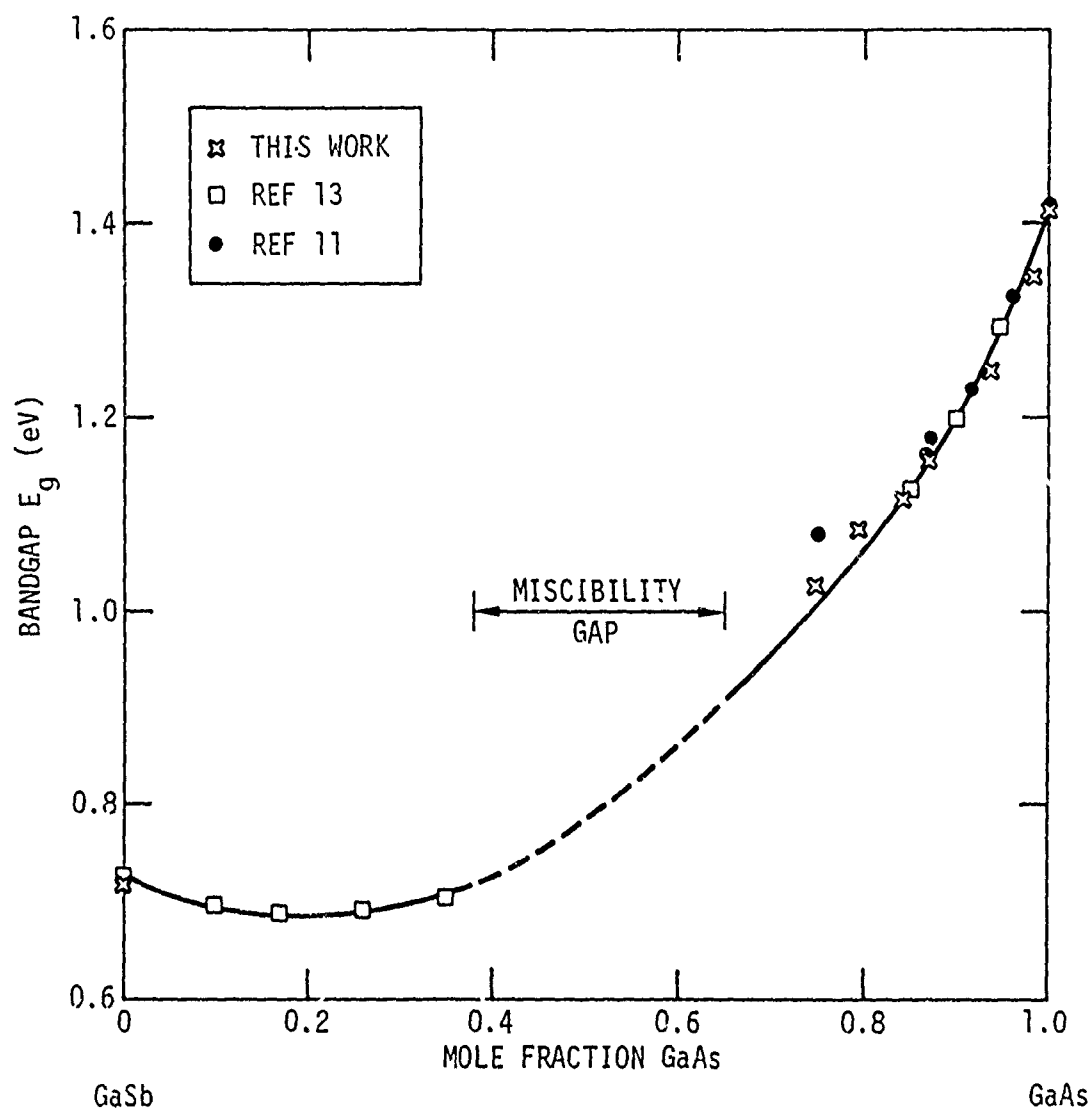


Fig. 3.4 Energy bandgap vs. composition for the $\text{GaAs}_{1-x}\text{Sb}_x$ alloy system. The region $0.4 < x < 0.65$ is inaccessible because of a miscibility gap in the alloy.

contact layers are Ge doped.

The epitaxial layer growth for any of the three layers follows the same sequence with only slight variations in the Sb concentration or the dopant to achieve the desired doping level and alloy composition. The substrates are prepared by a standard technique of mechanical lapping and polishing with successively finer grit alumina and finally a chemi-mechanical polish using Cabosil and $10\text{H}_2\text{O}:1\text{H}_2\text{O}_2$ in an oscillatory polisher. After removing the substrates from the polishing block, they are cleaned in trichloroethylene, acetone, water and methanol. The substrates are etched in $3\text{H}_2\text{SO}_4:1\text{H}_2\text{O}_2:1\text{H}_2\text{O}$ just prior to insertion into the furnace. The individual melts are made up with 6 9's Ga and 5 9's Sb from Alusuisse and Asarco respectively with between 10 and 25 atom percent Sb depending upon the desired solidus composition as shown in Fig. 3.3. Undoped polycrystal GaAs is used as the As source for saturating the melt. The substrate and melt are raised to 775°C and allowed to equilibrate for ~ 1 hr. The melt is then brought over the substrate and the furnace temperature decreased at a rate of $\sim 1^\circ\text{C}/\text{min}$. After the desired temperature drop, a second melt is pulled over, then the final melt is pulled over and after the desired ΔT , the melt is pulled free from the substrate. The furnace is then cooled to room temperature and the structure is removed for evaluation.

After the structure is removed, routine evaluation consists of cleaving along a $\langle 110 \rangle$ plane and etching for 2-3 sec. in the A-B etch⁽¹⁴⁾ to delineate the junctions. The layer thicknesses are then measured under an optical microscope. Next, "quick diodes" are fabricated by etching a mesa with a wax dot on a portion of the wafer. Tungsten probes are contacted to the diode and a photoresponse measurement is made. This measurement shows the bandgap of both the buffer and active layers and can then be used as feedback on control of the epitaxial layer compositions.

During the course of this work, considerable effort has been expended on studies of the microscopic operation of the APD. One of the

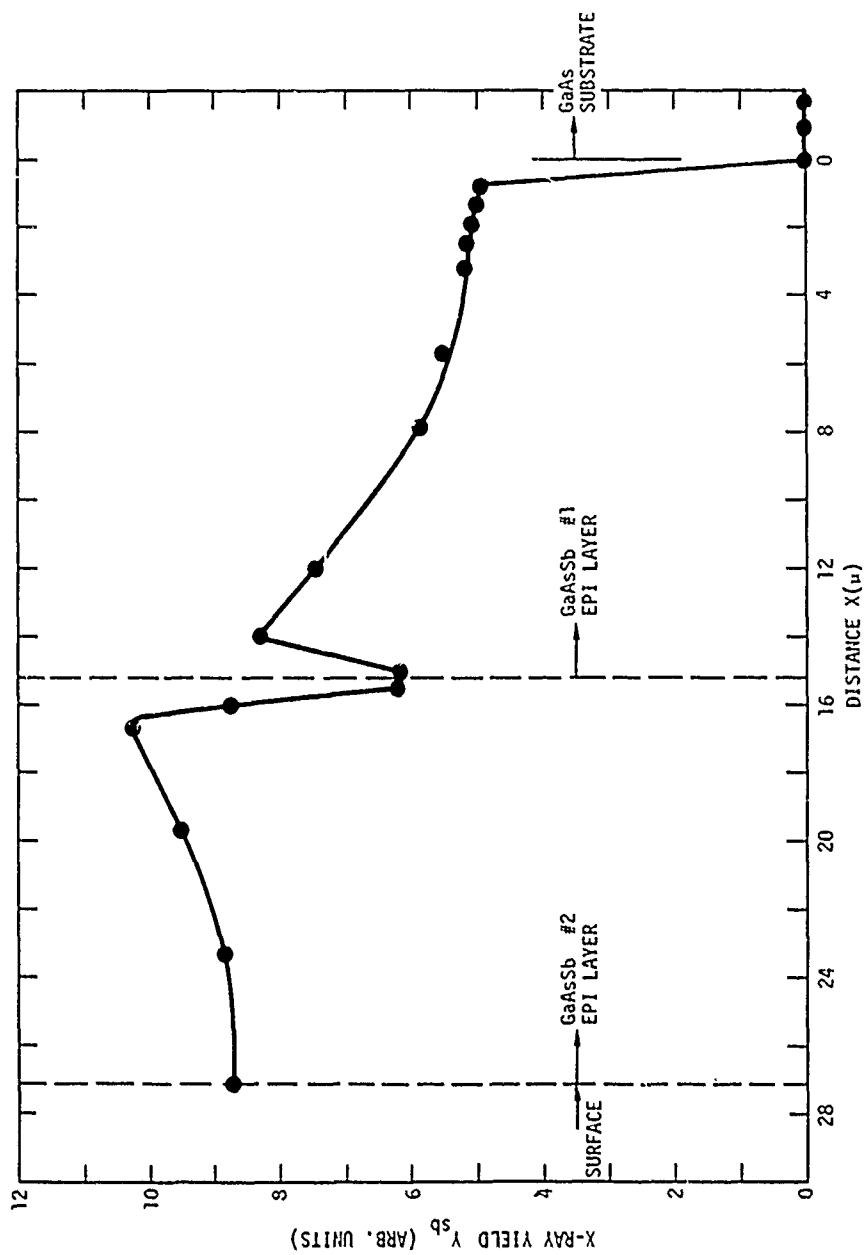


Fig. 3.5 Sb profile obtained from X-ray emission on SEM for two GaAsSb layers grown on a GaAs substrate. The melt composition for each epitaxial layer was identical but growth conditions at the time the second melt was brought over the substrate caused the Sb concentration to dip at the interface.

most useful tools is a scanning electron microscope (SEM), particularly when combined with an energy dispersive X-ray detector and a beam induced current amplifier and monitor. This enables us to measure the chemical composition vs. depth in the epitaxial layers, the current collection efficiency and multiplication as a function of position and bias voltage and to correlate these with surface features and defects in the layers to determine if they are due to growth faults (metallic inclusions or precipitates) or substrate originated faults (dirty substrate, poor wetting or high dislocation density).

Studies of these GaAsSb heterojunction APD's and comparison with GaAs homojunction and GaAlAs-GaAs heterojunction diodes revealed that the quality of the junction is adversely affected by mismatch between the two layers. As the degree of mismatch decreased, the junctions improved. The GaAsSb diodes did not, however, show the improvement we expected when we went to a homojunction GaAsSb diode (i.e., buffer and active layer of the same composition). The problem with this structure is revealed in the X-ray profile of Fig. 3.5. This is a plot of the Sb X-ray yield vs. position for this GaAsSb homojunction structure. The interface between the two layers shows a sharp drop in Sb at the interface. This drop is coupled with a corresponding increase in the As level and is due to the condition of melt non-equilibrium when the second melt is brought over the substrate. This makes it virtually impossible to achieve the high quality junction required in the APD by the use of two melts to grow the p-n junction.

The solution to this dilemma has been to grow a true GaAsSb homojunction from a single melt by the addition of dopant during the growth. In this way, the layer composition remains constant and the impurity incorporation just changes from n-type and p-type.

This dopant drop technique imposes a slight modification of the original device design. In the initial device, the p-n junction was between the buffer and active layers. With the dopant drop technique, the p-n junction occurs midway through the active layer as shown in Fig 2.7. This places an additional constraint on the active layer thickness. In

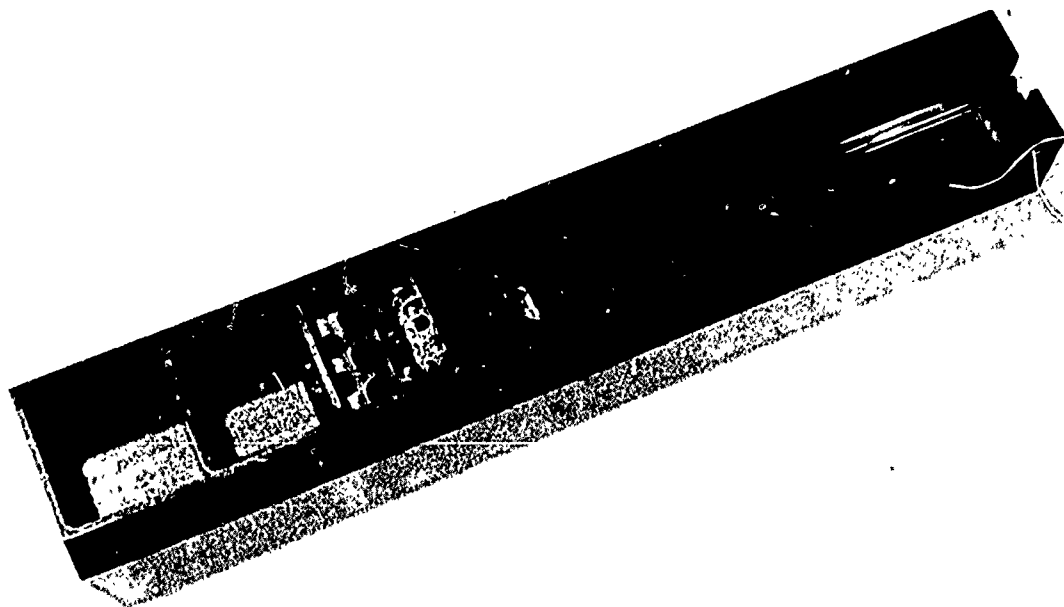


Fig. 3.6 Graphite slider boat used for "doping drop" growths. Top slider (small insert with holes) is where the dopant is placed and the quartz push rod is used to push this slider back to where the sets of holes line up and the dopant drops through into the melt to change the doping.

order to achieve the high quantum efficiency, the active layer must be nearly punched through to the buffer layer at the avalanche breakdown voltage. After several experiments with the dopant drop technique the required growth conditions were achieved.

The dopant drop technique utilizes a boat much like our earlier versions, except a small shelf is built into the top of the slider. The slider is moved with a quartz push rod, just as earlier, except that now the rod is pulled to move the slider and pushed to move across the shelf holding the dopant. This boat and slider arrangement are shown in Fig. 3.6.

Once this doping drop technique was worked out, the resulting APD's exhibited improved leakage and avalanche properties. This change in the growth has improved the device performance, however, higher avalanche gain is still necessary to achieve optimum system performance. Present studies of avalanche gain non-uniformities show a high correlation with the characteristic surface pattern of the GaAsSb heteroepitaxial structures. This pattern is shown in Figs. 3.7 and 3.8. This "basket weave" pattern is aligned along $\langle 110 \rangle$ crystallographic directions and these surface features are $\sim 4000\text{\AA}$ high. This pattern is a result of the lattice mismatch between GaAsSb and the GaAs substrate and it cannot be eliminated as long as there is lattice mismatch.

The results of this work strongly suggest that the area of avalanche gain uniformity in closely lattice matched structures is the most promising approach to the low uniform avalanche gain problem in the current structures.

3.2 Fabrication of the III-V Alloy Avalanche Photodiode Devices

The sequence of process for fabrication of the device is shown in Fig. 3.9. Each step in fabrication must be processed very carefully to avoid unnecessary problems that might occur. The substrate side is chemi-mechanically polished to obtain a mirror-like surface. A clean surface of the sample is essential before metals are evaporated. AuGe

SC571.16TRF

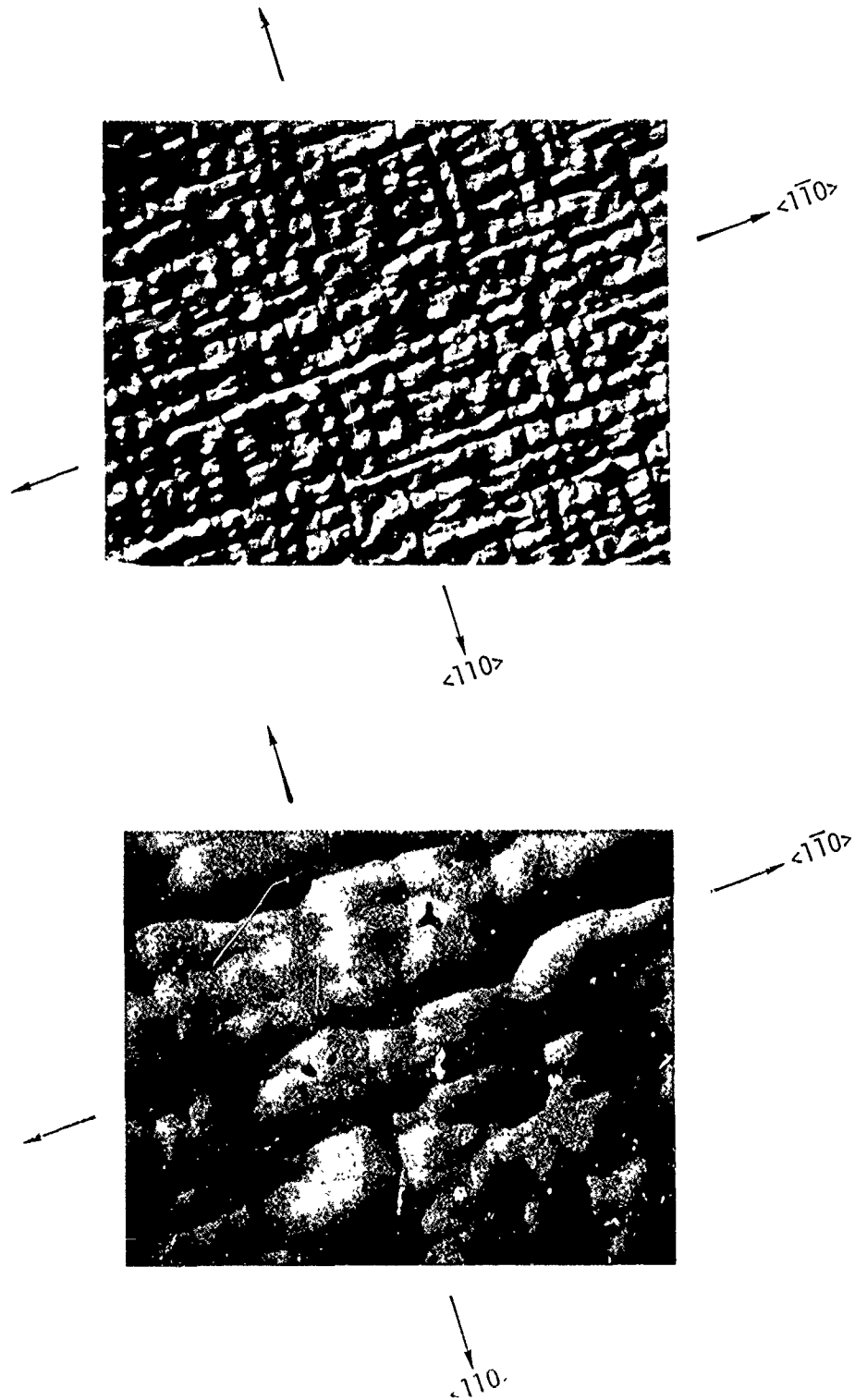


Fig. 3.7 Normarski phase contrast photomicrographs of the surface details of an APD structure. Note the alignment of surface features along $\langle 110 \rangle$ directions.

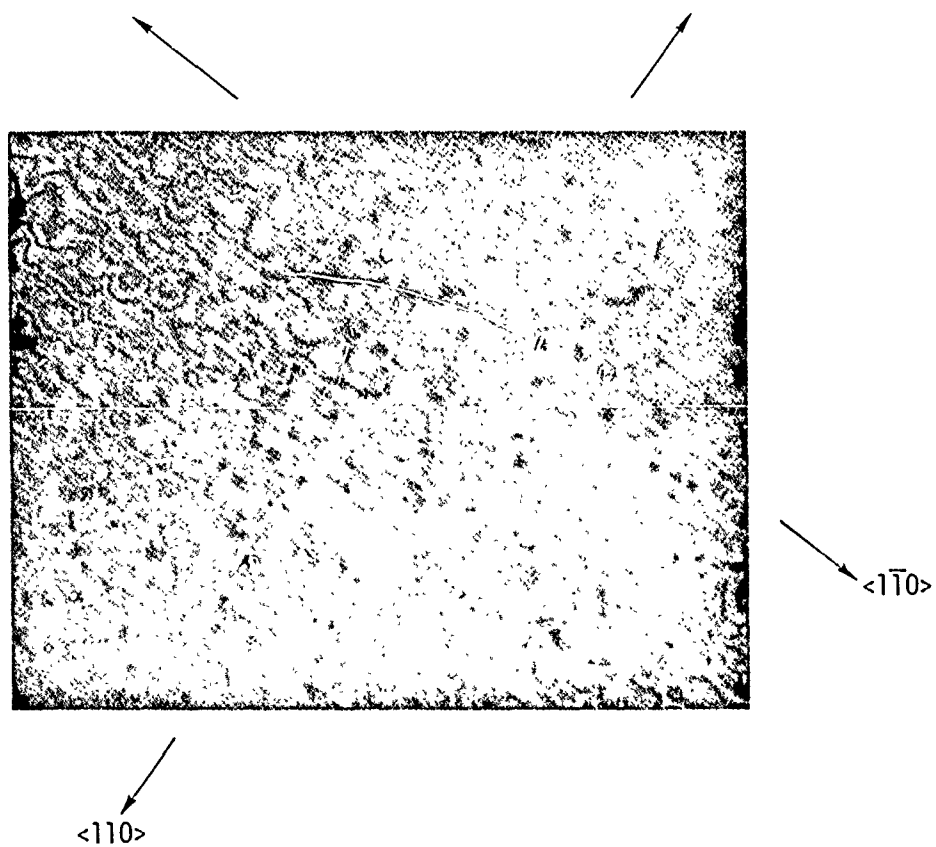
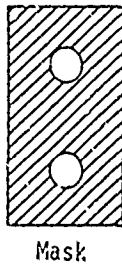
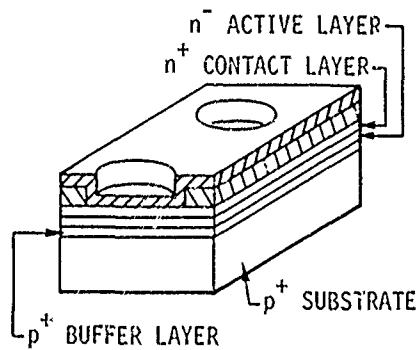


Fig. 3.8 Interference phase contrast photomicrograph of the surface of an APD structure. These surface features are between 1 and 2 fringes which corresponds to a height of 2700 to 5400Å.

SC571.16TRF

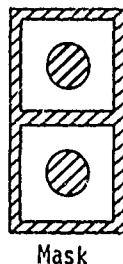
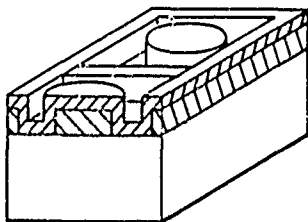
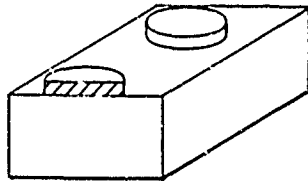


A. Metallization

1) Layer Side

Apply resist and photo etch 5 mil circular holes. Evaporate 1000Å of AuGe.

Remove resist lifting AuGe on top of resist and leaving 5 mil circular dots of AuGe.

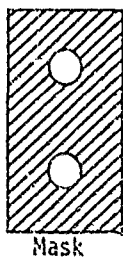
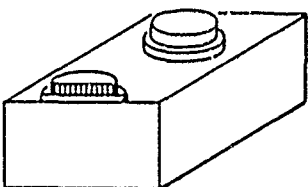
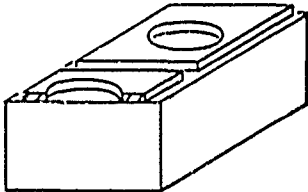


2) Substrate Side

Apply resist and photo etch 15 mil circular dots with 50 mil square outlines. Evaporate 1000Å of AgMn. Alignment of circular dots with AuGe dots on the layer side is made on an Infrared microscope.

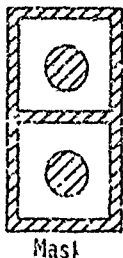
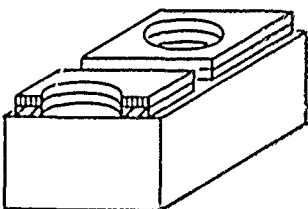
Remove resist lifting AgMn on top of resist and leaving 50 mil square of AgMn with 15 mil circular holes.

Alloy AuGe and AgMn at 500°C for 1 min.



3) Layer Side

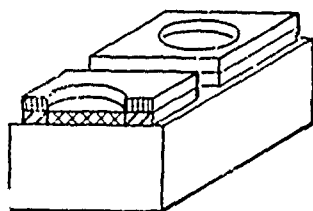
Apply resist and photo etch 4 mil circular holes over the AuGe dots. Electroplate 1 μm of Au. Remove resist leaving 4 mil circular dots of Au on top of AuGe dots.



4) Substrate Side

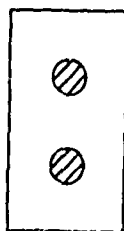
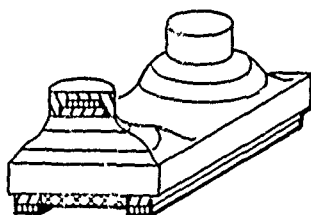
Apply resist and photo etch 15 mil circular dots with 50 mil square outlines. Electroplate 1 μm of Au. Remove resist leaving Au on top of AgMn squares with a 15 mil circular hole.

SC571.16TRF



B. Anti-reflection Coating

Deposit 1450Å of Si_3N_4 by sputtering to the substrate side. Remove Si_3N_4 on top of Au by scratching the substrate side on a paper leaving Si_3N_4 inside 15 mil circular holes only.



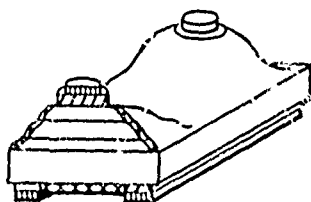
mask

C. Mesa Etch

1) Apply resist on the layer side and photo etch to leave 6 mil dots over Au and AuGe dots.

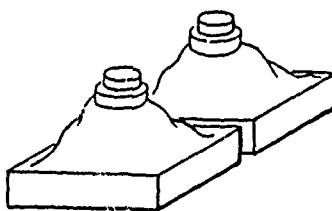
Etch mesa through n^+ and n layers and part of p^+ layer.

Remove resist.



D. Passivation

Apply surface passivation.



E. Device Mounting

Cleave the wafer into individual diodes. Mount the diode

Fig. 3.9 Device Fabrication Procedure for the Inverted Homo-Heterojunction Avalanche Photodiode (starting with the 3-layer epitaxial growth structure and ending with the APD chips ready for mounting or packaging).

and AgMn are used on n-type and p-type GaAs substrate or GaAsSb layers respectively for metallization. The photolithographical alignment of the metallization pattern on the substrate side to the metal dots already on the layer side is made using a special mask aligner under the infrared microscope. In the transmission mode the substrate metallization pattern and the circular dots on the layer side can be seen at the same time. After alloying the metal contacts, the ohmic contact resistance is checked. Au is electroplated over the metal contacts to protect them from pressure contacts or thermocompression bond contacts. The electroplated dots are smaller than the mesa dots to prevent Au from hanging over the mesa and shorting the diodes when undercutting occurs after the mesa etch. The mesa surface is passivated to protect the exposed p-n junction and to decrease the surface leakage current. To obtain maximum quantum efficiency, Si_3N_4 is deposited over the light entrance window on the substrate side for the anti-reflection coating. With a 1.06μ laser, a reflection coefficient of 0.15% is measured for a 1450\AA layer of Si_3N_4 on the GaAs substrate. Careful monitoring of the etch depth is important to obtain the desired mesa geometry which reduces electric field concentration at the p-n junction. The depth of the mesa is measured under a microscope after each mesa etch and compared to the layer thickness which is known from the measurement of the cleaved and stained edge of the layer. After checking the current-voltage characteristics and spectral responses of diodes, they are cleaved into individual diodes. Fig. 3.10 shows reflection and transmission photomicrograph of a diode taken through an infrared microscope. The diode is mounted as shown in Fig. 3.11 or it is placed into the hybrid microwave preamplifier package.

The new 50Ω microwave APD mount shown in Fig. 3.11 is smaller and more convenient than the older mount described in Ref. 1 and shown along with the new mount in Fig. 4.3. The mount and the sample mounting plate are designed so that the diode will be exactly over the spring loading pin and will make contact only to the gold contact pad. The general geometry gained by having the light brought in through the

SC571.16TRF

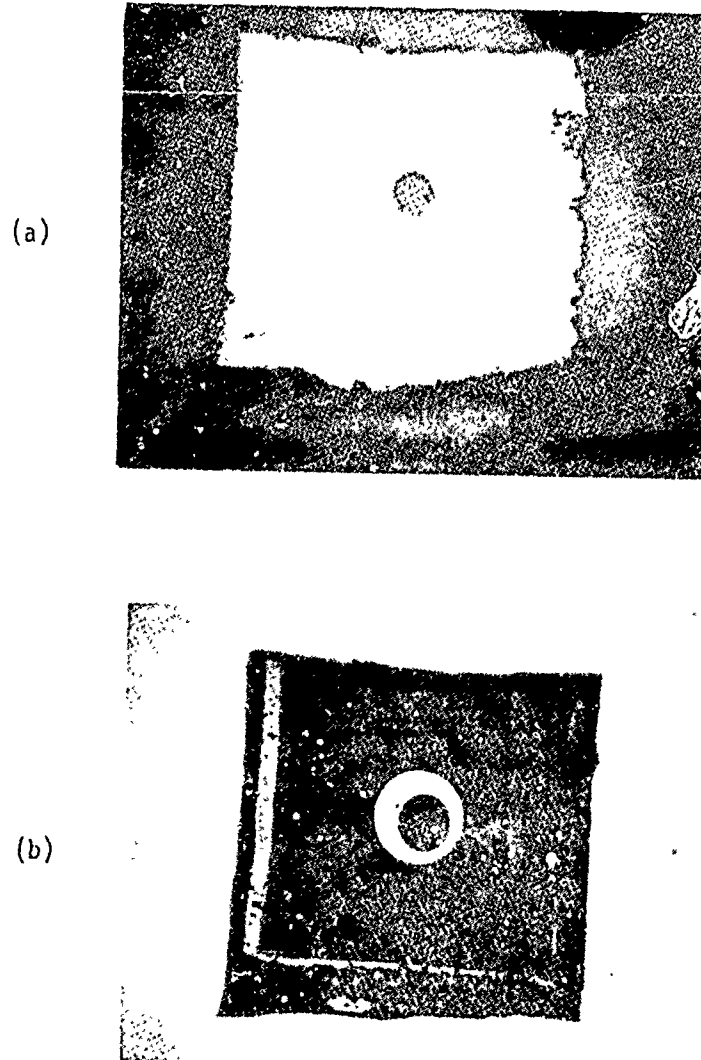


Fig. 3.10 a) Reflection photograph of a diode where the dark circular dot is the mesa outline and the metal contact in the center.
b) Transmission photograph of a diode is taken by the infrared microscope from the layer side. The dark square area is the metal contact on the substrate side. The large bright circle is the window on the substrate side. The dark circular dot is the outline of the mesa and metal contact to the contact layer.

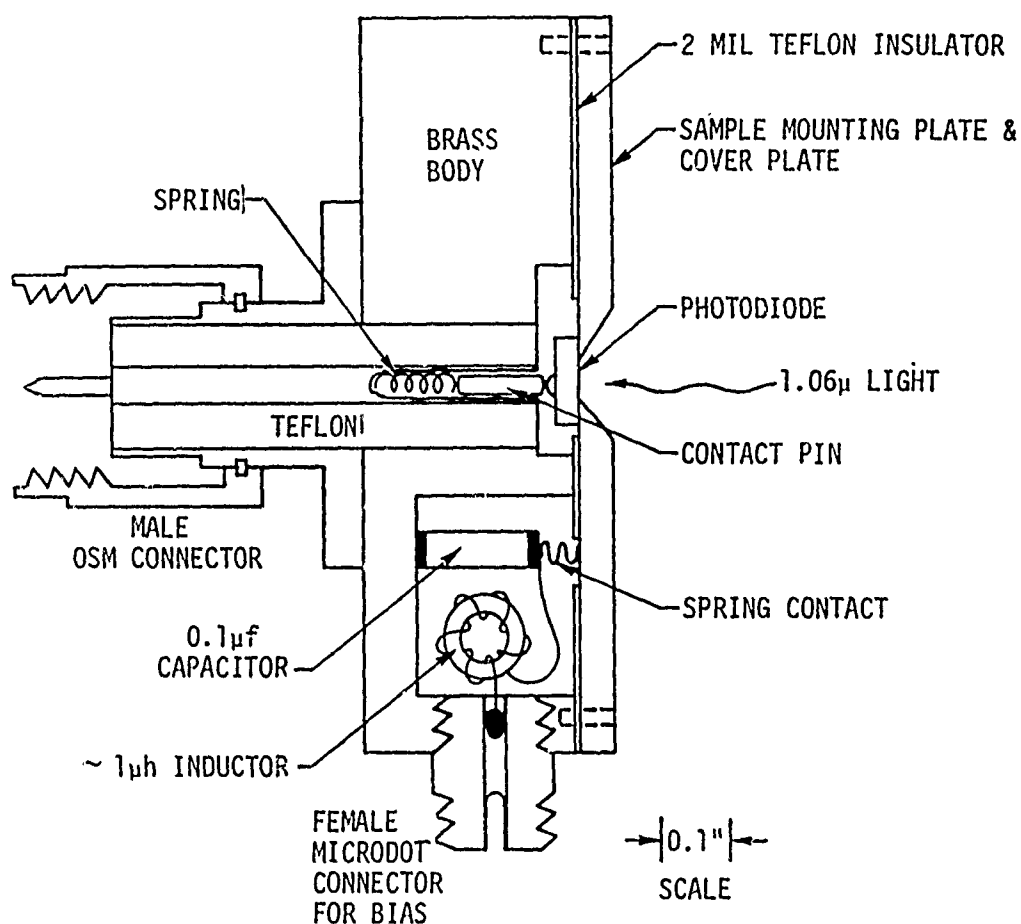


Fig. 3.11 New Compact 50 Ω Microwave Mount for Inverted Heterojunction Microwave Avalanche Photodiodes. Internal LC filter attenuates RFI on APD bias power supply. Note that the front sample mounting and cover plate floats at the APD substrate bias, so exposed metal should be covered with a suitable insulation if danger of accidental contact exists. Fig. 4.3 shows a photograph of this mount with an APD pulse response.

substrate, out of the way of microwave signal contacting to the mesa, makes effective microwave mounting of the device especially convenient. This package gives exceptional signal performance with very little stray capacitance and is rugged and convenient for coupling to optical systems. In the photograph at the upper right of Fig. 4.3, the Microdot APD bias connector is at the top and the 3 mm male OSM signal output connector is barely visible behind the sample holder. The pair of 3 mm OSM female connectors at the left and right comprise a capacitively-coupled "test-loop" as described in conjunction with Fig. 3.22 or 3.23. The value of C_C connecting this test loop to the signal output line is $C_C = 4.5 \times 10^{-14} \text{ f}$ for this package. This improved package was used for both of the 50 Ω -mounted APD's delivered under this contract.

Another method of device fabrication was established for structures in which the p-n junction is on the surface side of the active layer (rather than the substrate side). In this geometry (as in the homo-heterojunction diodes used in the delivered GAASFET receivers), the "normal" mesa etch would be expected to give surface electric field concentration and surface breakdown. The proper geometry would be to make mesas etched from the substrate side. Two techniques for obtaining this inverted mesa geometry were developed and discussed in Monthly Progress Reports. This process is a delicate fabrication procedure compared to the mesa etching process from the layer side. Fortunately, it was found that with proper passivation techniques, mesas etched from the layer side (wrong geometry for these homo-heterostructure diodes) gave the same measurement results as the mesa etched from the substrate side (no surface breakdown). Therefore this inverted mesa fabrication method did not prove necessary and the procedures need not be described here further.

3.3 Measurement Techniques

In a program of this type involving both the development of new device technology (in the heterojunction III-V alloy detector) and new circuit technology (the gigabit GAASFET transimpedance preamp), a key element to success is the development of the state-of-the-art measurement techniques with which to monitor progress. In this work, these measurement areas go from microscopic properties measurements on the epitaxially grown semiconductor materials through electrical and optical measurements on the fabricated photodiodes, and from specialized measurements of key characteristics of GAASFETs and other components for the integrated preamps to detailed stage-by-stage measurements on the preamps to determine the key parameters and predict system performance. It is only the results of detailed testing and measurements that lead to an identification of problem areas and provide a basis for an understanding of their nature that makes it possible to solve them.

3.3.1 Measurement Techniques Utilized in this Work but Described Elsewhere (with References)

Far too many different measurement techniques are employed in this work to discuss them all in detail here. Separate subsections here will be devoted to special pieces of equipment and techniques employed in this work that have not been discussed in previous reports (Refs. 1 and 2). Some of the techniques employed which have been discussed elsewhere include:

BASIC MATERIAL MEASUREMENTS APPLIED TO EPITAXIAL LAYERS:

OPTICAL ABSORPTION: We use a Cary 14R spectrophotometer with beam reduction optics to measure energy gap of epitaxial layers and (by a special deconvolution technique (Refs. 7 and 10)) bandgap grading.

PHOTOLUMINESCENCE: We use a Jarrell Ash Model 78-466 1 meter Czerny-Turner scanning spectrometer with a cooled S-1 PMT detector to measure sample photoluminescence in a cooled dewar excited

by either a Spectra Physics Model 125 50mw 6328Å HeNe laser or Metrologic 4416Å HeCd laser.

HALL EFFECT: Carrier mobilities and carrier concentrations in epitaxial layers can be determined by Hall effect measurements with our automated system described in Ref. 8.

IR MICROSCOPE: We use a Research Devices Model D infrared microscope to examine epitaxial layers for inclusions, etc. (Ref. 1), as well as check on device processing.

SEM X-RAY EMISSION ANALYSIS FOR ABSOLUTE COMPOSITION: Special computer codes for use with the X-ray analysis capability on our ETEK Autoscan Scanning electron microscope have been developed to give detailed composition (alloy content versus position) data on a submicron scale (Refs. 2, 9, 10).

SURFACE STUDIES: Our HP 5950A ESCA spectrometer can be used for surface studies on epitaxial layers, particularly for determining the surface effect of such processing steps as etching. In addition, our computer-controlled Auger electron SEM can study surface composition on a microscopic scale and measure surface potential variations over a junction region.

MATERIAL MEASUREMENTS MADE ON DIODE STRUCTURES:

SEM INDUCED CURRENT: We use our ETEK autoscan scanning electron microscope for junction depletion region measurements by electron beam induced current, in conjunction with other SEM measurement techniques (Refs. 2, 9, 10).

THERMALLY STIMULATED CURRENT: A TSC measurement system sensitive to 10^{-14} ampere currents can be used to identify defect levels in the depletion region of reverse-biased diodes (Ref. 9).

INJECTION LUMINESCENCE: The same spectrometer used for photoluminescence measurements can be used for injection luminescence studies in heterostructures to identify where recombination is taking place (Ref. 9.)

CAPACITANCE-VOLTAGE OR CARRIER CONCENTRATION, $n(x)$: Our Materials Development Corporation automatic doping profiler is used both for C-V measurements on devices and for capacitance-derived doping density versus depth, $n(x)$ measurements for the epitaxial photodiode layers on a routine basis.

SPECTRAL PHOTORESPONSE (η vs. λ): Another key routine evaluation made on the photodiode structures is the quantum efficiency versus wavelength. For these measurements, our Cary 14R spectrophotometer is operated with fixed slits and a feedback control over the light source power derived from a special "flat" detector in the reference compartment (Ref. 1) This fixes the number of photons/sec/cm² on the sample (independent of wavelength, λ) so that the photocurrent versus wavelength curves measured thru a feedback preamp and PAR 121 lock-in are relative quantum efficiency vs. λ curves. A special micropositioner probe plate is used so that measurements can be made on photodiodes at the wafer stage, as well as on packaged devices (Ref. 1).

ABSOLUTE QUANTUM EFFICIENCY: Reference photodiodes for measuring absolute quantum efficiency (usually at 1.064 μ) have been calibrated from NBS-standard calibrated thermopiles using the techniques described in Ref. 1. Our standard reference photodiode is an EG&G Model SGD-100 silicon guard-ring diode operated at a 60 volt bias which gives a quantum efficiency of $\eta_{1.064\mu} = 20.2\%$ with our Nd-YAG laser with defocused beam (numerical aperture of light, N.A. ~ 0.2).

3.3.2 Electrical Measurements on Chip or Wafer Devices

One of the inherent difficulties in working with microwave semiconductor devices such as the avalanche photodiodes or GAASFET's involved in this program is that the device dimensions become very small. In some of the dual-gate GAASFET's, bonding pad sizes are as small as

SC571.16TRF

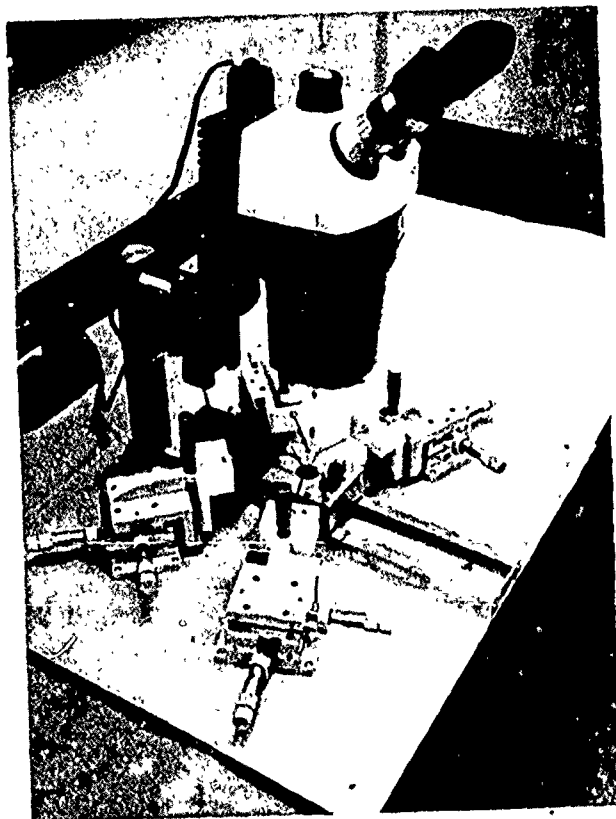


Fig. 3.12 Precision Micropositioner Probe Station
Fabricated for Working With Small Geometry
Devices.

2 mils x 2 mils (50 microns square; even in some of the silicon bipolar transistor chips they are 3 mils square). With the types of micropositioners we have employed previously in this work (Ref. 1), it is difficult to even hit a spot this small, let alone guard against an accidental slip of the probe which could wipe out the gate in a GAASFET worth \$150.00. Similar difficulties are found in doing electrical measurements on our APD's, some of which have total mesa diameters of only 3 mils (and the contact area is smaller than this).

To make it possible to work with such small-geometry devices with safety, the precision micropositioner probe station photographed in Fig. 3.12 was designed and fabricated. This station uses Line Tool Company X-Y-Z stages with 1 mil/division micrometers on each of the four main probes, with a Θ -rotatable vacuum chuck and provision for a standard Signatone probe for coarse (substrate) contact. A B&L Stereozoom 7 microscope is used with this station. Most device electrical measurements are performed with a Tektronix 576 curve tracer (either for transistor characteristic curves or APD leakage), though for very low leakage current devices, an external power supply, current amplifier (transimpedance type) and X-Y recorder can be used (Ref. 1).

3.3.3 High-Frequency Drain Resistance Measurements on GAASFET Chips

A specific problem encountered in the GAASFET preamp work is the necessity to measure, on chip devices, the high frequency drain resistance (R_D in Section 2.3.5) or open circuit voltage gain of the GAASFET. Because R_D values (if the device is to be useful!) are much higher than 50 ohms, conventional S-parameter measurements are not very helpful. To solve this problem, a special "active probe" was designed. The circuit diagram for this "active probe" is shown in Fig. 3.13. The circuit concept is to essentially operate the GAASFET into an open-circuit load with a known ac signal voltage applied to the gate, monitoring the drain voltage to measure the open-circuit gain. The "open-circuit" load is provided by the collector output resistance of a grounded base DN3250 PNP silicon bipolar chip transistor with a 50 Ω external source resistance. The collector

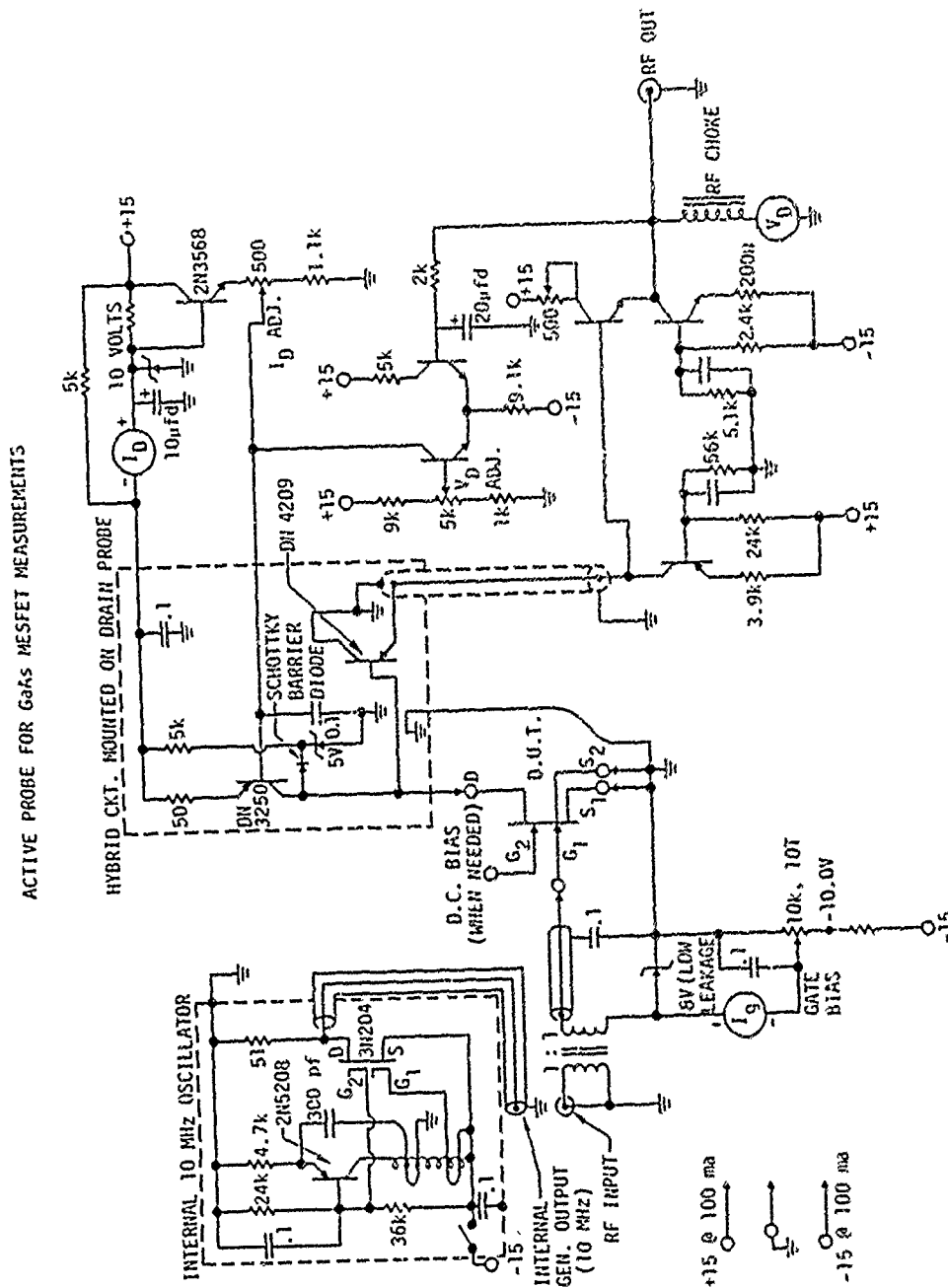


Fig. 3.13 Circuit diagram for active probe test setup for measuring open-circuit gain of GaAsFET's. The hybrid IC chip, 0.200" square, is mounted near the end of the probe so that the drain is supplied from a high impedance, low capacitance current source.

resistance under these conditions is much higher than the GAASFET drain resistance. The drain voltage (ac and dc) is monitored through the DN4209 emitter follower (also high impedance). An AERTECH A2S087 diode chip is used to protect the GAASFET drain from overvoltage. Of course, with high impedances, it is essential to minimize capacitance, so all of the above components are mounted on a 0.200 inch square hybrid substrate mounted about 1/2 inch from the tip of the micropositioner probe which contacts the GAASFET drain. On the GAASFET gate probe, a small MCL T1:1 wideband transformer is used to add the ac signal to the dc gate bias. The bias voltages are regulated from the control-power unit on the right of Fig. 3.13, with provision for setting gate bias voltage, drain current and drain-source voltage stabilization. In typical measurements, a 10 MHz internal oscillator is used for the generator with a GR1216-A 10 MHz IF amplifier unit as the detector, but other appropriate RF sources and receivers can be used. We have obtained good correlations with our R_D measurements from this equipment ($R_D = A_{oc}/g_m$) and the device performance obtained when measured GAASFET chips were employed in preamps.

3.3.4 Scanning Laser Microscope

The key APD optical measurements of quantum efficiency, quantum efficiency uniformity (spatial response), pulse response, avalanche gain and gain uniformity, as well as overall receiver performance are made on the optical table using laser sources and a scanning light microscope system. The optical table is a Newport Research Corp. MDL-RS-48-8 4 foot x 8 foot pneumatically isolated table. It holds three lasers: 1) a Quantronix 112A tungsten (quartz-iodine) lamp-pumped CW Nd-YAG 1.064 μ laser with a model 305A mode selection aperture for TEM₀₀ operation (unpolarized) and a model 302A acousto-optic mode locker for 273 MHz modelocked operation, 2) a Metrologic ML 684 6328Å internally modulable (to 100 KHz) He-Ne laser and 3) a CW Radiation Model S-106 1.152 μ He-Ne laser. Fig. 3.14 shows the layout of the optical table. The 1.152 μ and 1.064 μ beams are combined in the beamsplitter near the 1.064 μ laser, which splitter also taps off

part of the beams for the beam intensity reference photodiode (an EG&G SGD-100). These two beams are passed through the 1680 Hz chopper (if desired) down the centerline of the table, joining with the 6328Å laser beam in the second beamsplitter. Continuing down the table centerline is provision for a focusing objective for a high speed ($\text{GaAs}_{1-x}\text{Sb}_x$) reference photodiode in a 50Ω mount for use with a sampling oscilloscope to fine-tune the modelocker. The right angle path takes the combined 6328Å, 1.064μ and 1.152μ beams through a single spatial filter into the scanning light microscope. Getting the three beams simultaneously through the spatial filter requires that they be extremely accurately lined up in position and angle. Special precision-adjustable mounts are used on the two He-Ne lasers to make this possible (though still difficult).

The scanning laser microscope system is shown in detailed block diagram form in Fig. 3.15 . The purpose of the system is to be able to scan a finely-focused laser beam over a sample (usually a photodiode) in a TV-like raster pattern and to be able to measure and display the spatial variations of the desired physical parameters of the samples. Quantities which could be measured are things like optical transmission, optical reflection, "dc photoresponse", chopped light photoresponse, 273 MHz modelocked pulse response, etc. Display modes include intensity modulation (brightness proportional to photoresponse [$B \propto \text{P.R.}$]), differential intensity modulation [$B \propto (\text{P.R.} - Z_{\text{REF}})$], contour plotting (of $\text{P.R.} = (Z_{\text{REF}})_1, (Z_{\text{REF}})_2$, etc. lines), psuedo-color display by multiple exposures using optical filters with variations in device parameters or measured quantity for different primary color exposures, etc. In addition to these TV-like display modes, "shift modulation" plots involving summing the photoresponse and vertical scan signals are also useful.

In order to accommodate all of the desired operating modes, it is necessary to have a rather sophisticated electronic system, along with a versatile optical system capable of diffraction-limited performance. The optical system is shown schematically in the upper right of Fig. 3.15, and a photograph of the scanner unit is shown in Fig. 3.16 . The laser

SCANNING LASER MICROSCOPE SYSTEM

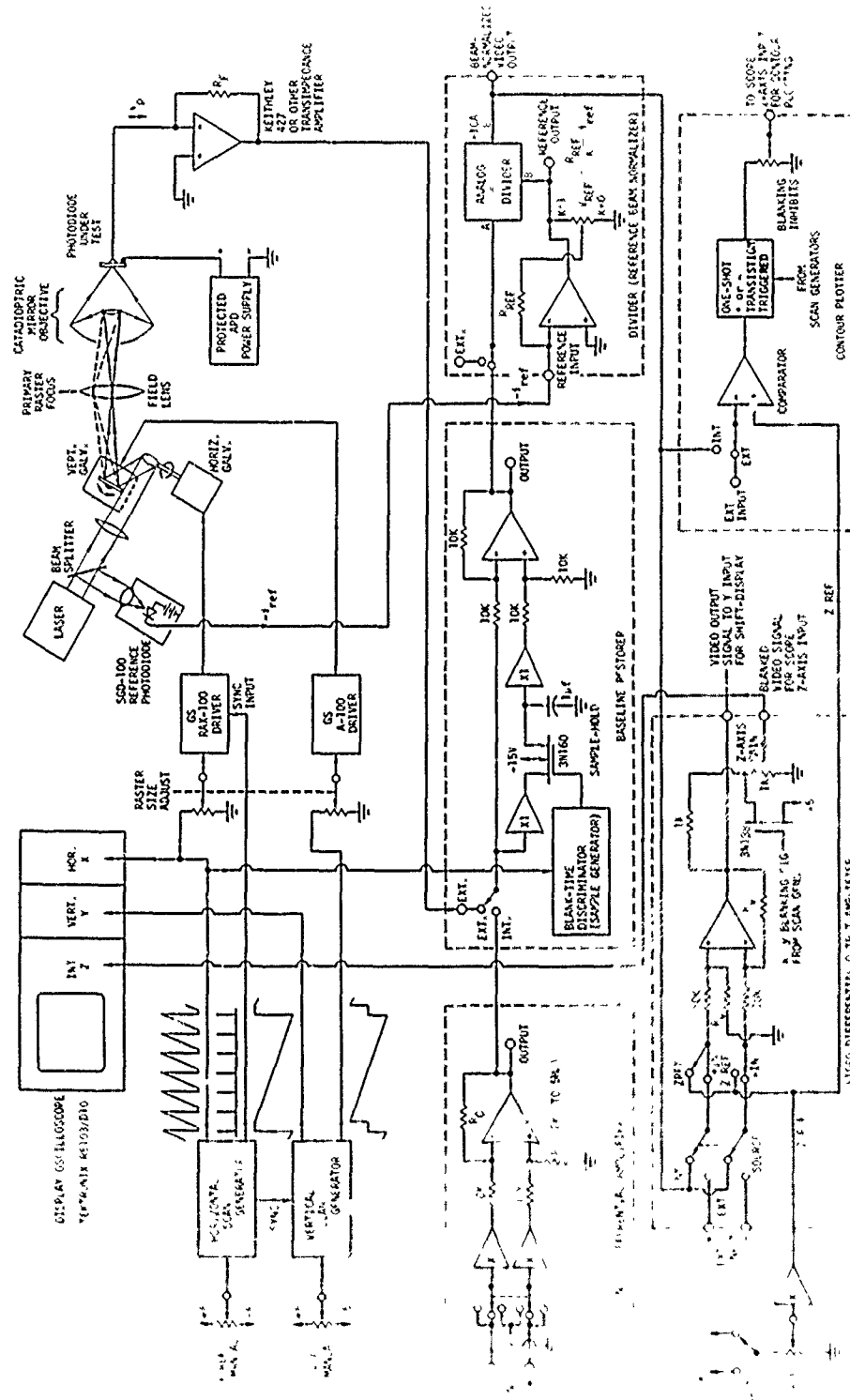


Fig. 3.15 Block-diagram of the scanning laser microscope system.

SC571.16TRF

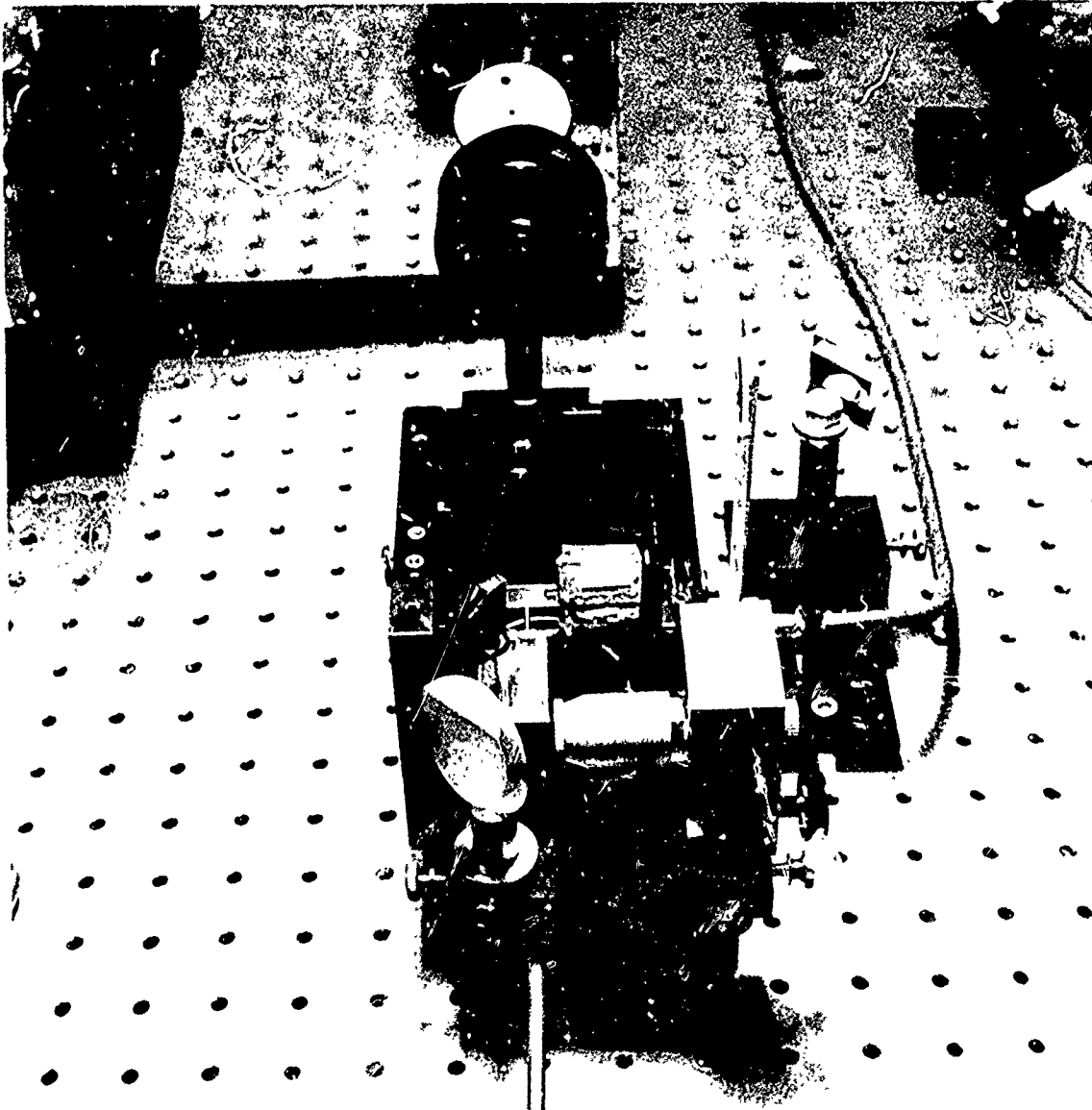


Fig. 3.16 a) Photograph of the Scanner Unit of the Scanning Laser Microscope taken along the direction of the exit beam. Beam enters the GC0401 spatial filter from the right.

SC571.16TRF

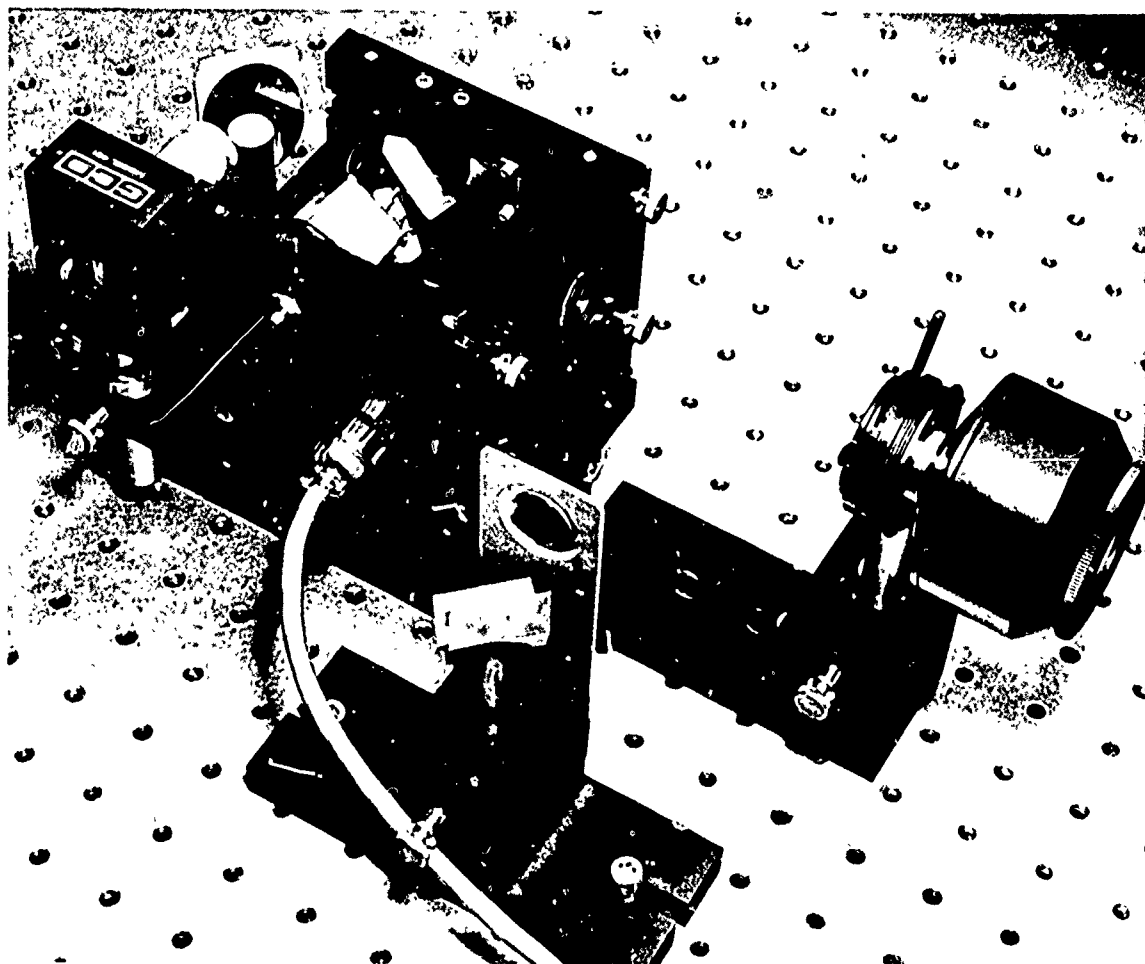


Fig. 3.16 b) Another view of the Scanner Unit of the Scanning Laser Microscope with the 40X 0.5NA Catadioptric Mirror Objective at the right.

beams (0.6328μ , 1.064μ or 1.152μ) are brought into the scanner through a spatial filter, reflected off of the 45° mirror and passed through a convex lens, the purpose of which is to image the spatial filter pinhole in the "primary raster focus" plane (which is at the position of the field lens). The beam is reflected off of an oblique mirror into the horizontal galvanometer mirror. The horizontal galvanometer is a General Scanning G-108 with a 5mm diameter circular mirror ($f_r = 1450$ Hz) mounted with its rotational axis 45° to the vertical. The beam reflects off of the horizontal scanning mirror to the vertical scanning mirror on a G.S. G-115 ($f_r = 900$ Hz) galvanometer with its rotational axis horizontal (perpendicular to the exit beam and the axis of the horizontal scanning mirror). The separation between the two scanning mirrors is only $0.43"$; keeping this separation small is required for the field lens to maintain proper illumination of the objective under all scan conditions. The primary raster focus is in or very near the plane of the field lens, with a raster size of $0.5" \times 0.5"$ or less (typically 10mm wide by 8mm high to give a 10 mil by 8 mil raster on the device with a $40\times$ objective or a 1 mil/major division display on the CRT). The field lens images the scanning mirrors into the input aperture of the objective. Usually a neutral-density filter in the range of an optical density of 1 (10% transmission) to 4 (0.01% transmission) is used in front of the objective to obtain the desired signal level. Various objectives are used, depending on sample size, from $2\times$ magnification (demagnification of the raster onto the subject) up to $20\times$ in normal microscope objectives, plus, as shown in Figs. 3.15 and 3.16, a $40\times$ 0.5NA long-working distance (1.7 cm) catadioptric mirror objective. The diffraction-limited spot size of a uniformly filled objective of numerical aperture, N.A. is given by

$$\Delta y = \frac{1.22\lambda}{\text{N.A.}} \quad (3.1)$$

where λ is the wavelength and Δy is the radius of the first dark diffraction ring or diameter of the central bright spot at the 37.7% maximum intensity point. For example, the $40\times$, 0.5 N.A. objective should have $\Delta y = 1.54\mu$

(0.06 mils) at 6328\AA or $\Delta y = 2.6\mu$ (0.1 mil) at 1.06μ , while a $10\times$, 0.25 N.A. objective gives twice this spot size. Other commonly used objectives such as the $10\times$, 0.17 N.A. (L.W.D.) and $5\times$, 0.10 N.A. microscope objectives are proportionately poorer (the latter gives $\Delta y = 13\mu$ [0.51 mils] at 1.064μ) in resolution but are useful for larger samples.

The horizontal and vertical scanning galvanometers are driven, respectively, by G.S. RAX-100 and A-100 drivers, the latter with the input retrace "halfway stepped" to give the same half-cycle resonant retrace that the RAX-100 does (see waveforms in Fig. 3.15). The horizontal scan generator is adjustable in frequency in 8 ranges from 2 Hz to 500 Hz max or a manual (X_{REF}) position adjust, while the vertical scan generator has 11 frame time-ranges from 30ms min to 1 minute min, plus manual (Y_{REF}). For high-resolution photographs, a one-shot mode with a typical one minute frame time and ~ 25 Hz horizontal rate would typically be used (for limited signal bandwidths of 30 KHz or so; wider bandwidths allow proportionately higher rates). The raster size may be adjusted for a given objective to a desired exact scale factor display with the ganged X and Y gain controls leading into the drivers.

The most difficult part of the system electronics in Fig. 3.15 is involved with the processing of the device response signal. This is best illustrated by an example, and the case shown in Fig. 3.15 is for measuring the "dc" (actually dc to 30^+ KHz) photoresponse uniformity of an n^+ substrate - p^+ mesa photodiode. The measured device is biased with a protected supply to its substrate and the photocurrent plus leakage current ($I_p + I_R$) is measured with an appropriate transimpedance amplifier such as the Keithley 427. The output of the 427 is a low-impedance voltage $V = -R_F (I_p + I_R)$, typically in the 1 to 10 volt range, so that we have no need for the input differential amplifier unit in the SLM system. This preamp has gains from $\times 0.2$ to $\times 500$, with differential $10M\ \Omega$ inputs and selectable bandwidths of 25 KHz, 250 KHz and about 4 MHz. For our case, we can go directly into the baseline restorer unit, the purpose of which

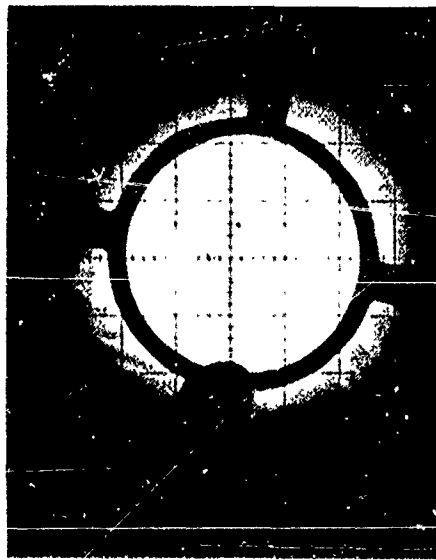
is to subtract off the device dark current from the photocurrent signal. ("Current bucking" in the 427 can do this to some extent, but for small photocurrent signals we must do much better.) This is accomplished in the baseline restorer in Fig. 3.15 by determining a time, just after scan retrace, when the laser spot is not on the sample ($I_p = 0$; provision is made at the primary raster focus for an occulting plate to insure this if desired), measuring I_R at this time and storing it with the sample-hold, and then subtracting this value from the $I_p + I_R$ signal during the rest of the horizontal scan. This process is repeated for each horizontal scan, so that drift of I_R does not interfere with the system. This circuit can also be used as a phase-sensitive detector if the sync from the chopper is inputted to the sample-hold instead of the horizontal scan signal. Not shown in Fig. 3.15 is an automatic default circuit such that if no sync is provided within 20 seconds or so, the circuit defaults to a non-baseline subtract mode (as in the manual, X_{REF} scan mode).

Having subtracted off the dark current signal, we are still faced with one additional problem in obtaining precision quantum efficiency, η , versus position data. That problem is that there is considerable beam intensity fluctuation from the laser source (sometimes up to 20% or so from our Nd-YAG laser). Since we want precisions approaching 1% in η , this must be corrected for. We accomplish this with the analog divider (reference beam normalizer) circuit. Here the output current, i_{REF} , of the SGD-100 reference photodiode (which monitors beam intensity through the beamsplitter) is converted to a near -10 volt level by adjusting the reference amplifier feedback resistance, R_{REF} , and gain factor, K . This reference output signal is applied to the denominator input of the 4 MHz analog divider, while the video signal (baseline subtracted) is applied to the numerator input, giving a beam-intensity-normalized output.

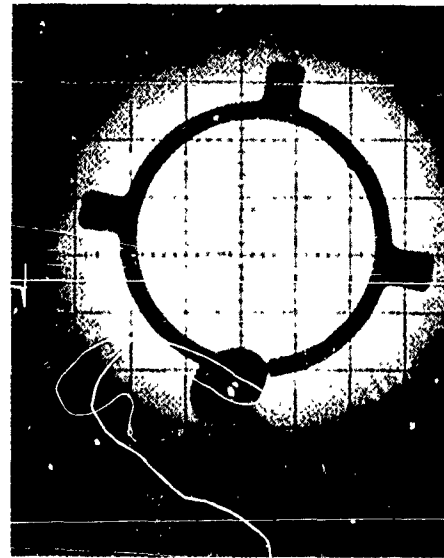
The display mode selected in Fig. 3.15 is an intensity-modulated or differential intensity-modulated display, obtained using the video differential output amplifier. This differential amplifier has gain ranges

from $\times 0.2$ to $\times 100$ and has both a fixed gain video output signal and a continuously variable gain output with blanking ($-5V$) pulses derived from the horizontal and vertical retrace intervals. Usually the video signal is applied to whichever input of the differential amplifier is required to make the beam brighter with increasing signal (positive Z-axis signal for the Tektronix R5103/D10 display unit shown), and the other input is connected to a variable reference voltage, Z_{REF} . In this way it is possible to increase the gain and do differential intensity modulated displays in which, for example, black on the display might represent a 90% quantum efficiency and bright white a 100% quantum efficiency (rather than 0% to 100%). Another convenient mode of display is "shift modulation", where the fixed-gain video output signal is summed with the vertical scan generator signal in a differential amplifier Y plug-in for the monitor oscilloscope to produce a series of traces representing η vs. x for stepped values of Y . This can be used simultaneously with intensity modulation to accent peaks. It should be noted that while normally Polaroid film records are usually made using the Tektronix C5 camera on the Tektronix R5103/D10 display, we have also used the Tektronix 7613 variable-persistence storage oscilloscope for temporary display of these grey-scale images from the SLM with good results. (However, the Z-axis input polarity is reversed so that the signal and blanking polarities must be reversed from Fig. 3.15).

Another display mode is contour plotting, wherein a comparator is used to trigger a one-shot to put a dot on the screen any time the normalized video signal equals the reference setting, Z_{REF} . By making a series of exposures with different Z_{REF} values, the resulting picture will show equal quantum efficiency contours for the device. An example of the application of these display modes in examining surface inversion problems in a commercial (HP4220) silicon PIN photodiode from 6328\AA SLM pictures is shown in Fig. 3.17. Pictures a) and b) in Fig. 3.17 are "straight" intensity-modulated ($Z_{REF} = 0$) displays of 6328\AA quantum efficiency at zero bias and 20 volts reverse bias respectively (the



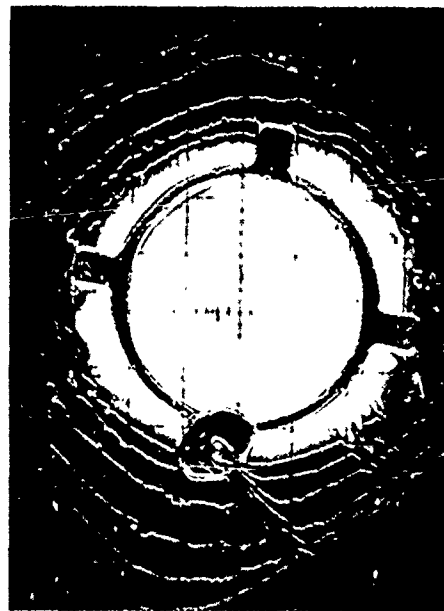
(a)



(b)



(c)



(d)

Fig. 3.17 Scanning light microscope micrographs of response of a Si photodiode at 6328\AA . (a) and (b) intensity modulated display for diode at 0 and 20 volts bias respectively. The dark ring indicating no response is the Ohmic contact to the diode. (c) and (d) are a combined intensity modulation and contour mapping display of the same diode at 0 and 20 volts bias respectively.

pictures are shown rotated 90° clockwise from the display orientation for convenience; the 10 div. side is "X" and the 6 div. "Y"). The gold contact circle with four bonding pads and the gold TC ball bond to the lower pad are clearly visible. Pictures c) and d) are combination contour plots and differential intensity modulation. Picture c), at zero bias shows contours at $Z_{REF} = 0.1$ (outer line), 0.2, 0.5, 1, 2, 3 and 4 volts, with $Z_{REF} = 4$ volts for the differential intensity modulation (DIM). Picture d) in Fig. 3.17 is for 20 volts reverse bias with contours for $Z_{REF} = 0.5$, 1, 2, 4, 6 and 8 volts and $Z_{REF} = 8$ volts for the DIM. Note how the differential intensity modulation pictures bring out the photoresponse irregularities, while the constant response contours show quantitatively the extent of the silicon surface inversion channel response. (For example, from picture d) we can see that the photoresponse to uniform illumination over the chip in this HP4220 will mostly come from the diode area within the contact at zero bias, but for -20 volts bias, far more response will come from the surface inversion region than from the central diode region.)

3.3.5 UHF Avalanche Gain Measurements with the Scanning Laser Microscope

While the examples just discussed (Figs. 3.15 and 3.17) treated the use of the SLM system for "dc" quantum efficiency measurements, this system is also very useful for high frequency gain and uniformity measurements. In this application, the laser source is the 1.064 μ Nd-YAG laser-operating modelocked at a 273 MHz repetition frequency. The optical receiver, followed by appropriate 50 Ω amplifiers to give the desired signal gain, feeds the input of a spectrum analyzer, operated as a narrowband receiver tuned to the fundamental or any of the harmonics of the 273 MHz modelocked pulse repetition frequency that lie within the receiver passband. For example, for fundamental detection with our Tektronix 7L13 spectrum analyzer plug-in, the center frequency is adjusted to 273 MHz, phase locked, and the frequency span/division setting is unlocked from the resolution bandwidth selector and set to 0 KHz/div. (fixed tuned) with the resolution bandwidth set at 30 KHz and the 30 KHz video filter on. The 7L13 is used

in the "linear" display mode and the "video output" pin jack to the 7L13 is connected to the positive input of the "input differential amplifier" of the SLM system (Fig. 3.15). The horizontal scan generator output from the SLM may be used to drive the horizontal of the spectrum analyzer by using the horizontal external input pin jack on the 7L13 and setting the time/div. knob to "EXT", in order to provide a line scan display on the spectrum analyzer to complement the SLM display. While the "video output" from the 7L13 is a zero-center, -50mV bottom and +50mV top output format, this doesn't represent a problem in the SLM system as long as the "baseline restorer" is used, as this will add the necessary 50mV to produce the "zero volts with zero light" required by the divider (reference beam normalizer) circuit for proper operation. In addition the baseline restorer will exclude any modelocker drive rf leakage which may happen to be present in the receiver output. In this configuration, the SLM system operates exactly like the "dc" response examples described previously, except that the displayed parameter is the high frequency/ quantum efficiency or gain. The same types of display options are possible.

While the high frequency gain measurements using the SLM system are most conveniently utilized with either 50 ohm packaged devices or completed GAASFET preamp receivers, we have also been successful in making these measurements on unpackaged wafer devices as well. The approach here was to develop a micropositioner probe with a very small 50 Ω coaxial line going to the probe tip (the tip is an extension of the center conductor) and a shield ground line which is connected to the device substrate through a blocking capacitor. While the arrangement has too much spurious inductance for transient measurements, the sine wave response is quite adequate for gain measurements, even at frequencies approaching a gigahertz. The most serious problem with this measurement is that there is considerable rf leakage from the modelocker drive signal on the optical table and this can easily produce a larger signal than the photocurrent. Fortunately, while the fundamental (273 MHz) and 2nd harmonic (546 MHz) signals are badly swamped out by this rf drive interference, there is very little

interference at the third harmonic (819 MHz; actually this is the 6th harmonic of the acousto-optic modelocked drive), and we have had excellent results obtaining 819 MHz gain and uniformity measurements on unpackaged devices by this technique,

In addition to the SLM measurements of high frequency gain uniformity, the 7L13 can be used in this same "narrowband receiver" mode to measure absolute responsivity, gain and N.E.P. for a receiver. In these measurements, the SLM system is simply used in "Manual" X and Y scan modes to focus the attenuated laser beam on the desired gain area of the APD. The spectrum analyzer output is connected directly to the Y-input of an X-Y recorder, with the X-axis driven from the APD power supply, to give gain versus V_{APD} plots. Usually in these measurements the "LOG 10db/div." display mode is utilized so that the divider (reference beam normalizer) in the SLM cannot be used, as the video signal is not proportional to I_p . Figs. 4.6 and 4.21 were recorded in this way.

The absolute output of the modelocked laser at all harmonics may be easily calculated from the dc output (average photocurrent) given the shape of the output pulses. Consider a laser having repetition frequency F (273 MHz for our laser) and having a short output pulse shape such that the Fourier transform of a single output pulse gives an envelope with magnitudes at dc, F , $2F$, $3F$, etc., of 1.0, f_1 , f_2 , f_3 , etc. Here (because light intensity cannot be negative) the various f 's will be less than one. (However, if the light pulse width, ΔT , is considerably shorter than the repetition period, $T = 1/F$, the coefficient for at least the first few harmonics will be very close to 1; i.e., $f_1 \approx 1$ for $\Delta T \ll T$.) In terms of the average output "photon current", I_{avg} , the laser output, $i_{ph}(t)$, can be described as

$$i_{ph}(t) = I_{avg} + 2I_{avg}f_1\cos(2\pi Ft) + 2I_{avg}f_2\cos(4\pi Ft) + \dots + 2I_{avg}f_n\cos(2n\pi Ft) + \dots \quad (3.2)$$

Hence the rms value of the nth harmonic of the modelocked laser is given by

$$(I_{ph})_n \text{ (rms)} = \sqrt{2} f_n I_{avg} \quad (3.3)$$

where I_{avg} is the dc level (this equation applies to either the "photon current" in the beam directly or to photocurrent in any linear detector having response time much faster than ΔT). For frequencies nf less than approximately $0.3/\Delta T$, where ΔT is the pulsewidth, we have $(I_{ph})_n \text{ (rms)} \approx \sqrt{2} I_{avg}$. Hence, we can calculate the absolute rms photocurrent from a dc or reference photodiode current using Eq. 3.3 and hence obtain the absolute responsivity of the receiver at a given harmonic by measuring the signal output (usually by means of amplitude-calibrated reference substitution for accuracy).

3.3.6 Precision Current-Protected Avalanche Photodiode Power Supply

One of the problems with any microwave-responding semiconductor device is that the small device geometries involved usually give the devices a somewhat limited ability to deal with gross power overloads. This failure mode, sometimes referred to as "failing the smoke test" can be avoided in these small avalanche photodiodes by using a carefully current-protected power supply. (This is because the device power dissipation is $P_D = P_L + I_p V_{APD}$, where P_L is the light power, or, from $I_p = \frac{\eta M P_L}{h\nu}$, $P_D = P_L \left(1 + \frac{\eta M}{h\nu} V_{APD}\right)$. With $\eta = .96$, $M = 10$, $h\nu = 1.165\text{eV}$ and $V_{APD} = 120\text{ volts}$, the bias power term is a thousand times the input light signal term, so by "crowbarring" the bias at gross P_L overload, we save the device.) Experience indicates that with overload protected supplies these $\text{GaAs}_{1-x}\text{Sb}_x$ operate virtually indefinitely without problems, whereas with unprotected supplies (batteries, etc.), it is usually just a matter of time before someone makes a mistake (forgetting to insert the beam attenuator, etc.) that destroys the APD.

Figure 3.18 shows the schematic diagram for a precision current-protected power supply which can give up to 200 volt outputs of either polarity and has provision for internally monitoring either dc output voltage or dc output current. The power supply is based on an INTECH A-300 high-voltage op-amp which amplifies a reference voltage taken from a temperature compensated zener diode. The output voltage range of the op-amp when used with the regulated ± 120 volt supply shown in Fig. 3.19 is about ± 115 volts, but since only one polarity is required at any given time, higher voltages are attained by adding the +90 volt "boost battery" to the op-amp output to make its range -25 to +205 or +25 to -205 volts when voltages over ± 115 volts are required. Instantaneous current limiting is provided by making all load current pass through the feedback resistance, R_F , of the BB3521K FET op-amp (connected in the transimpedance mode) which floats on the "high" side of the A-300 output (i.e., at the supply output voltage with respect to common). Long-term (many μ sec) overcurrent protection is obtained by monitoring the dc load current by measuring the voltage across R_F (from pin 6 to the "floating common"). If this voltage exceeds the trip point voltage setting, V_1 , the supply output is crowbarred by turning on the triac between the common and the floating common by means of the optical isolator. A 4 1/2 digit digital panel meter reads the output voltage (0 to ± 199.99 volts) from floating common to ground, and can also be connected across R_F to read load current. A more convenient approach, however, is to have a separate meter between pin 6 of the BB3521K and floating common with different series resistances for scales of 50mV to 10 volts full scale, allowing simultaneous readings of load current (to small values) and supply voltage.

3.3.7 Digital Processing Oscilloscope System

The most important tool utilized in the checkout and evaluation of the hybrid integrated GAASFET optical receivers is our Tektronix Digital Processing Oscilloscope system. This system utilizes all of the versatility of a Tektronix 7704A four plug-in oscilloscope as a data acquisition input to a computer mounted on the scope cart. The computer is a PDP 11/05

SC571.16TRF

REGULATED ± 120 VDC SUPPLY

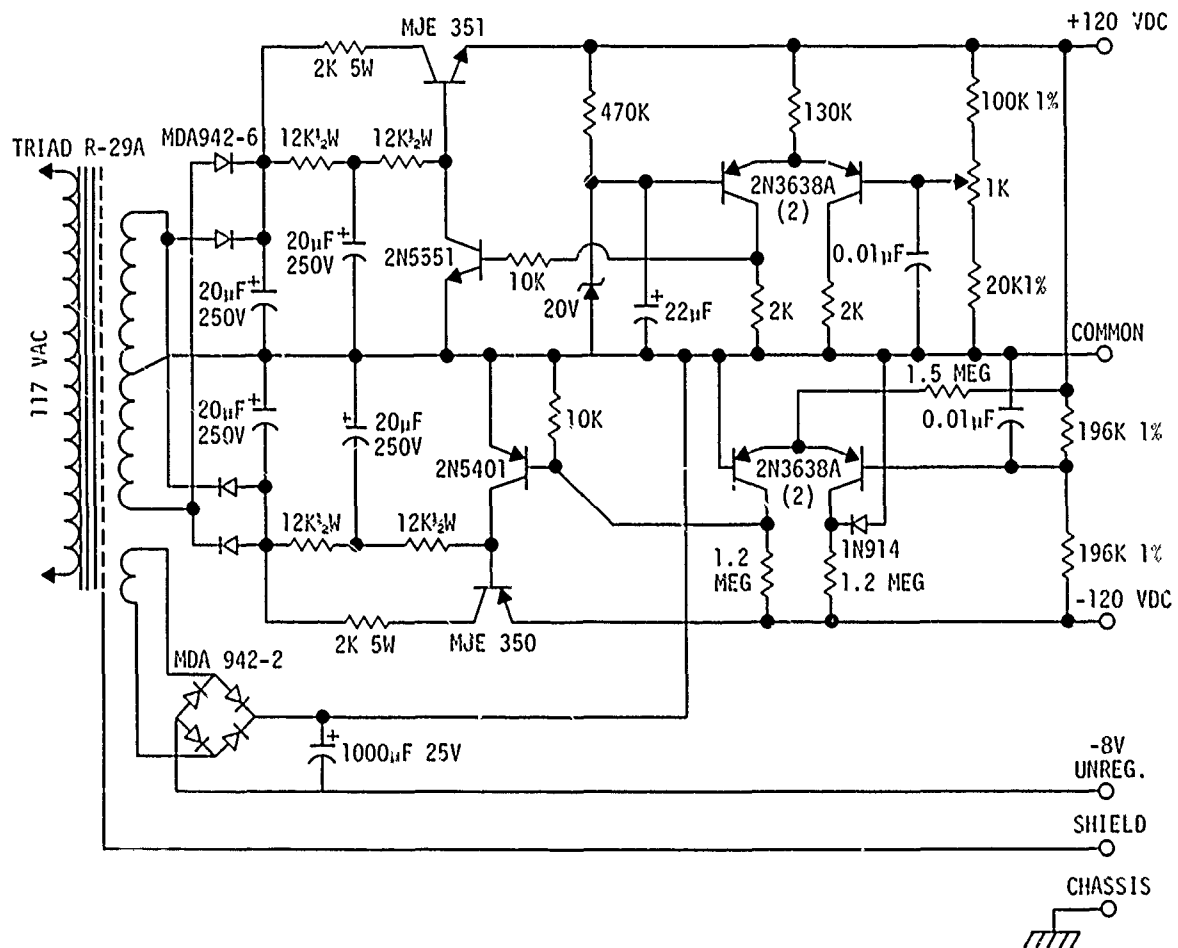


Fig. 3.19 Regulated ± 120 Vdc power supply for use in the APD supply of Fig. 3.18.

with a 24K (16-bit word) memory with interfaces to a Tektronix 4010-1D graphics terminal as well as the P7001 processor. A Tektronix 4911 (Remex) high speed paper tape reader-punch is used to input or store software or data. The P7001 processor stands between the upper (display) section and the lower plug-in (signal acquisition) section of a conventional Tektronix 7704A oscilloscope. The P7001 contains high speed analog to digital converters to digitize signals from the plug-ins and a 4K (10-bit word) memory divided into four waveforms (A, B, C and D). Each waveform consists of 512 values of the measured vertical signal (i.e., 512 horizontal points) measured with 10-bit accuracy (1024 vertical resolution elements). Along with each waveform is stored the scale factor and zero reference information required to make the waveform meaningful. The P7001 contains a digital to analog converter (display generator) which allows the 7004 to display either the input analog signal(s) or one or more stored waveforms or both. The processor waveforms may be transmitted to the computer memory (in correspondingly named arrays; A, B, C and D) by either front-panel or program control.

The power of the DPO system comes, on the analog side, from the selection of plug-ins for the 7704A. We regularly make use of such real-time plug-ins as 7A26, 7A22 and 7A11 vertical amplifiers and 7B70 and 7B71 time bases along with a 7D12/M1 digital multimeter plug-in to monitor bias voltage, temperature, etc. For sampling work we use a 7S12 time domain reflectometer and 7S11 vertical sampling plug-ins with S-6 or S-4 samplers with either an S-52, 25pS, 250mV pulse generator head for TDR or preamp response tests or an S-53 trigger recognizer for sampling modelocked pulse response, etc. In addition, the 7L13 spectrum analyzer can be used with the DPO, although it is usually used with the Tektronix 7613 variable persistence storage oscilloscope as in Fig. 3.20. The test equipment shown in this figure is what is typically used in the stage-by-stage testing of one of the GAASFET preamps. The equipment shown includes (from far left to far right), the 4010-1 terminal for the DPO, the 7613 oscilloscope with 7L13 spectrum analyzer, the DPO cart with

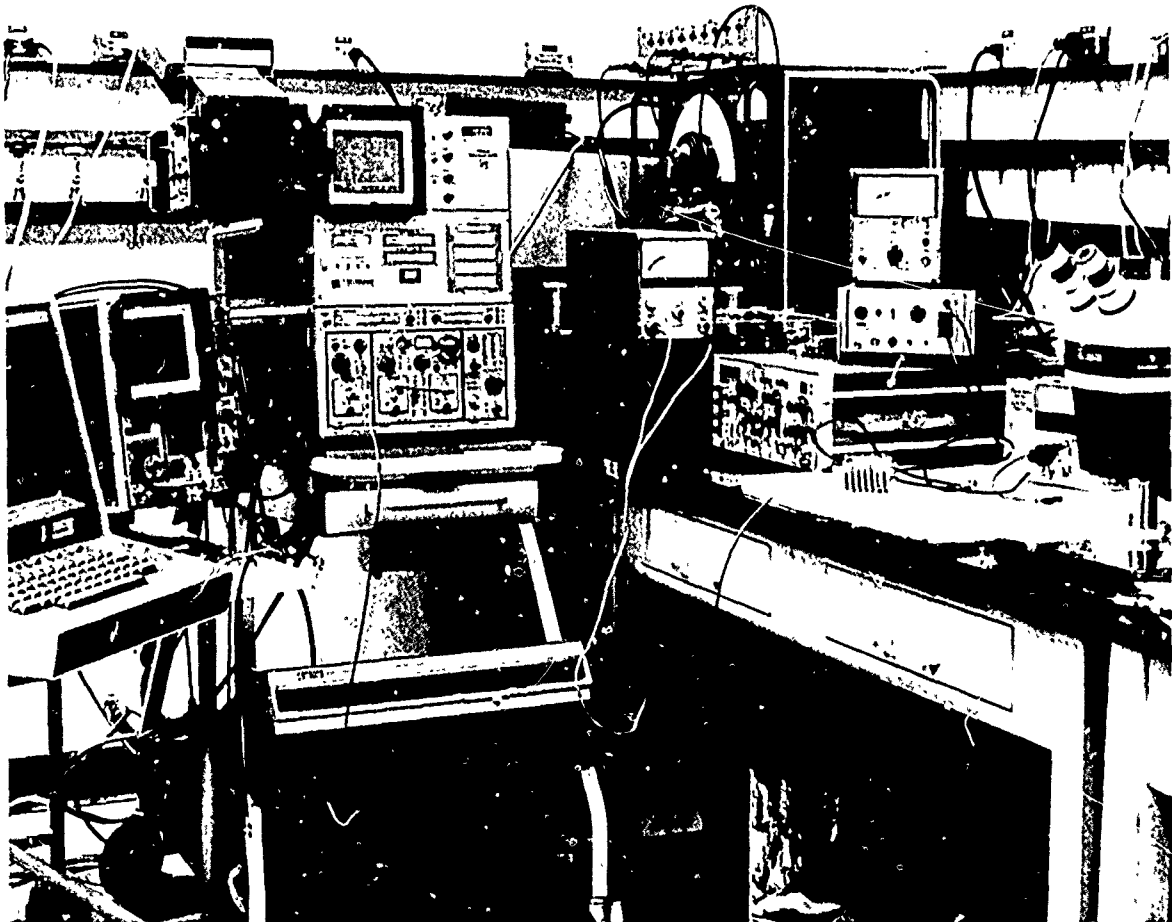


Fig. 3.20 Measurement Equipment Routinely Used For
GAASFET Preamp Evaluation, including the
Tektronix Digital Processing Oscilloscope.

7704/P7001 (with sampling plug-ins) on top and the PDP 11/05 on bottom, the HP435C power meter used in noise measurements, a Tektronix TM504 measurement system with DC505 counter, FG502 waveform generator, PG502 250 MHz pulse generator and PG506 calibration generator, GAASFET Preamp #8 with power supply-controller unit, and a B&L Stereozoom 7 microscope probe station for open-package probe measurements (a dangerous procedure used only when absolutely necessary).

Much of the saving in time and expansion in measurement capability realized in using the DPO system comes from the convenience and power of the system software. The TEK BASIC software for the DPO system is an extension of BASIC oriented towards applying the DPO measurement capabilities to electrical engineering-type problems. It is a fairly large software package, requiring nearly 16K of the 24K of core available in our PDP 11/05 computer, but the sophisticated command structure means that relatively little additional space is required for user programs. The software contains four permanently defined arrays (A, B, C and D) corresponding to the P7001 processor waveforms (which are called PA, PB, PC and PD in the language). The command "LET A = PA", for example causes waveform A of the processor to be transferred into computer array A with the correct vertical scale factor and zero reference values noted so that absolute values of voltage (or whatever) for each of 512 horizontal points are obtained in A (including interpolation of points missing in PA). Arithmetic operations may be performed "en mass" on the array with a single command, such as "LET C=log(D)" or "LET PA=A-B", which subtracts array B from array A and sends the result to the processor waveform A for display. The software allows direct manipulation of the scale factors for the processor display without interfering with the computer waveform (i.e., a trace stored at 10nS/cm, 5mV/cm can be displayed at 1 nS/cm, 1mV/cm with selectable starting point for expansion).

While the convenient waveform-handling format facilitates the use of the DPO, it is the power of the software system commands which makes

the system so powerful. For example, the command "AVERAGE PA, 1024" signal averages the waveform 1024 times to extract the repetitive signal from the random noise. The command "INTEGRATE A, B" integrates waveform A and places the resulting integral waveform in B, taking proper account of horizontal scale factors and units. Similarly "DIFFERENTIATE C, D, 1" carries out the derivative with a two point or three-point algorithm with step size selected by the final "1". The command FFT A, PC, PD takes the Fourier transform of A, displaying the real and imaginary parts of the result in processor waveforms C and D (and it accomplishes this 512 point FFT in 2.5 seconds). Similarly, FFT A, PC, PD, POL does the FFT of a pulse transient response in A with the magnitude and phase of the frequency response (respectively) displayed in C and D. Similarly, the IFT command can be used to go from a frequency-domain response to a time domain response. The command "CONVOLVE A, B, PC, PD" might be used to convolve an input pulse waveform, A, with the δ -function (impulse) response of a circuit, B, to give the output pulse waveform from the circuit (displayed in waveforms C and D). Similarly, CORRELATE is a single command in TEK BASIC. In addition to the P7001 display capability via the 7704 oscilloscope screen, the command "GRAPH PA, PB" draws a reproduction of the CRT face on the 4010 terminal storage screen and graphs the two processor waveforms within this graticule. More general graphics capability is provided by the "PLOT" command. While TEK BASIC contains many other important special functions, etc., the examples cited illustrates what the system can do and how easy it is to get it to do it, and should be sufficient to allow a reader with some familiarity with BASIC to understand the workings of the various user programs listed in Appendix A.

3.3.8 Application of the DPO System for Gigabit Preamp Noise Measurements

In Section 2.1.3 the communications system performance of an avalanche photodiode receiver was related (Eq. 2.20) to the "minimum detectable current pulse", N_0 of the preamp (the number of electrons in a charge impulse required to make the peak output voltage equal the rms

noise output). N_o is given by

$$N_o = \frac{v_{no}}{q(V/Q)_p} \quad (\text{electrons}) \quad (2.19)$$

where v_{no} is the rms noise output and $(V/Q)_p$ is the "pulse gain" or ratio of peak output voltage to the charge in the input pulse. Hence to measure N_o , we must measure both this pulse gain, $(V/Q)_p$ and the rms noise output v_{no} for the preamp. Techniques for accurately measuring both of these quantities using the Digital Processing Oscilloscope (DPO) system have been developed and are described here.

3.3.8.1 Noise Histogram Analysis for Predicting Receiver BER

In fact, simply measuring the rms noise output, v_{no} , for a preamp is not sufficient to guarantee its performance in low bit error rate (BER) optical communications. The assumption that is made in the analysis of Sections 2.1.2 to 2.1.4 is that the noise is Gaussian, that is, defined by the probability distribution or probability density

$$P(V) = \frac{1}{\sigma\sqrt{2\pi}} e^{-\frac{(V-\bar{V})^2}{2\sigma^2}} \quad (3.4)$$

(the probability of measuring the voltage in any given range is obtained by integrating $P(V)$ over that range, as in Eq. 2.7). The quantity σ is the standard deviation of the distribution; for pure Gaussian noise, we have

$$v_{no} \text{ (rms)} = \sigma \quad (3.5)$$

that is, σ is just the rms value of $V-\bar{V}$. The communications performance of the receiver is dependent on the probability distribution "far out in the wings" (of the order of 5 standard deviations from the mean), whereas most of the probability density that defines the rms of a distribution

is within 2 standard deviations of the mean. This means that two noise distributions might have the same rms noise but give greatly different error probabilities "out in the wings" at the 10^{-6} to 10^{-8} BER range. Hence it is highly desirable to be able to test whether the output noise is in fact Gaussian, with probability densities in the wings equal to those predicted from Eq. 3.4 with $\sigma = v_{no}$.

The probability density or probability distribution, $P(V)$, can in effect be experimentally measured for a preamp by constructing a noise histogram. For the wideband preamp measurements, this is accomplished using the same 50 ohm amplifiers after the preamp and the same S-6 sampler head in the 7S11 sampler that are used in the time response measurements (Section 3.3.10), so that even if small gain calibration errors exist, the same gains are used for v_{no} and $(V/Q)_p$ so that the N_0 value will be correct. The procedure is to sample the random noise output of the preamp with the S-6 sampler[†] at random intervals, constructing a histogram of the number of times each discrete voltage range was measured from a large number of such samples.

The TEK BASIC program for carrying out this noise histogram measurement on the DPO is listed in Appendix A.6, lines 100-181. A randomly-sampled noise waveform in the P7001 consists of 512 horizontal points with a 10 bit number (1024 vertical resolution elements) describing the noise voltage measured at each point. For the noise histogram we specifically select the 7S11 voltage range so that all points measured fall within a ± 2.5 cm CRT deflection, which corresponds to ± 256 vertical resolution elements from center screen. The stored noise waveforms are in array B in the program, while in lines 130-140, array A is set up as a noise

[†] Because the noise is truly random, it is essential to have the "dot response" or sampler loop gain of the 7S11-S4 sampler combination accurately adjusted to unity. This is accomplished according to the procedures described in the Tektronix manual for the 7S11.

histogram array (and initialized to zero), with each horizontal address in A (from 0 to 510) corresponding to a vertical resolution element in the sampled noise waveform (B). Then each horizontal (time) address in the stored noise waveform is examined and one count is added to the horizontal address of the histogram array which corresponds to that voltage (line 172). Hence, if a value of zero volts were measured at that point in the noise waveform, a count of 1 would be added to element 256 of the noise histogram waveform (this is the element corresponding to the left-right center of the display screen which we take as 0 volts for the display, with + noise excursions to the right and - noise excursions to the left). Similarly, for each of the samples in the stored noise waveform, a count is added to the element of the histogram array corresponding to the measured voltage. This process is repeated for many noise waveforms until a highly statistically significant noise histogram is built up. Typically, from 10^5 to 10^6 total points are taken for the histograms as this is required to verify the extreme "wings" of the distribution corresponding to error rates of 10^{-5} to 10^{-6} . Reasonably accurate RMS noise values can be obtained with 10^4 or fewer points, however, if that is all that is desired. (Processing time is about 1500 points per minute.)

The rms noise is calculated from the completed noise histogram (in array A) by the program listed in Appendix A.6, line numbers 200-240. This program goes through the noise histogram, voltage slot at a time (J from 0 to 511), and if there are S counts in a voltage slot J, then S counts are added to the total counts sum, N, $S(J-256)$ counts added to the first moment count, N_1 , and $S(J-256)^2$ counts added to the second moment, N_2 . After going through all the J values, we have that the total number of measured points is N, the mean value of the distribution is $MI = N_1/N$ and the rms noise is $RI = \sqrt{N_2/N - MI^2}$ resolution elements (converted to voltage by the horizontal scale factor).

Given the noise histogram and the exact root mean square noise of the distribution, we would like to be able to see how accurately the distribution corresponds to a Gaussian distribution, particularly in the

wings. The program listed in Appendix A.7, line numbers 300-364, does this comparison. Line numbers 300 to 312 generate in array B the log of a slightly smoothed version^{††} of the original distribution. The log is used, of course, in order to be able to see the probability densities "out in the wings", hardly visible in a linear histogram display, with the same relative resolution with which you see the distribution peak. The rest of the program is used to calculate for comparison an exact log of a Gaussian distribution in array C, i.e., of the form (from Eq. 3.4).

$$\log P = K_0 - \frac{(V-V_0)^2}{2\sigma^2} \quad (3.6)$$

In lines 316 to 328 K_0 , the height of the log distribution at the center is determined from the log distribution in B by averaging over the $\pm 0.3 \sigma$ range (and adding 0.015 to correct the average to peak). The calculated log Gaussian is then obtained in lines 330-350 using for σ , the rms of the distribution obtained in the previous program, RI. Comparing the experimental log histogram (in B) and the calculated Gaussian log histogram (in C) shows very clearly whether the measured noise is Gaussian.

An example of the application of these three programs is shown in Fig. 3.21. This 10^6 sample noise histogram was measured for GAASFET Preamp #6 at $V_{APD} = 80$ volts (dark) thru cascaded B&H (3 GHz) preamps with a gain of 77.2 into the S-6 sampler with the 7S11 set to the 50 mV/cm scale (and dot response adjusted to unity gain). The bell-shaped histogram curve, with zero four divisions below center is displayed at 2500 counts/cm vertical, 25mV/cm horizontal (512 total horizontal bins). The log curves,

^{††} The smoothing subroutine, lines 2200 to 2212, approximates convolving the histogram in A with a Gaussian "window function" with a 1.5 element standard deviation, with the smoothed result in waveform D.

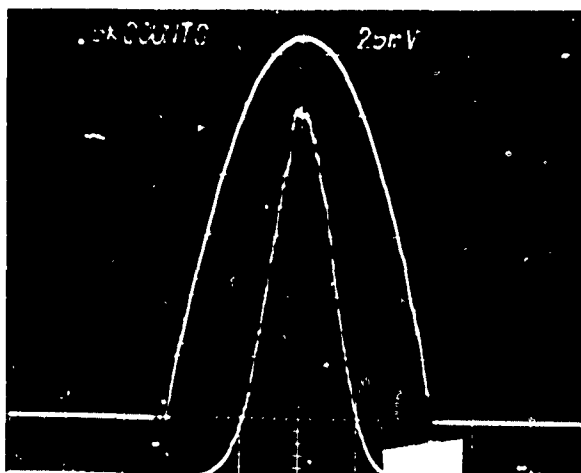


Fig. 3.21 10^0 Sample Noise Histogram Measured for Mark III GAASFET Preamp #6 at $V_{APP} = 80$ volts Through Cascaded B&H's. Histogram (lower curve, zero at bottom) displayed at 2500 counts/cm vertical. Horizontal for all curves is 25 mV/cm, positive to right, zero center. The log of the experimental distribution and the calculated log curve ($K_0 = 9.628$, $\sigma = 12.96$ mV) are displayed at $e^{1.535}$ per cm., or 1.5 divisions vertical equals 1 decade.

displayed with zero at 3 div below center and $e^{1.535}$ per centimeter vertical, have one decade in probability density equal to 1.5 cm vertical (i.e., the 6.8 cm difference between the peak and the lowest log values corresponds to a difference in measurement probability of 3×10^4). The rms value of the noise histogram was calculated to be 26.54 elements or 12.96mV. Taking this value for σ and taking $K_0 = 9.628$ ($e^{K_0} = 15,180$ counts for the averaged peak), the theoretical log Gaussian curve was calculated and displayed in Fig. 3.21, superimposed over the experimental log distribution. As can be seen in the figure, the experimental log distribution follows almost exactly the calculated log Gaussian curve down to the last few counts in the wings of the distribution. This means that the noise is almost perfectly Gaussian and the analysis of Section 2.1.2 to 2.1.4 should accurately predict the receiver communications performance. Noise outputs measured using this technique have given excellent agreement with rms noise values measured using our HP435A (with 8481A Sensor) power meter.

3.3.8.2 Use of the DPO System for 1/f Noise Characterization

The noise analysis in the previous section is based upon making an amplitude histogram of randomly-timed samples of the noise output. At sufficiently low frequencies, we can take time-sequential noise output samples and infer from this the frequency spectrum of the noise. In the DPO system, one-shot sampling at a rate of 0.5mS/cm will obtain virtually a complete 512 point waveform, corresponding to a Nyquist frequency of 51.2 KHz. Of course, for accurate noise spectra, frequencies above the Nyquist frequency must be filtered out as the short sampling times in the P7001 will alias noise components of hundreds of MHz. The program listed in lines 400-440 carries out this noise spectral density by averaging the magnitudes of the Fourier transforms of many one-shot noise waveforms. This low-frequency noise spectrum shows clearly the 1/f preamp noise plus any discrete interference frequencies (from power supply ripple, etc.) which may be present in the preamp output. For more general noise spectral density measurements, at higher frequencies, the 7L13 spectrum analyzer is used.

3.3.9 Absolute Noise Spectral Density Measurements Using the Tektronix 7L13 Spectrum Analyzer

While it is the total rms voltage noise, v_{no} , and the shape of its probability density that is most relevant to the optical communications performance of a preamp, total noise gives little information about where the noise is coming from. Noise spectral density measurements, on the other hand (as illustrated in the feedback preamp noise analysis in Section 2.3.2) give detailed information about the noise mechanisms and preamp parameters. What we need is to obtain absolute noise voltage spectral density (volts/ $\sqrt{\text{Hz}}$) data from spectrum analyzer measurements. We can use this data to compare with the noise model (e.g., listing in A.2) to determine critical noise parameters and to calculate N.E.P. at any given frequency, or, if we integrate the noise curve (squared), we can obtain the total preamp noise output (which should be the same as v_{no} measured by other techniques - the difference is that here we know what part of the noise is caused by each noise mechanism). While most of the procedures here would apply to the use of any spectrum analyzer for noise measurements, some details of the noise response depend on the type of IF detector in the instrument (and the possibility of spurious responses), so we specifically address the case of the use of the Tektronix 7L13 spectrum analyzer plug-in for this purpose.

For our purposes, the 7L13 may be thought of as a narrowband tuned receiver which measures either the average value of the magnitude of the voltage received in its passband (the IF voltage) in the linear mode, or the average of the log of the magnitude of the IF voltage in the log mode. A video filter with long time constant is used to average fluctuations in the measured noise level with time. The absolute amplitude of the display (either linear or log) is determined by inputting a sine-wave source of known amplitude into the 50 Ω r.f. input of the 7L13 as a basis of calibration. The 7L13 response is very flat over its dc-1.8 GHz range and hence it is usually sufficient to calibrate the amplitude at a single frequency (typically 50 MHz). An input low pass (<1.8 GHz) filter is used so that

there are no significant spurious responses and no noise aliasing in the 7L13.

Only two things are needed to obtain absolute noise spectral density (volts/ $\sqrt{\text{Hz}}$) data with the 7L13: 1) knowledge of the exact noise bandwidth and 2) knowledge of the rms noise voltage within the passband.

The noise bandwidth of the 7L13 is selected by picking one of six IF crystal filters giving "resolution" bandwidths as wide as 3 MHz or as small as 30 Hz (in decade steps). The first order of business is to measure the noise bandwidth for each of these filters. The noise bandwidth, ΔF , is defined by

$$\Delta F = \frac{1}{A_{\text{MAX}}^2} \int_0^{\infty} A(f)^2 df \quad (3.7)$$

where A_{MAX} is the peak (linear) voltage gain and $A(f)$ is the voltage gain as a function of frequency. Actually, if several different crystal filters are used and only one is used for the sine-wave amplitude calibration (the 3 MHz resolution setting for the 7L13), then these small amplitude variations can be taken into account in ΔF by using A_{MAX} for the calibrated scale instead of the peak response. This can be referred to as an effective noise bandwidth, $\Delta F'$ (where of course $\Delta F' = \Delta F$ on the amplitude calibrated range. The ΔF calibrations for our 7L13 were obtained by installing and calibrating the unit in our DPO system and scanning a stable (amplitude and frequency) source with the 7L13 in the linear display mode, so that the display is $A(f)$. The computer was then used to square $A(f)$, integrate and either divide by $\text{MAX}(A(f))^2$ or A_{MAX}^2 for the reference filter setting to get ΔF or $\Delta F'$.

TABLE 3.1

7L13 Spectrum Analyzer Noise Bandwidth Calibrations

NOMINAL RESOLUTION BANDWIDTH SETTING	NOISE BANDWIDTH RELATIVE TO PEAK ΔF	NOISE BANDWIDTH RELATIVE TO 3MHz PEAK $\Delta F'$	WHITE-NOISE VOLTAGE OUTPUT RELATIVE TO 3 MHz (db)
3 MHz	1.897 MHz	1.897 MHz	0 db
300 KHz	200.2 KHz	200.2 KHz	-9.6 db
30 KHz	26.79 KHz	26.07 KHz	-18.7 db
3 KHz	2.597 KHz	2.590 KHz	-29.2 db
300 Hz	246.1 Hz	217.3 Hz	-30.5 db
30 Hz	22.53 Hz	22.28 Hz	-49.3 db

The amplitude calibration of the 7L13 is based on a sine-wave signal of known rms value, while we are in fact interested in measuring Gaussian noise. In fact, a correction factor must be used to correct the measured amplitudes to real noise voltages, and this correction factor depends on whether the "linear" or "log" display mode is used. The "linear" correction between an average (magnitude)-reading meter reading a sine wave and a Gaussian noise distribution is easily obtained. Since the average value of a sine wave $V_S(t) = V_m \sin \omega t$ is $V_S(\text{avg}) = (2/\pi)V_m$ while the rms value is $V_S(\text{rms}) = V_m/\sqrt{2}$, the sine wave meter calibration will incorporate an average to rms correction factor of

$$V_S(\text{rms})/V_S(\text{avg}) = \pi/2\sqrt{2} = 1.11072 \text{ (sine wave)}. \quad (3.8)$$

The average value of Gaussian noise of rms value $V_g(\text{rms})$ is given by

$$V_g(\text{avg}) = \frac{2}{V_g(\text{rms})\sqrt{2\pi}} \int_0^\infty V e^{-\frac{1}{2}[V/V_g(\text{rms})]^2} dV = \sqrt{\frac{2}{\pi}} V_g(\text{rms}) \quad (3.9)$$

or
$$V_g(\text{rms})/V_g(\text{avg}) = \sqrt{\frac{\pi}{2}} = 1.25331 \quad (3.10)$$

Since the spectrum analyzer is calibrated with a sine wave source, the scale reading, V_S , will be related to $V(\text{avg})$ by Eq. 3.8 as $V_S = V(\text{avg})\pi/2\sqrt{2}$. Using this for $V_g(\text{avg})$ in Eq. 3.10 we have the relationship between the actual Gaussian noise rms voltage, $V_g(\text{rms})$, and the scale reading, V_S as

$$V_g(\text{rms}) = \frac{2}{\sqrt{\pi}} V_S(\text{rms}) = 1.1284 V_S(\text{rms}) \quad (3.11)$$

for the linear display mode (i.e., in the linear display mode, we would add 1.05 dB to measured voltages to convert to correct Gaussian rms noise values).

When the display mode is "log", what is averaged is the log of the magnitude of the IF voltage. Clearly, the average of the log is not equal to simply the log of the average, so that additional correction is required. This correction (which could depend on details of the log amp-detector arrangement) was measured on our 7L13 to be an additional 1.35 db between measuring Gaussian noise in the "LOG 10dB/div" and the "LINEAR" display modes (determined by comparing white noise measurements directly to a calibrated sine wave reference in each mode). That is, when measuring Gaussian noise in the "LOG 10dB/div" display mode, we have

$$\left[V_g(\text{rms}) \right]_{\text{LOG}} = 1.318 V_S(\text{rms}) \quad (\text{i.e., } +2.40 \text{ dB}) \quad (3.12)$$

(where the 2.40 dB figure comes from the sum of the linear correction of 1.05 dB plus the log correction of 1.35 dB.) This means, then, that if we measure on the "LOG 10dB/div", then the noise voltage spectral density is just ($\text{OdBm} = \sqrt{55} \approx 0.2236 \text{ VOLTS}$)

$$V_n(\text{prHz}) = \frac{0.2236}{\sqrt{\Delta F}} 10^{\frac{(V_n(\text{dBm})+2.40)}{20}} \quad (\text{VOLTS}/\sqrt{\text{Hz}}). \quad (3.13)$$

(If the spectrum analyzer amplitude is calibrated on the usual 3 MHz resolution setting rather than the setting used, simply use $\Delta F'$ from Table 3.1 rather than ΔF .)

The total noise output for a receiver may be obtained by integrating $[V_n(\text{prHz})]^2$ from Eq. 3.13 over the measurement bandwidth (usually dc to 1.8 GHz) or doing the integral over the noise power, $P_n(\text{/Hz})$

$$P_n(\text{/Hz}) = \frac{10^{-3}}{\Delta F} 10^{\frac{(V_n(\text{dBm})+2.40)}{10}} \quad (\text{watts/Hz}) \quad (3.14)$$

and converting total power to voltage at the end. The TEK BASIC program listed in Appendix A.9 carries out this integral from manually-entered $V_n(\text{dBm})$ vs. F points from 7L13 LOG 10dB/div display noise curves. The calculational method is exact for any straight line segment of the dBm (LOG) curve given the endpoints, so a relatively few points is adequate to define a typical curve. Note that in the program the 2.40 dB correction factor is not included, so that it must be added to each input point or the end

result corrected by +2.40 dB. The program is designed to integrate over a number of curves covering different frequency ranges to integrate from $1/f$ noise to the high frequency noise rolloff. Agreement between total noises calculated from the spectral curves and rms noise values obtained from histogram or power meter reading is good, with the spectrum analyzer results usually giving a value of total noise voltage of the order of 95% of the value obtained in the histogram measurements.

3.3.10 Use of the DPO System for Measuring the Current Impulse Response and $(V/Q)_p$ to Determine Preamp N_o

As discussed in Section 2, the important characteristics of a preamp for an avalanche photodiode receiver are its response time (the response must decay to a small fraction of peak response in one bit time to prevent inter-symbol interference) and its minimum detectable current pulse, N_o , which determines the required photocurrent level. To calculate N_o we need both the output noise v_{no} (the measurement of which is discussed in Section 3.3.8, and the pulse gain $(V/Q)_p$. Described here is a method for measuring the current pulse response, including $(V/Q)_p$, for a preamp, under appropriate small-signal conditions and with the preamp input shunted by the avalanche photodiode conductance (capacitance).

Determining the current pulse response parameters for a preamp is conveniently carried out using our Tektronix Digital Processing Oscilloscope system with the 7S12 TDR sampling plug-in. In general, instead of trying to use the experimental light pulse shape to measure $(V/Q)_p$, we measure the response to a δ -function current input and convolve the δ -function response with any input light pulse shape to get the response and peak response $(V/Q)_p$ for that light pulse input. (In most cases, the light pulse width is sufficiently faster than the preamp response [$\Delta T \ll \Delta T_o$ in Fig. 2.2] that $(V/Q)_p$ is only slightly less than $(V/Q)_\delta$. Hence we will discuss only $(V/Q)_\delta$ here.)

The experimental measurement approach, illustrated in Fig. 3.22 is based on the use of an extremely small (2×10^{-14} pf) coupling capacitor between a properly terminated pulse (step) generator and the preamplifier input in order to produce a short current pulse by a capacitive differentiation of the fast rise step from the pulse generator. The current pulse, $i(t)$ in Fig. 3.22 is given by

$$i(t) = C_c \frac{d}{dt} [V_g(t) - V_{IN}(t)] , \quad (3.15)$$

where V_g is the pulse generator voltage appearing across the 50Ω line termination, C_c is the tiny coupling capacitor between the pulse generator line and the preamp input, and V_{IN} is the (small) voltage appearing across the preamp input ($V_{IN} = i/(G_{IN} + G_I)$) where G_I is the input conductance ($G_I \cong 1/R_i$) of the preamp and G_{IN} is the shunt conductance (small capacitance) placed across the preamp input to simulate the avalanche photodiode conductance). Integrating Eq. 3.15 from a time prior to the input voltage step (when V_g is constant) to some considerable time after the step, after i_p (and hence V_{IN}) have returned to zero, we have

$$Q_p = \int_0^T i_p(t) dt = C_c (V_g(T) - V_g(0) - V_{IN}(0) + V_{IN}(T)) = C_c V_{STEP} \quad (3.16)$$

where we have used the fact that $V_{IN}(0) = V_{IN}(T) = 0$ and $V_{STEP} \equiv V_g(T) - V_g(0)$ is the input step height. The width of the current pulse, $i(t)$, is determined both by the risetime of the voltage step $V_g(t)$ and by the RC time of the capacitive differentiator. Since the impedance of the generator side is 25Ω (50Ω termination in parallel with the 50Ω line)

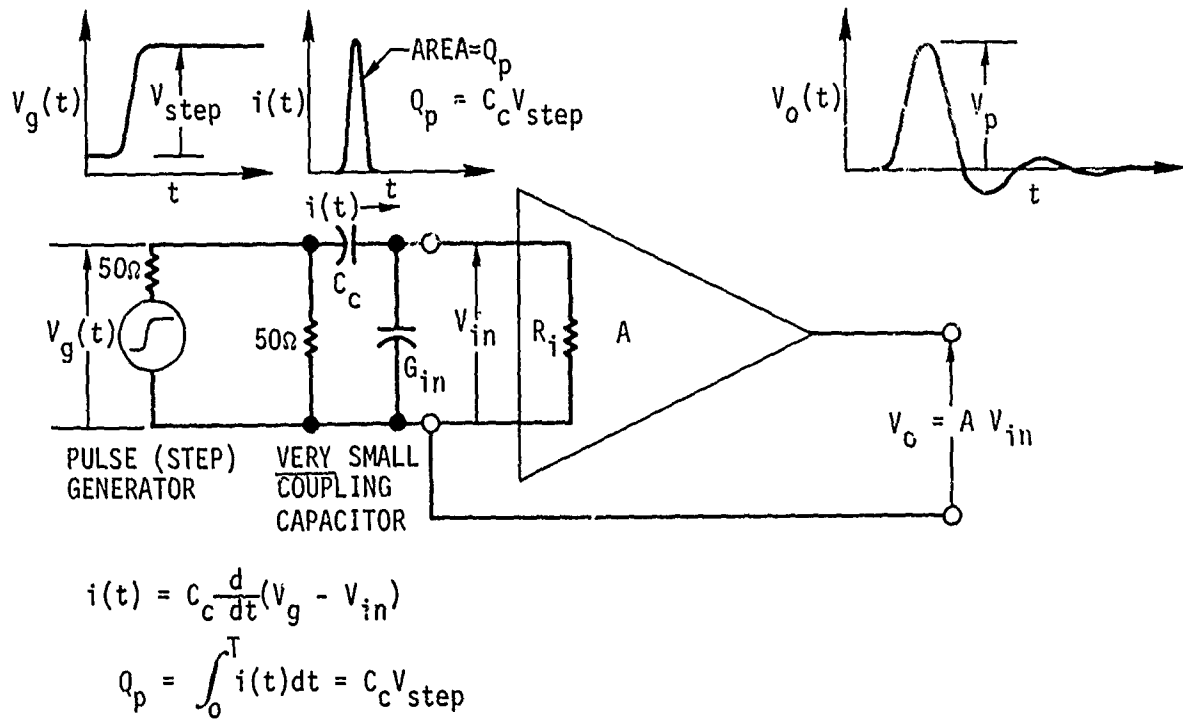


Fig. 3.22 Measurement approach for determining current pulse response and (V_p/Q_p) for a preamplifier.

and the input resistance of a feedback mode preamp is about R_F/A , with $C_C = 2 \times 10^{-14}$ fd (typical) and taking for GAASFET Preamp #8 $R_F = 5000\Omega$, $A_O = 20$, we have $R = 25 + 5000/20 = 275\Omega$ or $RC_C = 5.5$ pS, so the current pulse width is limited by the generator risetime. For the S-52 generator used with the 7S12 TDR sampling system, T_{10-90} is about 25ps, much narrower than the output pulsewidth, so we measure essentially the δ -function response.

This C_C coupling capacitance is built into the hybrid integrated GAASFET preamps as the stray capacitance between a 50 ohm microstrip test pulse line and the input (APD- Q_1 gate tiepoint in the preamp). We have also made C_C 's by modifying a preamp cover plate to carry a 50 Ω line with a hole through the plate and line shield to accommodate a short probe leading from the center conductor of the line to the vicinity of the preamp input. For measuring 50 Ω preamps a coupling capacitor, C_C , was formed by making a Tee out of a 3mm (SMA) elbow, adding a third connector, the center conductor of which does not actually touch, but only comes near, the center conductor of the elbow. The signal, V_g , from the generator comes into the original elbow and a termination is placed on the other leg of the original elbow, while the small capacitively coupled signal is coupled into the preamplifier through the new connector. The value of the coupling capacitance was measured two ways. The first was using a conventional Boonton capacitance meter in a standard 3-terminal measurement with the shield conductor of the connectors of course grounded. A value of 0.02pf was measured by this approach. A second approach, more precise, was to couple the output, not into a preamp input, but into the type S-4 sampling head directly (actually, through a 3db attenuator for isolation). This gives us an accurately known 50 Ω load across which to measure the induced voltage, $V_L(t) = 50i(t)$. V_L is very small (~ 6 mV max), deeply buried in sampler input noise, but signal averaging the waveform from 2^{12} to 2^{15} times using the Digital Processing Oscilloscope (DPO) gives a nice clean signal. This induced current pulse is then integrated (digitally on the DPO) and the resulting step is a good replica of the input step $V_q(t)$, except for a difference in magnitude from which C_C is determined by

$$C_c = \frac{1}{R_o V_{STEP}} \int_0^T V_L(t) dt \quad \text{where } R_o = 50\Omega. \quad (3.17)$$

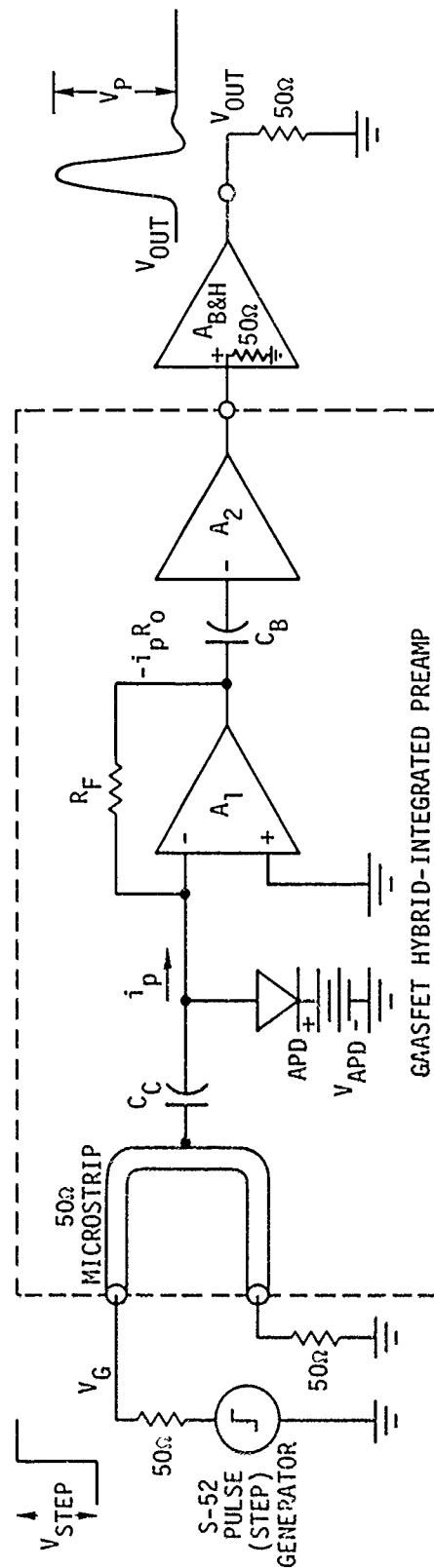
This is a very sensitive method of measuring tiny coupling capacitances. The value of C_c determined by this approach was the same as that measured on the capacitance meter ($2 \times 10^{-14} f$). The 50Ω sample mounts (Figs. 3.11 and 4.3) used for the two 50Ω -packaged Air Force delivered APD's have internal coupling capacitors of $C_c = 4.5 \times 10^{-14} f$ between the test line and the signal output line which can be used for this calibration function.

For the case of the hybrid-integrated preamps, the coupling capacitance is built-in and cannot be connected to a capacitance meter or known load for calibration. Fig. 3.23 shows the generalized "op-amp" representation of a Mark III or IA GAASFET preamp. The voltage gain stage has gain A_1 and transimpedance $R_o \approx R_F/(1+1/A_1)$ and is followed by an internal line driver stage of gain A_2 (into a 50Ω load). The preamp is usually followed by cascaded B&D DC3002 and AC3020 amplifiers before going into the 50Ω terminated S-6 sampler. The gain of these external preamps is called $A_{B\&H}$. The overall input current to output voltage relationship for the preamp will be given by (steady state)

$$V_{OUT} = R_o A_2 A_{B\&H} i_p. \quad (3.18)$$

With a short risetime step input, the measured output pulse, $V_{OUT}(t)$, which is usually signal averaged 2^{10} to 2^{12} times by the DPO to remove noise, represents the current impulse response of the preamp. It can then be directly examined to determine the maximum data rates possible without intersymbol interference, and the Fourier transform may be taken to find the frequency-domain response.

However, to find $(V/Q)_\delta$, we measure V_p (the peak value of $V_{OUT}(t)$), but we must know Q_p . Since C_c is not, in general, known, we cannot



$$Q_p = i_p dt = C_C V_{STEP}$$

$$R_o \cong \frac{R_F}{1 + 1/A_1}$$

$$V_{OUT} = R_o A_2 A_{B\&H} i_p$$

$$\int V_{OUT} dt = R_o A_2 A_{B\&H} Q_p$$

$$(V/Q)_\delta = \frac{V_p}{Q_p} = \frac{R_o A_2 A_{B\&H} V_p}{V_{OUT} dt}$$

Fig. 3.23 Block diagram of a Mark 1 or Mark III GAASFET preamp showing the C_C measurement procedure for $(V/Q)_\delta$.

use $Q_p = C_c V_{STEP}$. However, integrating 3.18 we have

$$\int V_{OUT}(t) dt = R_o A_2 A_{B\&H} \int i_p(t) dt = R_o A_2 A_{B\&H} Q_p. \quad (3.19)$$

Hence we have

$$Q_p = \frac{\int V_{OUT}(t) dt}{R_o A_2 A_{B\&H}} \quad (3.20)$$

or

$$(V/Q)_\delta = \frac{R_o A_2 A_{B\&H} V_p}{\int V_{OUT}(t) dt} \quad (3.21)$$

Similarly, we can obtain the response to any general input pulse shape by convolving the input pulse with $V_{OUT}(t)$ for the δ -function case (which will reduce V_p somewhat) and then use Eq. 3.21 to find the new $(V/Q)_p$. If we have measured V_{no} as described previously, then, the minimum detectable current pulse of the preamp is given by (substituting in Eq. 2.19)

$$N_o = \frac{V_{no}}{q(V/Q)_\delta} = \frac{V_{no} \int V_{OUT}(t) dt}{q R_o A_2 A_{B\&H} V_p} \quad (3.22)$$

Each of these quantities is measured in the DPO preamp measurements.

Another method of determining Q_p is to calibrate C_c in the preamp. This can be done by applying a triangular wave input in place of V in Fig. 3.22 or 3.23 (usually at least 10 V p-p, ~ 10 MHz). From $i_p = C_c (dV_g/dt)$ and $V_{OUT} = R_o A_2 i_p$ (no B&H's are used), we can obtain C_c as $C_c = V_{OUT} / R_o A_2 (dV_g/dt)$. This approach (and the similar approach using a sine wave V_g) give nearly identical results to the pulse integral normalization method.

3.3.11 Techniques for Applying the DPO System to Preamp Evaluation

While the most important noise histogram and current impulse response measurement techniques for using the DPO system with the GAASFET preamps have been discussed in Sections 3.3.8 and 3.3.10, there are a number of additional routinely-used procedures and programs used in various stages of the preamp evaluation that should be spelled out.

In measuring the current impulse, the signal average command is used. This is typed in as a direct keyboard command such as

AVERAGE PA, 4096

which averages the current impulse response into waveform a 4096 times (usually 1024 to 4096 averages are used with sampling). In general, there will be a baseline error in the average result which must be removed. If the pulse response begins 2 cm from the left (102.4 horizontal elements) the program listed in Appendix A.8 line numbers 1000 to 1074 would be used to obtain the average value of A from $J = 0$ to 100 (for example) with this result stored as the variable name "AV". Then the command

LET PA = A - AV

is used to correct the baseline in the computer and processor arrays (A and PA). For an impulse response in A, the accuracy of the baseline is checked by integrating A into waveform B, for example

INTEGRATE A, PB

to check that both the regions left of the pulse and to the right of the step in B are flat. Assuming the baseline is satisfactory, then the integral step height (as required in the normalizations in Eqs. 3.17 through 3.20) can be obtained by using the "Average" routine again (Appendix A.8 line 1000-1074) over a suitable portion of the right hand side of B (for example $J = 300$ to 500) with the result $AV = \int V_{OUT}(t)dt$. For an impulse response in PA, with the baseline corrected, the FFT may be used to obtain the frequency domain response by

FFT A, PC, PD, POLAR

which puts the magnitude of the frequency response $A(f)$ into PC and the phase (which will include a large linear phase shift because the pulse does not start at $t = 0$; this can be subtracted off) in PD. To obtain the 3 db bandwidth of the magnitude array in C, the program lines 600-640 in Appendix A.8 is used. Starting at line 600 it gives the 3 db bandwidth relative to the peak amplitude, or by using

LET CØ = C(256): GOTO 620

the result (F3) will be relative to the amplitude at dc. The noise bandwidth (defined by Eq. 3.7) is calculated in the program lines 1300 to 1390 Appendix A.8. Again, straight execution from line 1300 gives the result relative to the peak response, .. e

LET CØ = C(256): GOTO 1346

will calculate the noise bandwidth (NB) relative to the dc response.

While the foregoing was based on an impulse response measurement (as in Section 3.3.10), many measurements are made of straight pulse response (step in, step out). An example of this is in the hybrid preamps when initially measuring the op-amp open-loop voltage gain, A_1 , (in Fig. 3.23) by connecting the gate of Q_1 directly to the 50 Ω microstrip test line and measuring the pulse gain. The low-frequency gain, $(A_1)_0$ will be given by

$$(A_1)_0 = \frac{V_{OUT}(STEP)}{A_2 V_{IN}(STEP)} \quad (3.21)$$

where A_2 is the output stage gain. We want to know, of course, the frequency dependence of A_1 . We obtain this by taking the derivative of the step response with

DIFFERENTIATE A, PB, 0

where the step size is determined by the final index (from -1 to 3 depending on the resolution-noise tradeoff desired; it is sometimes desirable to combine fast, noisy derivatives [index -1 or 0] at the step with slower, smoother [index 1 or 2] derivatives away from the step). Since the derivative of the step response of a linear system is equal to the impulse response, we obtain the frequency response and bandwidths from

FFT B, PC, PD, POL

as before.

In some cases of derivative response measurements, considerable "hash" from ground and transmission line, ringing from the input pulse generator step may be noticed in the derivative after the preamp response has died out. While the amplitude of this tends to be small, the effect of this is to considerably "roughen" the FFT-derived frequency response, adding spurious responses outside of the passband, etc. The program in Appendix A.8 lines 1200-1250 can be used to attenuate this "hash" in the derivative response tail in B to make the results of the FFT smoother and more meaningful (AF is usually taken as about 0.95).

4.0 AVALANCHE PHOTODIODE AND GIGABIT RECEIVER PERFORMANCE RESULTS

The avalanche photodiodes used in all of the hybrid-integrated optical receivers have been from the same epitaxial wafer (K-9) of homo-heterojunction APD's. Hence the device characteristics for all of the APD's are very similar, so that we can discuss the general characteristics of these homo-heterojunction APD's in one section (4.1) and discuss the performance characteristics of each type of hybrid-integrated GAASFET preamp in separate sections (4.2 - 4.4).

4.1 Inverted Homo-Heterojunction GaAs_{1-x}Sb_x Avalanche Photodiode Results

All of the inverted homo-heterojunction GaAs_{1-x}Sb_x avalanche photodiodes used in hybrid-integrated receivers were from the same epitaxial growth (K-9). The device structure, as shown in Fig. 2.7 was grown using the dopant-drop technique for producing the p-n homojunction discussed in Section 3.1. The diodes were fabricated using the techniques described in Section 3.2 and either mounted directly on the metallized alumina hybrid preamp substrate (for the Mark IA preamps) or mounted on a small (100 mils diameter) gold plated copper carrier which mounts on the hybrid substrate in the Mark II or Mark III preamps to provide for APD interchangeability.

4.1.1 Active Layer Doping Profile

Figure 4.1 shows the $N(x)$ profiles derived from derivative-capacitance measurements on two similar K-9 devices. The carrier concentration in the active n^- layer (see Fig. 2.7) is of the order of $N_D = 7.5 \times 10^{15} \text{ cm}^{-3}$ and the full depletion width at high biases is of the order of 5μ ($4-5\mu$ for most diodes). The dropoff in $N(x)$ at low depletion widths probably reflects grading effects near the junction, while the rise in $N(x)$ near 4.5 to 5μ in Fig. 4.1 represents punchthrough of the depletion region from the p-n junction through the n-active layer to the n^+ buffer layer. The sloping of $N(x)$ near punchthrough is due either to fluctuations in active layer thickness over the diode, doping density increase near the n^+ buffer - n^- active layer heterojunction, or (most likely) both. The punchthrough occurs at a bias of around 50 volts, and the typical breakdown

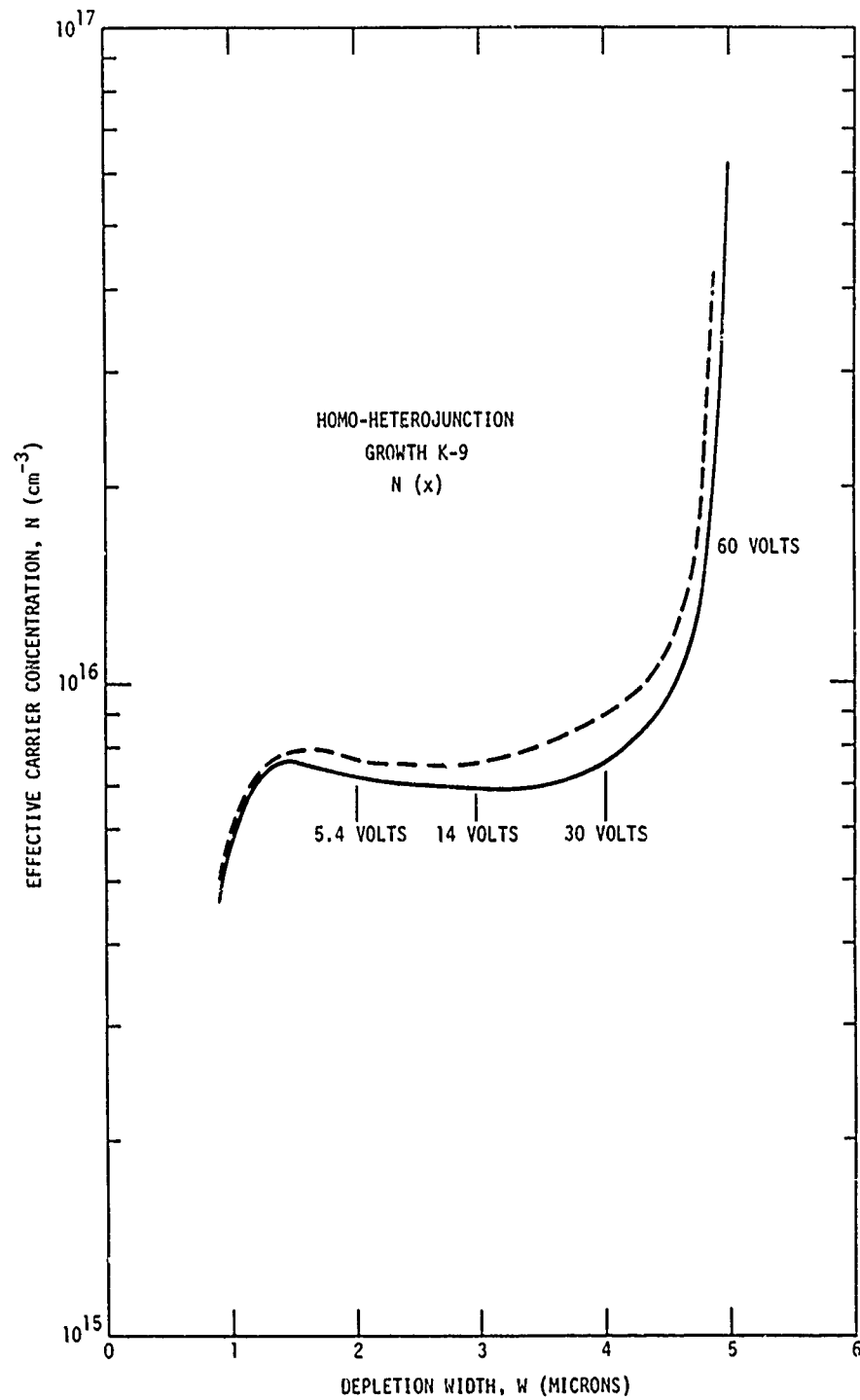


Fig. 4.1 Carrier concentration versus depth, $N(x)$, measured on two different 5 mil diameter diodes on the K-9 epitaxial growth used for these homo-heterojunction APD's (structure of Fig. 2.7).

voltages are about 120 volts, so that the peak electric field at the p-n homojunction at breakdown is about 3×10^5 V/cm.

4.1.2 APD Junction Capacitance

The actual capacitance versus voltage curve for a 5 mil diameter (0.127mm) K-9 APD is shown in Fig. 4.2. The zero-bias junction capacitance is about 1.65pf, but the capacitance drops rapidly with reverse bias to a value of 0.31pf above punchthrough (2450pf/cm^2). The capacitance is nearly independent of bias for $V_{\text{APD}} > 60$ volts (because the depletion region thickness is bounded by the physical active layer thickness between the n^+ buffer layer and the p-n homojunction). A 3-mil (0.0762mm) diameter APD with a junction area of $A_j = 0.456 \times 10^{-4} \text{cm}^2$ will have, in comparison to the 5 mil diameter ($A_j = 1.27 \times 10^{-4} \text{cm}^2$) device a capacitance of $C_j = 0.11\text{pf}$ above punchthrough, or about one third of the $C_{\text{APD}}(V_{\text{APD}})$ values of Fig. 4.2.

4.1.3 Response Time of Delivered 50 Ω - Packaged Devices

The response time of these $\text{GaAs}_{1-x}\text{Sb}_x$ photodiodes is so fast that for all practical purposes, in the integrated preamps, the APD may be considered an infinitely fast current generator with a small shunt capacitance, C_{APD} . The worst case carrier transit time in the K-9 APD's, for example is

$T_{\text{TR}} = W/V_{\text{SAT}} = 5 \times 10^7 \text{cm/sec} = 50\text{ps}$ (40ps 10% to 90%), which is much faster than the preamp response time. Hence from a standpoint of receiver speed, the important thing is the junction capacitance, C_{APD} discussed previously.

Since these inverted heterojunction $\text{GaAs}_{1-x}\text{Sb}_x$ photodetectors are also of interest for high-speed reference diodes in sampling oscilloscope measurements, their high-speed 50 Ω response time is also of interest. Fig. 4.3 shows sampling oscilloscope measurements of the output (double) pulse structure from our modelocked Nd-YAG laser as measured simultaneously with two M8-1 epi growth 3 mil diameter inverted heterojunction $\text{GaAs}_{1-x}\text{Sb}_x$ photodiodes. The upper curve (downward response) was measured for the device in the older 50 Ω mount on the left (Ref. 1) with a Tektronix S-4 sampler head, while the lower curve (upward response) was measured using the new 50 Ω APD mount (described in Section 3.2) with a Tektronix S-6 sampler with precision 50 Ω termination. The new mount is shown at the upper

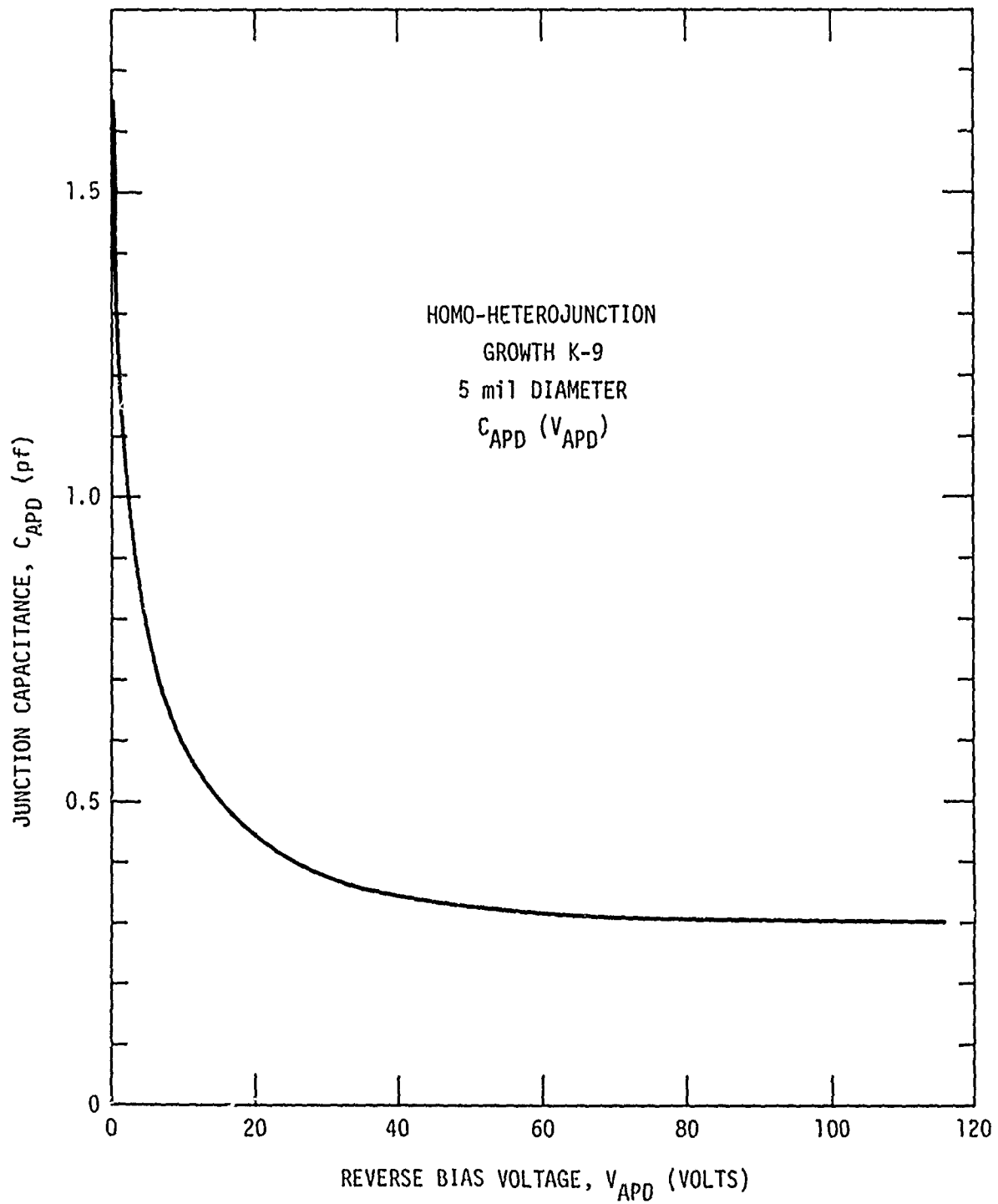


Fig. 4.2 Capacitance-Voltage Relationship for a 5 mil diameter K-9 APD. Capacitances for a 3 mil APD are about one third of this

right in Fig. 4.3. The output connector (3mm male) is coaxial with the light entrance and is barely visible in the picture. The upper Microdot connector is the bias lead, while the left-right opposing pair of 3mm female connectors provide a feedthru capacitive coupling test line to the output ($C_c = 4.5 \times 10^{-14} \text{f}$).

As can be seen in Fig. 4.3, the response of the diode in the new mount with the S-6 sampler gives extremely "clean" response with sharp fall time from the first light pulse peak down to a flat baseline before the second (smaller) pulse arrives 370ps after the first. The FWHM on the pulses is under 100ps and the 90% - 10% fall time is about 60ps; these figures probably represent a fairly accurate estimate of the laser pulse parameters (as opposed to the APD or sampling oscilloscope response times, as both have frequency responses of the order of 14GHz).

4.1.4 APD Reverse Dark Current

The surface passivated K-9 APD's have generally low leakage currents. Fig. 4.4 shows the total dark reverse current, I_R , versus reverse bias voltage at room temperature for 3 mil and 5 mil diameter inverted homo-heterojunction APD's. The total APD leakage current I_R can be considered as the sum of a "bulk" leakage I_B (essentially as used in Eq. 2.24) and a "surface" leakage, I_S . Calculation of the bulk leakage (thermal generation current in the depletion region) for these devices has been discussed in Ref. 5 and will not be repeated here. Assuming $N_i = 10^9 \text{cm}^{-3}$ and $\tau_e = 10^{-8}$ seconds, we have $I_B = qn_i A_j W / \tau_e = 1 \text{nA}$ for a 5 mil diameter APD or $I_B \sim 0.35 \text{nA}$ for a 3 mil diameter APD at punchthrough ($W = 5\mu$). At biases of a few volts, the leakage current is predominantly bulk and the ratio between the leakage of the 3 mil device to the 5 mil device should be the ratio of their junction areas or about 0.36. As seen in Fig. 4.4, this is indeed the case for biases up to 4 or 5 volts (i.e., at 3 volts reverse bias $(I_R)_{5 \text{ mil}} = 0.68 \text{nA}$ while $(I_R)_{3 \text{ mil}} = 0.24 \text{nA}$ or $(I_R)_{3 \text{ mil}} / (I_R)_{5 \text{ mil}} = 0.353$).

The bulk leakage would be expected to increase only very slowly with bias above $V_{APD} = 10$ volts, and not at all above punchthrough ($V_{APD} = 60$ volts) until avalanche gain sets in. In fact, as seen in Fig. 4.4 the total reverse current increases exponentially with reverse bias over this bias range where the bulk leakage is constant. This leakage is the "surface" current, I_S .

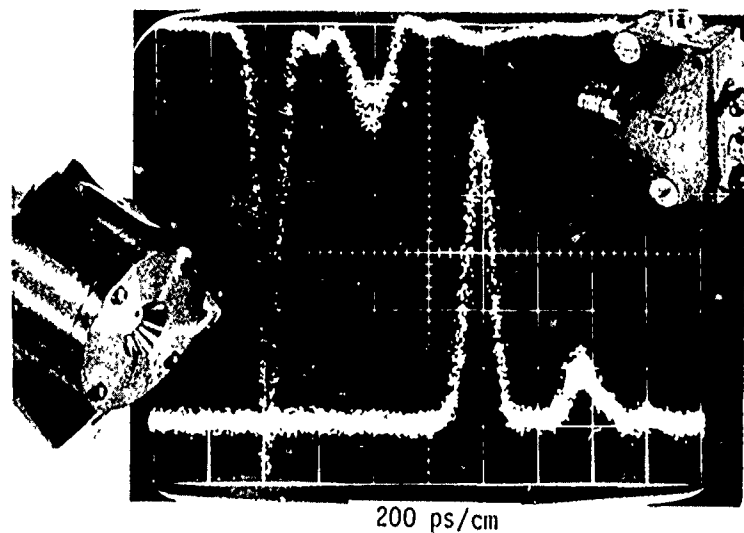


Fig. 4.3 Response of Two 3 mil M8-1 Inverted Heterojunction Microwave Avalanche Photodiodes to Modelocked Nd-YAG Laser Pulses. Upper curve (inverted) is from older mount (Ref. 1) shown on left into S-4 sampler, whereas lower (upward-going) curve is for similar APD in the new compact 50 Ω mount shown at the upper right and Fig. 3.11 into an S-6 sampler. Both curves at 200pS/cm. Note the clean fall and return to baseline between the two laser pulses for the new diode mount.

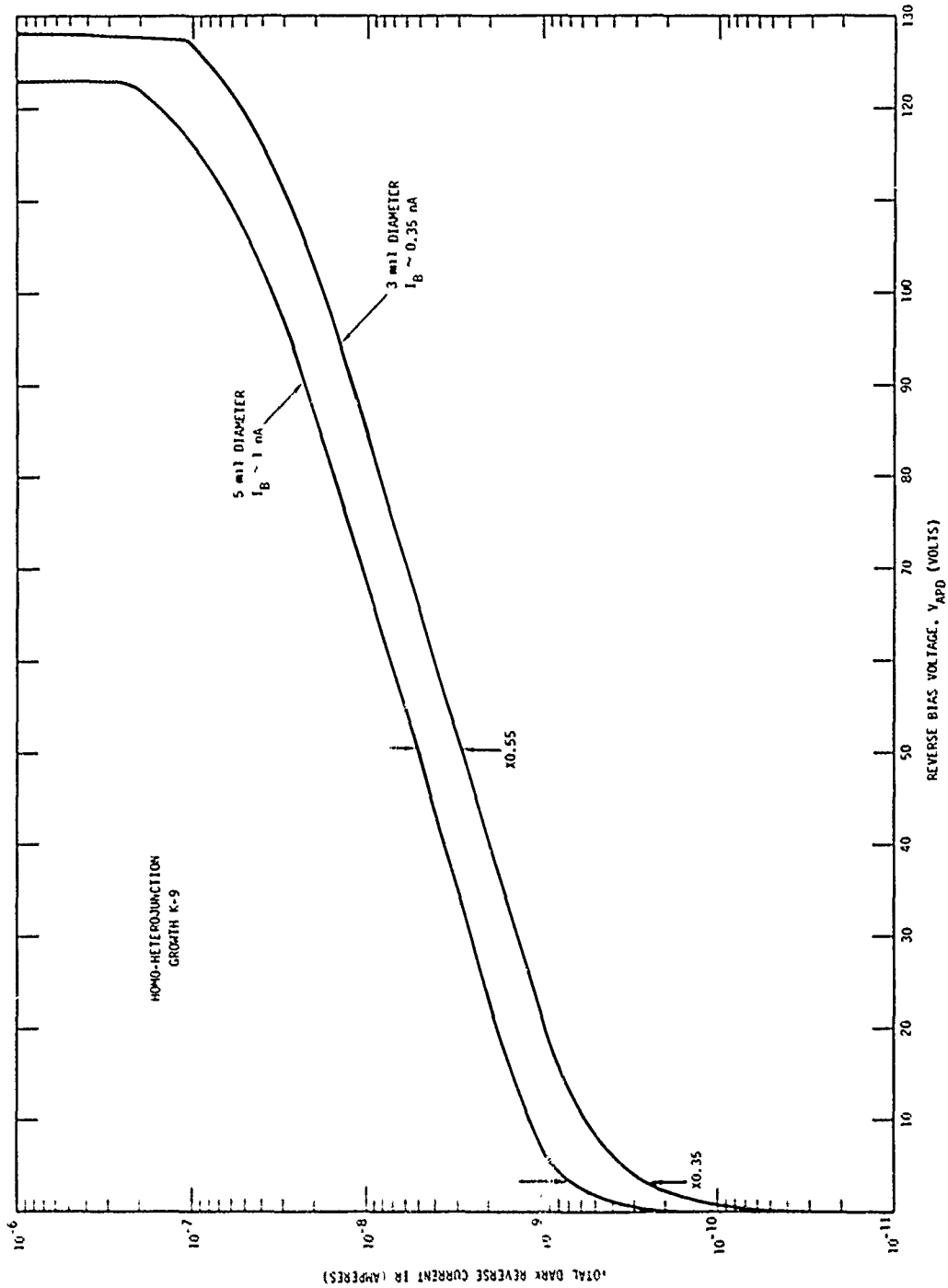


Fig. 4.4 Total Reverse (Dark) Current for 3 mil (lower curve) and 5 mil (upper curve) diameter K-9 Homo-Heterojunction APD's. Note that the bulk leakage at low biases scales with area while surface current, dominant at higher biases, scales with perimeter.

This surface leakage increases the total leakages from the nanoampere range of bulk leakages at low biases to the 10 nanoampere range at mid biases (punchthrough) up to leakages of the order of 100 nanoamperes in the avalanche gain region near breakdown. If this "surface" leakage is really due to the surface of the junction, then I_S should scale with the device perimeter (as opposed to area for I_B). At a bias of 50 volts we measure $(I_R)_{5 \text{ mil}} = 5.1 \text{ nA}$ and $(I_R)_{3 \text{ mil}} = 2.8 \text{ nA}$. Assuming $(I_B)_{5 \text{ mil}} = 1 \text{ nA}$ and $(I_B)_{3 \text{ mil}} = 0.36 \text{ nA}$ we have for $I_S = I_R - I_B$, $(I_S)_{5 \text{ mil}} = 4.1 \text{ nA}$ and $(I_S)_{3 \text{ mil}} = 2.44 \text{ nA}$ or $(I_S)_{3 \text{ mil}} / (I_S)_{5 \text{ mil}} = 0.60$, exactly the ratio of the perimeters.

Both the surface and bulk leakage currents in these homo-heterojunction $\text{GaAs}_{1-x}\text{Sb}_x$ APD's are so low that they have no significant effect on the noise properties of the integrated GAASFET receivers. For example, for GAASFET preamp #8, $R_f = 5 \text{ K}\Omega$ or $i_{nj} = 1.8 \times 10^{-12} \text{ amps}/\sqrt{H_z}$, whereas the shot noise from the $I_S = 100 \text{ nA}$ surface leakage of its 3 mil APD is only $i_{ns} = 1.79 \times 10^{-13} \text{ amps}/\sqrt{H_z}$, or taking $M=10$ and $X_n=0.25$, the multiplied shot noise from an $I_B = 0.36 \text{ nA}$ bulk leakage is $i_{ns} = 1.43 \times 10^{-13} \text{ amps}/\sqrt{H_z}$ (for a 5-mil APD these would be about $2.5 \times 10^{-13} \text{ A}/\sqrt{H_z}$ and $2.4 \times 10^{-13} \text{ A}/\sqrt{H_z}$ respectively), well below the Johnson noise level. As higher gain levels are attained, the bulk leakage current will contribute significant noise (which can be reduced by cooling, of course) but recalling that the average pulsed photocurrent for $N_{ph} = 1000$ photons/bit, $\Delta T = 0.5 \text{ ns}$ is 320 nA, a 1nA bulk leakage current is not very significant.

4.1.5 Spectral Dependence of Photoresponse and Absolute Quantum Efficiency

The spectral photoresponse or quantum efficiency - gain product, ηM , versus wavelength, λ , for a K-9 APD is shown in Fig. 4.5. (More typical K-9 APD's have about a 15% to 20% higher breakdown voltage and 0.01μ to 0.02μ longer wavelength response than the particular device in Fig. 4.5, but are otherwise the same). This measurement was made with uniform illumination over the device area.

In a somewhat heuristic sense, the wavelength scale in Fig. 4.5 may be visualized in terms of the physical depth in the device at which the light absorption takes place; i.e., from the surface of the GaAs substrate (light

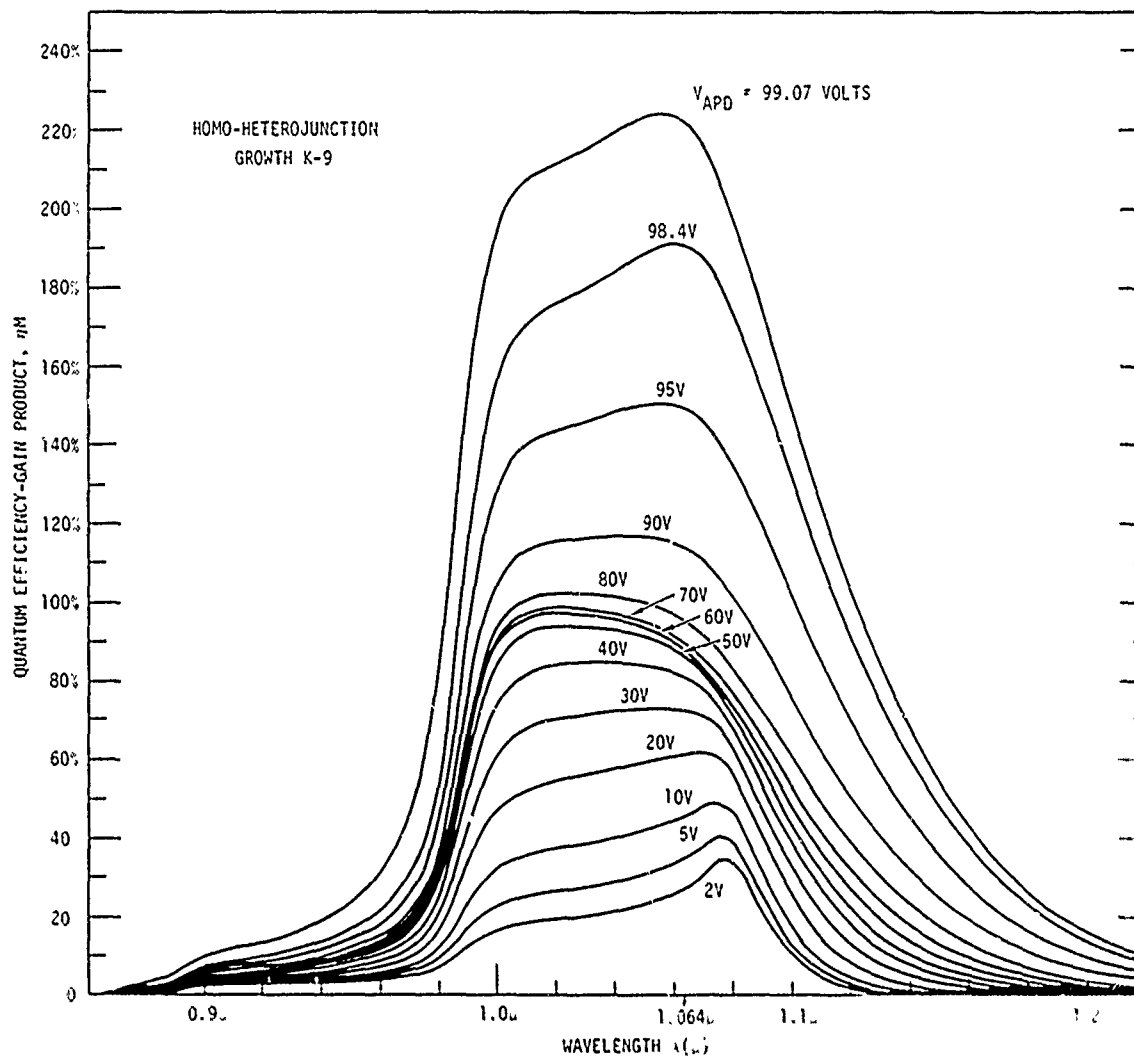


Fig. 4.5 Spectral Photoresponse for a 5 mil Diameter K-9 APD for Biases from $V_{APD} = 2$ volts to $V_{APD} = 99.07$ volts. Ordinate is quantum efficiency (quantum efficiency-gain product for $V_{APD} = 70$ volts) versus wavelength. More typical K-9 APD's as used in the GAASFET receivers have 15% to 20% higher V_B 's and 0.01 μ to 0.02 μ longer wavelength response than this particular device.

entrance window) for $\lambda < 0.86\mu$, the n^+ buffer layer from $0.9\mu < \lambda < 0.98\mu$, the n^- active layer from 0.98μ out to the p-n junction at $\lambda \sim 1.08\mu$. This position - wavelength correlation exists both because of the stepped reductions in energy gap in the heterostructure going from layer to layer, and because of the fact that in a single layer the optical absorption coefficient drops as the photon energy is reduced toward its energy gap (i.e., longer λ , deeper absorption depth). Light of wavelength below 0.88μ is absorbed largely in the GaAs substrate, very near the surface at short wavelengths, so that no photo-induced holes reach the p-n junction. At 0.9 to 0.92μ , most of the light is absorbed near the GaAs substrate in the n^+ GaAsSb ($E_g \sim 1.2\text{eV}$) buffer layer. From this point the photogenerated holes have a considerable distance ($\sim 4\mu$) to diffuse to reach the n^- active layer, and hence the photoresponse at 0.91μ is only about 5% to 15% of the response at 1.01μ . At 1.01μ , the light absorption takes place in the n^- active layer very near the n^+ buffer - n^- active layer heterojunction. At low biases, this region is neutral as the depletion region is near the p-n junction several microns away. Hence photogenerated holes must diffuse several microns to cause junction photocurrent, which is why the 1.01μ quantum efficiency is only 15% at $V_{APD} = 2$ volts. As the bias is increased to punchthrough (where the depletion region reaches all of the way through the n^- active layer to the n^+ buffer), at 50 to 60 volts for the APD of Fig. 4.5, the quantum efficiency at this wavelength reaches nearly 100%. As bias is increased further, considerable avalanche gain is seen, even with uniform illumination, though not as much gain as is seen at longer wavelengths. The implications of this ($\alpha_n > \alpha_p$) were discussed at the end of Section 2.2.2.

At a wavelength of 1.08μ in Fig. 4.5, the light is absorbed in the active layer, but at a much greater average depth. Here it is possible for a significant fraction of the light at low-bias voltages to penetrate through the undepleted n^- layer to the junction region giving the long - wavelength peaking in quantum efficiency characteristic of a deep homojunction. Of course at this wavelength the absorption depth is comparable to the active layer thickness so that a significant fraction of the light passes through the device unabsorbed. Hence at higher biases the quantum efficiency at 1.08μ is

considerably below 100%.

As was mentioned previously, the typical K-9 device has a slightly longer wavelength response than the device in Fig. 4.5 (which means that 1.064μ falls fairly close to the peak response at punchthrough) and typical 115 to 120 volt breakdowns, as opposed to $V_B \sim 100$ volts for the device in Fig. 4.5 (which means that a normal unity-gain bias will be about 80 volts instead of 60 to 70 volts as in Fig. 4.5). We have measured the unity-gain 1.064μ quantum efficiencies for the APD's in the receivers and have gotten values at $V_{APD} = 80$ volts of $\eta_{1.06\mu} = 96\%$ or 97% . These values are excellent, of course, but reasonable, since the substrates are carefully antireflection coated, the free-carrier light-absorption in the substrate is low, and the optical absorption depth ($\sim 1\mu$) is sufficiently smaller than the depletion width (5μ) to insure that the 1.06μ light is absorbed in the depletion region.

Devices which exhibit nearly 100% quantum efficiencies usually show a very flat region in η vs. V_{APD} (50V to 80 volts in Fig. 4.5, particularly 60V-70V), a reasonably flat region in λ (1.01μ to 1.06μ in Fig. 4.5) and very flat spatial photoresponse (i.e., virtually no fluctuation in sensitivity over the device area when measured with bias and wavelength values in the "flat regions"). These K-9 APD's show all of these characteristics (Figs. 4.5, 4.7, 4.21, etc.).

4.1.6 High-Frequency Avalanche Gain

In measuring avalanche gain, it is important to be able to differentiate between useful (high frequency) bulk avalanche gain and the apparent (low frequency only) gain associated with defect breakdown (microplasmas - see Ref. 1). To avoid possible confusion, we measure only the high-frequency avalanche gain at 273 MHz (or a multiple of 273 MHz) using the 7L13 spectrum analyzer as a receiver as discussed in Section 3.3.5.

The high frequency avalanche gain measured on a 5 mil K-9 APD in GAASFET preamp #7(a) is shown in Fig. 4.6. This 273 MHz gain curve was measured with the modelocked 1.064μ laser focused on the most sensitive gain area on the APD with a light spot diameter of 7.6μ (0.3 mils) and an average light power of 33nW. At low biases, the capacitance of the APD increases,

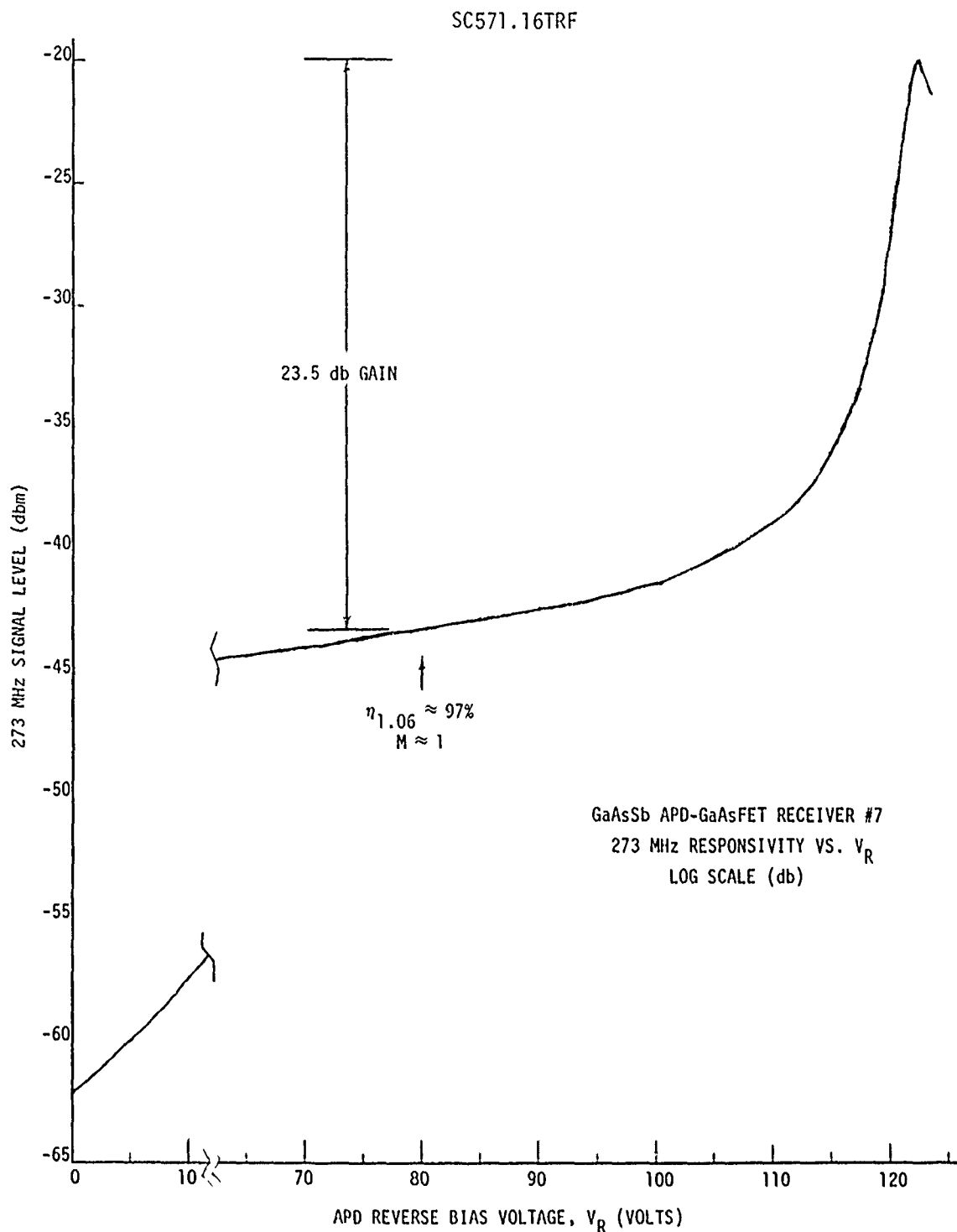


Fig. 4.6 High frequency avalanche gain versus APD reverse bias for the 5 mil diameter K-9 GaAs_{1-x}Sb_x APD in GAASFET preamp #7 (a). Complete curve, including noise, for the final delivered GAASFET preamp #7 is shown in Fig. 4.21.

reducing the bandwidth of the preamp below the signal frequency, causing a reduction in signal amplitude greater than the reduction in quantum efficiency seen in Fig. 4.5. (The complete signal and noise versus V_{APD} curves for a different APD are shown in Fig. 4.21.) Taking $V_{APD} = 80$ volts as our unity-gain reference, $M = 1$, $\eta = 97\%$, we see that the signal level increases with V_{APD} from -43.7 dBm at $V_{APD} = 80$ volts to -20 dBm at $V_{APD} = 122$ volts. However, there is an abrupt onset of detector noise at $V_{APD} = 121.7$ volts (a microplasma turning on), so that the useful peak avalanche gain is about 23 dB ($M = 14$). It should be noted that this result is for the highest gain area on the APD. At high gains on these devices the gain (for reasons which will be discussed in the next section) becomes nonuniform and typically only a few areas over an APD achieve gains over 5 or so. The average gain, as measured with a defocused beam, would typically be more like $M = 2$ to 3, as seen in Fig. 4.5.

4.1.7 Spatial Uniformity of Quantum Efficiency and Avalanche Gain

The spatial uniformity of quantum efficiency and avalanche gain are of interest not only from a device application standpoint, but also for the insight they may provide about problems in the device itself. Fig. 4.7 shows scanning light microscope measurements of the 273 MHz, 1.064μ response of a 5 mil diameter K-9 inverted homo-heterojunction avalanche photodiode in GAASFET preamp #4. The four photographs represent intensity-modulated displays of the photoresponse for various reverse biases (V_{APD}). Fig. 4.7a, for example, shows the response at $V_{APD} = 80$ volts, above punchthrough (i.e., the n^- active layer is fully depleted), but below the onset of significant avalanche gain. As would be expected for a photodiode of almost unity quantum efficiency, the response is highly uniform. As we increase the APD bias to 100 volts in (b), we begin to see some avalanche gain, but at the same time we begin to see a pattern appearing in the photoresponse due to nonuniformities in this avalanche gain. This pattern becomes considerably more noticeable in Fig. 4.7c for a 110 volt APD bias, as the avalanche gain is higher. Certain areas which have clearly higher gain than the rest of the diode are obvious here. This effect is most dramatic in Fig. 4.7d, $V_{APD} = 115$ volts, where very high gain is seen in the two areas 1.4 and 2 mils below the center (because these areas are

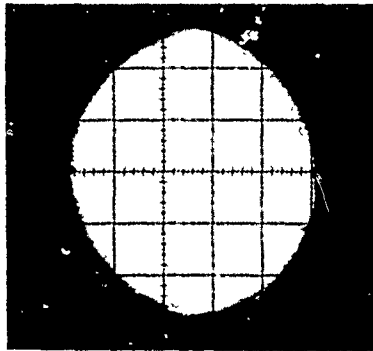
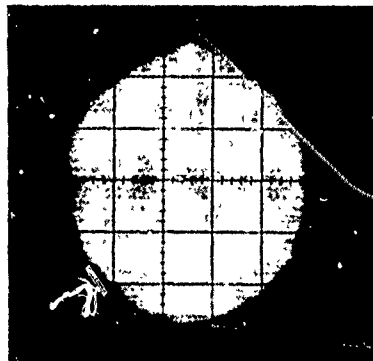


Fig. 4.7 Scanning (Modelocked) Laser Microscope intensity-modulated pictures of the 273 MHz photo-response of Mark IA Preamp #4. Scale is 1 mil/div, 10X 0.17 NA objective.

a) $V_{APD} = 80$ VOLTS.



b) $V_{APD} = 100$ VOLTS.



c) $V_{APD} = 110$ VOLTS.



d) $V_{APD} = 115$ VOLTS.

Note that orientation of all SLM pictures is looking squarely into the preamp oriented horizontally as in Fig. 4.1.

approaching breakdown), more modest gains are seen in a dozen or more other areas, and the rest of the device has fairly low avalanche gain. It is important to note here that the areas approaching breakdown are not at the device perimeter, so that surface breakdown is not a problem in this K-9 APD, even though the p-n junction is toward the surface side of the n^- active layer (see Section 2.2.2).

Clearly, the question to ask is why do some areas of these APD's have lower breakdown voltages than other areas (which limits the maximum bias to less than the breakdown of the lowest area and hence limits the available gain everywhere except these few lowest breakdown areas)? Some insight into the gain nonuniformity problem can be seen in Fig. 4.8. Fig. 4.8a shows an SLM picture of the 273 MHz response of the 5 mil diameter K-9 APD in GAASFET preamp #5 at a bias of $V_{APD}=110$ volts (fairly high avalanche gain). A characteristic spatial gain pattern is seen, similar to that in Fig. 4.7. A very interesting thing is to compare this high-gain pattern to the below-punchthrough pattern shown in Fig. 4.8b, showing the variation of quantum efficiency (also measured at 273 MHz) over the APD. Comparing Fig. 4.8a and 4.8b, we immediately perceive a strong similarity between the general pattern of the high gain and low bias spatial photoresponses, and on closer examination we find close correspondence in their detailed features. In general, we find that points with higher than average avalanche gain are points which give higher than average quantum efficiency at low biases (before the n^- active layer is fully depleted). This immediately suggests a cause for this gain variation. Remember, from Section 4.1.5, that the low quantum efficiency below punch-through is caused by the fact that the light is absorbed in the n^- active layer close to the n^+ buffer layer (in Fig. 2.7), but at low biases this region is not depleted. The closer the edge of the depletion region is to the n^+ buffer, then, the higher will be this before-punchthrough quantum efficiency, since the photogenerated holes will have a shorter distance to diffuse to the depletion region. This would say, then, that the variations in the low bias quantum efficiency represent variations in the thickness of the n^- active layer (epitaxial growth thickness between the n^+ buffer layer and the dopant-drop produced p- n^- junction); high quantum efficiency regions.

Fig. 4.8 K-9 5 mil Diameter APD in GAASFET Preamp #5.

a) 273 MHz Response at $V_{APD} = 110$ volts
(Avalanche Gain Region).

b) 273 MHz Response at $V_{APD} = 20$ volts
(Active Layer Not Fully Depleted).

c) Photograph of APD Mesa taken by

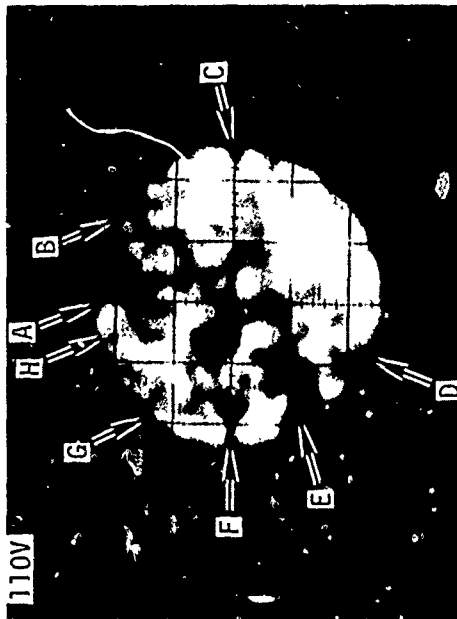
removing blank cover plate from preamp.

Since the light in a) and b) is brought

into the APD from the substrate while

Photo c) is from mesa side, corresponding

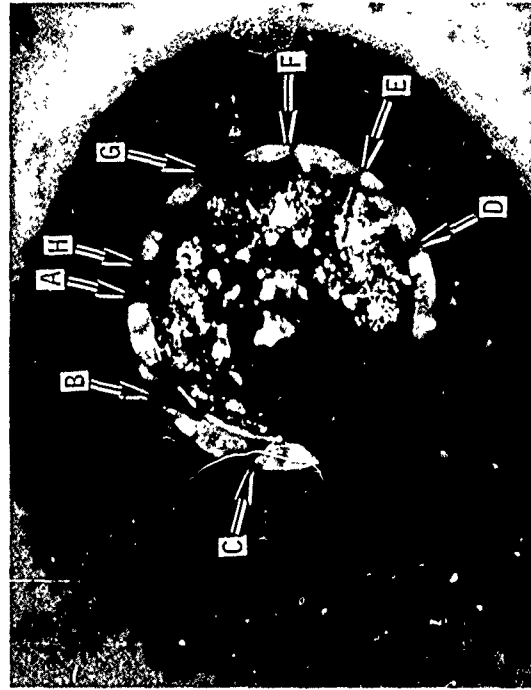
features appear left-right reversed.



a)



b)



c)

corresponding to thin n^- layer regions and vice versa. This explanation also accounts, then, for the high-gain response pattern, since the width of the depletion region at high gain, W , is essentially this distance between the n^+ buffer layer and the p - n^- junction, and the average electric field is V_{APD}/W . Hence points of narrow W are points of higher electric field and hence higher avalanche gain. This explanation, then, associates points of high low-bias quantum efficiency and high avalanche gain with points where the n^- active layer is the thinnest, and vice versa. (That such variations in the thickness of the n^- active layer exist in these K-9 diodes is already suggested by the apparent gradual rise in $N(X)$ with depletion region width in the 3.5μ to 5μ range in Fig. 4.1.)

Such n^- active layer thickness variations as postulated here might be expected to show up in the surface morphology of the epitaxial layer in a way that might be seen in ordinary microscopic examination. Fig. 4.8c is a micro-photograph of the 5 mil K-9 APD in GAASFET preamp #5 (as in a and b). The orientation of the photo is the same as that of the SLM pictures except, of course, that since this picture in Fig. 4.8c was taken from the mesa side of the APD (by removing the preamp cover plate) whereas the SLM pictures are viewed through the GaAs substrate, Fig. 4.8c appears left-right reversed from 4.8a and 4.8b. In this photo, the top of the mesa shows up as the light round circle in the middle of the dark annular ring (the sloping sides of the mesa.) Metallization can be seen over most of the central area of the mesa, with gold-ball bond in the center with the bonding lead going toward the lower left (out of focus). Comparing the photo of Fig. 4.8c with the SLM response pictures in (a) and (b) (remembering the left-right flip), we can indeed correlate between features in the response pattern with topological "hills and valleys" in the surface of the device. In Fig. 4.8 a few of the more prominent comparison features between the three pictures are pointed out with arrows labeled A through H. We see that in general the high gain (thin n^- active layer) areas are associated with "hills" and the low gain, thick n^- active region, areas in the APD correspond to "valleys" in the surface.

4.2 Performance Results for the Preliminary, Lower Bandwidth, Preamp Designs

While the Mark IA and Mark II GAASFET preamp designs do not have adequate bandwidth for gigabit data rate communications and were not Air Force delivered devices, they do represent an important technological base for the successful gigabit Mark III receivers (Section 4.3) and their performance results are relevant to understanding the performance of the gigabit receivers.

4.2.1 Results for Mark IA GAASFET Preamps

4.2.1.1 Circuit Description for GAASFET Preamps #4 and #5

The simplified circuit diagram for the Mark IA preamps is described and the circuit function explained in Section 2.3.4.1, Fig. 2.9. The complete circuit diagram for the Mark IA hybrid-integrated GAASFET preamps is shown in Fig. 4.9, with the power supply-monitor unit circuit diagram shown in Fig. 4.10. Note that while the circuit diagrams for the Mark IA GAASFET receivers #4 and #5 are the same, the mating power supply-monitor unit for each preamp is adjusted for that particular unit and must not be used with any other preamp. In addition to the integrated preamp and the power supply-monitor units, operation of the receiver also requires a current-protected stable floating avalanche photodiode supply as described, for example, in Section 3.3.6. (Figs. 3.18 and 3.19).

The overall operation of the receiver can best be understood by referring to the block diagram of Fig. 4.11, in which the receiver is outlined in terms of the "op-amp" model of Fig. 2.8 (Section 2.3.2) with key parameter values as experimentally determined from GAASFET Preamp #5. As shown in Fig. 2.9, the "op-amp" in Fig. 4.11 is a single GAASFET. In the experimental Mark IA receivers (#4 and #5), Q_1 was a 2μ gate length single-gate unit (FMX-950; Fig. 4.27b) operated at a drain current of about 10mA, giving a transconductance of about 12mmhos ($V_{DS}=4V$, $I_D=10mA$, $V_{g1}=-1.7V$). The level shift of the output (indicated by battery V_2 in Fig. 2.9) is

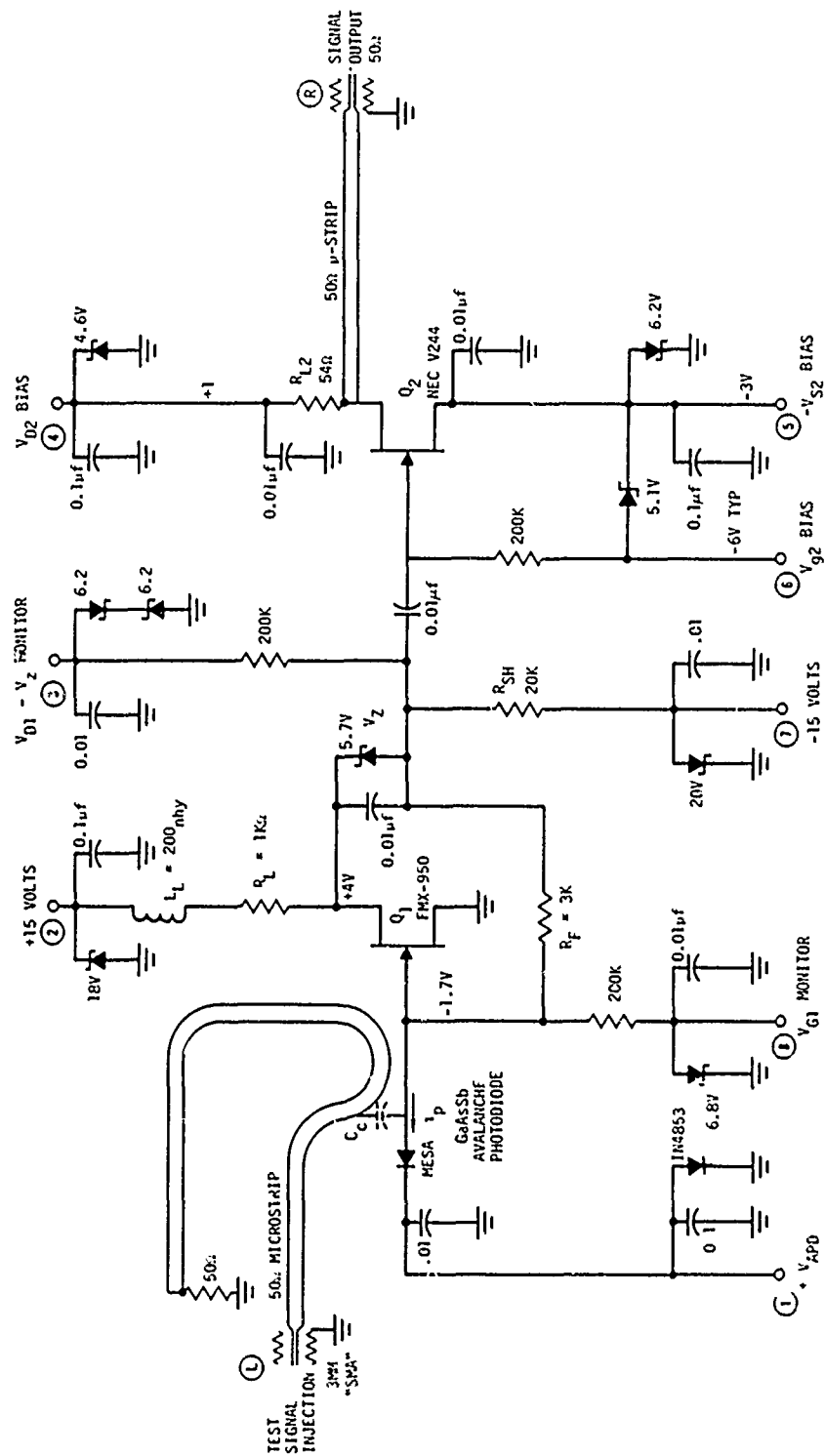


Fig. 4.9 Circuit diagram for Mark IA preamp design with specific values for GAASFET preamp #5.

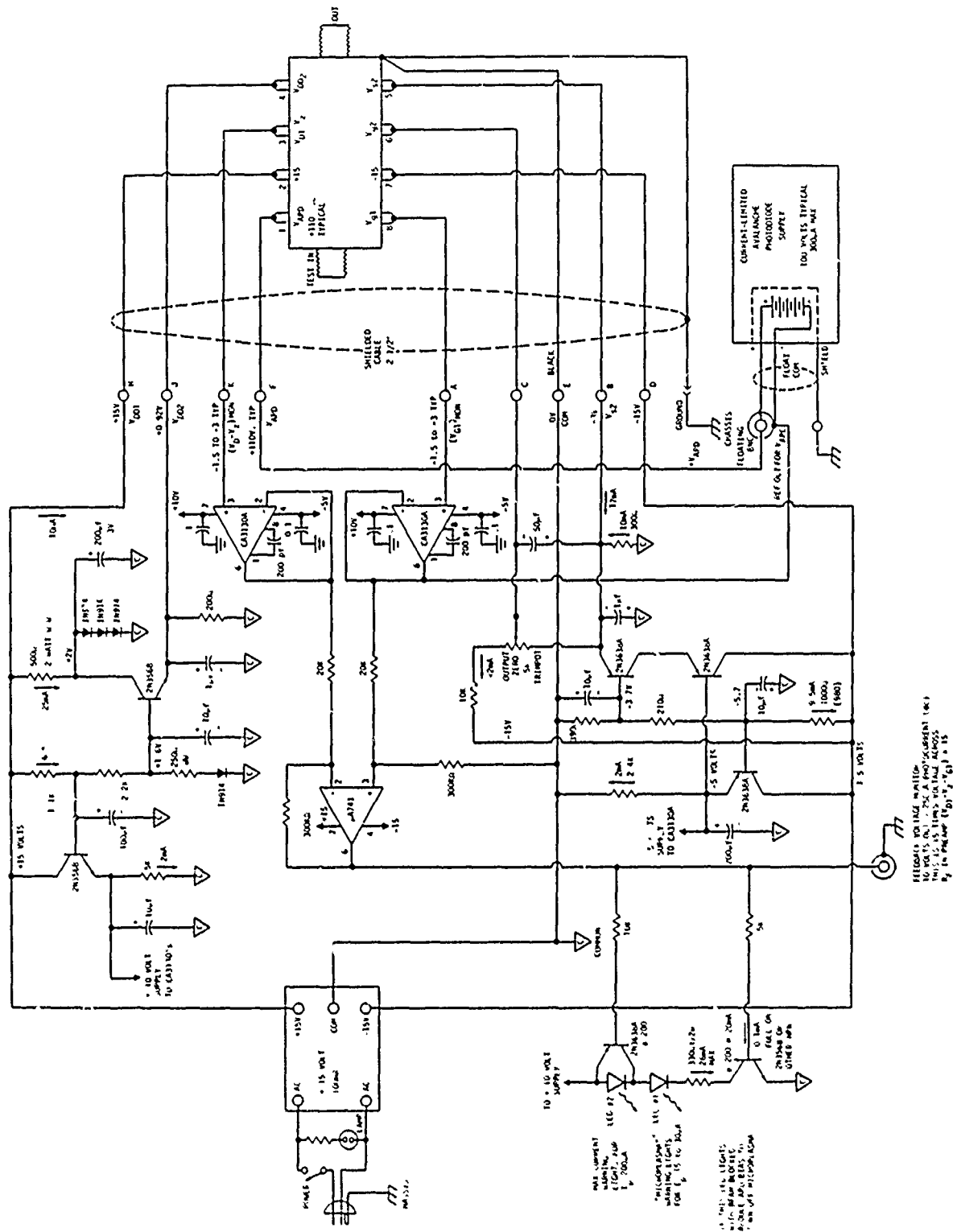
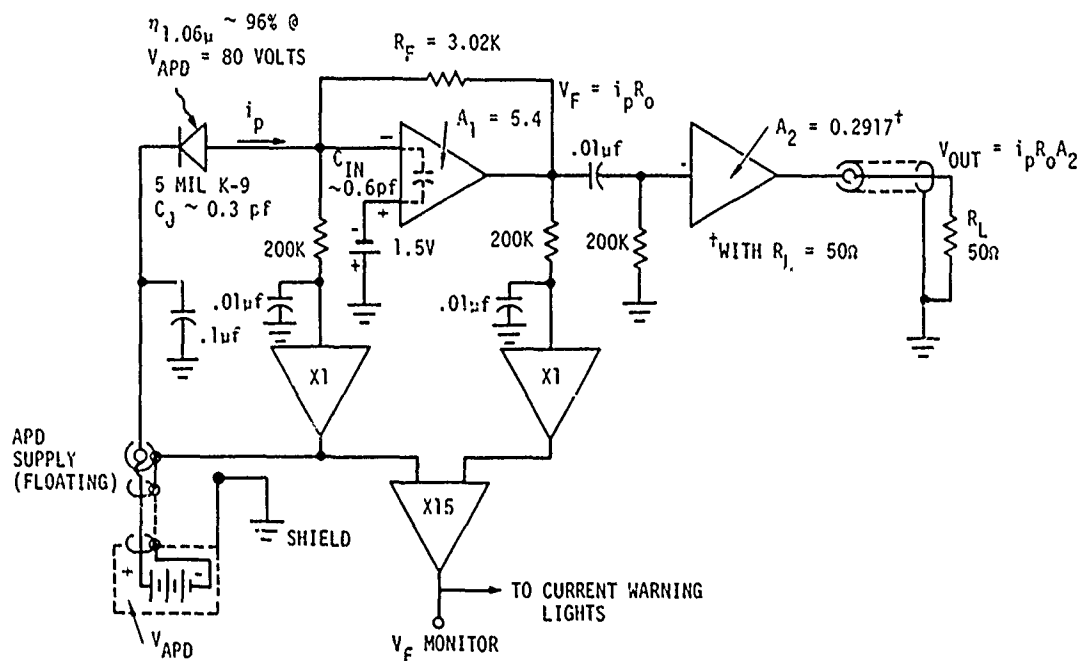


Fig. 4.10 Circuit diagram for the power supply-monitor unit for the Mari 1A GAASFET preamps (#4 and #5). Note that power supply units are not interchangeable between preamps.

SC571.16TRF

GAASFET PREAMP #5 MARK 1A



GaAsSb APD:

DIAMETER: 5 MILS

$C_J \approx 0.3$ pf

$\eta_{1.06\mu} \approx 96\%$ ($V_{APD} \geq 80V$)

$V_B = 116.5V$

PEAK GAIN $M_{MAX} \approx 8$

PREAMP PARAMETERS:

$C_{IN} \approx 0.6$ pf

OPEN-LOOP GAIN $A_1 = 5.4$

($f_{3db} = 32.5$ MHz)

OPEN-LOOP GAIN-BW ~ 1.2 GHz

$A_2 = 0.2917$ INTO 50Ω LOAD

$R_F = 3.02K\Omega$

$R_o \approx \frac{R_F}{1 + (1/A_1)} = 2548\Omega$

RECEIVER PERFORMANCE:

CLOSED-LOOP B.W. $f_{3db} \sim 410$ MHz

PULSE RESPONSE $\tau_{WTM} < 1.7$ ns

THROUGH CASCADED B&H PREAMPS: ($A = 77.2$)

$(V/Q)_\delta = 5.6 \times 10^{13}$ V/COUL

$v_{no} = 6.912$ mV (WITHOUT HI-PASS FILTER)

$N_o = 770$ ELECTRONS w/o FILTER, 3 GHz BW

$N_o = 592$ ELECTRONS w/o FILTER, 714 MHz BW
(PERHAPS 550 WITH 1/f NOISE REMOVED)

Fig. 4.11 Block diagram of the Mark 1A preamps, with specific values and performance parameters for GAASFET preamps #5.

provided by a zener diode chip, V_z in Fig. 4.9, shunted by a bypass capacitor, with the $\sim 0.7\text{mA}$ bias current for the zener obtained through R_{sh} . With $R_L = 1\text{K}\Omega$, $R_{sh} = 20\text{K}\Omega$ and the GAASFET drain resistance $R_D \cong 850\Omega$, we have from Eq. 2.39, $A_1 = g_m (450\Omega) = 5.4$ as the open-loop gain of the op-amps. (Actually, A_1 is measured experimentally by measuring the "op-amp" gain from a 50Ω source, and the value of drain resistance, R_D , is inferred from A_1 .) The open-loop gain in preamp #5 is 3db down at 320 MHz, with a gain-bandwidth product for higher frequencies of about 1.2 GHz. The gain-bandwidth product for a capacitively-loaded current generator with transconductance g_m and capacitance C_L is

$$\text{GBW} = (A/F) = \frac{g_m}{2\pi C_L} . \quad 4.1$$

Hence, for GAASFET preamp #5 we have $C_L \cong 1.6 \text{ pf}$ for the first stage capacitive loading ($C_L + C_D$ in Fig. 2.10 a)). This rather sizeable load capacitance represents a significant high-frequency performance limitation in the Mark IA preamp (largely overcome in the Mark III design). (The open-loop gain for Mark IA preamp #4 was 5.3 with a 3db frequency of 260 MHz and a gain-bandwidth product of about 1.35 GHz.)

Another performance limitation in the experimental Mark IA preamps is the relatively high input capacitance of the 2μ gate GAASFET's used for Q_1 . (The manufacturer's figure for C_{gs} in Fig. 2.10 for the FMX950 is 0.4pf.) The total input capacitance for GAASFET preamp #5 was 0.5-0.6 pf (plus 0.3pf APD capacitance). If Q_1 in the Mark IA preamps were a 1μ gate (dual gate) GAASFET, C_{IN} would be significantly reduced and the gain-bandwidth product would be improved because of the higher g_m of these devices, so that better performance could be attained than was achieved with the experimental Mark IA preamps (#4 and #5).

While the interstage coupling between Q_1 and Q_2 is through a .01 μf blocking capacitor, the output stage, Q_2 is actually directly coupled to the 50Ω output line, with the dc balance adjusted by a trimpot

in the power-supply monitor. The output stage has its own internal termination, R_{L2} , selected so that the parallel combination of R_{L2} and R_{D2} (the Q_2 drain resistance) is exactly 50 ohms. This means that the output line is almost perfectly terminated so that signal reflections from following amplifiers (most commercial 50 Ω preamps have poor input VSWR's or bad reflection coefficients) will be totally absorbed in this termination and will not cause intersymbol interference. Time-domain reflectometry measurements on preamps #4 and #5 give reflection coefficients of +3% and -3% respectively for pulsewidths of the order of the signal pulsewidth or greater. (Output TDR's for GAASFET preamps #6 and #8 are shown in Figs. 4.40 and 4.28.) The gain of the output stage will be essentially $A_2 = g_{m2} (25\Omega)$, assuming the output is 50 Ω terminated, or about twice this open circuit. For the two experimental Mark IA preamps, we measured $A_2 = 0.34$ for #4 and $A_2 = 0.292$ for #5. The output stage bandwidth, including the interstage coupling capacitor is about 10^2 to 10^{10} Hz. It would be relatively easy to extend this response to dc by re-injecting the dc photocurrent signal through the 200K Ω Q_2 gate resistor, but this was not done in the experimental preamps as dc response was not desired.

While the dc photoresponse is not carried to the 50 Ω signal output, the first "op-amp" stage is dc coupled and the dc photocurrent is taken out through the power supply-monitor unit. As shown in Fig. 4.11, the actual dc voltage across R_F is monitored through the 200K Ω isolation resistors in Fig. 4.11 or 4.9 with MOSFET op-amps connected as voltage followers (Fig. 4.10). A differential amplifier with a gain of 15 amplifies this voltage drop across R_F and presents the result at the " V_F monitor" jack on the power supply monitor. This signal is also used to drive a pair of warning lights in Fig. 4.10. The first light turns on at a dc current of about 25 μ A which would indicate that the APD bias was so high as to cause microplasma breakdown in the APD if this light is on with no light signal input. The second warning light turns on at a dc photocurrent of 250 μ A and means that the APD power dissipation limit is being approached (assuming V_{APD} near breakdown) and either the light level

or the APD bias, V_{APD} , should be reduced immediately.

The MOSFET follower connected to the gate of Q_1 also serves to establish the floating potential for the APD supply. If the APD supply were grounded, the actual bias voltage on the APD would be the APD supply potential plus the magnitude of the negative bias on the Q_1 gate. By floating the APD supply, the value of V_{APD} is exactly that read on the digital voltmeter in the APD supply (Fig. 3.18), and is unchanged by drifts in V_{g1} .

4.2.1.2 Performance Results for GAASFET Preamp #5

The key performance parameter for a preamp for optical pulse detection is the minimum detectable current pulse, N_0 (the number of electrons in a charge impulse required to make the peak output voltage equal the rms noise output). This is determined experimentally from current impulse response and noise measurements as described in Sections 3.3.10, 3.3.11, and 3.3.8. Fig. 4.12 shows the current impulse response obtained with GAASFET preamp #5 (trace with zero three divisions below center, 10mV/cm vertical, 1ns/cm horizontal. This response was measured using the S-52 pulse generator (246mV step, $T_R \sim 25ps$) through a cover plate coupling capacitor, C_C to the preamp input, with the preamp output amplified through a B&H DC3002 50 Ω 3 GHz preamp followed by a 3db pad followed by a B&H AC 3020 50 Ω 3 GHz preamp with its output driving the S-6 sampler head. The overall gain from GAASFET preamp output to S-6 input for this amplifier chain (hereafter described simply as "cascaded B&H's") is 77.2. The current impulse response was measured at a bias of $V_{APD} = 80$ volts, but the response is virtually constant for APD biases above 50 volts or so (since C_{APD} is constant). The peak output measured under these test conditions was $V_p = 73.01mV$.

Also shown in Fig. 4.12 is the integral of this current impulse (which is also the step response), shown in the lighter curve with zero 4 divisions below center (bottom of picture). The ordinate on this trace is 10pVs/cm, again at 1ns/cm. The 10% to 90% risetime of this step is

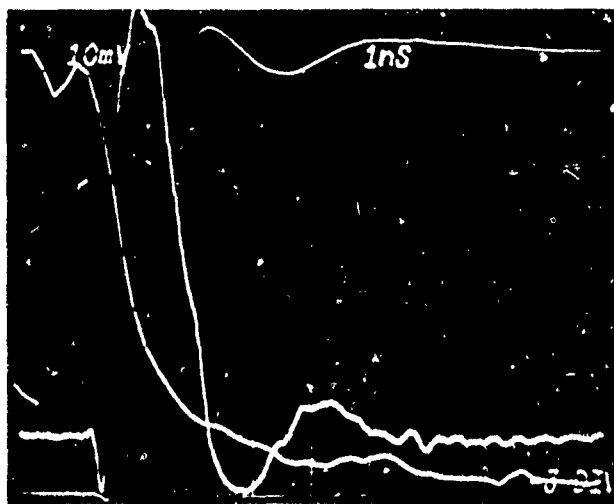


Fig. 4.12 Current Impulse Response for Mark IA GAASFET Preamp #5 for a current impulse input of $N_e = 8154$ electrons (output through cascaded B&H 50Ω preamps). Current impulse response displayed at 10 mV/cm (zero 3 div below center), 1nS/cm. Also shown are the integral response, displayed at 10 pVs/cm (zero at bottom), and the frequency response obtained from the FFT of the current impulse response, displayed at 500 μ V/cm vertical (zero at bottom) and 256 MHz/cm horizontal ($f = 0$ at left edge).

0.956ns, while the step height is $\int V_{OUT}(t) dt = 7.496 \times 10^{-11}$ Vs. From Eq. 2.35 we have $R_o = R_F / (1 + 1/A_1) = 2548\Omega$ (for $R_F = 3.02K\Omega$ and $A_1 = 5.4$), so that from Eq. 3.18 we can obtain the magnitude of the charge in the input pulse as $Q_p = 1.306 \times 10^{-15}$ coulombs or $N_e = 8154$ electrons (using $A_2 = 0.2917$, $A_{B\&H} = 77.2$). From this we obtain $(V/Q)_\delta = 5.59 \times 10^{13}$ volts/coulomb as the pulse gain for GAASFET preamp #5. The total noise output for this preamp with the same cascaded B&H 50 Ω post-amplifiers was measured with the S-6 sampler by the histogram method and found to be Gaussian with an rms value of 6.912 mV measured in a <2KHz to ~ 3 GHz bandwidth. The N_o value obtained from this measurement is (Eq. 3.22) $N_o = 770$ electrons for this non-optimum measurement bandwidth.

Also shown in Fig. 4.12 is the preamp frequency response, as obtained from the Fourier transform of the current impulse response. The FFT trace in Fig. 4.12 is the "dashed line" with zero at -4 divisions below center, displayed at a vertical scale factor of 500 μ V/cm and a horizontal scale factor of 256 MHz/cm with $f = 0$ at the left side of the picture (each dash is a frequency interval of 50 MHz). Note that the frequency response is quite flat out to 300 MHz, with the magnitude of the transimpedance (V_{OUT}/i_p) 3db down at $f_{3db} = 402$ MHz. The "noise bandwidth" calculated for this curve is $f_N = 412$ MHz (Appendix A.8).

The spectral dependence of the output noise for GAASFET preamp #5 is shown in three frequency ranges in Fig. 4.13. These curves were measured with the same cascaded B&H preamp arrangement discussed previously, but with the Tektronix 7L13 used in place of the S-6 sampler. The scale readouts here may require some explanation. For example, in Fig. 4.13 b), the "10db/" at the lower left means the display is log with 10 db per major-vertical division, while the "-30 dBm" at the upper left means that the top of the scale (+4 div above center) is exactly calibrated for a -30 dbm sine wave. Note that as discussed in Section 3.3.9 it is necessary to add 2.40 db to the indicated dbm values for absolute Gaussian noise values. The "10 MHz" at the lower right means that the horizontal frequency scale is 10 MHz/cm, while the "0050 MHz" at the top center means

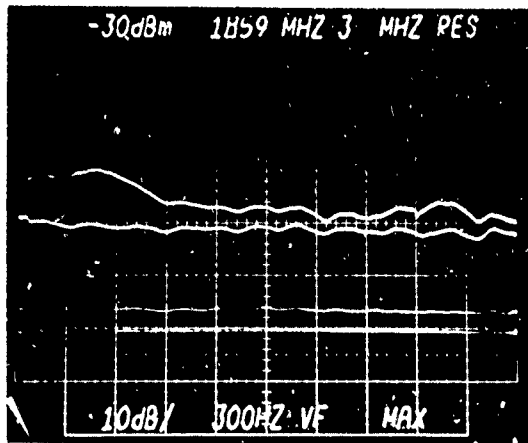
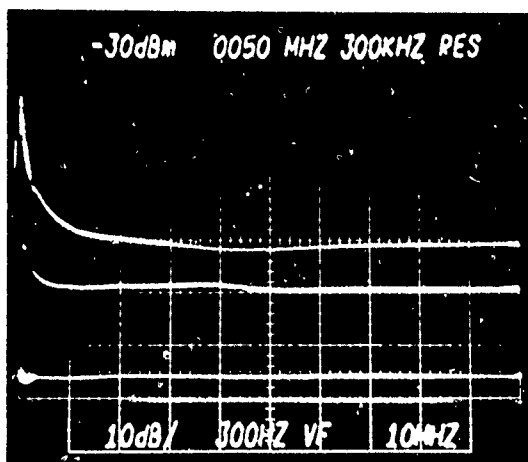
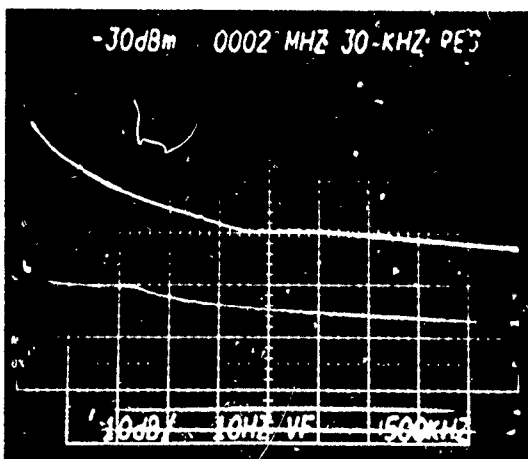


Fig. 4.13 Noise output spectra from GAASFET Preamp #5 through cascaded B&H's.

- a) 0 to 1820 MHz Frequency Range (182 MHz/cm). The thermal noise for $R_F=3K\Omega$ would be -62.64dBm.



- b) 0 to 100 MHz Frequency Range (10 MHz/cm). The thermal noise for $R_F=3K\Omega$ would be -72.4dBm.



- c) 0 to 5 MHz Frequency Range (500 KHz/cm). The thermal noise for $R_F=3K\Omega$ would be -81.3dBm.

the scale center is at a frequency of 50 MHz. For all spectra reported here, the 7L13 is accurately adjusted to put $f = 0$ exactly at the far left division marker. The "300 KHz RES" at the upper right is the nominal resolution setting, from which the exact noise bandwidth, ΔF can be obtained from Table 3.1. The "300 HZ VF" at bottom center simply describes the amount of time filtering used to provide good noise averaging and is not related to the noise bandwidth for the noise measurement.

The four noise traces in each of the noise spectra in Fig. 4.13 simply indicate the noise contribution from each amplifier stage. For example, in 4.13 a), the lowest curve (-90.6 dBm) is the noise level of the 7L13 itself, while the next higher curve (-86.5 dBm) is the noise level when the B&H AC 3020 is connected to the 7L13 input (with input terminated). The next higher curve (-71 dBm) is obtained with the B&H DC 3002 with terminated input driving the AC 3020 (through the 3dB pad used to reduce cable reflections), while the uppermost curve was obtained when GAASFET preamp #5 was connected to the input of the B&H DC 3002 ($V_{APD} = 80$ volts, no light signal input). While it may appear from the log display in Fig. 4.13 a) that most of the noise comes from the B&H 50 Ω amplifiers and only a little from our GAASFET preamp, this is not the case. For example, at 200 MHz the noise output with the GAASFET preamp is 10dB above the B&H noise level! This means that 90% of the measured noise power in the upper curve is from the GAASFET preamp and only 10% from the B&H's, or in other words, the measured noise voltage is only 5% higher than if there were no B&H noise at all. (If the noises differ by 15dB the voltage error is only 1.6% and for 20dB it is only 0.5%.)

We note in Fig. 4.13 a) that the noise over most of the receiver passband is only slightly above the calculated Johnson noise from the 3K Ω feedback resistance except for the high-frequency noise "bump" from 200 to 400 MHz (this is a reflection of the e_1 voltage noise term in Eq. 2.33) and the "1/f" noise below 25 MHz. We should note that at frequencies above 600 MHz the noise is due mainly to the Q_2 output stage

and the B&H preamps and we would anticipate that lower N_0 performance could be achieved by limiting the bandwidth to eliminate much of this noise. The "1/f" noise, noticeable below 20 to 30 MHz in Fig. 4.13 b) and dominating the preamp noise in Fig. 4.13 c), provides a significant contribution to the overall output noise. This noise is caused by e_1 in Fig. 2.8 becoming very large at low frequencies (see Fig. 4.38) presumably because of noise-generating trapping states in the Q_1 GAASFET at either the gate metal-GaAs interface or the n GaAs-semi insulating GaAs interface. It is anticipated that technological improvements in these devices in the future will reduce this 1/f noise. However, for many applications the 1/f contribution can be reduced simply by limiting the low frequency measurement limit with a high-pass filter in the output. (V_Z also contributes some 1/f noise - See pp. 212 - 214.)

As mentioned above, the 3 GHz measurement bandwidth is, from Fig. 4.13 c), clearly too wide for optimum N_0 performance with preamp #5. For example, if we convolve the impulse response of Fig. 4.12 with a double-pole filter response with a time constant of 0.2 nS (corner frequency of 796 MHz or f_{3dB} of 510 MHz) we obtain less than a 14% reduction in peak height, but get rid of much of the unnecessary noise above 500 MHz in Fig. 4.13 a). For example, experimentally when we used cascaded HP 35002A preamps ($A \approx 100$, $f_{3dB} = 714$ MHz) instead of the B&H's, we obtained a lower N_0 for preamp #5 (even though the noise figure for the HP's is not as good as the B&H's). With the cascaded HP's, GAASFET preamp #5 gave $(V/Q)_\delta = 7.06 \times 10^{13}$ V/coul and $v_{no} = 6.707$ mV in the 40 KHz to 714 MHz bandwidth to give $N_0 = 590$ electrons. If lower bandwidth filtering were used with an appropriate high-pass filter for 1/f noise rejection, N_0 values under 550 electrons could probably be achieved with GAASFET preamp #5.

The noise equivalent power, NEP, at any given frequency may be calculated from the noise output spectrum of Fig. 4.13 and the preamp transimpedance (R_0 and its frequency dependence as given in 4.12) and associated gains. Over most of the preamp bandpass the noise output is

reasonably close to the Johnson noise level from the $3K\Omega$ feedback resistance. For example, at $f = 200$ MHz, the NEP obtained from Fig. 4.11 a) assuming $M = 1$, $\eta = 0.96$, $h\nu = 1.165\text{eV}$ (1.064μ) is (Eq. 4.2) $\text{NEP} = 4.2 \times 10^{-12} \text{ W}/\sqrt{\text{Hz}}$ whereas the theoretical NEP for $R_F = 3K\Omega$ is $2.82 \times 10^{-12} \text{ W}/\sqrt{\text{Hz}}$. While we can directly measure NEP values only at harmonics of our modelocked laser frequency (Section 3.3), we have obtained good agreement between the measured NEP values and those calculated from the noise spectrum.

The current impulse response shape in Fig. 4.12 is slightly oscillatory, which could lead to some intersymbol interference, particularly if the data rate were of the order of 600 Mb/s. At a data rate of 400 Mb/s this would not be significant since the ringing is at a null 2.5 ns beyond the peak. The maximum usable data rate for δ -function pulsed data would be about 800-900 Mb/s before the "peak to zero" fall time would begin to generate massive intersymbol interference. Most of the key performance parameters for this preamp are summarized in Fig. 4.11. The area photoresponse or quantum efficiency-gain product versus position for the APD in preamp #5 is shown in Fig. 4.8. The orientation of this picture is as seen looking at the light entrance window side of the preamp with the signal output connector and power supply monitor cable going to your left and the test input connector to your right (the conical light entrance hole toward the right of center), as in Fig. 1.1.

4.2.1.3 Performance Results for GAASFET Preamp #4

The Mark IA GAASFET preamp #4 is similar to #5 and most of the same comments apply. Fig. 4.14 shows the current impulse response for preamp #4 with $V_{APD} = 80$ volts measured through cascaded B&H's (20mV/cm vertical with zero 3 cm below center, 1ns/cm, zero at 4 cm below center, 1ns/cm horizontal), together with its integral (20 pVS/cm, zero at 4 cm below center, 1ns/cm) and FFT frequency response displayed at 250 μ V/cm vertical, 204.8 MHz/cm horizontal, with zero frequency at the left edge (vertical zero 4 cm below center). For GAASFET preamp #4, $R_F = 3K\Omega$ and $A_1 = 5.3$, giving $R_O = 2525\Omega$, and the measured output stage gain is

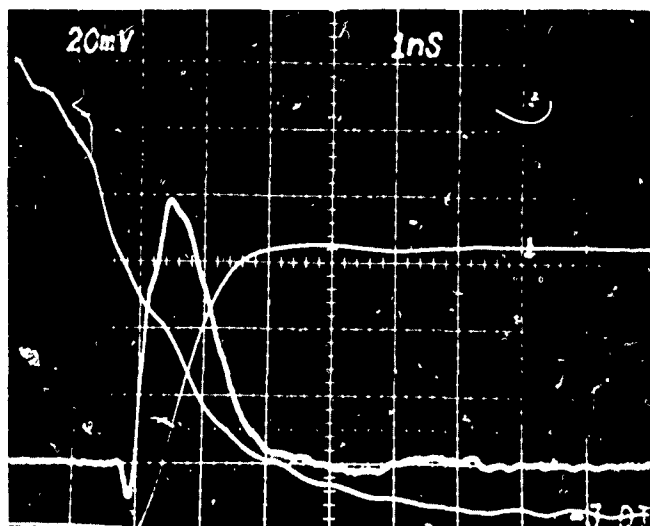


Fig. 4.14 Current Impulse Response for Mark IA GAASFET Preamp #4 Measured Through Cascaded B&H's. Input pulse was $N_e = 8005$ electrons. Current impulse response displayed at 20 mV/cm vertical (zero 3 div below center), 1nS/cm horizontal, with integral at 20 μ V/cm. Also shown is the FFT-derived frequency response, displayed at 250 μ V/cm vertical (zero at bottom), 204.8 MHz/cm horizontal (zero at left edge).

$A_2 = 0.34$ into a 50Ω load. From Fig. 4.14 we have $V_p = 78.82\text{mV}$ and $\int V_{\text{OUT}} dt = 8.501 \times 10^{-11} \text{ Vs}$, so the charge pulse magnitude was $Q_p = 1.28 \times 10^{-15} \text{ COUL}$ or $N_e = 8005$ electrons. The pulse gain, then, is $(V/Q)_\delta = 6.145 \times 10^{13} \text{ volts/coul}$. The measured rms noise output with the B&H preamps using a 375 KHz high-pass filter (blocking capacitor) for $1/f$ rejection was 7.822mV rms (Gaussian), so for this 375 KHz to 3 GHz measurement bandwidth we obtain $N_o = 795$ electrons. From the FFT we have (relative to the response at 60 MHz), $f_{3\text{db}} = 303 \text{ MHz}$ and $f_N = 357.3 \text{ MHz}$, considerably lower bandwidth than preamp #5. However, the shape of the current impulse response for #4 is nice, with only minimal overshoot, though it is slower, dropping from peak to $<5\%$ of peak in 1.55ns , which would make the receiver applicable for data rates up to about 650 Mb/s before the onset of major intersymbol interference.

The spectral density of the noise output measured for Mark IA GAASFET preamp #4 is shown in Fig. 4.15. As in preamp #5, the noise output over most of the preamp passband is quite close to the Johnson noise on the feedback resistance. The NEP is calculated from the noise voltage for $M=1$ by

$$\text{NEP} = \frac{h\nu V_n}{\eta R_o(f) A_2 A_{\text{B\&H}} \sqrt{\Delta F}} \quad (4.2)$$

where V_n is obtained from Fig. 4.15 using Eq. 3.13 and $R_o(f)$ is corrected from the baseband value of $R_o = 2525\Omega$ for #4 using the FFT frequency response in Fig. 4.14. For example, at $f = 100 \text{ MHz}$ we have the noise level from Fig. 4.15 a) is -59.3 dBm or from Eq. 3.13 using ΔF from Table 3.1, $V_n = 2.32 \times 10^{-7} \text{ volts}/\sqrt{\text{Hz}}$. Taking $h\nu = 1.165\text{eV}$, $\eta = 0.96$, $A_2 = 0.34$, $A_{\text{B\&H}} = 77.2$ and $R_o(100 \text{ MHz}) = 2248\Omega$ we have $\text{NEP} = 4.77 \times 10^{-12} \text{ W}/\sqrt{\text{Hz}}$, not quite as good as #5. The reason for the poorer noise performance of #4 stems both from its more limited bandwidth and from higher voltage noise, e_1 , in the Q_1 GAASFET. This is noticeable both in the $1/f$ noise, which is typically 10db higher in #4 below 10 MHz as compared to #5, and in the high-frequency noise "bump", which extends well above 600 MHz in #4

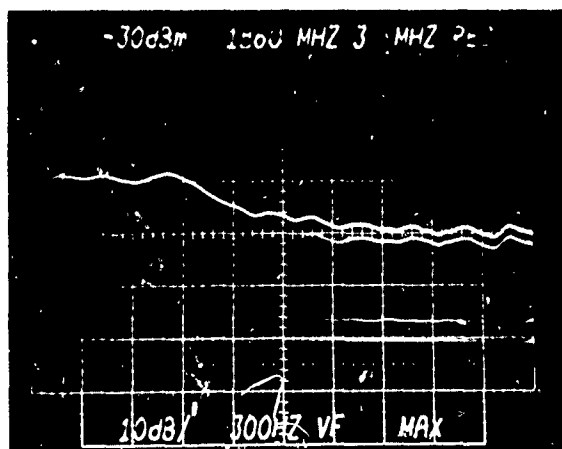
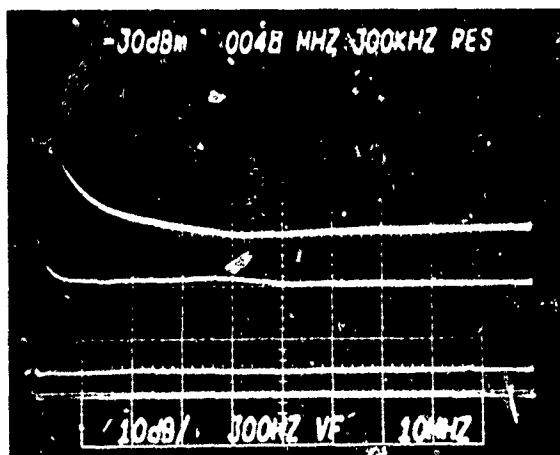
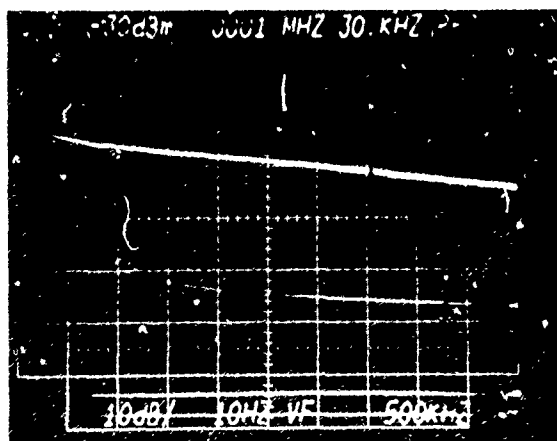


Fig. 4.15 Noise output spectra from GAASFET Preamp #4 through cascaded B&H's.

- a) 0 to 1820 MHz Frequency Range (182 MHz/cm). The thermal noise for $R_F=3K\Omega$ would be -61.34dBm.



- b) 0 to 100 MHz Frequency Range (10 MHz/cm). The thermal noise for $R_F=3K\Omega$ would be -71.1dBm.



- c) 0 to 5 mHz Frequency Range (500 KHz/cm). No high-pass filter used. The thermal noise for $R_F=3K\Omega$ would be -80.0dBm.

as compared to 400 MHz in #5, even though the bandwidth in #5 is larger. While some of this high-frequency noise could come from larger C_{IN} and C_F in #4, it is most likely that the FMX-950 GAASFET, Q_1 , in #4 is just unusually noisy.

As with preamp #5, reducing the measurement bandwidth for #4 gave improved N_o results. With preamp #4 followed by a B&H DC 3002, a blocking capacitor, a 3db pad and an HP 35002 preamp into the S-6 sampler for a 375 KHz to ~ 714 MHz measurement bandwidth, we obtained $(V/Q)_\delta = 5.38 \times 10^{13}$ and $V_{no} = 6.222$ mV rms for a value of minimum detectable current pulse of $N_o = 720$ electrons. Somewhat smaller bandwidths would be closer to optimum for this preamp so probably better N_o values could be obtained, but not as good as for #5 which would probably give N_o under 550 electrons with the $1/f$ noise filtered out. The spatial photoresponse (gain versus position) for the APD in preamp #4 is shown in Fig. 4.7, with the same preamp orientation as discussed for preamp #5.

4.2.2 Results for Mark II GAASFET Preamp

4.2.2.1 Circuit Description for GAASFET Preamp #7

The "Mark II" GAASFET preamp design represents an extension of the Mark IA approach directed toward obtaining nearly-optimum results in the laboratory 400 Mb/s 1.06 μ communications system bit error rate tests at McDonnell Douglas, St. Louis (carried out on these preamps by Dr. Samuel Green). It became clear in this testing that the "EMI" environment present in the test facility could cause sufficient pick up through cable grounds, power supplies, etc., to degrade the bit error rate performance of the Mark IA preamps. Hence extra internal gain in the hybrid integrated preamp would be desirable. Further effective wide-bandwidth, short sampling pulse data detection, as required for the optimum communication performance of these wideband integrated GAASFET preamps was not implemented in the McDonnell test facility, so that a preamp optimized for lower bandwidth would better match their

measurement system. The "Mark II" preamp design, shown in simplified form in Fig. 2.11, incorporates these changes, and further represents a more sophisticated approach in terms of carrying out much of the peripheral electronics handled in the power supply-controller in the Mark IA preamps right on the hybrid substrate. (For example, instead of the five power supply potentials required in the Mark IA preamps, the Mark II operates off of a standard ± 15 volt power supply.)

The circuit diagram for the Mark II GAASFET preamp #7 is shown in Fig. 4.16, with the power supply-monitor unit shown in Fig. 4.17. Fig. 4.18 shows a functional block diagram for the receiver, including key performance parameters. The Q_1 "op-amp" stage in Fig. 4.16 and 4.18 is essentially identical to that in the Mark IA receiver design. Q_1 is a 2μ gate, single gate GAASFET with $g_m = 13$ mmho and $R_D \cong 1K\Omega$ (the best value we have measured for a single-gate GAASFET), giving $A_1 = 6.4$. The gain bandwidth of this "op-amp" in #7 is about 50% higher than in the Mark IA preamps, achieved by careful redesign to minimize C_L . The feedback resistance is $R_F = 4K\Omega$ or $R_O = R_F/(1+1/A_1) = 3460\Omega$. The Q_2 gain stage is similarly designed, giving similar gain bandwidth product, only in this case an FMX-950 with similar g_m (0.0127 mho) but lower R_D (580 Ω) is used to give a lower gain ($A_2 = 4.6$) but wider bandwidth stage ($f_{3db} \cong 500$ MHz as opposed to ~ 375 MHz for the Q_1 stage). The second stage is, of course, operated open-loop, with bias stabilization provided through a low frequency silicon bipolar transistor differential amplifier hybrid integrated on the alumina substrate (indicated by $A = 160$ in Fig. 4.18). A 50 Ω microstrip line from an extra 3mm connector ("2nd stage test input-output") is tapped into the load resistance R_{L2} at point 50 Ω from ground. This test port may be used to inject test signals (such as a "pedestal" pulse for data sampling, etc.) to be summed with the photocurrent signal, or to tap off a signal from the Q_2 stage.

The Q_3 output line driver stage is again of similar design

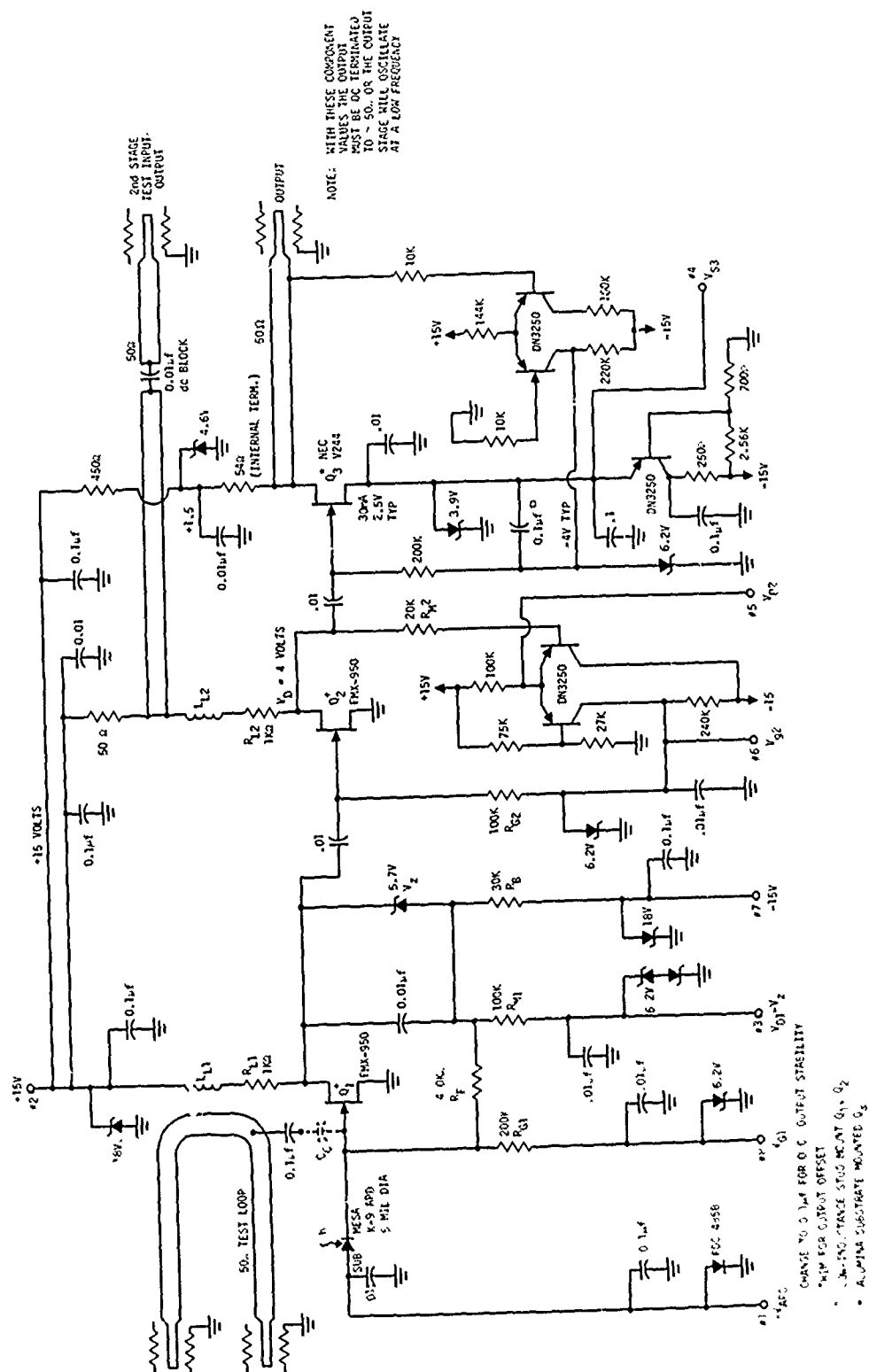


Fig. 4.16 Circuit diagram for Mark II GAASFET preamp #7.

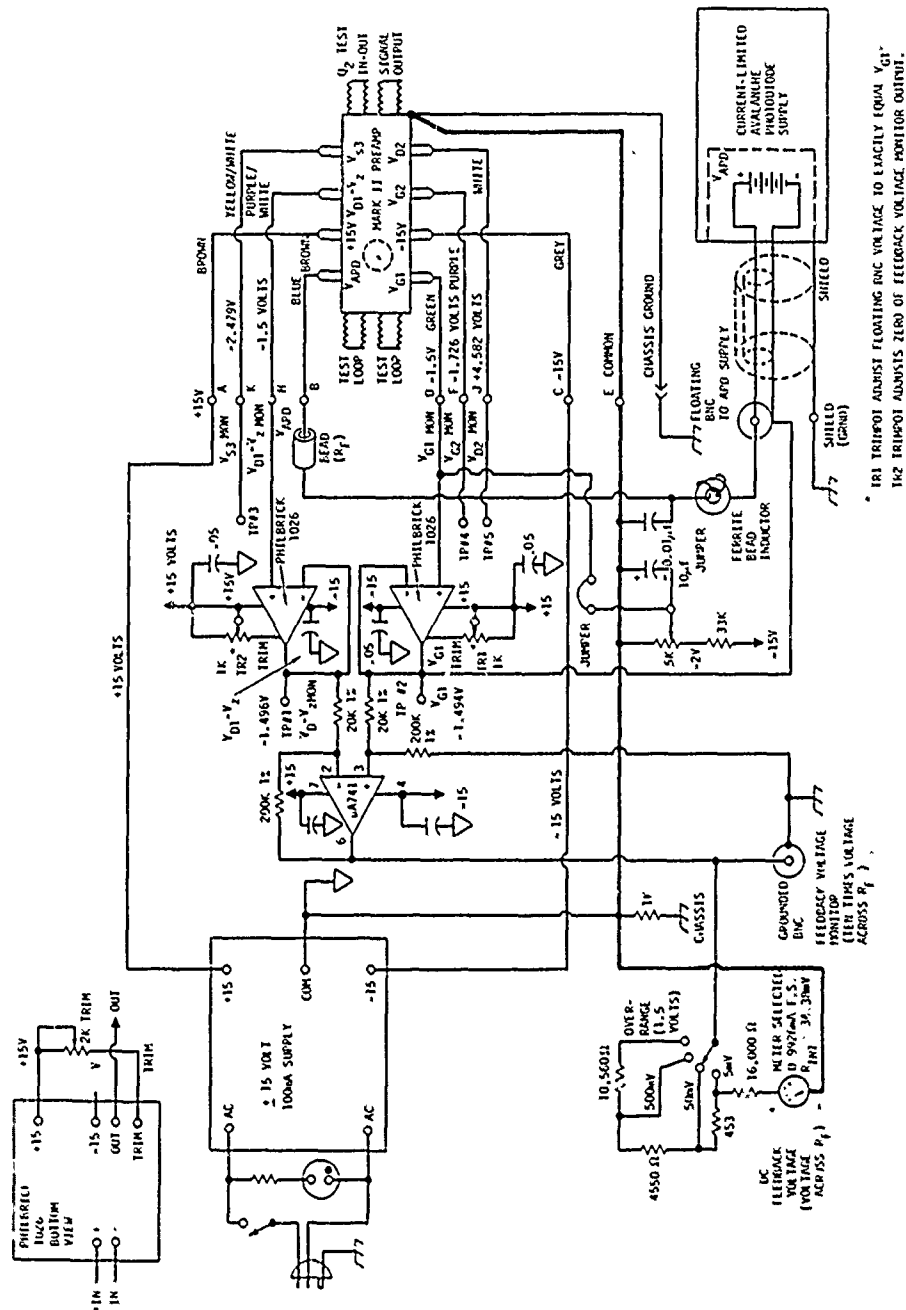


Fig. 4.17 Circuit diagram for the power supply-monitor unit for Mark II GAASFET preamp #7.

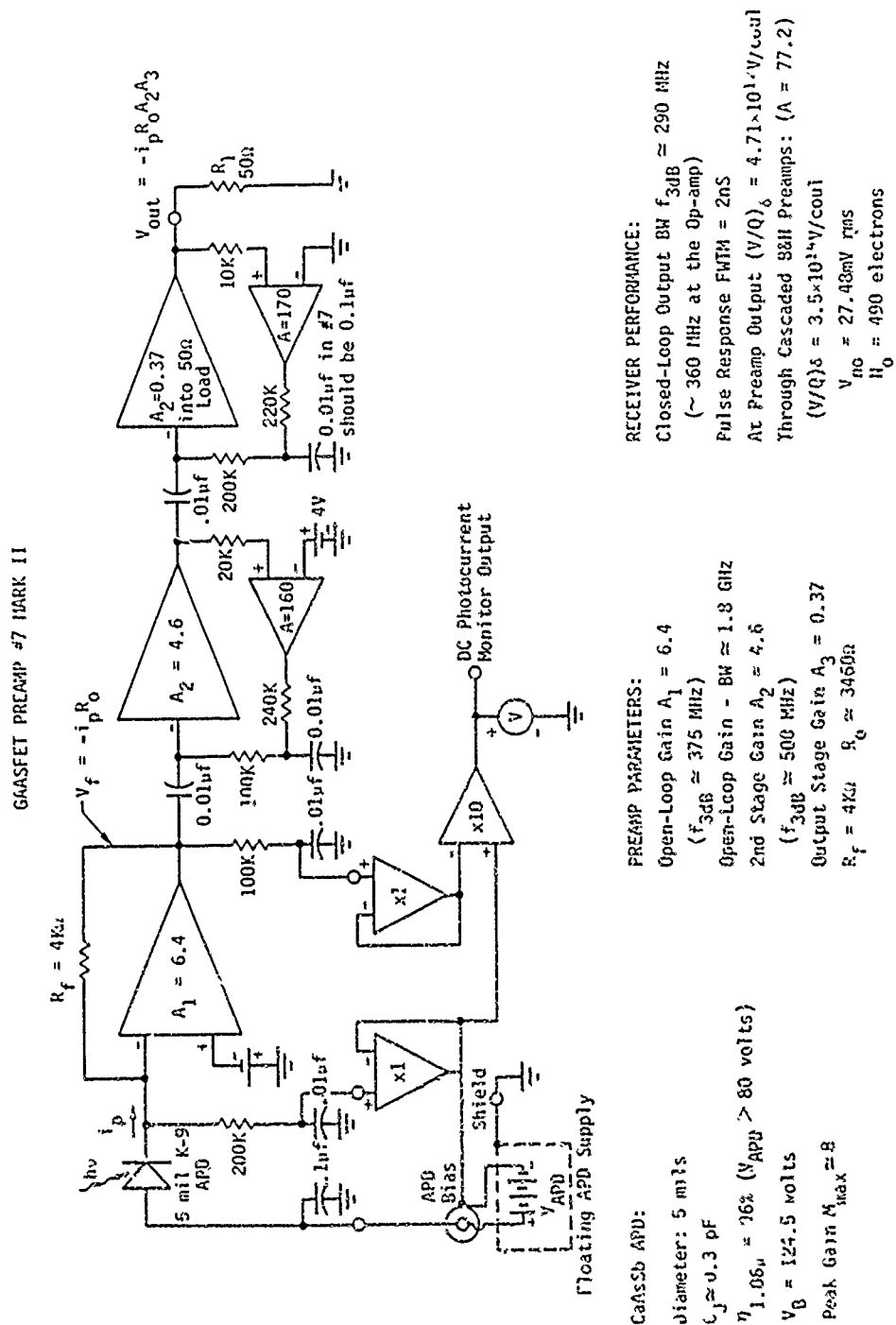


Fig. 4.18 Function block diagram for the Mark II GAASFET preamp design with specific values and performance parameters for preamp #7.

to the Mark IA receiver, giving the same very low VSWR output ($\rho = +2\%$). However, since this is now the 3rd stage in the receiver where noise is less important, Q_3 is operated at a drain current of 30mA, giving higher g_m so that $A_3 = g_{m3} (25\Omega) = 0.37$ and allowing larger output voltage swings (+.75 V to $-1V$ into $R_L = 50\Omega$). The dc output balance in preamp #7 is maintained by a differential amplifier similar to that used for the Q_2 stage. The preamp dc output is maintained at $0 \pm 2mV$ or less by this bias feedback amplifier. It should be noted, however, that in preamp #7, with the $0.01\mu f$ diff-amp output capacitor shown in Fig. 4.16 and 4.18, the output stage will gently oscillate at a low frequency if the output is not dc terminated with 50Ω (~ 100 ohms or less). If this capacitor is changed to $0.1\mu f$, the output stage should be open-circuit stable as well. The power supply-monitor unit for the Mark II preamp #7 is simpler than for the Mark IA's, since the power supply functions are done on the hybrid IC itself. A gain of 10 is used in the dc photocurrent monitor and, instead of warning lights, a meter is incorporated to directly read the voltage across the feedback resistor (with ranges corresponding to 5mV, 50mV, 500mV and 1.5 volts across R_F), where the dc photocurrent is this voltage divided by R_F , 4000Ω .

4.2.2.2 Performance Results for GAASFET Preamp #7

The current impulse response for $V_{APD} = 100$ volts for Mark II GAASFET preamp #7 is shown in Fig. 4.19. The test charge pulse for this figure was produced by applying a $V_{STEP} = 244.2$ mV (see Section 3.3.10) pulse from the S-52 pulse generator into the "50 Ω test loop" of the preamp with a 50 Ω termination on the other end of the loop. The charge impulse is produced by capacitive differentiation of the input step by the internal proximity capacitance from the test loop to the input, $C_c = 3.45 \times 10^{-14}$ f (as calibrated from Fig. 4.19). The preamp output in Fig. 4.19 is connected directly to the S-6 sampling oscilloscope head and the signal-averaged output is the (downward going) pulse with its zero 2 cm above center (10mV/cm vertical, 1ns/cm horizontal). The 5 GHz damped ringing on the front of the pulse has been smoothed out digitally in the upper

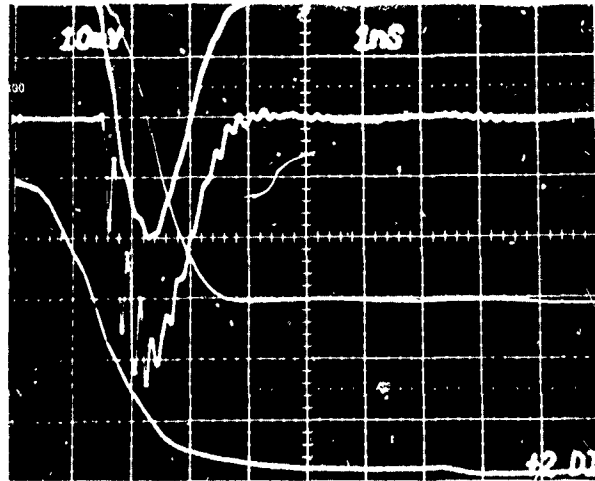


Fig. 4.19 Current Impulse Response for Mark II GAASFET Preamp #7 Measured With Output Directly into S-6 Sampler. Input pulse was $N_e = 53,000$ electrons. The current impulse response is displayed directly (zero at 2 div above center) and digitally smoothed (zero at top), both at 10 mV/cm, 1 nS/cm, with the integral response at 10 pV/cm. Also shown is the FFT-derived frequency response displayed at 500 μ V/cm vertical (zero at bottom), 256 MHz/cm horizontal (zero at left edge). Note that the bandwidth of the Q_2 internal gain stage is about 500 MHz.

curve (zero at 4 cm above center, 10mV/cm, 1ns/cm) to simulate the response which would be measured with any bandwidth-limiting preamp following the GAASFET receiver. Also shown in the lighter curve starting at 4 cm above center is the integral of the current impulse response (10 pVs/cm, 1ns/cm), with a step height of $\int V_{OUT} dt = -5.068 \times 10^{-11}$ Vs. Note that for the Mark II preamps, the output polarity is negative for a positive photocurrent pulse because of the extra inverting gain stage in the Mark II as compared to the Mark IA or Mark III designs. From Eq. 3.20 we have, using $R_0 = 3460\Omega$, $A_2 = 4.6$ and $A_3 = 0.375$, $Q_p = 8.5 \times 10^{-15}$ coul or $N_e = 53,000$ electrons. The peak height of the smoothed impulse response in Fig. 4.19 is $V_p = -40.02$ mV, so that we have $(V/Q)_\delta = 4.71 \times 10^{12}$ volts/coul at the preamp output (with any wideband amplifier following, it would be essentially this value times the amplifier gain). We have also measured this pulse gain with cascaded B&H preamps (3 GHz BW) following #7, giving $(V/Q)_\delta = 3.5 \times 10^{14}$ volts/coul, and with the B&H DC 3002 feeding an HP 35002 (~ 714 MHz BW) 50 Ω preamp, giving $(V/Q)_\delta = 4.4 \times 10^{14}$ volts/coul. The voltage noise outputs for these amplifier arrangements were $v_{no} = 27.48$ mV (Gaussian) for the cascaded B&H's (with 375 KHz hi-pass filter) and $v_{no} = 34.50$ mV for the B&H DC 3002-HP 35002A configuration (also with Hi-pass filter). The N_0 values for these two 50 Ω amplifier arrangements are $N_0 = 490$ electrons for the 375 KHz to 3 GHz bandwidth and $N_0 = 492$ electrons for the 375 KHz to ~ 714 MHz bandwidth. This insensitivity to the post-amplifier measurement bandwidth is reasonable, since the measurement bandwidth and noise level is in fact largely established by the internal gain stage (Q_2) with about a 500 MHz bandwidth.

Also shown in Fig. 4.19 is the FFT-derived frequency response (frequency dependence of transimpedance) of preamp #7 (dashed curve with zero 4 cm below center, 500 μ V/cm vertical, 256 MHz/cm horizontal with zero frequency at the left edge). (The display range of this FFT does not show the high frequency ringing peak at 5 GHz; it is about 1 GHz wide with an amplitude of about 350 μ V.) The 3dB bandwidth of the preamp is $F_{3dB} = 290$ MHz as measured at the preamp output ($f_N = 305$ MHz), but note that this includes the limitation

of the 2nd stage bandwidth. Assuming a 500 MHz bandwidth of Q_2 , the first stage "op-amp" probably has a closed loop bandwidth of about $f_{3db} = 360$ MHz, better than the Mark IA preamps even with a larger R_F (4K rather than 3K). This is due to the improved gain bandwidth product of the Mark II preamp. The output pulse shape in Fig. 4.19 is very nice, with critical damping and virtually no inter-symbol interference for its designed 400 Mb/s data rate. Its "peak to 5%" fall time is about 1.4ns, limiting the maximum data rate to about 700 Mb/s before the onset of massive intersymbol interference.

The output noise spectra for Mark II GAASFET Preamp #7 with $V_{APD} = 80$ volts are shown in Fig. 4.20. Figure 4.20 a) is the output with cascaded B&H preamps ($A_{B\&H} = 77.2$), while 4.20 b) and c) are with a single B&H DC 3002 preamp ($A = 9$). (Actually, Fig. 4.20 b) and c) were measured with $R_F = 5K\Omega$ and without an APD, but this will not change the noise in the 1/f region significantly.) We note in Fig. 4.20 a) that in the receiver passband, the receiver output noise is about 25 db above the B&H preamp noise, by virtue of the higher R_F and extra Q_2 gain between the "op-amp" and the output (A_2A_3 is +4.62 db in #7 as opposed to $A_2 = -10.7$ db in preamp #5, for example). The noise level of the Q_2 gain stage (measured by saturating Q_1 in the open-loop testing) would lie at about -57 dBm in the passband in Fig. 4.20 a) from about 180 to 360 MHz increasing gradually below 180 MHz to about -54.5 dBm at -45 MHz and peaking on the high frequency side at 450 MHz at -55 dBm before falling off. We can use Fig. 4.20 a) to calculate the NEP for receiver #7 by Eq. 4.2. At 200 MHz, we have a noise level of -44.8 dBm or $v_n = 1.23\mu V/\sqrt{Hz}$, so taking $h\nu = 1.165$ eV, $\eta = 0.96$, R_o (200 MHz) = 2.943Ω , $A_2 = 4.6$, $A_3 = 0.37$ and $A_{B\&H} = 77.2$, we have $NEP = 3.85 \times 10^{-12}$ watts/ \sqrt{Hz} . By a more accurate calibration method, that of using a dc light source to inject a measured photocurrent for which the shot noise can be calculated, a 100 MHz value of $NEP = 2.86 \times 10^{-12} W/\sqrt{Hz}$ was obtained in preamp #7 with $R_F = 4950\Omega$, which would scale to $3.2 \times 10^{-12} W/\sqrt{Hz}$ with $R_F = 4K\Omega$ (assuming i_{nj} limits NEP). These NEP figures are, of course,

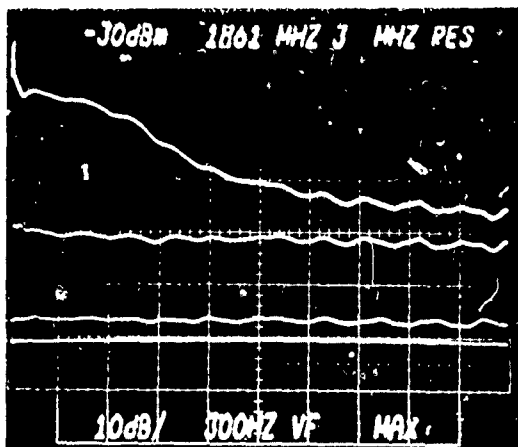
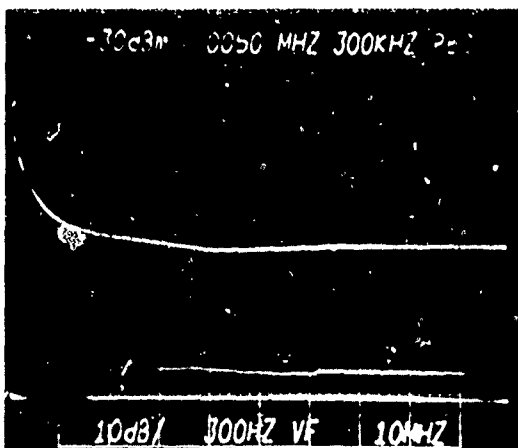
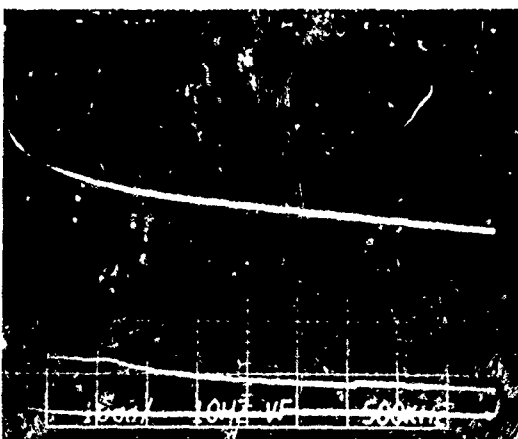


Fig. 4.20 Noise output spectra from Mark III GAASFER Preamp #7.

- a) 0 to 1820 MHz Frequency Range (182 MHz/cm). $V_{APD} = 80$ VOLTS, through cascaded B&H's. The thermal noise for $R_F = 4K\Omega$ would be -46.1dBm. The 2nd stage preamp noise level would be at about -57dBm in the pass-band.



- b) 0 to 100 MHz Frequency Range (10 MHz/cm) measured through B&H AC 3020 only (as in c). W/o APD, $R_F = 5K\Omega$. The thermal noise for $R_F = 5K\Omega$ would be -73.1 dBm.



- c) 0 to 5 MHz Frequency Range (500K Hz/cm). W/O APD, $R_F = 5K\Omega$. The thermal noise for $R_F = 5K\Omega$ would be -81.95dBm.

with no avalanche gain ($M = 1$) and would improve as M^{-1} in the preamp noise limited region.

The gain dependence of the NEP for GAASFET Preamp #7 can be seen from Fig. 4.21, which shows the 273 MHz signal and noise outputs of preamp 7 (as measured with the Tektronix 7L13 spectrum analyzer) with a 19.6 mW signal input from our modelocked Nd-YAG laser focused on the gain area at the lower right in Fig. 4.22 c). (This measurement technique was discussed in Section 3.3.5). The modelocked laser was "slow" (i.e., putting out wide pulses) during this measurement, but stable, so the pulsed shape was measured and the FFT taken with the DPO to give the fundamental (273 MHz) form factor $f = 0.785$ for this waveform. (When the laser is putting out short pulses, $f_1 \sim 0.95$ to 0.98 .) Using Eq. 3.3, we calculate the rms photocurrent as $I_1 = 18.68 \text{ nA}$ rms at 273 MHz. The NEP will be given by

$$\text{NEP} = \frac{h\nu I_1}{\sqrt{\Delta F}} \frac{V_{\text{no}} (\text{rms})}{V_{\text{SIG}} (\text{rms})} \quad (4.3)$$

where $h\nu = 1.165 \text{ eV}$ for $\lambda = 1.064 \mu$ and $\Delta F = 26.79 \text{ KHz}$ for the nominal "30 KHz" resolution setting (Table 3.1). The noise and signal levels at $V_{\text{APD}} = 80 \text{ volts}$ in Fig. 4.21 were accurately calibrated using an HP608C generator as an amplitude reference.

The calculated signal level for $\eta = 0.96$, $M = 1$ (at $V_{\text{APD}} \approx 80 \text{ volts}$) would be

$$V_{\text{SIG}} = \eta M I_1 R_o A_2 A_3 A_{\text{B\&H}} \quad (4.4)$$

or with $R_o (273 \text{ MHz}) = (0.72)(3460) = 2490 \Omega$, $A_2 = 4.6$, $A_3 = 0.37$ and $A_{\text{B\&H}} = 8.89$ at 273 MHz, we have $V_{\text{SIG}} = 0.669 \text{ mV} = -50.5 \text{ dBm}$, in excellent agreement with the measured -50.9 dBm output at $V_{\text{APD}} = 80 \text{ volts}$. We note

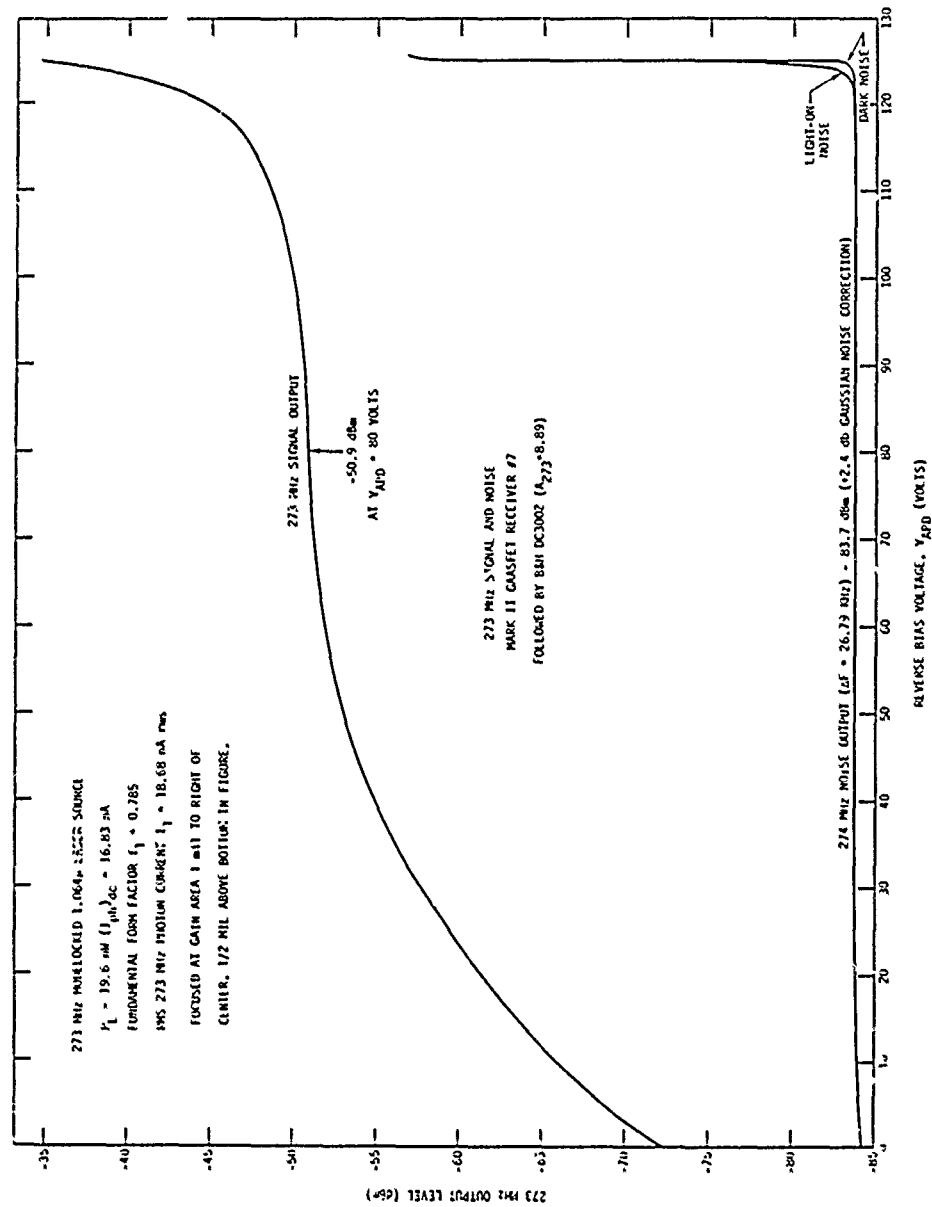


Fig. 4.21 Variation of 273 MHz Signal Output and Illuminated and Dark Noise Outputs for Mark II GAASFET Preamp #7 (b) with final delivered APD. Noise curves are measured by detuning spectrum analyzer off of modelocked laser frequency.

in Fig. 4.21 that while the gain increases with increasing V_{APD} above punchthrough, the preamp noise stays essentially constant to bias voltages very near breakdown (125V). In the dark (lower noise curve near V_B), the noise increases by only 0.6 dB from $V_{APD} = 80$ volts ($M = 1$) to $V_{APD} = 124.9$ volts ($M \approx 16.5$ db) because of the low multiplied dark current of the APD. With the light signal applied, the multiplied shot noise on the photocurrent increases the noise level up to several db near breakdown, so that the optimum signal to noise ratio occurs at a lower bias at higher signal levels. Another way of expressing this is that the NEP at optimum bias is a function of the dc light signal (or background light) level.

We can obtain the value of V_{no}/V_{SIG} required to calculate NEP directly as the vertical separation between the signal and noise curves, i.e.,

$$\frac{V_{no}}{V_{SIG}} = 10^{(V_n(\text{dBm}) + 2.4 - V_s(\text{dBm}))/20} \quad (4.5)$$

where the 2.4 db correction to the noise level is as discussed in Section 3.3.9 (Eq. 3.13). Hence for $V_{APD} = 80$ volts, we have $V_n = -83.7 + 2.4$ dBm and $V_s = -50.9$ dBm or from Eq. 4.3, $NEP = 4.0 \times 10^{-12} \text{ W}/\sqrt{\text{Hz}}$ at $f = 273$ MHz, $M = 1$. With this signal level applied (19.6 nW), the optimum bias for this spot on the device is $V_{APD} = 124.3$ volts, where $V_n = -81.0 + 2.4$ dBm and $V_s = -37$ dBm for $NEP = 1.1 \times 10^{-12} \text{ W}/\sqrt{\text{Hz}}$ (light on). On the other hand, for low signal levels (dark noise curve) we would have at $V_{APD} = 124.9$ volts, $V_n = -83.0 + 2.4$ dBm and $V_s = -34.7$ dBm for $NEP = 6.7 \times 10^{-13} \text{ W}/\sqrt{\text{Hz}}$ (low light level or dark). This illustrates how the NEP at optimum gain is a strong function of the light signal or background light level.

The spatial variation of the quantum efficiency and gain over the area of the 5 mil $\text{GaAs}_{1-x}\text{Sb}_x$ APD in preamp #7 is shown in Fig. 4.22 for biases of a) 20 volts (below punchthrough; displayed at high contrast

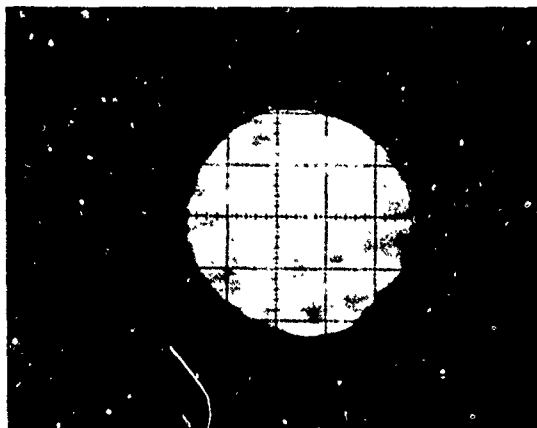
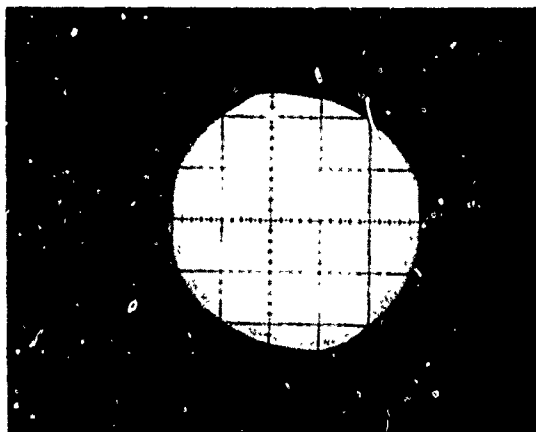
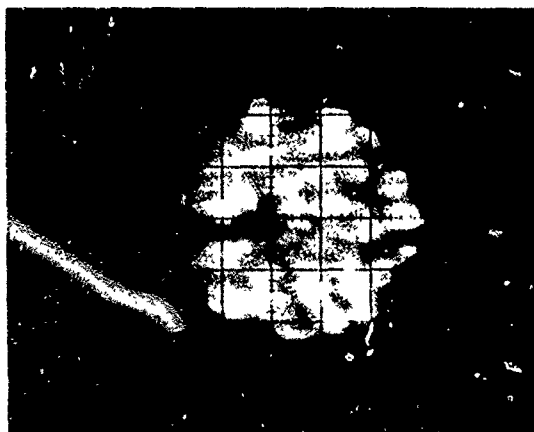


Fig. 4.22 Scanning light microscope pictures of the 273 MHz photoresponse of Mark II GAASFET Preamp #7. Scale is 1 mil/div.

a) $V_{APD} = 20$ volts
(high contrast display)



b) $V_{APD} = 110$ volts
Normal Contrast
Intensity Modulation



c) $V_{APD} = 124$ volts
Normal Contrast
Intensity Modulation

to show pattern effect), b) 110 volts showing the onset of noticeable variation of gain with position, and c) 124 volts with reduced gain to show the location of the high gain areas. The highest gain regions are the area noted in Fig. 4.21 and the area 1.5 mils to the left and just slightly above the APD center. The quantum efficiency of the APD above punchthrough shows virtually no spatial variation over the device until the onset of gain. Note in Fig. 4.17 the correlation of the crossings of the bright lines in a) with the high-gain points in c), as discussed in Section 4.1.7.

4.2.2.3 Performance of Mark II GAASFET Preamp #7 in a 400 Mb/s PGBM 1.064 μ Optical Communications System

Because the Mark II preamplifier design was specifically optimized for use with the 400 Mb/s PGBM communications test system at McDonnell Douglas Astronautics, St. Louis, it is particularly interesting to compare the results of their measurements on GAASFET preamp #7 with our calculated performance. The test results are measured in terms of the average light power level, P_L , required to achieve a given probability of error per bit (or bit error rate, BER). In the test 64 bit PN code used in the measurements there are 32 "1's" and 32 "0's" so that $P_L \sim 1/2 q h \nu R N_{ph}$ where R is the data rate (4×10^8) and N_{ph} is calculated from Eq. 2.20. Actually, the factor of 1/2 assumes that all "1's" are exactly the same height and all "0's" are exactly zero, which is not the case in the actual system. Figure 4.39 shows the 64 bit PN code data stream measured on the McDonnell system. As can be seen, there is both significant zero feedthrough (McDonnell estimates this at a worst-case extinction ratio of 30:1 when the modulator is properly adjusted), and sizeable variation in the transmitted pulse heights, presumably due to laser output fluctuations. (In Fig. 4.39 a), the peak-to-peak amplitude fluctuations for a transmitted "1" are $\sim 12\%$ of the mean). In the BER calculation for preamp noise limited operation (Section 2.1.3), the important signal quantity is the difference in amplitude between a "1" and a "0". When these amplitudes are not exactly fixed, we might take as a worst case treatment the difference between the lowest transmitted

"1" and the highest transmitted "0" as the signal difference, i.e.,

$$STN = \frac{(V_1)_{MIN} - (V_0)_{MAX}}{2 V_{no}} \quad (4.6)$$

as the worst case BER condition for Eq. 2.12. The average signal level, however, will be

$$P_L = \frac{q h \nu R}{2} (\bar{N}_{ph1} + \bar{N}_{ph0}) \quad (4.7)$$

In other words the average light power measured experimentally depends on the sum of the average pulse height on a one plus the average pulse height on a zero, whereas the worst case BER depends on the difference between the minimum pulse height on a one and the maximum pulse height on a zero. Using this worst case analysis assuming a worst case $(N_{ph1})_{MIN}/\bar{N}_{ph1}$ of 0.94 (from Fig. 4.39) and a worst case E.R. of 30:1 with an average E.R. of 40:1 we would have as a worst case required signal level $P_L = 0.565 q h \nu R \bar{N}_{ph}$ where \bar{N}_{ph} is calculated from Eq. 2.20 with $S=0$ (the S-factor is included in the 0.565). Clearly this worst case analysis is too severe as it would predict that if we made a bad fluctuation in the height of a single bit in the stream (as in transmitting a zero instead of a one for example), the BER would go to 1/2 whereas in fact it would go to 1/64 for a 64 bit code. In other words, a major amplitude reduction on a single bit increases the error probability only on that bit, not on all of the others. Hence we should adopt a slightly more liberal criterion for the pulse height deviation and modulator extinction ratio than the absolute worst cases assumed in 4.6. If we take, for example, an average 3.5% mean to minimum pulse height fluctuation (rather than the 6% worst case) and assume a 40:1 value for average extinction ratio, we get

SC571.16TRF

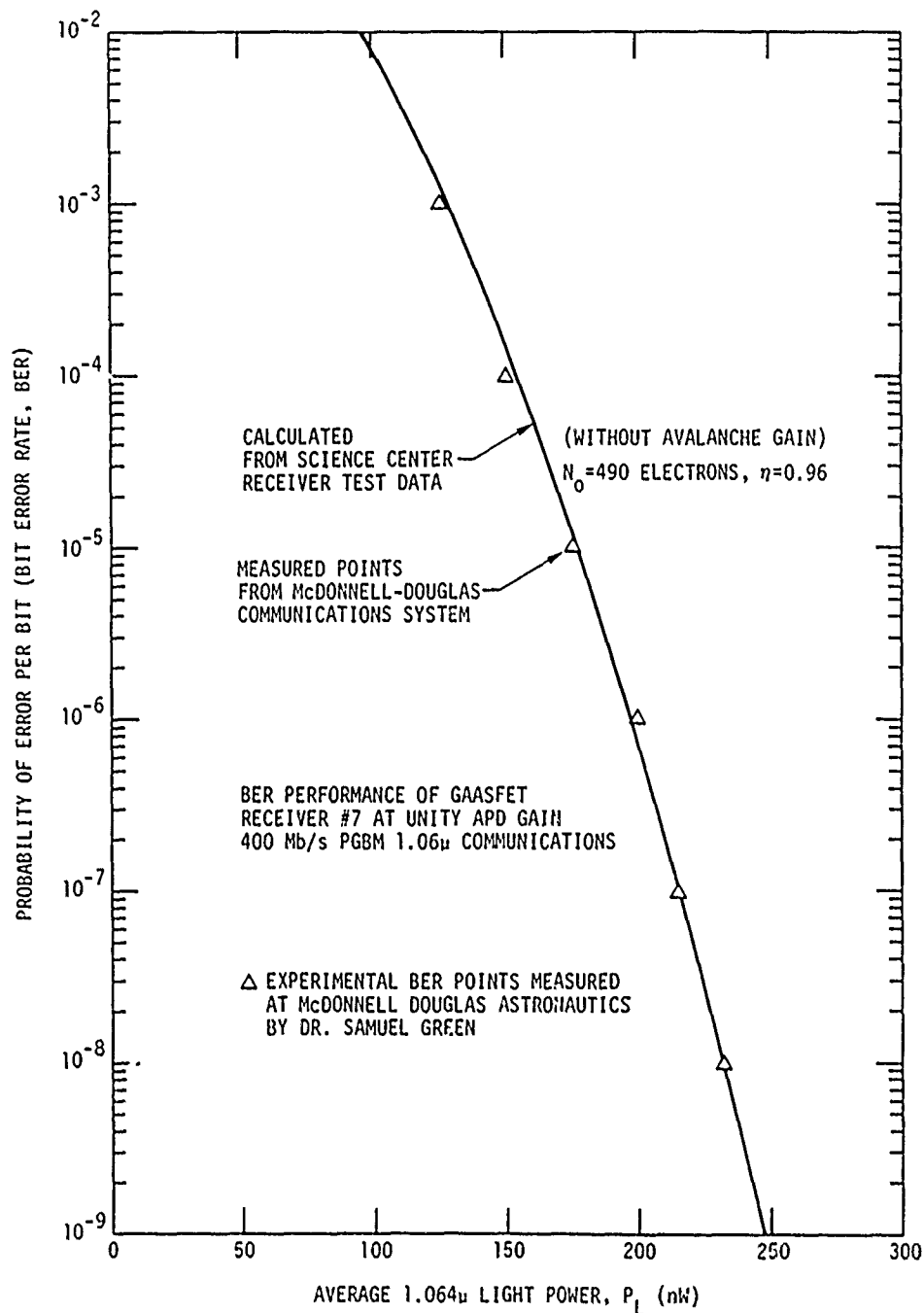


Fig. 4.23 Comparison of Calculated Average Power Required to Achieve a Given BER for GAASFET Preamp #7 (Mark II) With Experimental Points from McDonnell Douglas measurements.

$$P_L = 0.545 q h\nu R N_{ph} = 1.09 \frac{q h\nu R}{\eta M} N_0 \text{ (S.T.N.)} \quad (4.8)$$

for the average light power, where the value of S.T.N. is obtained from the BER from Table 2.1.

In Fig. 4.23 (solid line), Eq. 4.8 is plotted for the parameters measured for preamp #7; $q = 1.6022 \times 10^{-19}$, $h\nu = 1.165$ eV, $R = 4 \times 10^8$, $\eta = 0.96$, $M = 1$ at $V_{APD} = 80$ volts, and $N_0 = 490$ electrons. At $BER = 10^{-6}$, for example, $STN = 4.75342$ and we calculate $P_L = 197$ nW average 1.064μ light power. The results of the McDonnell measurements of BER versus P_L for preamp #7 at $V_{APD} = 80$ volts ($M = 1$) are shown as the data points in Fig. 4.23, and are seen to be in excellent agreement with our calculated curve. (For example, the P_L for a BER of 10^{-6} was measured to be 199 nW at $M = 1$, with proportionately lower values of P_L for avalanche gains greater than unity.) This close agreement is satisfying in that it validates both the theoretical detection model of Section 2.1 and our preamp model and measurement techniques. Further, it allows us to estimate with confidence the performance which can be obtained with such high-speed receivers as the Mark III designs which require fast sampling decision logic for optimum data detection (which was not available in the McDonnell test facility).

4.3 Performance Results for the Gigabit Mark III GAASFET Preamps

While the original Mark IA and Mark II GAASFET preamplifier designs perform well, as discussed in section 4.2, neither is fast enough to achieve the Air Force gigabit data rate requirements. The "Mark III" preamp design represents an extension of the original Mark IA design developed to obtain both gigabit signal bandwidths and (simultaneously) reduced minimum detectable current pulse values.

In order to improve bandwidths and reduce noise in the feedback-mode preamp, we must improve the "op-amp" to a) reduce the input capacitance, C_{IN} , b) increase the open loop gain, A_1 , (so that we can increase R_F to reduce

Johnson noise) and c) increase the gain-bandwidth product of the "op-amp". We can increase the open-loop gain and gain-bandwidth product by using a GAASFET as Q_1 which has a higher transconductance, g_m . We can further improve the open-loop gain by increasing the output drain resistance, R_D , of Q_1 by going to a dual-gate GAASFET (see section 2.3.5). Further, if we use a dual 1μ gate GAASFET instead of a 2μ gate device as used in the Mark IA and Mark II preamps, we can reduce C_{IN} . To improve the gain-bandwidth product over and beyond the g_m improvement, we must greatly reduce C_L , which we can accomplish by using a source follower directly on the drain of Q_1 . All of these changes are incorporated in the Mark III GAASFET preamp #8, and the results are excellent, both in terms of bandwidth and noise. These results are discussed in sections 4.3.1 and 4.3.2. In GAASFET preamp #6, however, the higher- g_m , dual 1μ gate GAASFET's used in #8 were not used, as they were not yet available at the time of delivery of the receiver. A commercially-available dual gate GAASFET with lower g_m and wider gates was used instead, so that the performance improvement over the Mark IA preamps is not very dramatic, though it did attain adequate bandwidth for gigabit data rate communication. The performance data for the Mark III GAASFET preamp #6 as originally delivered to the Air Force are presented in section 4.3.3, though this data is not of great interest, since this receiver is currently undergoing modification to replace Q_1 to bring it up to the specifications of GAASFET preamp #8 (sections 4.3.1 and 4.3.2).

4.3.1 Circuit Description for the Mark III Preamps

The simplified circuit diagram for the Mark III preamp design is shown in Fig. 2.12. The circuit diagram for GAASFET preamp #8 is shown in Fig. 4.24; preamp #6 is essentially identical except for Q_1 and the value of R_F . The circuit diagrams of the power supply-monitor units for these Mark III preamps are shown in Fig. 4.25. The block diagram of the receiver design is shown in Fig. 4.26 along with key performance data for GAASFET preamp #8 (#6, after modification, should be similar to this). The block

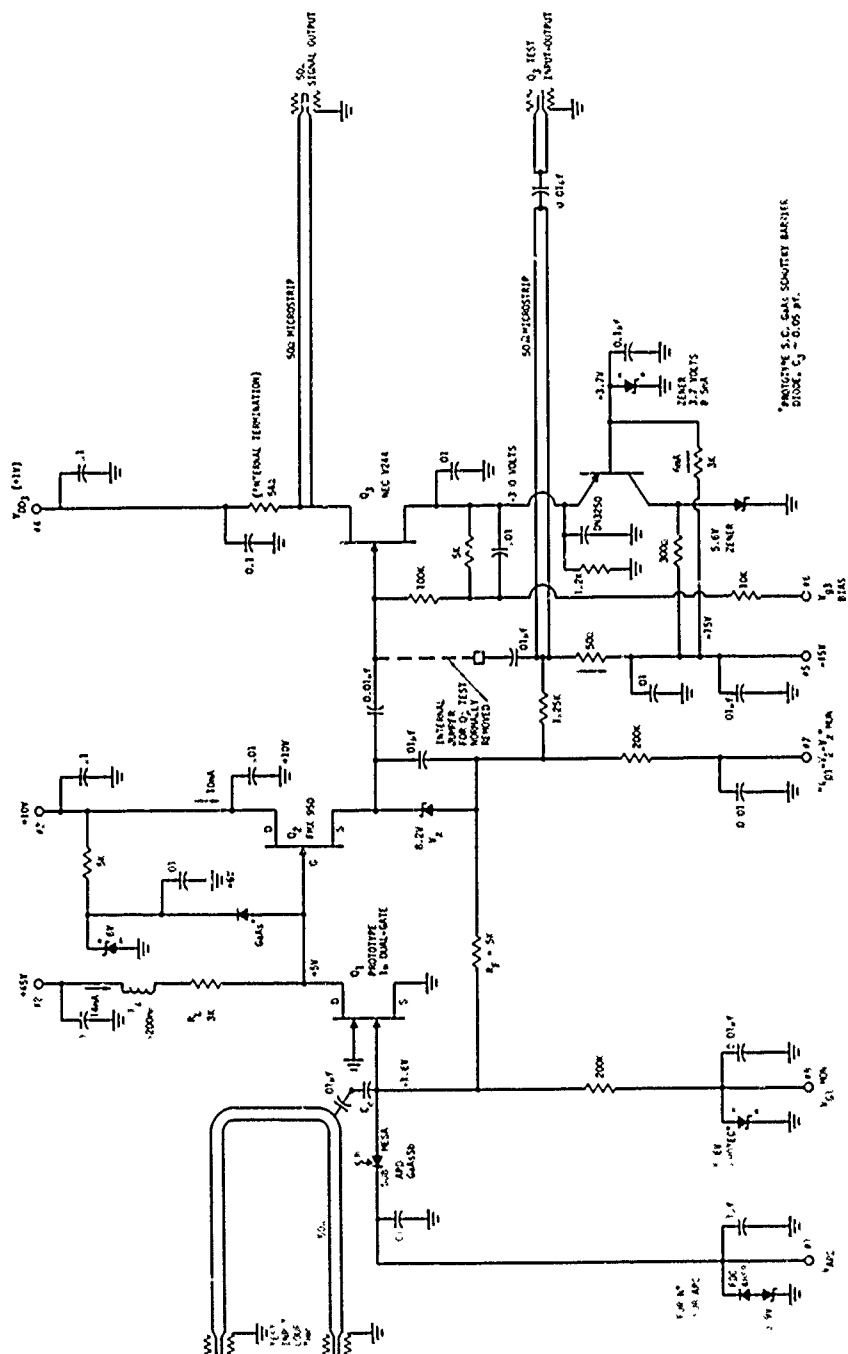


Fig. 4.24 Circuit diagram of the Mark III GAASFET preamp design with specific values for preamp #8.

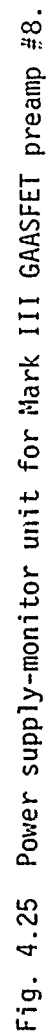


Fig. 4.25 Power supply-monitor unit for Mark III GAASFET preamp #8.

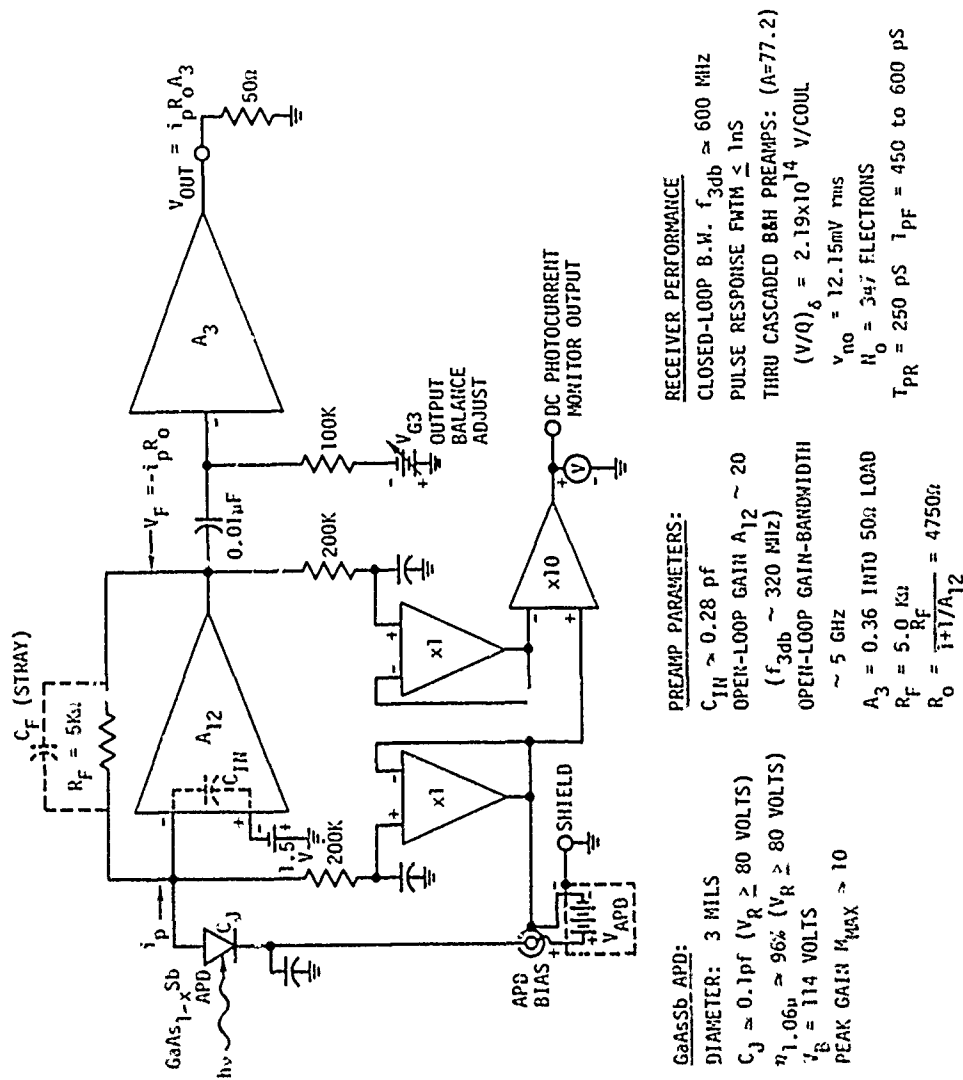


Fig. 4.26 Function block diagram for the Mark III preamp design, with specific values and performance parameters for GAASFET preamp #8.

diagram for the Mark III receiver is very similar to that of the Mark IA, only the specifications of the "op-amp" first stage are radically improved. The monitor portion of the power supply-monitor unit is identical to that of the Mark II, including the meter to read dc photocurrent, but the power supply portion is more complicated, since the Mark III requires several supply potentials. (Note that in the circuit diagram of Fig. 4.25, as in Fig. 4.10, small- $10\ \Omega$ or $100\ \Omega$ -resistors are used in the collector of each emitter follower to avoid high-frequency oscillations; these have been omitted from the drawing.)

The Q_3 output stage in the Mark III preamp, Fig. 4.24 is essentially the same as Q_2 in the Mark IA except that the -3 volt source voltage is derived internally from the -15 volt supply with the DN3250 PNP transistor chip, as in the Mark II. Unlike the Mark II, however, the output dc balance adjustment is made from the power supply-monitor unit rather than from an internal differential amplifier. Q_3 , a 1μ gate GAASFET, operates at a bias current of $I_D = 17\text{mA}$ with a transconductance of about 15 mmho (as shown in Fig. 4.27c). The actual Q_3 stage gain, A_3 , was measured by bonding (temporarily) the " Q_3 test input" line to the gate of Q_3 and measuring the pulse gain, $A_3 = 0.36$ into $R_L = 50\ \Omega$, with very wide bandwidth.

The output TDR for this Q_3 output stage of preamp #8 is shown in Fig. 4.28, along with the TDR trace when the preamp is replaced by a precision $50\ \Omega$ termination (upper curve-without ripples-to the right of center). The +5 cm step at $t = 2\text{ ns}$ in Fig. 4.28 is the original S-52 pulse going through the S-6 sampler to the output connector of preamp #8, while the small fluctuations at $t = 4.4\text{ ns}$ and $t = 4.9\text{ ns}$ represent reflections from the coax to microstrip connection and from the drain of Q_3 (with its bonding wires) respectively. The fact that the preamp #8 trace falls slightly below the $50\ \Omega$ reference trace for $t > 5\text{ ns}$ is a reflection of the fact that the parallel combination of R_{L3} ($54\ \Omega$) and R_{D3} is slightly less than $50\ \Omega$. We see that the peak reflection coefficients are -11% at 4.85 ns and +10% at 4.90 ns, but these are seen only by exceedingly short ($\sim 50\text{ ps}$) pulsewidths, much less than the preamp signal

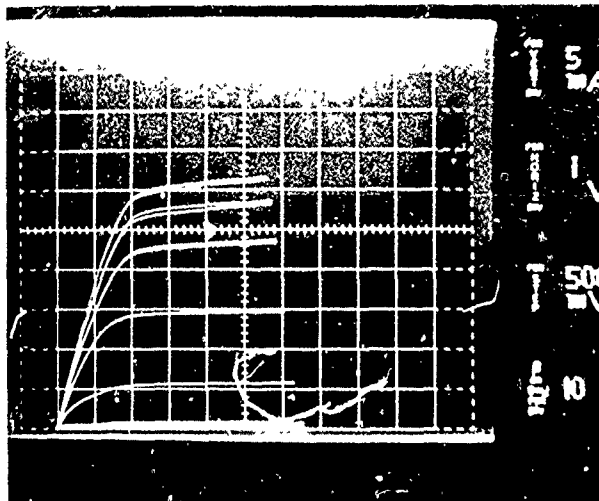
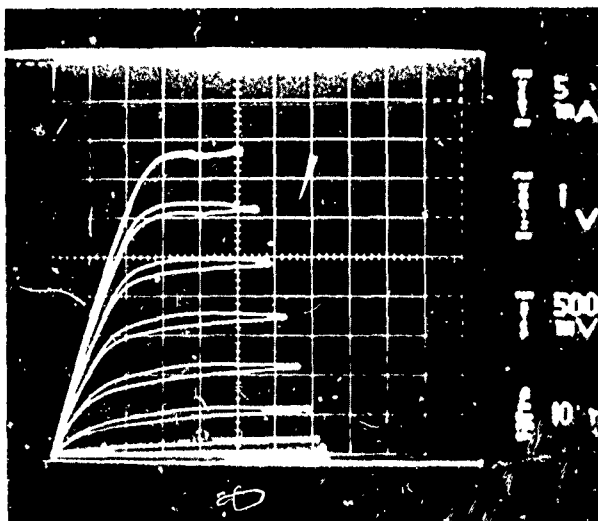
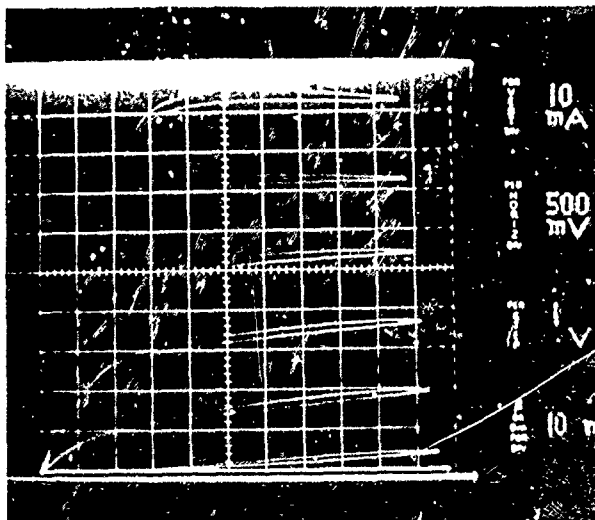


Fig. 4.27 I_D vs. V_{DS} curves for GaAs MESFETS in Preamp #8.

a) Q_1 (dual 1μ Gate, G_2 grounded).
 $g_m = 18.1 \text{ mmho}$ @ $I_D = 13 \text{ mA}$.



b) Q_2 (single 2μ gate).
 $g_m = 12.1 \text{ mmho}$ @ $I_D = 10.3 \text{ mA}$.



c) Q_3 (single 1μ gate).
 $g_m = 15 \text{ mmho}$ @ $I_D = 17 \text{ mA}$.

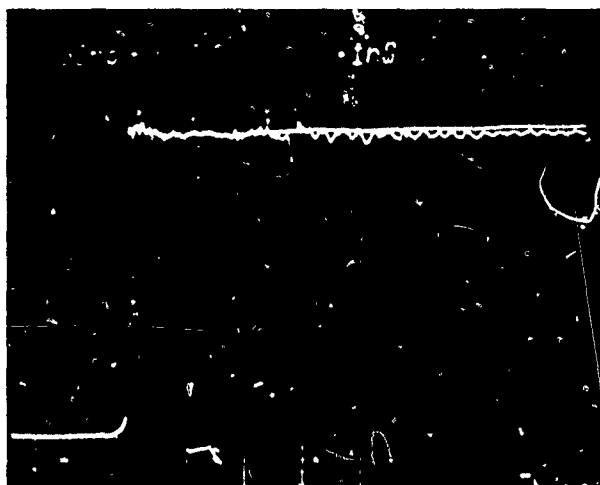


Fig. 4.28 Output time domain reflectometry traces for GAASFET Preamp #8 and a precision 50Ω reference termination (upper trace is right). 50mV/cm vertical, 1nS horizontal, 30 ps time resolution.

pulsewidths. For reasonable pulsewidths, the reflection coefficient is $\rho \sim -2.8\%$. Note that if the preamp power is turned off, Q_3 goes into "saturation" ($V_{gs} = 0$, $V_{DS} = 0$ in Fig. 4.27c), with R_{D3} very low so that a large negative reflection coefficient is observed. (See Fig. 4.40).

In order to see the contribution of the output stage noise to the total preamplifier noise output, Fig. 4.29 shows noise output spectra from the preamp with the gate of Q_3 bonded to ground (through 25Ω) instead of to Q_2 (i.e., the same configuration used to measure A_3). We see that above the $1/f$ region, the output stage noise plus the B & H DC3002 noise is only 2 db over the B&H noise itself, or the noise output of Q_3 is less than the input voltage noise of the B & H DC3002 preamp. Below 30MHz the Q_3 noise exceeds the B&H noise, with the $1/f$ noise from GAASFET Q_3 much greater (10 db or more) below 5MHz.

In the Mark III preamp design, a high open-loop gain is attained by using a high g_m high R_D dual-gate GAASFET as Q_1 with a high value of R_L . Fig. 4.27 a) shows the I_D vs. V_{DS} characteristics of the prototype dual 1μ gate GAASFET used as Q_1 in preamp #8. This device has $g_m = 18.1 \text{ mmho}$ at its $I_D = 13.3 \text{ mA}$ bias current. The output drain resistances for single 1μ gate GAASFET's of this type are usually about $R_D = 300\Omega$, which would give an open loop gain of less than 5.4, not nearly high enough. However, as was discussed in section 2.3.5, the dual gate device looks like a cascode amplifier of higher output impedance, given by Eq. 2.43. For example, from Eq. 2.43 with $R_{D1} = R_{D2} = 300\Omega$ and $g_{m2} = 18.1 \text{ mmhos}$, we have $(R_D)_{CAS} = 2230\Omega$. In order to exploit this high R_D , we must also have or high R_L value ($R_{L1} = 3K\Omega$ in #8) and hence a high supply voltage to give adequate dc drain current ($V_{DD1} = +45 \text{ volts}$). With $R_D = 2230\Omega$, $R_L = 3K\Omega$ and $g_m = 18.1 \text{ mmhos}$, we calculate $A_1 = 23.2$ (very close to our $A_1 = 23.0$ experimental value).

Of course, with such a high (1300Ω) impedance level at the drain of Q_1 , it is essential that the loading capacitance C_L be held to an absolute minimum. (A value of $C_L = 1.6 \text{ pf}$ as in preamp #5 would give an open-loop corner frequency of only 77 MHz, far too low to be useful.)

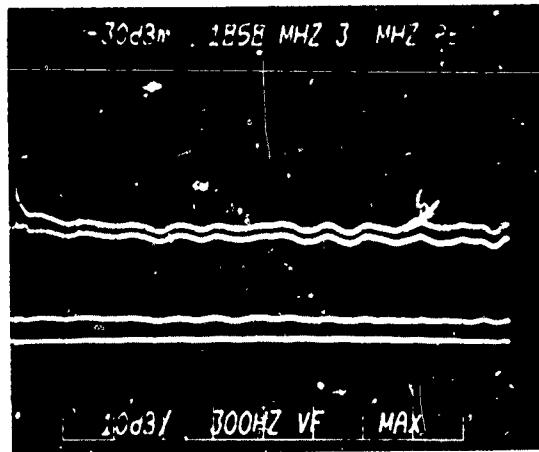
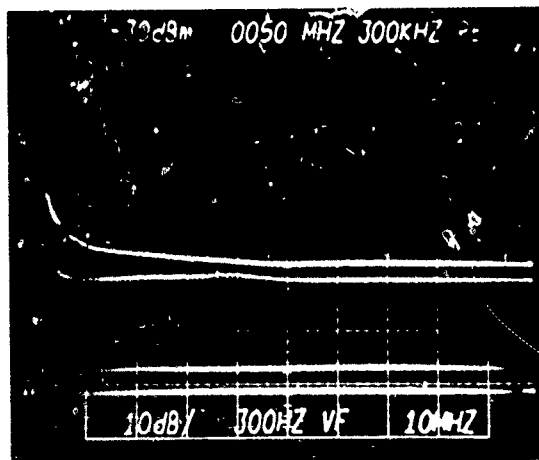
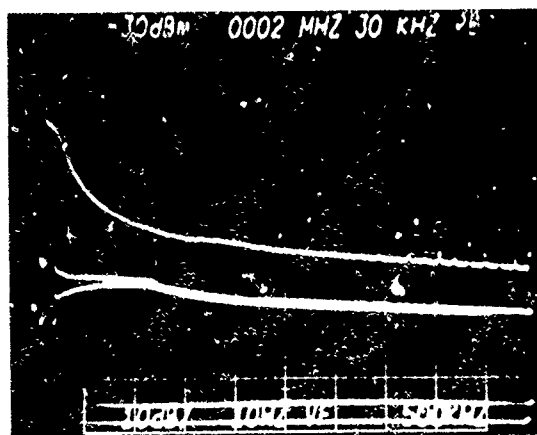


Fig. 4.29 Noise Output Spectra from the output stage Preamplifier #8 with the gate of Q₃ terminated 25Ω to ground. Measured through cascaded B&H preamps.

a) 0 to 1820 MHz Frequency Range (182 MHz/cm).



b) 0 to 100 MHz Frequency Range (10 MHz/cm).



c) 0 to 5 MHz Frequency Range (500 KHz/cm).

This is accomplished in the Mark III design by buffering the output stage and level shifter stray capacitances from the Q_1 drain by the source follower, Q_2 . In preamp #8, Q_2 is a 2μ gate length, single gate GAASFET (see Fig. 4.27b) with $g_{m2}=12.1$ mmhos at $I_{D2}=10.3$ mA and $R_{D2}=800\Omega$. The gain of the Q_2 source follower should be approximately

$$A_2 = 1/[1+1/g_{m2}(R_{D2}||R_{S2})] \quad (4.9)$$

or for $R_{S2}=1250\Omega+50\Omega$, $R_{D2}=800\Omega$ and $g_{m2}=12.1$ mmho we get $A_2=0.85$, or $A_{12}=A_1A_2=20$ as the open-loop gain of the "op-amp".

It should be noted that operating Q_1 , which has a breakdown voltage of the order of $V_{DS} \sim 10$ volts from a 45 volt power supply represents a dangerous condition in that if V_{g1} becomes too negative, V_{D2} will rise and Q_1 may very well "fail the smoke test". In order to avoid this possible disaster, a diode is connected from the drain of Q_1 to a +5 volt zener-limited potential. This diode is normally reverse biased, but if V_{D1} exceeds 5.5 volts or so, this diode will begin conducting and keep V_{D1} from exceeding a safe $V_{DS}=6$ volts. The diode used is a special ultra low capacitance ($< .05$ pf) beam-leaded GaAs Schottky barrier mixer diode fabricated at the Science Center. The open-loop (i.e., R_F open) "dc transfer characteristic" of this "op-amp" Q_1 - Q_2 stage is shown in Fig. 4.30. The horizontal scale is the applied Q_1 gate bias, V_{g1} , with zero at the right hand side, displayed at 0.5 volts/cm, while the vertical in Fig. 4.30 is the voltage on the lower side of the level shifter (pin #7 in Fig. 4.24) as taken from the output of the lower CA3130 voltage follower in Fig. 4.25 (let us call this V_F). V_F , displayed at 1 V/cm goes from -6 volts at the bottom to +2 volts at the top of Fig. 4.30. V_F differs from V_{D1} by V_{gs2} (-2.0 volts) and the level shifter zener voltage, V_Z (8.2 volts), or $V_F = V_{D1} - 6.2$ volts. For $0 > V_{g1} > -1.5$ volts, Q_1 is "saturated" (below pinchoff V_{ds}), as V_{g1} is increased from about -1.55 to -1.65 volts, Q_1 passes through its normal high-gain active region from $V_F=-5$ to -0.5 volts

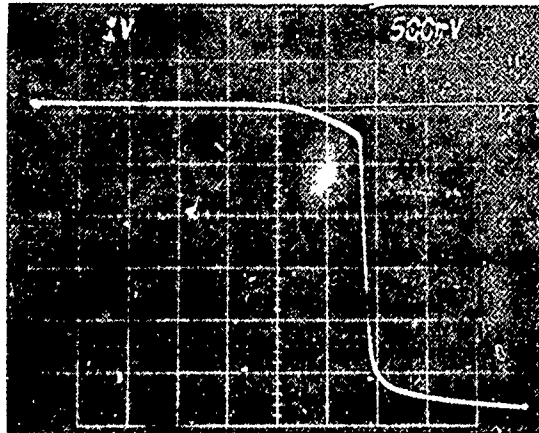


Fig. 4.30 Open-Loop dc Transfer characteristic of the Q_1 - Q_2 "op-amp" in Pre-amp #8. Horizontal is V_{g1} (1 V/cm, zero at right) and vertical is V_F , the op-amp dc output voltage (0.5V/cm, zero 2 cm from top). Normal feedback operation point is at $V_F = V_{D1} = -1.65V$. V_{DS} of $Q_1 \approx V_F + 6.2$ volts.

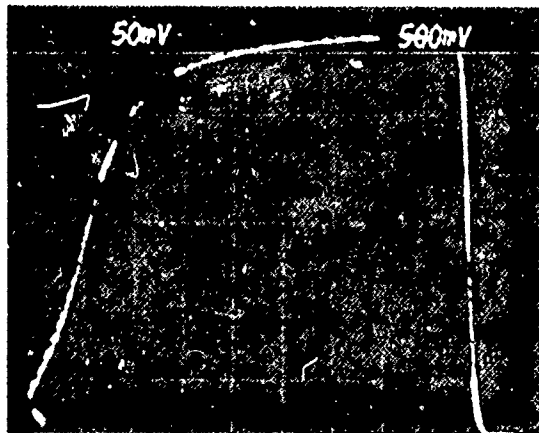


Fig. 4.31 100 MHz Open-Loop Gain of Mark III GAASFET Pre-amp #8. Vertical is linear display of 100 MHz output, -30 dBm full scale, Horizontal is V_F , 0.5 volts/cm (zero at right). Measured gain at balance is $A_{12} A_3 = 17.5$ dB.

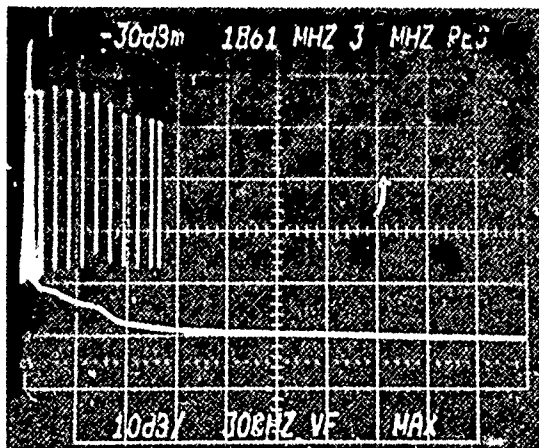


Fig. 4.32 Open-Loop Gain and noise, GAASFET Preamp #8, 0 to 1820 MHz frequency range. Preamp output straight into 7L13. Discrete frequency lines are inputs at frequencies of 20, 42, 50, 100, 150, 200, 250, 300, 350, 400, 450 and 480 MHz.

or $V_{D1} = 1.2$ to 5.7 volts. For $V_{g1} < -1.7$ volts the GaAs protection diode begins conducting, and finally for $V_{g1} < -2.5$ volts Q_1 is essentially cut off ($I_{DS} = 0$; see Fig. 4.27a) so that V_F increases no further with increasing V_{g1} . The normal operating point of the $Q_1 - Q_2$ "op-amp" will be at $V_F = V_{g1} = -1.65$ volts and the slope of the transfer characteristic (measured on an expanded scale) here is a dc voltage gain of 42. This is higher than the ac gain because of the high GAASFET dc R_D , discussed in section 2.3.5, and thermal feedback.

The variation of the open-loop 100 MHz ac gain (A_{12}) of $Q_1 - Q_2$ in preamp #8 as V_{g1} (and consequently V_F) are varied is shown in Fig. 4.31. This is a linear display of the spectrum analyzer output (-30 dBm full scale) with a -47 dBm input into the gate of Q_1 . The horizontal is V_F at 0.5 volts/cm with zero at the right side. At the far left, V_{g1} is about -1.5 volts, $V_{D1} \approx +1.2$ volts, so that Q_1 is nearly saturated, giving low ac gain. As V_{g1} is increased (negatively), Q_1 comes out of saturation and the ac gain increases. As we proceed further to the right in Fig. 4.31, the 100 MHz gain is nearly constant until the limiting diode begins to conduct, reducing the gain sharply (and finally to zero when Q_1 is cut off). Then the normal operating point, $V_F = -1.65$ volts, is near the maximum 100 MHz gain value, with an input to output gain of 17.5 dB or 7.45 ($A_{12} = 20.7$ for $A_3 = 0.36$).

The variation of open-loop gain with frequency is shown in Fig. 4.32, along with the output noise, with the output of preamp #8 connected directly into the 7L13 spectrum analyzer input. The discrete frequency spikes are with an rf signal of -60 dBm applied to the gate of Q_1 at the various frequencies indicated in the caption. Fig. 4.32 (and the FFT of the open-loop pulse response - not shown) indicates that, due to a slight "ringing" tendency at 100 MHz, the 100 MHz gain shown in Fig. 4.31 is slightly above the "baseband gain", so that an open-loop gain value of $A_{12} = 19.5$ is probably a more accurate figure than the 20.7 figure obtained at 100 MHz above. The 3 dB bandwidth of this open-loop gain is about $f_{3dB} = 320$ MHz and the open-loop gain-bandwidth product for the op-amp

is about 5 GHz (a remarkable improvement over the Mark IA design).

The open-loop noise output spectrum from GAASFET preamp #8, again taken with Q_1 in balance ($V_F = V_{g1} = -1.65$ volts), is shown in Fig. 4.33. This output noise should be approximately

$$V_{no}(f) = e_1(f)A_{12}(f)A_3A_{B\&H} \quad (4.10)$$

where e_1 is the equivalent input voltage noise (see Fig. 2.8). We should note that over most of the preamplifier passband, the closed-loop output noise (i.e., with R_F installed) will be less than this open-loop noise by an amount which could approach the open-loop gain. In order to obtain an accurate value for e_1 at a selected frequency (250 MHz), the noise output was measured through the 7L13 in a 26.79 KHz bandwidth. An input signal was applied to V_{g1} and its amplitude increased until the signal + noise exceeded the noise by exactly 3 db (signal level = -117.9 dBm), at which we should have $V_{sig} = e_1$. From this we obtain $e_1/\sqrt{Hz} = 1.74 \times 10^{-9}$ Volts/ \sqrt{Hz} at 250 MHz. Using the noise output from 4.33a) at 250 MHz (-47.4 dBm+2.4 dB Gaussian correction), we get $e_1/\sqrt{Hz} = V_{no}/A_{12}A_3A_{B\&H}\sqrt{\Delta F} = 1.73$ nV/ \sqrt{Hz} (fortuitously close to the more accurate signal substitution result).

Fig. 1.1 shows a photograph of the completed Mark III GAASFET receiver #8. The conical hole is for light entrance into the APD substrate. The large fins are not because the power dissipation is high, rather they are only to maintain temperature stability of the preamp to keep the APD temperature (and hence V_B) constant. The preamp unit dissipates only about 1.5 watts.

4.3.2. Performance Results for GAASFET Preamp #8

The voltage output pulse produced from Mark III GAASFET preamp #8 with $V_{APD} = 100$ volts by a δ -function input of $N_e = 4125$ electrons is shown in Fig. 4.34. The upper trace shows the output as seen directly on the sampling oscilloscope with the preamp output connected to the S-6

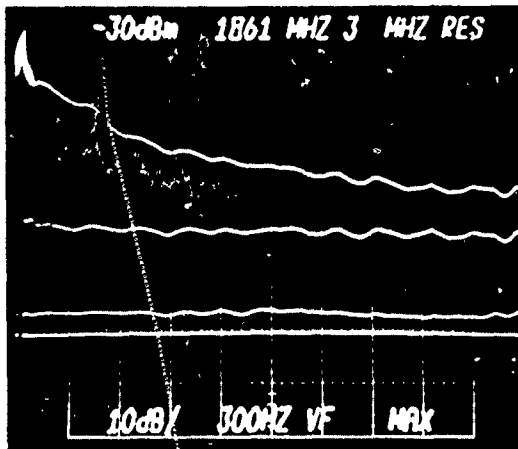
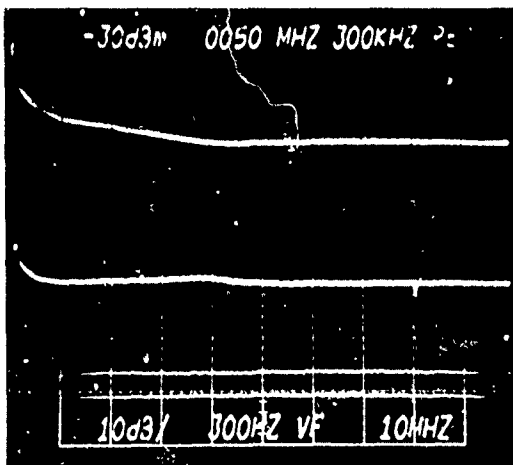
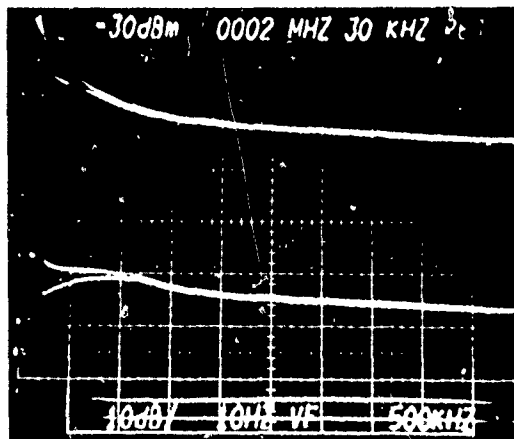


Fig. 4.33 Open-Loop Noise Output Spectrum from GAASFET Pream #8. Q_1 in balance, $V_F = -1.65$ Vdc, gate of Q_1 terminated 25Ω to ground. Measured through cascaded B&H preamps.

a) 0 to 1820 MHz frequency range (182 MHz/cm).



b) 0 to 100 MHz frequency range (10 MHz/cm).



c) 0 to 5 MHz Frequency Range (500 KHz/cm). With (lower traces) and without (upper traces) OSM model OS 201103A blocking capacitor between output of B&H DC3002 and 3db pad at input of B&H AC3020.

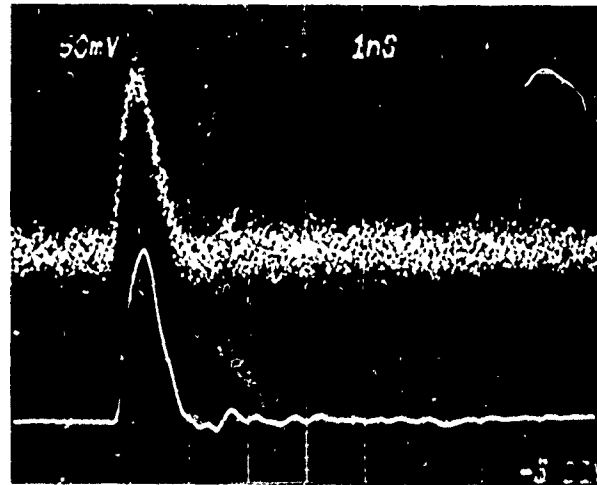


Fig. 4.34 Current impulse response of GAASFET Preamp #8 (with $V_{APP} = 100$ volts) to a 4125-electron current impulse (receiver output amplified thru cascaded B&H wideband 50Ω amplifiers). Upper curve output directly as seen on sampling oscilloscope (12.15 mV rms voltage noise). Lower curve is a 1024 waveform signal average of output. Both curves at 50 mV/cm, 1 ns/cm.

sampler input through the cascaded B&H preamps (#8-B&H DC3002 -3 db pad - B&H AC3020-S6) with $A_{B\&H} = 77.2$. The input pulse was generated from a 25.38 mV step from the S-52 pulse generator (with 20 db attenuator) through the $C_c = 2.60 \times 10^{-14}$ f internal coupling capacitor (see Fig. 3.22 or 3.23). (C_c and N_e were calibrated from pulse measurements without the B&H preamps for greater accuracy.) The signal pulse in the upper trace of Fig. 4.34 rides on a $V_{no} = 12.15$ mV Gaussian noise level (as measured both by the noise histogram technique of Section 3.3.8 and with an HP435 power meter) which is removed in the lower trace by signal averaging with the DPO (see section 3.3.11).

This signal-averaged current impulse response from Fig. 4.34 is more readably displayed in Fig. 4.35 (25 mV/cm vertical, 1ns/cm and 200 ps/cm horizontal). The peak height is $V_p = 0.1443$ volts, so for $Q_p = C_c V_{step} = 6.61 \times 10^{-16}$ coul, we have the pulse gain through the cascaded B&H's as $(V/Q)_\delta = 2.19 \times 10^{14}$ volts/coul (this is nearly four times that obtained for the Mark IA preamps). From Eq. 2.19, we have as the minimum detectable current pulse of preamp #8, $N_o = V_{no}/q(V/Q)_p = 347$ electrons. Another method of calibrating N_o is to use the integral of the current impulse response in Eq. 3.20. The integral curve (not shown) of Fig. 4.35 has a rise time (10% to 90%) of 634 ps and a step height of 9.0×10^{-11} volt seconds. From Eq. 3.22, then, with $R_o = 4750\Omega$, $A_2 = 0.36$ and $A_{B\&H} = 77.2$, we have $N_o = 358$ electrons which is reasonably close to the more accurate capacitor-calibrated value ($N_o = 347$ electrons).

The current impulse response waveform of Fig. 4.35 is very fast, 1ns wide at the 10% points (FWTM) and with virtually no overshoot or tail. The peak to 5% fall time, 650 ps, would allow over 1.5 Gb/s δ -function pulse communication, or about 1.4 Gb/s with reasonable modelocked laser pulsewidth, before the onset of massive intersymbol interference. The frequency response of GAASFET preamp #8 is shown in Fig. 4.36 from the Fourier transform of the current impulse response without the B&H preamps. Shown are the current impulse response (5mV/cm, 1ns/cm), its integral (2pVs/cm, 1ns/cm) and its FFT (150 μ V/cm, 256 MHz/cm). The

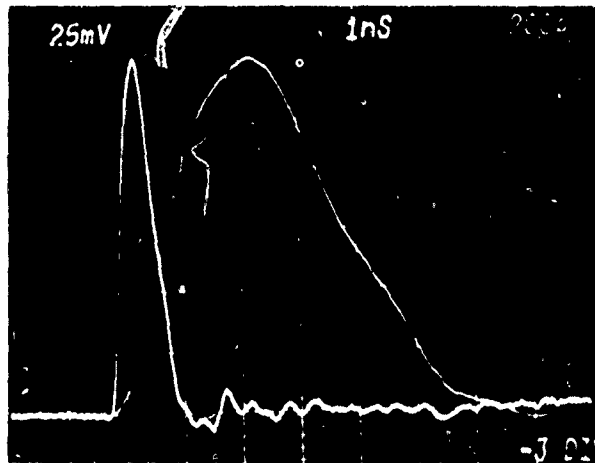


Fig. 4.35 Current impulse response of Mark III GAASFET
Preamp #8 (signal-averaged result from Fig. 4.34)
displayed at 25mV/cm vertical, 1ns/cm and (light
trace) 200ps/cm horizontal.

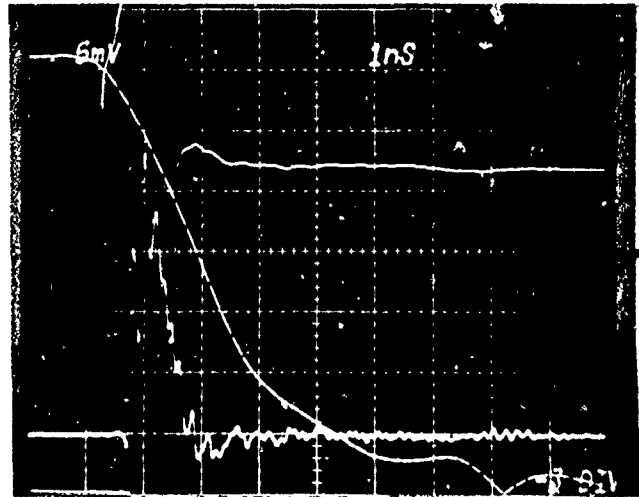


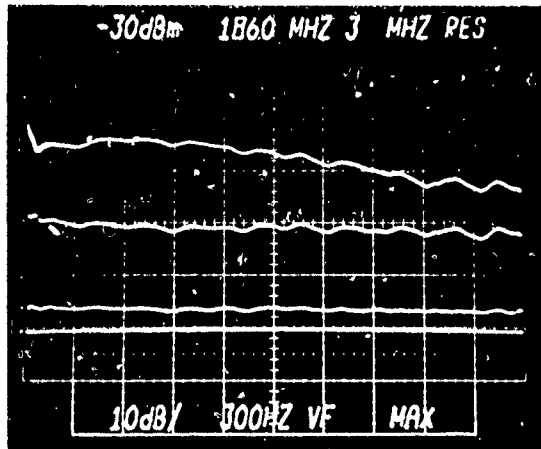
Fig. 4.36 Current impulse response of GAASFET Preamp #8 with $V_{APD} = 100V$ measured directly into S-6 (without B&H preamps). Input Step; $V_{STEP} = 0.2442$ volts through internal C_C . Current impulse at $5mV/cm$, $1ns/cm$, zero 3 cm below center. Integral at $2pVs/cm$, $1ns$, zero at bottom ($-4cm$). FFT at $150\mu V/cm$, $256MHz/cm$ horizontal, with $f=0$ at left edge (vertical zero at bottom).

integral step is 1.085×10^{-11} Vs or from Eq. 3.20, $Q_p = 6.35 \times 10^{-5}$ coul (39,600 electrons), or since $V_{\text{step}} = 0.2442$ V, $C_c = 2.60 \times 10^{-14}$ f. The "10-90" risetime of the integral step is 585 ps. The FFT-derived frequency response (magnitude of transimpedance versus frequency), the dashed curve in Fig. 4.36, shows nearly flat response to over 300 MHz, with $f_{3\text{dB}}$ at 620 MHz. Not shown in this display is the high-frequency ringing response which is about 1 division vertical in the 4-6 GHz region (not seen through a 3 GHz preamp).

The noise spectral output for GAASFET preamp #8 with $V_{\text{APD}} = 100$ volts is shown in Fig. 4.37. The interpretation of these noise output curves was discussed in conjunction with Fig. 4.13 (section 4.2.2). We can use Fig. 4.37a) with Eq. 4.2 to calculate the NEP for the receiver. From Fig. 4.13 a), at $f = 200$ MHz we have $v_{\text{no}} = 55.5$ dBm which gives for $\eta = 0.96$, $h\nu = 1.165$ eV, $\text{N.E.P.} = 3.3 \times 10^{-12}$ W/ $\sqrt{\text{Hz}}$, or at $f = 273$ MHz, -54 dBm noise gives $\text{N.E.P.} = 3.9 \times 10^{-12}$ W/ $\sqrt{\text{Hz}}$ (higher, due to increased $e_1 \omega(C_{\text{in}} + C_{\text{APD}})$ noise). However, in 273 MHz measurements with $\Delta F = 26.79$ KHz using an amplitude reference generator to determine the noise level more accurately, a noise output of -74.5 dBm was measured, giving $\text{N.E.P.} = 3.1 \times 10^{-12}$ W/ $\sqrt{\text{Hz}}$, which would give about $\text{N.E.P.} = 2.7 \times 10^{-12}$ W/ $\sqrt{\text{Hz}}$ at 200 MHz. These should be more accurate values than those above. Since C_c , the 50 Ω test loop coupling capacitor, is accurately known for preamp #8 (2.6×10^{-14} f), a more accurate method for measuring N.E.P., given η , $h\nu$, and C_c , would be to apply an rf signal to the (terminated) 50 Ω test line and reduce the amplitude until the signal + noise output on the spectrum analyzer is 3dB over the noise output (call this input signal level $(V_s)_{3\text{dB}}$). Then the N.E.P. would be given by (for $M = 1$)

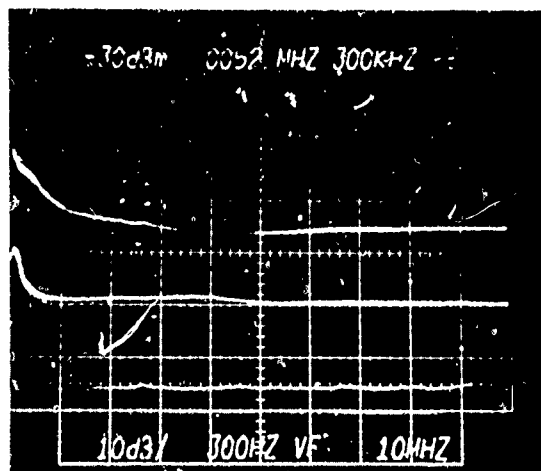
$$\text{N.E.P.} = \frac{2\pi f h\nu C_c}{\eta \sqrt{\Delta F}} (V_s)_{3\text{dB}} S+N/N \quad (4.11)$$

where f is the generator frequency (or this divided by M for small avalanche gains). This approach doesn't require knowing the preamp transimpedance,

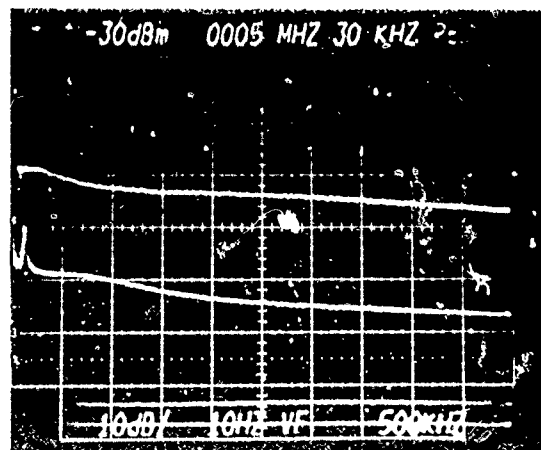


4.37 Closed-Loop ($R_F=5K\Omega$)
Noise Output Spectra
from GAASFET Preamp
#8 through cascaded
B&H's.

a) 0 to 1820 MHz Frequency
Range (182 MHz/cm). The
thermal noise for $R_F=5K\Omega$
would be -58.62 dBm.



b) 0 to 100 MHz Frequency
Range (10 MHz/cm). The
thermal noise for $R_F=5K\Omega$
would be -68.38 dBm.



c) 0 to 5 MHz Frequency
Range (500 KHz/cm). The
thermal noise for $R_F=5K\Omega$
would be -77.24 dBm.
Noise output measured
through OSM 201103A
blocking capacitor (375
KHz hi-pass filter).

R_o , or the other amplifier gains, but it does assume, as do Eqs. 4.2 and 4.3 of course, that the APD transit time is much faster than $1/f$ so that n or nM equal their dc values (well satisfied for these $\text{GaAs}_{1-x}\text{Sb}_x$ APD's below 5 GHz). We did not use this approach for measuring N.E.P. values of these experimental preamps.

The noise spectral outputs for GAASFET preamp #8, both closed-loop and open-loop are shown in Fig. 4.38. Here the data from Figs. 4.37 and 4.33 are reduced to output voltage noise/ $\sqrt{\text{Hz}}$ as a function of frequency from 20 KHz to 2 GHz, as measured through the cascaded B&H preamps. Also shown is the closed-loop gain from Fig. 4.36 and the calculated Johnson noise from the $R_F = 5000\Omega$ feedback resistor (which takes into account this gain for $f > 300$ MHz). We see that over most of the frequency range, the noise output in normal closed-loop operation (given by Eq. 2.33) is less than the noise output measured under open-loop conditions (Eq. 4.10) due to the fact that the amplified e_1 noise gets fed back through R_F to almost completely cancel this voltage noise contribution out (except at higher frequencies where $|G_1| \gg |G_F|$). Of course at frequencies near the closed-loop $f_{3\text{dB}}$ and above, the feedback, due to phase shift through the "op-amp", A , and the $R_F - C_I$ feedback path (which approaches 90° above its 30 MHz corner frequency) is actually positive, so the combination of amplified e_1 noise plus R_F Johnson noise exceeds the open-loop noise. At frequencies of the order of 1 MHz and below, the total output noise is comparable to the noise of the output stage alone (compare Fig. 4.37 with Fig. 4.29; noting that 4.37c) is with a blocking capacitor and 4.29 c) is without). The output stage noise contribution is similar to that shown for #6 in Fig. 4.42 (dashed curve). An extra gain stage, as used in the Mark II preamp design, could probably minimize this contribution of the output stage $1/f$ noise to the total noise output at low frequencies, since in the Mark II GAASFET preamp #7, the ~ 500 KHz output noise in closed-loop operation is about 8 dB above the output noise with Q_1 saturated (the Q_2 and Q_3 noise). In the 1-10 MHz region there is some noise contribution noticeable due to the level-shift zener. This is discussed in section 4.3.3 in conjunction with Fig. 4.42.

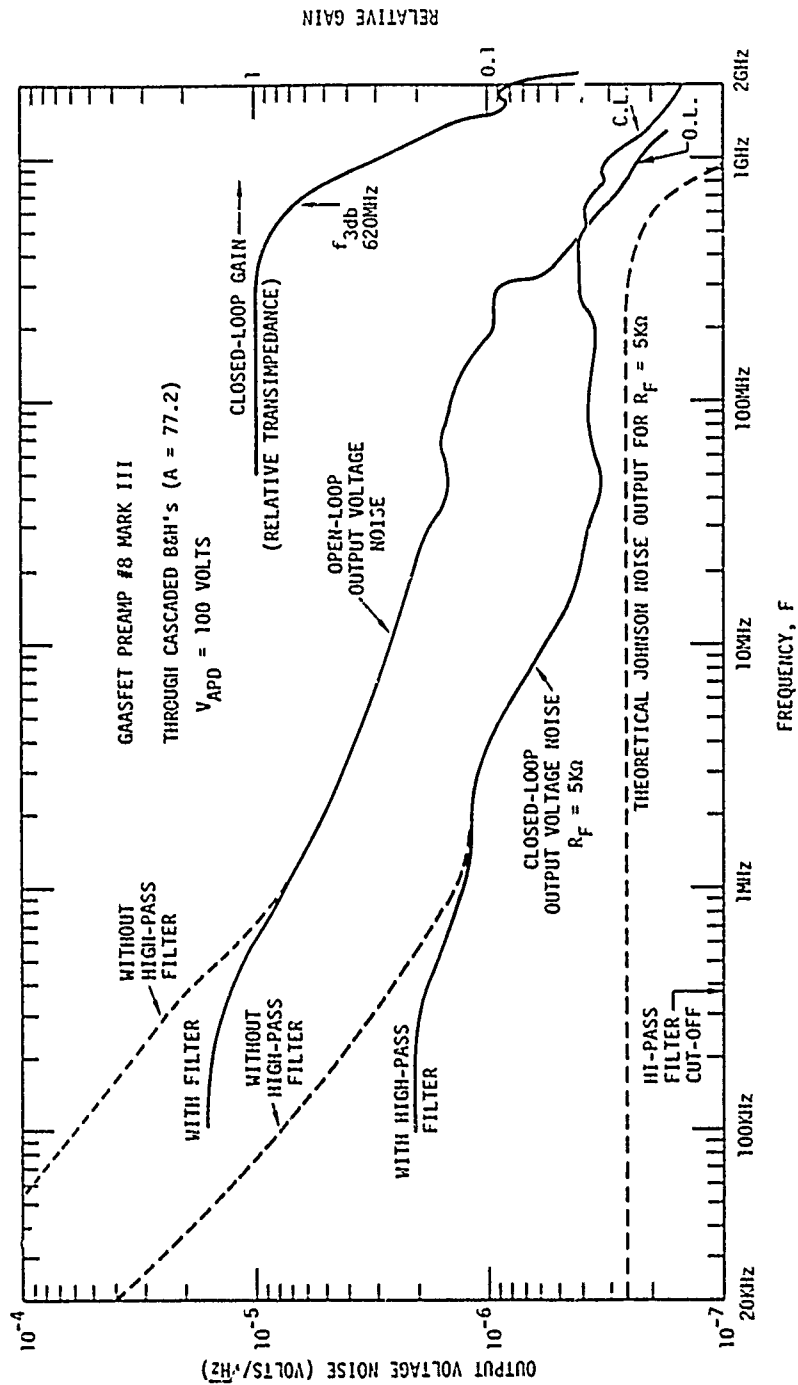


Fig. 4.38 Spectral dependence of noise output voltage (open-loop and closed-loop) for Mark III GAASFET preamp #8.

To summarize, the Mark III preamp design gave excellent results (summarized in Fig. 4.26). As compared to the Mark IA or Mark II models, GAASFET receiver #8 gave wider bandwidth ($f_{3dB} = 620$ MHz) and faster pulse response (1ns FWTM) even though it had a larger feedback resistance ($R_F = 5$ K Ω). At the same time it had lower equivalent input noise current (lower N.E.P.) and a lower value of minimum detectable current pulse ($N_0 = 347$ electrons). In other words, from Eq. 2.20, with a properly peak-sampled detection approach, this preamp should be able to achieve unity gain ($M = 1$), 10^{-6} BER gigabit data reception with of the order of 3500 photons/bit (or proportionately less with gain). The response of GAASFET preamp #8 to actual PGBM 1.06 μ modelocked laser pulses is shown in Fig. 4.39. These sampling oscilloscope traces were obtained by Dr. Samuel Green at McDonnell Douglas on their laboratory 400 Mb/s PGBM optical communications system. At the time these measurements were made, preamp #8 had an earlier 5 mil diameter (175 volt V_B) APD with higher capacitance than the final 3 mil K-9 APD with which the rest of the data in this section was taken. Hence the fall time of the current impulse response was a bit slower in the measurements of Fig. 4.39 than in Fig. 4.35. Other than that, Fig. 4.39c) represents the convolution between the optical pulseshape of the McDonnell laser and the current impulse response of preamp #8 (similar to 4.35). The optical pulsewidth is sufficiently narrow that V_p is very close to the same height as a δ -function peak of the same charge so that $(V/Q)_p \approx (V/Q)_\delta$ in Eq. 2.6 or $(N_0)_p \approx (N_0)_\delta = N_0$ in Eq. 2.20. Unfortunately, while optimized communication with preamp #8 requires sampling pulse widths (for the decision process) of the order of 200 ps, narrow pulse sampling was not available in the McDonnell 400 Mb/s test system (in fact for much of their data, the sampler was not used). Hence, while the N_0 for optimized narrow pulse detection is 350 electrons for #8 and 490 electrons for the Mark II preamp #7 (which was slow enough not to require short pulse sampling), #8 required over 30% more photo-electrons per bit to achieve 10^{-6} BER communication on the McDonnell test system than did preamp #7. (Of course, the additional gain stage in #7 was probably of help here as well.) This

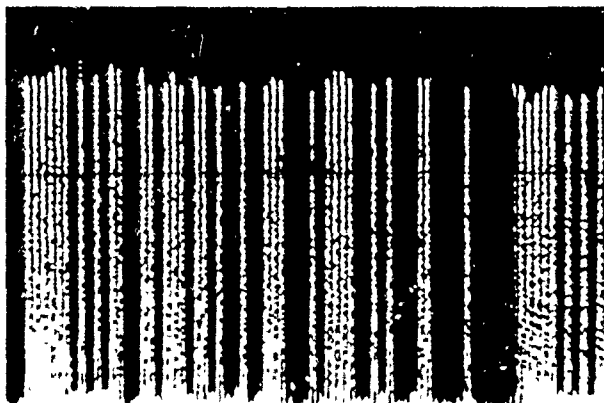
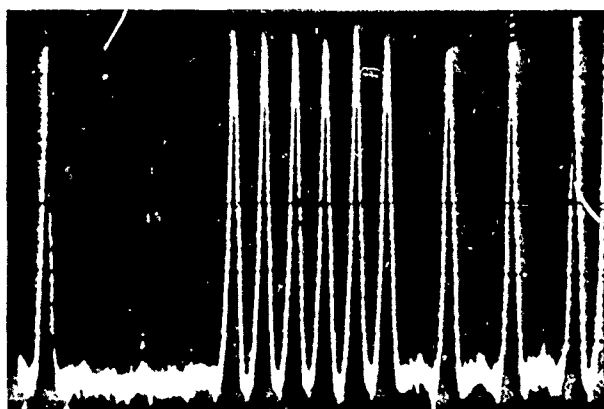
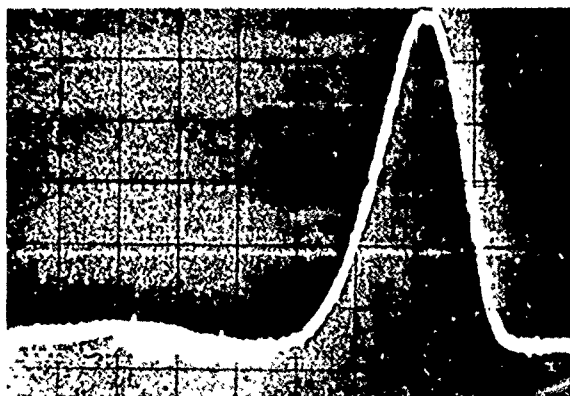


Fig. 4.39 Response of GAASFET Preamp #8 with 5 mil APD to 400 Mb/s 1.06 μ PGBM modelocked laser data stream. Measured on McDonnell-Douglas Test Communications System. 10mV/cm vert. (through B&H DC 3002 preamp). $(I_p)_{AVE}=1\mu A$.

a) 20nS/cm showing entire 64 bit data stream (with some repeated).



b) 5nS/cm showing response to repeated "1's".



c) 500pS/cm showing response to isolated "1". This would be the same as the current impulse response if the modelocked laser pulsewidth were short enough.

does point out, however, the necessity of mating the preamp properly with appropriate "decision making" logic (sample and hold, threshold set, etc.), for optimum results to be achieved in a communications system application.

4.3.3 Performance Results for AF Delivered GAASFET Preamp #6 (As Originally Delivered - Before Modification)

The circuit diagram for the preamp and power supply-monitor units for Mark III GAASFET preamp #6 are essentially the same as shown in Fig. 4.24 and 4.25. The main difference between #6, as delivered to the Air Force, and preamp #8 (described in sections 4.3.1 and 4.3.2) is that at the time of delivery, the prototype dual 1μ gate GAASFET chip devices, used as Q_1 in #8, were not yet available. Instead, in #6 a commercial Hitachi HCRL-94 dual-gate GAASFET chip was used for Q_1 . This device has wider gate widths and higher input capacitance than the device used for Q_1 in preamp #8. Further, the (gate 1) transconductance of the HCRL-94 was only 11.1 mmhos (as compared to 18.1 for Q_1 of #8) and the gate 2 transconductance is even less (since it lies over a thicker n-layer than gate 1), so that the output drain resistance (Eq. 2.43), $R_D \sim 1700 \Omega$, is not as high as in Q_1 of #8 ($R_D \approx 2200 \Omega$). Because of this (see Eqs. 2.41 and 4.1) the open loop gain, $A_{12} = 10.8$ and gain-bandwidth product (~ 2.2 to 3 GHz) are not as good as preamp #8 ($A_{12} = 19.5$, GBW = 5 GHz). This, together with the fact that C_{IN} (C_{gs} of Q_1) is also larger in #6, means that in order to achieve adequate bandwidth for gigabit communications in preamp #6, R_F must be much smaller than in #8 (2.5 K Ω as compared to 5 K Ω). This means that the transimpedance in preamp #6 is lower and the noise performance is not nearly as good as in #8.

Other than Q_1 and R_F , the two Mark III preamps are nearly identical. Q_3 is very similar to that shown in Fig. 4.27c, only with $g_{m3} = 13.2$ mmho @ $I_D = 17$ mA for $A_3 = g_{m3} (25 \Omega) = 0.33$ measured. The output TDR for preamp #6, shown in normal operation (upper curve) and with power off (lower curve at right) in Fig. 4.40 shows a very low reflection coefficient, $\rho \sim +1\%$ for reasonable signal pulsewidths. Of course, with power off, Q_3 is "saturated", representing a low impedance to the TDR pulse, so that $\rho \sim -53\%$ with power off. The short positive peak 4.25 ns from the left side is the preamp output connector and the

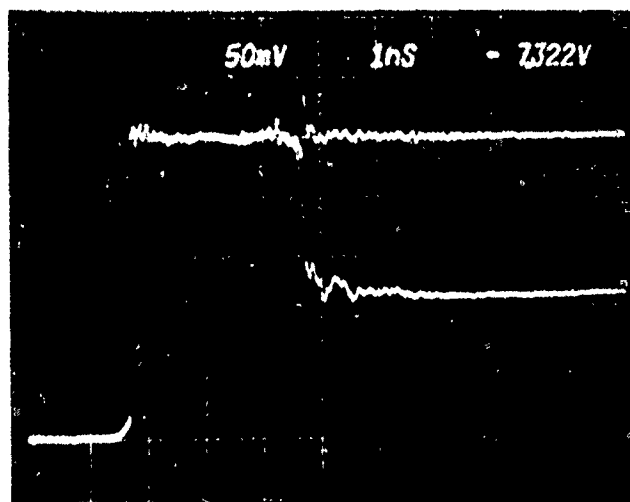


Fig. 4.40 Output time-domain reflectometry traces for GAASFET Preamp #6 with power on (upper trace) and power off lower trace at right (Q_3 "saturated").

sharp negative-going step with power off shows the pulse arrival at the drain of Q_3 . Q_2 in preamp #6 is essentially the same as in Fig. 4.27 b), with $g_{m2} = 12.1 \text{ mmho}$ @ $I_{D2} = 10.5 \text{ mA}$. R_{D2} is about 590Ω , so that from Eq. 4.9, $A_2 = 0.83$.

The open-loop "op-amp" measurements on preamp #6 give $A_{12} = 10.8$ with $f_{3dB} = 275 \text{ MHz}$. The input capacitance is of the order of $C_{IN} \sim 0.7$ or 0.8 pf . It is difficult to accurately define gain-bandwidth product from the FFT of the open-loop pulse response, but it is of the order of 2.2 to 3 GHz. The equivalent input noise voltage, e_1 , was measured using the technique described below Eq. 4.10 in section 4.3.2, giving $e_1/\sqrt{\text{Hz}} = 2.5 \text{ nV}/\sqrt{\text{Hz}}$ at 100 MHz (this would be lower at higher frequencies). The open-loop output noise versus frequency and the noise due to the Q_3 output stage only (with the noise of the following cascaded B&H preamps, of course) are shown in Fig. 4.42. The open-loop voltage noise output from preamp #6 in the 30 MHz to 300 MHz range is about 56% of that of #8 (comparing Fig. 4.42 and Fig. 4.38, whereas from Eq. 4.10, the difference in $A_{12}A_3$ gain factors would predict 51% (assuming e_1 were the same in both preamps). Hence we conclude that in this frequency range, e_1 for preamp #6 is about 10% higher than in #8. At lower frequencies, however, e_1 seems to be considerably larger in preamp #6.

The closed-loop current impulse response from GAASFET preamp #6 (through cascaded B&H preamps) with $R_F = 2500 \Omega$ and its 3 mil diameter K-9 APD reverse biased to $V_{APD} = 100 \text{ volts}$ is shown in Fig. 4.41 for a current input of $Q_p = 3.32 \times 10^{-15} \text{ coul}$, $N_e = 20,700 \text{ electrons}$. The pulse gain $(V/Q) = 1.022 \times 10^{14} \text{ V/coul}$, less than half that of preamp #8 (2.2×10^{14}). The noise output with the 3 mil APD (as delivered), $V_{no} = 12.81 \text{ mV rms}$, was slightly less than that measured with the 5 mil APD in the 10^6 point noise histogram for preamp #6 shown in Fig. 3.21 ($V_{no} = 12.96 \text{ mV}$). From Eq. 2.19 we have that the minimum detectable current pulse for GAASFET preamp #6 is $N_0 = 782 \text{ electrons}$. Also shown in Fig. 4.41 are the integral

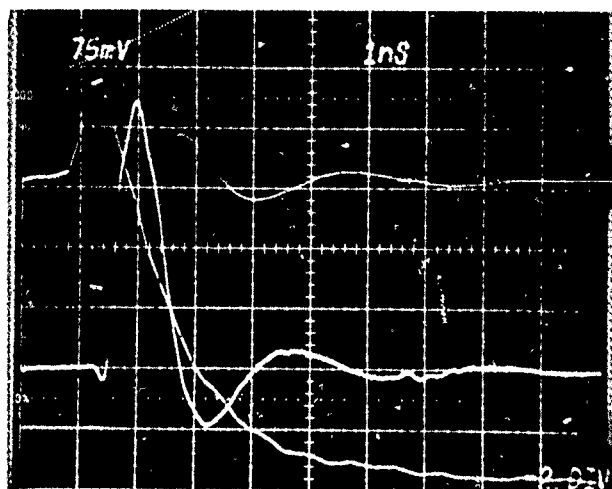


Fig. 4.41 Output Response of GAASFET Preamp #6, measured through cascaded B&H preamps ($A=77.2$), to a current impulse of $N_e = 20,760$ electrons (75mV/cm , 1nS/cm , zero 2 cm below center). Also shown are the integral response (50pVS/cm , 1nS/cm , zero 3 cm below center) and FFT - derived frequency response (2mV/cm vertical, zero 4 cm below center, 256 MHz/cm horizontal, $f = 0$ at left edge).

(step) response and the FFT. The integral of the impulse response shows a 10% to 90% step risetime of 570 ps and the step height is 2.05×10^{10} Vs. The FFT-derived frequency response for preamp #6, the dashed curve in Fig. 4.41, is displayed at 256 MHz/cm with $f=0$ at the left. Note that the op-amp transimpedance (R_o in Fig. 3.23) is about $R_o = 2290 \Omega$ below 150 MHz or so, but peaks at about $R_o = 3120 \Omega$ at $f = 313$ MHz. This high frequency peaking is, of course, caused by the oscillatory tail on the current impulse response. The 3dB bandwidth, $f_{3dB} = 580$ MHz in Fig. 4.41 or $f_{3dB} \sim 596$ MHz without the B&H's, would be lower if the transient response were not oscillatory.

The current impulse response of GAASFET preamp #6, as shown in Fig. 4.41, is fast enough for gigabit data rate communication, but is not optimum. The width of the response to a current impulse is about 1.15 nS at the 10% points (FWTM) and the critical peak to 5% fall time, 720 ps, would allow δ -function pulse communication at data rates approaching 1.4 Gb/s before the onset of massive intersymbol interference. However, the oscillatory "tail" on the response can lead to some fairly bad intersymbol interference even at lower data rates. For example, at 1Gb/s, the worst-case combination of negative overshoots could lower a "1" by 25% or the worst case combination of positive overshoots could raise a "0" by up to 7%, so that the worst case reduction in $V_{p1} - V_{po}$ (from Eq. 2.11) would be over 3dB. (Of course, as discussed in conjunction with Eq. 4.18, this does not mean that the signal level would have to be raised the full 3dB to attain the same B.E.R. performance as compared to a receiver of the same N_o but with no intersymbol interference.) Because of this intersymbol interference, preamp #6 would require a signal level for gigabit communication significantly above that predicted from Eq. 2.20 with $N_o = 782$ electrons. This is in contrast to Mark III GAASFET preamp #8 which would give no significant intersymbol interference for gigabit communication so that the required signal levels should be as given by

Eq. 2.20 with $N_o = 347$ electrons.

It is of interest to understand why the N_o of preamp #6 is 7 dB worse than that of preamp #8. Because the feedback resistance in #6 ($R_F = 2.5 \text{ k}\Omega$) is half that in #8 ($R_F = 5 \text{ k}\Omega$), we would expect $(V/Q)_p$ to be lower by approximately a factor of 2 in #6 and the noise output lower by approximately a factor of $\sqrt{2}$. In fact, $(V/Q)_p$ is experimentally a factor of 2.2 lower in #6, but the noise output voltage is actually higher in #6 than in preamp #8 (12.81mV versus 12.15mV). The origin of this unexpectedly high noise output can best be identified by looking at the frequency dependence of the closed-loop output noise in Fig. 4.42 and comparing this to the preamp #8 results in Fig. 4.38. We see in Fig. 4.42, that for frequencies around 50 MHz to 100 MHz, the noise from #6 is lower than that in #8 by about the factor (1.6) predicted from the difference in R_F and A_3 between the preamps. At higher frequencies, particularly from 250 to 500 MHz, however, the noise output from #6 is just as high as from #8. Since this high frequency region of 150 MHz to 1.5 GHz is where much of the total noise power from the preamp is generated, this explains a great deal of the reason the two noise outputs are comparable. This high level of high-frequency noise in preamp #6 is caused by its high input capacitance (relative to #8), producing a large noise current from the e_1 input voltage noise (2nd term in Eq. 2.33). We know from the magnitudes of the open-circuit noise output curves of Figs. 4.42 and 4.38 discussed previously that e_1 is only about 10% higher in preamp #6 than preamp #8, so that it must be the larger input capacitance of #6 that leads to the larger high-frequency noise. This is not unreasonable since $C_J + C_{IN}$ for #6 is of the order of 2 to 2.5 times that for GAASFET preamp #8.

While most of the excess noise in preamp #6 is due to its higher input capacitance, there is also a significant contribution from the large noise "shoulder", particularly noticeable from 3 or 4 MHz to 30 MHz in

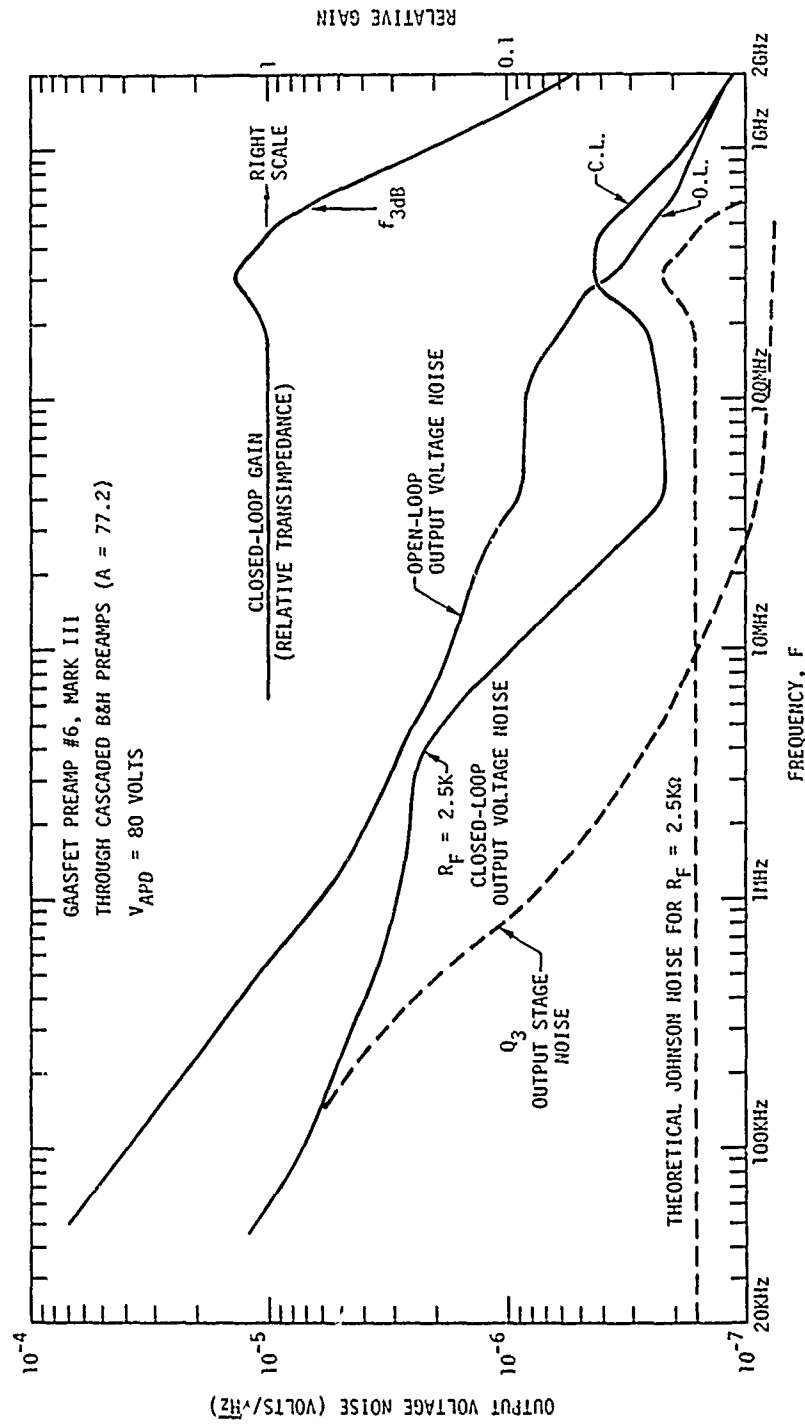


Fig. 4.42. Frequency Dependence of the Voltage Noise Output (per Root Hertz) from Mark III GAASFET Preamp #6. In addition to the normal closed-loop output noise spectrum, the open-loop and the Q_3 output stage [only] (plus B&H preamp) noise spectra are shown, along with the theoretical Johnson noise for $R_F = 2.5K\Omega$.

Fig. 4.42. This noise shoulder is so large that it causes the closed-loop output noise to approach the open-loop noise output near 4 MHz. The source of this noise cannot be a high input voltage noise, e_1 , as it doesn't show up in the open-loop noise output (Eq. 4.10). It is not due to a spurious "1/f" input noise current mechanism, because measurements made with $R_F = 5000 \Omega$ gave virtually identical noise output at 4 MHz as the $R_F = 2.5 \text{ K}\Omega$ curve in Fig. 4.42. (If it were indeed a noise current, the output would have doubled.) Similarly, measurements with different APD's gave the same results. The conclusion from this is that the probable cause of this excess noise "shoulder" in preamp #6 is the level-shift zener diode, V_Z (at the source of Q_2 in Fig. 4.24). In closed-loop operation, the input of the "op-amp" (gate of Q_1) is a "virtual ground", and hence for no signal input, the voltage at the right hand (output) side of R_F is constant. Since this point is also the bottom (negative side) of V_Z , this means that most of the zener diode noise voltage will appear at the top of the zener, from which the output to the gate of Q_3 is taken (unfortunately). In preamp #6, a Centralab type C6014 "8.2V N/P" zener chip was used for V_Z (selected for 7.6 volts V_Z at 10mA). Subsequent measurements on one of these 8.2V N/P chips gave a noise output of $V_{nz} = 1.5 \times 10^{-7}$ volts/ $\sqrt{\text{Hz}}$ at 4 MHz (varying as $f^{-0.6}$) and TDR measurements showed a resistance of $R_Z = 4.5$ ohms, with both the noise and resistance measurements at the 10mA operating bias current. Note that the 3dB rolloff frequency for the 0.01 μf bypass capacitor - R_Z combination is 3.5 MHz, very near the location of the "noise shoulder" in Fig. 4.42. Above this capacitance cutoff frequency the noise voltage should drop as 1/F, as observed in Fig. 4.42. The magnitude of the output noise should be of the order of $V_{no} = V_{nz} A_{3B\&H}$ or 3.8×10^{-6} V/ $\sqrt{\text{Hz}}$, reasonably close to the noise amplitude observed at the shoulder in Fig. 4.42.

If this prominent "noise shoulder" at 3-4 MHz in Fig. 4.42 is due to the level-shift zener diode, V_Z , in preamp #6, why isn't it observed in

the data for preamp #8? Actually, if you examine Fig. 4.38 carefully, you see that preamp #8 also has a noise "shoulder" at about 3 MHz, but that its amplitude is lower and it is less noticeable because the Johnson noise voltage level is higher (because R_F is larger than in #6). The reason that the zener diode noise is smaller in preamp #8 is that the opposite polarity zener chip was used for V_Z . Subsequent measurements on a Centralab C6114 "8.2V P/N" zener chip as used in preamp #8 gave a noise output of $V_{nz} = 2 \times 10^{-8} \text{ V}/\sqrt{\text{Hz}}$ (flat with frequency). This should produce an output noise contribution of about $5 \times 10^{-7} \text{ volts}/\sqrt{\text{Hz}}$, a fraction of the total noise output at 3 MHz. Hence, by changing V_Z to the lower-noise P/N type in preamp #6, we should be able to avoid this excess noise shoulder and its contribution to the overall noise. After the preamp modification, then, when Q_1 is changed to the lower-capacitance, higher transconductance dual-gate GAASFET, we should be able to attain the same excellent performance from preamp #6 that we obtained from preamp #8.

5.0 CONCLUSIONS

The objective of this program was to develop a solid state receiver for gigabit optical communications which would be able to achieve 10^{-6} bit error rate data detection of pulse-gated binary modulated (PGBM) 1.06μ mode-locked Nd-YAG laser data with a signal level difference of 1000 photons/bit (or fewer) between a transmitted "1" and a transmitted "0". The program involved two major areas of effort: (1) the development of a high speed, high quantum efficiency, low capacitance $\text{GaAs}_{1-x}\text{Sb}_x$ avalanche photodiode (APD) and (2) the development of an extremely charge sensitive, low-noise preamp using GaAs Schottky barrier FET's (GAASFET's) to be hybrid-integrated with the APD. These two major areas of work have necessitated certain other corollary efforts: (3) the development of special analytical tools for the avalanche photodiode development, (4) the development of a model for laser communications involving the detection of short PGBM modelocked laser pulses and (5) the development of a signal and noise model for the GAASFET preamps and special preamp measurement techniques capable of experimentally determining the parameters required for this model. Our achievements in each of these areas are reviewed in the summary, section 1.2, and need not be repeated here. Suffice it to say that we have developed ultra low capacitance $\text{GaAs}_{1-x}\text{Sb}_x$ inverted homo-heterojunction avalanche photodiodes with nearly 100% quantum efficiencies and with peak rf gains up to 24 dB which, when hybrid-integrated with the wide bandwidth feedback-mode preamp give better detection performance than any other 1.06μ receiver. The pulse-mode communications detection analysis of section 2.1 has been used with the preamp model, the parameters of which were determined using special measurement techniques developed for use with our Tektronix Digital Processing Oscilloscope system, to accurately predict the results of actual high data rate, 1.06μ optical communications system measurements of bit error rate performance of the receiver at McDonnell Douglas (Fig. 4.23). This excellent agreement between the calculated system performance based on our models and receiver measurements and the actual PGBM data detection performance gives us confidence in the validity of our system analysis, preamp model and receiver measurement techniques and our ability to calculate the performance

which can be obtained in different types of electro-optical systems.

While only one complete receiver (plus two 50 Ω -packaged APD's) were delivered under this contract, a total of five receivers were fabricated. The key performance parameters obtained for each of the five GaAs_{1-x}Sb_x APD-GAASFET integrated preamp receivers are indicated in Table 5.1. The Mark IA modification of the original 2-GAASFET preamp design, used in preamps #4 and #5 represents the starting point for this hybrid-integrated transimpedance-mode GAASFET preamp technology. Here it was demonstrated that indeed it was possible to construct an "op-amp" so fast that it could be used in the negative feedback mode for frequencies of a sizeable fraction of a gigahertz and still be stable. Extension of feedback mode "op-amp" circuit concepts to a frequency range far beyond where they have been used before must be considered a major accomplishment of this work. The closed-loop bandwidths were not quite high enough for gigabit data rate use, however.

The Mark II and Mark III preamp designs represent more complex (3-GAASFET plus bipolar transistors) extensions of the Mark IA technology base to achieve better performance in specified areas. The Mark II was designed to have internal gain and limited bandwidth to perform best with the broad-sampling-pulse 400 Mb/s PGBM modelocked Nd-YAG laser communications system at McDonnell Douglas Astronautics. As shown in Fig. 4.23, Mark II receiver #7 performed admirably in communication tests, giving almost exactly the BER performance calculated from our test data, achieving 10^{-6} BER with no avalanche gain at all with a lower signal level than required for a III-V alloy photocathode photomultiplier tube and requiring only 60% more signal to achieve a 10^{-8} BER than that required by two silicon avalanche photodiodes optically in series (electrically in parallel) operated at an avalanche gain of 100 (the photomultipliers could not achieve a 10^{-8} BER). Since average avalanche gains of 6 to 10 dB are available in the K-9 GaAs_{1-x}Sb_x APD's in these receivers, even with these modest avalanche gains, the receivers developed in this program demonstrated the best performance for 400 Mb/s

1.06 μ laser communication of all available 1.06 μ detectors. Their closest competitor, the series-parallel silicon APD's, are far too slow for gigabit data rate use, so that these III-V alloy APD-integrated GAASFET receivers represent by far the best performance in gigabit data detection at 1.06 μ . In future work, as higher APD gains are attained in these GaAs_{1-x}Sb_x APD's, these receivers could achieve performances perhaps 20 dB better than competing 1.06 μ detectors.

While the Mark IA and Mark II preamp designs clearly demonstrated the validity of the integrated feedback-mode ("op-amp"-type) GAASFET receiver approach, neither was fast enough to achieve the gigabit data rate requirements of the Air Force 405B satellite laser communications system. The Mark III preamp design was initiated to extend the bandwidth of the receiver to data rates in excess of 1 Gb/s and to improve the receiver pulse sensitivity. This was accomplished in the Mark III design by making major improvements in the performance of the "op-amp", increasing its gain to 20 and its gain-bandwidth product to a remarkable 5 GHz. This allows the use of a higher feedback resistance ($R_F = 5\text{ K}\Omega$) to achieve lower current noise (better NEP) and at the same time achieve higher bandwidths and pulse gains nearly four times that of the Mark IA's. As originally delivered to the Air Force, Mark III receiver #6 gave adequate signal bandwidth for gigabit data rate operation, but was considerably inferior to preamp #8 in its transient response and noise characteristics (as indicated in Table 5.1). This receiver is presently being modified at the Science Center to change the input GAASFET to the higher-gain, lower capacitance unit used in preamp #8, so that after modification its performance should be essentially identical to that of preamp #8.

Mark III receiver #8 exhibits excellent charge sensitivity, requiring a photocurrent charge pulse of only $N_0 = 347$ electrons to give a peak signal output equal to the rms noise output. This is fully 3 dB lower than the minimum detectable current pulse (N_0) for Mark II preamp #7 (discussed above), and hence it should be possible to achieve data reception for a given BER at a specified avalanche gain, M (in the low M region),

TABLE 5.1

GAASFET PREAMP SER. NO. DESIGN	4 MARK IA Figure 2.9 Similar to Fig. 4.11	5 MARK IA Figure 2.9 Fig. 4.11	6 MARK III Figure 2.12 Similar to Fig. 4.26	7 MARK II Figure 2.11 Fig. 4.18	8 MARK III Figure 2.12 Fig. 4.26
Open-Loop "op-amp" gain	5.3	5.4	10.8	6.4	19.5
Open-Loop F_{3dB} (O.L.)	260 MHz	320 MHz	275 MHz	~375 MHz	320 MHz
Open-Loop Gain-Bandwidth Product	1.35 GHz	1.2 GHz	~2.2-3 GHz	~1.8 GHz	5 GHz
Output Stage Gain	$A_2 = 0.34$	$A_2 = 0.292$	$A_3 = 0.33$	$A_2 = 4.6$ ($f_{3dB} \approx 600$ MHz)	$A_3 = -0.36$
Feedback Resistance, R_f	3000 Ω	3020 Ω	2500 Ω	4000 Ω	5000 Ω
Transimpedance, R_o (V_f/i_p)	2525 Ω	2550 Ω	2290 Ω	3460 Ω	4750 Ω
Preamp Output Voltage V_{out} (Baseband, $n=96\%$ for $V_{APD} \geq 80$ Volts)	$V_{out} = 858$ I _p (V/amp) $V_{out} = 824$ M I _{ph} at 1.064 μ	$V_{out} = 743$ I _p (V/amp) $V_{out} = 714$ M I _{ph} at 1.064 μ	$V_{out} = 755$ I _p (V/amp) $V_{out} = 725$ M I _{ph} at 1.064 μ	$V_{out} = 5890$ I _p (V/amp) $V_{out} = 5650$ M I _{ph} at 1.064 μ	$V_{out} = 1712$ I _p (Volts/amp) $V_{out} = 1644$ M I _{ph} at 1.064 μ
3db Bandwidth (Closed-loop) F_{3dB}	303 MHz	402 MHz	596 MHz	290 MHz at output (360MHz at Q_1)	620 MHz
Output Pulsewidth thru cascaded B & H Preamps (6-Function Input)	1.8 nS FWTM	1.6 nS FWTM	1.15 nS FWTM	2nS FWTM	1nS FWTM
Pulse Gain (V/Q) ₆ ; through cascaded B&H Preamps, $A=77.2$	6.15×10^{13} volts/Coulomb	5.59×10^{13} volts/Coul	1.02×10^{14} Volts/Coul	3.5×10^{14} Volts/Coul (B&H)	2.19×10^{14} Volts/Coul
RMS Output Noise through Cascaded B&H Preamps, 3GHz B.W.	7.822 mV rms 375KHz to 3 GHz	6.912 mV rms 2KHz to 3GHz	12.81 mV rms 375KHz to 3GHz	27.48 mV rms 375 KHz to 3 GHz	12.15 mV 375 KHz to 3 GHz
Minimum Detectable Current Pulse, N_o (in best measured Bandwidth)	720 Electrons 375 KHz to 714 MHz	590 Electrons 40 KHz to 714 MHz (~550 E w/o 1/f)	782 Electrons 375 KHz to 3 GHz	490 Electrons 375 KHz to 3 GHz	347 Electrons 375 KHz to 3 GHz
Required Signal Level for 10^{-6} BER Modulated Laser PGM Communication (Minimum Number of Photons on "1" minus photons on "0")	$N_{ph} = \frac{7130}{M}$ ph/bit (valid for low M)	$N_{ph} = \frac{5840}{M}$ ph/bit (~5450 p/b with 1/f filtered)	$N_{ph} = \frac{7750}{M}$ ph/bit (Intersymbol Interference Degrades <3dB)	$N_{ph} = \frac{4850}{M}$ ph/bit (Experimentally measured 4900 at M=1)	$N_{ph} = \frac{3440}{M}$ photons/bit (valid for low M with fast sampling)
200 MHz Noise Equivalent Power NEP at 1.064 μ (calculated from noise, assuming $n=96\%$)	$NEP = \frac{4.8 \times 10^{-12}}{M}$ Watts/ \sqrt{Hz} (valid for Low M)	$NEP = \frac{4.2 \times 10^{-12}}{M}$ Watts/ \sqrt{Hz}	$NEP = \frac{5.3 \times 10^{-12}}{M}$ Watts/ \sqrt{Hz}	$NEP = \frac{3.2 \times 10^{-12}}{M}$ Watts/ \sqrt{Hz}	$NEP = \frac{2.7 \times 10^{-12}}{M}$ Watts/ \sqrt{Hz}

with 3 dB less optical signal. Of course, attaining this requires sampling the output data stream with a short-gate sample and hold, such as that used in the 405B gigabit data rate laser communications system. Unfortunately, in the McDonnell Douglas 1.06μ test system used in the communications tests on these receivers, only a rather "vintage" discrete bipolar transistor sample-hold was available (the system worked about the same whether or not it was operative). Of course, without short-pulse sampling to make use of the higher peak pulse gain in preamp #8 and to reject between-bit noise, it was not possible to demonstrate on their test system the improved BER performance attainable from the Mark III receiver design.

From the standpoint of the Air Force 405B laser communications system requirements, the important receiver parameters in Table 5.1 are the receiver bandwidth (maximum useable data rate) and the required signal level for communications. In terms of N_0 or N_{ph} (the required number of photons/bit for 10^{-6} BER communications), we see a rapid "learning curve" of improved N_0 in succeeding preamps, achieving $N_0 = 347$ electrons in preamp #8. Similarly, we have improved bandwidth to $F_{3dB} = 620$ MHz in #8, which would be capable of modelocked laser communication at data rates of the order of 1.4 to 1.5 Gb/s (depending on optical pulsewidth) before the onset of serious intersymbol interference. There is no reason to assume that the learning curve in Table 5.1 ends at preamp #8. It is probably reasonable to expect that with additional work, maximum data rates of 2 Gb/s or possibly more could be attained with this approach and N_0 values of 200 to 250 electrons seem reasonable. With these preamp parameters with the present $\eta_{1.06\mu} = 96\%$ APD performance, the communications system performance should be as given by the lower curve in the N_{ph} versus M plot in Fig. 2.3. (Actually, even better performance could be obtained at higher gains, since our bulk photocurrents, $I_b \sim 1$ nA at room temperature, are lower than assumed in Fig. 2.3.)

While significant preamp improvements remain to be made, and these should be pursued, the greatest achievements in gigabit communications performance will be attained by improving the avalanche gain of the $\text{GaAs}_{1-x}\text{Sb}_x$ avalanche photodiodes. While we might be able to achieve a further 6 dB

improvement in N_o , which would reduce N_{ph} by 6 dB, if we could obtain uniform avalanche gains of $M=10$ to 50, we could attain far greater reductions in the signal level required for communications. In terms of noise equivalent power, in the McDonnell Douglas NEP measurements on preamp #7, reductions in NEP of 26.5 dB ($M=21.1$ in Table 5.1, lower line) were obtained between unity gain bias and optimum gain bias operation, but this is only in a small area on the device. At a general point on the same device they obtained a much smaller 11.3 dB ($M=3.7$), improvement in NEP. Clearly what we would like is to obtain uniform APD gains so that the entire device is as good or better than the highest gain areas are in the present APD devices. The K-9 growth inverted homo-heterojunction $GaAs_{1-x}Sb_x$ avalanche photodiodes used in all four of these hybrid-integrated GAASFET receivers represents a considerable improvement in gain characteristics over earlier approaches. As discussed in section 4.1, however, their performance is limited by a) the fact that the wrong complimentary device type was selected (i.e., the holes are being drifted through the high-field region whereas it appears that electrons have the higher ionization coefficients) and b) the fact that there are significant fluctuations in the active layer thickness which leads to variations in electric field and gain over the device. There is no reason to believe that these problems cannot be rectified in these $GaAs_{1-x}Sb_x$ APD's and the desired uniformly high gains achieved. When this is attained, we may see the number of 1.06μ photons per bit, N_{ph} , required for high data optical communication drop, not only well under 1000 photons/bit, but possibly under 100 photons/bit.

It is worthwhile at this point to consider where this 1.06μ receiver work stands in relation to the overall Air Force 405B satellite laser communications system effort. The initial demonstration system will use the 0.53μ (doubled Nd-YAG) green line for the high data rate transmission with photomultiplier detectors. Use of the green line has certain advantages and certain disadvantages. The principal advantages are that it is much easier to fabricate a gigabit modulator with high extinction ratio at 0.53μ (compared to 1.06μ) and that reasonable quantum efficiencies ($\eta_{0.53\mu} \approx 25\%$)

should be attainable in photomultiplier tubes as a receiver approach. The disadvantages of going to 0.53μ operation include the fact that it requires the use of a frequency doubler which entails both a loss in signal power and a significant reliability hazard in a space system and the fact that in links passing through the atmosphere, the light scattering is 16 times worse for 0.53μ than 1.06μ . Further, the photomultiplier tubes, which seem at the outset such a simple and ideal solution to the receiver problem, in fact have been beset by problems of instability, poor quantum efficiency, and spurious signal-generated noise mechanisms which make it impossible to achieve the 10^{-8} BER and better error rates that would be desirable in a gigabit data rate system. (Remember that a 10^{-6} BER in a gigabit system would require software identification and correction of an error every millisecond.)

It would be impossible in the present context to discuss in detail the trade-offs between the 0.53μ and 1.06μ system approaches to gigabit laser communications, but a few comments regarding the impact of this receiver work on that decision are relevant. While photomultiplier approaches to data detection require, for reasonable performance, very high modulator extinction ratios and low background light levels (see Fig. 2.4), the avalanche photodiode receivers developed here are, at least for reasonably low gains, quite insensitive to background light or modulator extinction ratio. This means that with reasonable effort, a gigabit 1.06μ modulator suitable for this detection approach could probably be fabricated from the same electro-optic materials presently being used for the green modulators. (Other, far better, electro-optic materials for 1.06μ modulators could probably be utilized with some research.) Given a reasonable gigabit "red" modulator, the same PQM approach used in the present gigabit green system could be used at 1.06μ . It is difficult to make an exact comparison of the signal sensitivities of the receivers in the 0.53μ and 1.06μ approaches because the relevant quantity is how much power is required at the transmitter laser to achieve a given bit error rate at the receiver. From just an energy standpoint ($E=h\nu$), green photons are twice as "expensive"

(in terms of transmitter power) as 1.06μ photons. As we achieve higher, more uniform avalanche gains in these III-V alloy APD's, reductions in required signal level approaching 20 dB could be realized. Clearly this would, from a power standpoint strongly shift the balance toward the 1.06μ system approach. The prospect of using a lower power, simpler laser transmitter (without doubler) with a reliable, stable, all solid state receiver for the gigabit satellite laser communications system represents a very attractive alternative for the future direction of the 405B system.

6.0 REFERENCES

1. R. C. Eden, "1.06 Micron Avalanche Photodiode", Tech. Rep. AFAL-TR-72-343, Jan. 1973.
2. R. C. Eden, "1.06 Micron Sensor Array for Track and Receive", Tech. Rep. AFAL-TR-73-345, Dec. 1973.
3. M. Abramowitz and I. A. Stegun, Handbook of Mathematical Functions, NBS Applied Mathematics Series 55, p. 977, U. S. Dept. of Commerce (1964).
4. T. P. Pearsall, private communication and T. P. Pearsall, R. E. Nahory, and M. A. Pollack in 1975 Device Research Conference (Ottawa) paper.
5. R. C. Eden, "Heterojunction III-V Alloy Photodetectors for High-Sensitivity 1.06 μ m Optical Receivers", Proc. IEEE, Vol. 63, #1, Jan. 1975.
6. G. D. Vendelin, G. E. Brehm and N. G. Bechtel, "Gallium Arsenide Field-Effect Transistor Applications", Fairchild Semiconductor Publications, Fig. 11, April 1974.
7. W. F. Hall, W. E. Tennant, J. A. Cape and J. S. Harris, Jr., "Non-Destructive Determination of Energy Gap Grading in Thin Films by Optical Transmission Measurements", to be published in the Proceedings of the 3rd Annual Conference on the Physics of Compound Semiconductor Interfaces (San Diego, Feb. 1976) in the Journal of Vacuum Science and Technology, May-June 1976.
8. R. C. Eden and W. H. Zakrzewski, "Semiautomatic Hall Effect Measurements System", Review of Scientific Instruments, Vol. 41, No. 7, pp. 1030-1033, July 1970.
9. J. S. Harris, Jr., "1.06 Micron High Sensitivity IR Photocathode", Tech. Rep. AFAL-TR-73-239, Aug. 1973.
10. J. S. Harris, Jr., "1.06 Micrometer High Sensitivity IR Photocathode", Tech. Rep. AFAL-TR-74-341, Jan. 1975.
11. G. A. Antypas and L. W. James, J. Appl. Phys. 41, 2165 (1970).
12. M. B. Panish and M. Ilegems, Progress in Solid State Chemistry, ed. by H. Reiss and J. McCaldin (Pergamon Press, New York, 1972) Vol. 7, P. 39.

13. M. B. Thomas, W. M. Coderre and J. C. Woolley, Phys. Stat. Sol. A2, K141 (1970).
14. G. H. Olsen and M. Ettenberg, J. Appl. Phys. 45, 5112 (1974).

APPENDIX A.1

```

      \ AVAL
[11] C=1.607E-19
[12] A1=1.31056E-3
[13] FFP=1.95
[14] '
[15] '                                     /AVALANCHE PHOTOIODE NOISE CALCULATION'

[16] '
[17] '           SYSTEM PARAMETERS ASSUMED:
[18] '
[19] ' /ATA RATE, R (LITS/SEC)'
[20] R
[21] ' (ON-TO-OFF) LIGHT OVER RATIO, F'
[22] F
[23] ' DESIRED SIGNAL TO NOISE, S0; S0=5.61200 GIVES 1E-6 ERROR RATE, S0=3.71902 GIVES 1E-6, ETC.'
[24] S0
[25] '
[26] '           PREAMPLIFIER PARAMETERS:
[27] '
[28] ' LOAD RESISTANCE, RL (OHMS)'
[29] RL
[30] ' PREAMP NOISE FACTOR, NF'
[31] NF
[32] RN=R11
[33] INJSQ=((1/NF)*KB*TEMP*RN)/PL
[34] ' PREAMP INPUT NOISE CURRENT, INP (AMP)'
[35] INJSQ*0.5
[36] '
[37] '           AVALANCHE PHOTOIODE DETECTOR PARAMETERS:
[38] '
[39] ' QUANTUM EFFICIENCY, QE'
[40] QE
[41] ' DARK CURRENT, ID'
[42] ID
[43] ' EXCESS NOISE FACTOR, AN'
[44] AN
[45] '
[46] '
[47] '
[48] '
[49] '
[50] '
[51] '
[52] '
[53] '
[54] '
[55] '
[56] '
[57] '
[58] '
[59] '
[60] '
[61] '
[62] '
[63] '
[64] '
[65] '
[66] '
[67] '
[68] '
[69] '
[70] '
[71] '
[72] '
[73] '
[74] '
[75] '
[76] '
[77] '
[78] '
[79] '
[80] '
[81] '
[82] '
[83] '
[84] '
[85] '
[86] '
[87] '
[88] '
[89] '
[90] '
[91] '
[92] '
[93] '
[94] '
[95] '
[96] '
[97] '
[98] '
[99] '
[100] '
[101] '
[102] '
[103] '
[104] '
[105] '
[106] '
[107] '
[108] '
[109] '
[110] '
[111] '
[112] '
[113] '
[114] '
[115] '
[116] '
[117] '
[118] '
[119] '
[120] '
[121] '
[122] '
[123] '
[124] '
[125] '
[126] '
[127] '
[128] '
[129] '
[130] '
[131] '
[132] '
[133] '
[134] '
[135] '
[136] '
[137] '
[138] '
[139] '
[140] '
[141] '
[142] '
[143] '
[144] '
[145] '
[146] '
[147] '
[148] '
[149] '
[150] '
[151] '
[152] '
[153] '
[154] '
[155] '
[156] '
[157] '
[158] '
[159] '
[160] '
[161] '
[162] '
[163] '
[164] '
[165] '
[166] '
[167] '
[168] '
[169] '
[170] '
[171] '
[172] '
[173] '
[174] '
[175] '
[176] '
[177] '
[178] '
[179] '
[180] '
[181] '
[182] '
[183] '
[184] '
[185] '
[186] '
[187] '
[188] '
[189] '
[190] '
[191] '
[192] '
[193] '
[194] '
[195] '
[196] '
[197] '
[198] '
[199] '
[200] '
[201] '
[202] '
[203] '
[204] '
[205] '
[206] '
[207] '
[208] '
[209] '
[210] '
[211] '
[212] '
[213] '
[214] '
[215] '
[216] '
[217] '
[218] '
[219] '
[220] '
[221] '
[222] '
[223] '
[224] '
[225] '
[226] '
[227] '
[228] '
[229] '
[230] '
[231] '
[232] '
[233] '
[234] '
[235] '
[236] '
[237] '
[238] '
[239] '
[240] '
[241] '
[242] '
[243] '
[244] '
[245] '
[246] '
[247] '
[248] '
[249] '
[250] '
[251] '
[252] '
[253] '
[254] '
[255] '
[256] '
[257] '
[258] '
[259] '
[260] '
[261] '
[262] '
[263] '
[264] '
[265] '
[266] '
[267] '
[268] '
[269] '
[270] '
[271] '
[272] '
[273] '
[274] '
[275] '
[276] '
[277] '
[278] '
[279] '
[280] '
[281] '
[282] '
[283] '
[284] '
[285] '
[286] '
[287] '
[288] '
[289] '
[290] '
[291] '
[292] '
[293] '
[294] '
[295] '
[296] '
[297] '
[298] '
[299] '
[300] '
[301] '
[302] '
[303] '
[304] '
[305] '
[306] '
[307] '
[308] '
[309] '
[310] '
[311] '
[312] '
[313] '
[314] '
[315] '
[316] '
[317] '
[318] '
[319] '
[320] '
[321] '
[322] '
[323] '
[324] '
[325] '
[326] '
[327] '
[328] '
[329] '
[330] '
[331] '
[332] '
[333] '
[334] '
[335] '
[336] '
[337] '
[338] '
[339] '
[340] '
[341] '
[342] '
[343] '
[344] '
[345] '
[346] '
[347] '
[348] '
[349] '
[350] '
[351] '
[352] '
[353] '
[354] '
[355] '
[356] '
[357] '
[358] '
[359] '
[360] '
[361] '
[362] '
[363] '
[364] '
[365] '
[366] '
[367] '
[368] '
[369] '
[370] '
[371] '
[372] '
[373] '
[374] '
[375] '
[376] '
[377] '
[378] '
[379] '
[380] '
[381] '
[382] '
[383] '
[384] '
[385] '
[386] '
[387] '
[388] '
[389] '
[390] '
[391] '
[392] '
[393] '
[394] '
[395] '
[396] '
[397] '
[398] '
[399] '
[400] '
[401] '
[402] '
[403] '
[404] '
[405] '
[406] '
[407] '
[408] '
[409] '
[410] '
[411] '
[412] '
[413] '
[414] '
[415] '
[416] '
[417] '
[418] '
[419] '
[420] '
[421] '
[422] '
[423] '
[424] '
[425] '
[426] '
[427] '
[428] '
[429] '
[430] '
[431] '
[432] '
[433] '
[434] '
[435] '
[436] '
[437] '
[438] '
[439] '
[440] '
[441] '
[442] '
[443] '
[444] '
[445] '
[446] '
[447] '
[448] '
[449] '
[450] '
[451] '
[452] '
[453] '
[454] '
[455] '
[456] '
[457] '
[458] '
[459] '
[460] '
[461] '
[462] '
[463] '
[464] '
[465] '
[466] '
[467] '
[468] '
[469] '
[470] '
[471] '
[472] '
[473] '
[474] '
[475] '
[476] '
[477] '
[478] '
[479] '
[480] '
[481] '
[482] '
[483] '
[484] '
[485] '
[486] '
[487] '
[488] '
[489] '
[490] '
[491] '
[492] '
[493] '
[494] '
[495] '
[496] '
[497] '
[498] '
[499] '
[500] '
[501] '
[502] '
[503] '
[504] '
[505] '
[506] '
[507] '
[508] '
[509] '
[510] '
[511] '
[512] '
[513] '
[514] '
[515] '
[516] '
[517] '
[518] '
[519] '
[520] '
[521] '
[522] '
[523] '
[524] '
[525] '
[526] '
[527] '
[528] '
[529] '
[530] '
[531] '
[532] '
[533] '
[534] '
[535] '
[536] '
[537] '
[538] '
[539] '
[540] '
[541] '
[542] '
[543] '
[544] '
[545] '
[546] '
[547] '
[548] '
[549] '
[550] '
[551] '
[552] '
[553] '
[554] '
[555] '
[556] '
[557] '
[558] '
[559] '
[560] '
[561] '
[562] '
[563] '
[564] '
[565] '
[566] '
[567] '
[568] '
[569] '
[570] '
[571] '
[572] '
[573] '
[574] '
[575] '
[576] '
[577] '
[578] '
[579] '
[580] '
[581] '
[582] '
[583] '
[584] '
[585] '
[586] '
[587] '
[588] '
[589] '
[590] '
[591] '
[592] '
[593] '
[594] '
[595] '
[596] '
[597] '
[598] '
[599] '
[600] '
[601] '
[602] '
[603] '
[604] '
[605] '
[606] '
[607] '
[608] '
[609] '
[610] '
[611] '
[612] '
[613] '
[614] '
[615] '
[616] '
[617] '
[618] '
[619] '
[620] '
[621] '
[622] '
[623] '
[624] '
[625] '
[626] '
[627] '
[628] '
[629] '
[630] '
[631] '
[632] '
[633] '
[634] '
[635] '
[636] '
[637] '
[638] '
[639] '
[640] '
[641] '
[642] '
[643] '
[644] '
[645] '
[646] '
[647] '
[648] '
[649] '
[650] '
[651] '
[652] '
[653] '
[654] '
[655] '
[656] '
[657] '
[658] '
[659] '
[660] '
[661] '
[662] '
[663] '
[664] '
[665] '
[666] '
[667] '
[668] '
[669] '
[670] '
[671] '
[672] '
[673] '
[674] '
[675] '
[676] '
[677] '
[678] '
[679] '
[680] '
[681] '
[682] '
[683] '
[684] '
[685] '
[686] '
[687] '
[688] '
[689] '
[690] '
[691] '
[692] '
[693] '
[694] '
[695] '
[696] '
[697] '
[698] '
[699] '
[700] '
[701] '
[702] '
[703] '
[704] '
[705] '
[706] '
[707] '
[708] '
[709] '
[710] '
[711] '
[712] '
[713] '
[714] '
[715] '
[716] '
[717] '
[718] '
[719] '
[720] '
[721] '
[722] '
[723] '
[724] '
[725] '
[726] '
[727] '
[728] '
[729] '
[730] '
[731] '
[732] '
[733] '
[734] '
[735] '
[736] '
[737] '
[738] '
[739] '
[740] '
[741] '
[742] '
[743] '
[744] '
[745] '
[746] '
[747] '
[748] '
[749] '
[750] '
[751] '
[752] '
[753] '
[754] '
[755] '
[756] '
[757] '
[758] '
[759] '
[760] '
[761] '
[762] '
[763] '
[764] '
[765] '
[766] '
[767] '
[768] '
[769] '
[770] '
[771] '
[772] '
[773] '
[774] '
[775] '
[776] '
[777] '
[778] '
[779] '
[780] '
[781] '
[782] '
[783] '
[784] '
[785] '
[786] '
[787] '
[788] '
[789] '
[790] '
[791] '
[792] '
[793] '
[794] '
[795] '
[796] '
[797] '
[798] '
[799] '
[800] '
[801] '
[802] '
[803] '
[804] '
[805] '
[806] '
[807] '
[808] '
[809] '
[810] '
[811] '
[812] '
[813] '
[814] '
[815] '
[816] '
[817] '
[818] '
[819] '
[820] '
[821] '
[822] '
[823] '
[824] '
[825] '
[826] '
[827] '
[828] '
[829] '
[830] '
[831] '
[832] '
[833] '
[834] '
[835] '
[836] '
[837] '
[838] '
[839] '
[840] '
[841] '
[842] '
[843] '
[844] '
[845] '
[846] '
[847] '
[848] '
[849] '
[850] '
[851] '
[852] '
[853] '
[854] '
[855] '
[856] '
[857] '
[858] '
[859] '
[860] '
[861] '
[862] '
[863] '
[864] '
[865] '
[866] '
[867] '
[868] '
[869] '
[870] '
[871] '
[872] '
[873] '
[874] '
[875] '
[876] '
[877] '
[878] '
[879] '
[880] '
[881] '
[882] '
[883] '
[884] '
[885] '
[886] '
[887] '
[888] '
[889] '
[890] '
[891] '
[892] '
[893] '
[894] '
[895] '
[896] '
[897] '
[898] '
[899] '
[900] '
[901] '
[902] '
[903] '
[904] '
[905] '
[906] '
[907] '
[908] '
[909] '
[910] '
[911] '
[912] '
[913] '
[914] '
[915] '
[916] '
[917] '
[918] '
[919] '
[920] '
[921] '
[922] '
[923] '
[924] '
[925] '
[926] '
[927] '
[928] '
[929] '
[930] '
[931] '
[932] '
[933] '
[934] '
[935] '
[936] '
[937] '
[938] '
[939] '
[940] '
[941] '
[942] '
[943] '
[944] '
[945] '
[946] '
[947] '
[948] '
[949] '
[950] '
[951] '
[952] '
[953] '
[954] '
[955] '
[956] '
[957] '
[958] '
[959] '
[960] '
[961] '
[962] '
[963] '
[964] '
[965] '
[966] '
[967] '
[968] '
[969] '
[970] '
[971] '
[972] '
[973] '
[974] '
[975] '
[976] '
[977] '
[978] '
[979] '
[980] '
[981] '
[982] '
[983] '
[984] '
[985] '
[986] '
[987] '
[988] '
[989] '
[990] '
[991] '
[992] '
[993] '
[994] '
[995] '
[996] '
[997] '
[998] '
[999] '

```

APPENDIX A.2

```

1100 REMARK RR FEEDBACK OP-AMP CLOSED-LOOP NOISE ANALYSIS
1101 LET DF=2E7
1102 PRINT "SIGNAL AND NOISE ANALYSIS OF SIMPLE FEEDBACK PREAMP"
1104 PRINT "PF=";PF;" OHMS. CF=";CF*1E12;" PF. CI=";CI*1E12;" PF. AO=";AO
1106 LET WO=1/(RF*(CI+CF));LET WA=FA*6.238;LET WF=1/(RF*CF)
1108 PRINT "FO=";WO/6.238E6;" MHZ. OPEN-LOOP F3DB, FA=";FA*1E-6;" MHZ"
1109 PRINT "FF=";WF/6.238E6;" MHZ";PRINT
1110 LET WP=1/(1/WF+1/(AO*WO)+1/(AO*WA))
1111 LET B=0;LET C=0;LET D=0
1112 LET TB=256;LET TC=256;LET TD=256
1113 LET SB=51.2*DF;LET SC=SB;LET SD=SB
1114 LET HB$="HZ";LET HC$="HZ";LET HD$="HZ"
1115 LET VB$="V/HZ";LET VC$="V/I";LET VD$="V/I"
1120 FOR K=0 TO 255
1121 LET V=K*DF*6.238
1122 LET DR=1+1/AO-(V*W)/(AO*WO*WA)
1126 LET DV=DR*DR+V*W/(WR*WR)
1128 LET RN=(DR+W*V/(WO*WR))/DV;LET JN=((DR-1)*W/WR)/DV
1130 LET C(256+K)=RF*DR/DV
1132 LET D(256+K)=-V*PF/(WR*DV)
1134 LET B(256+K)=RN*RN+JN*JN
1136 LET C(256-K)=C(256+K)
1138 LET D(256-K)=-D(256+K)
1140 LET B(256-K)=B(256+K)
1142 NEXT K
1143 LET HB=SB/2;LET HC=SC/2;LET HD=SD/2
1144 LET PB=B;LET PC=C;LET PD=D
1146 IF C,D,PA,X: INTEGRATE A,X:LET A=A*C(256)/X(100)
1147 LET VAS$="V/COUL";LET PA=A;LET VQ=MAX(A);PRINT "(V/C)PEAK=";VQ;"
    VOLTS/COULOMB";LABEL PA"IMPULSE RESPONSE"
1148 PRINT "CALCULATION OF GAIN FACTORS COMPLETE. ENTER ANY NO. TO
    START NOISE CALC."
1149 INPUT NG
1150 PRINT "NOISE CALCULATION; TO CHANGE EN VALUE,ETC. GOTO 1170"
1154 LET PD=C+C*D*D
1156 LET PC=SQR(D)
1158 INTEGRATE D,X
1160 LET NB=X(510)/(2*D(256))
1162 LET F3=(SC/51.2)*(CRS(C(256),.7071*C(256))-256)
1164 PRINT "CLOSED-LOOP F3DB=";F3;" HZ. NOISE BW=";NB;" HZ"
1168 LET C=D
1170 REMARK P RESTART POINT AFTER CHANGING LN FOR NOISE CALC
1172 LET IN=1.629E-20/RF
1174 PRINT "EN=";EN;" V/ROOT HZ. IN=";SQR(IN);" AMPS/ROOT HZ."
1176 LET D=EN*EN*B+IN*C
1178 INTEGRATE D,X
1180 LET N1=X(510)/2
1181 LET N0=(SQR(N1))/(VQ*1.602E-19)
1182 LET PD=SQR(D)
1184 PRINT "TOTAL OUTPUT VOLTAGE NOISE=";SQR(N1);"VOLTS"
1185 PRINT "MINIMUM DET'BL CURRENT IMPULSE NO=";N0;" ELECTRONS"
1186 PRINT "PEAK NOISE=";MAX(D);"V/RT HZ. HF=LF NOISE AT F=";(1E-6
    *SD/51.2)*(CRS(D(258),D(256))-256)
1188 STOP

```

APPENDIX A.3

```
8000 PRINT "GAUSSIAN FILTERED NOISE OUTPUT. T1=";T1*1E12;" PS."
8008 LET A=0
8010 LET GW=1/(6.283*T1)
8012 PRINT "STANDARD DEVIATION FREQUENCY=";GW;" HZ"
8020 LET JW=GW*51.2/SD
8022 LET C1=1/(2*JW*JW)
8025 LET J1=ITR(4.515*JW)
8028 IF J1>255 GOSUB 8190
8030 FOR J=0 TO J1
8040 LET A(J+256)=EXP(-(C1*J*J))
8050 NEXT J
8060 FOR J=1 TO J1
8062 LET A(256-J)=A(256+J)
8064 NEXT J
8066 LET TA=256:LET HA=HD:LET SA=SD:LET HAS="HZ"
8070 LET PA=A
8100 LET B=A*A
8105 LET PB=B*D*D
8110 INTEGRATE B,X
8120 LET NI=X(510)/2
8130 LET PB=SQR(B)
8140 PRINT "TOTAL OUTPUT VOLTAGE NOISE=";SQR(NI);" VOLTS"
8150 STOP
8190 LET J1=255
8192 RETURN
```

APPENDIX A.4

```

8300 PRINT "GAUSSIAN CONVOLUTION ON B. T1=";T1*1E12;" PS- (T1 IS STD.
      DEV."
8302 LET A=0
8310 LET SA=1.25E-9;LET HAS="S"
8320 LET JW=T1*51.2/SA
8330 LET C1=-1/(2*JW*JW)
8332 LET J1=ITR(4.515*JW)
8334 IF J1<T0 GOTO 8340
8336 LET J1=T0
8340 FOR J=0 TO J1
8342 LET A(T0+J)=EXP(C1*J*J)
8343 NEXT J
8344 FOR J=1 TO J1
8346 LET A(T0-J)=A(T0+J)
8348 NEXT J
8349 INTEGRATE A,X;LET PA=(A/(4E10*X(510)))
8350 PRINT "GAUSSIAN SAMPLING PULSE CALC'D IN A. RESTART AT 8350."
8352 LET PD=A
8360 CONVOLVE D,B,PC,X
8370 PRINT MAX(C),MAX(C)/MAX(B)
8380 STOP
8200 FOR J=0 TO 255
8210 LET B(2*J)=C(J);NEXT J
8220 LET B(1)=0;LET B(509)=0;LET B(511)=0
8230 FOR J=3 TO 507 STEP 2
8240 LET B(J)=(9*B(J-1)+9*B(J+1)-B(J-3)-B(J+3))/16
8250 NEXT J
8260 STOP

```

APPENDIX A.5

The computer program written to solve 2.36 for both the frequency and time domain response of the circuit of 2.10 is listed in this Appendix. The language is TEK BASIC, an extension of the Harvard BASIC for the Tektronix Digital Processing Oscilloscope. The program will run with TEK BASIC in a PDP 11/05 with 24K or more of memory (TEK BASIC uses nearly 16K, while this program with its defined arrays uses less than 8K). The program is oriented for use with a Tektronix 4010 display terminal for graphing, special function plotting, and rapid display of the extensive parameter data. The complete calculation is carried out by calling successively line numbers 100, 200, 300 (+ 700 for hard copy) and 400 (+ 800 for hard copy), with lines 900 and 1000 for additional parameter output. Lines 100-154 initializes (if necessary) and displays the circuit parameters along with the dc V_o/i_p in order to verify that everything is right before the calculation is begun. The frequency-domain solution of 2.36 is called out in lines 200 to 260, with the actual calculation organized in the subroutine lines 2000-2244. Because of the complexity of the calculation and the fact that most of the "action" is at low frequencies, in order to save time, 2.36 is solved at every discrete frequency point only from $J = 0$ to $J = 34$ (where $F = J \times FE$, where F.E. is the frequency per element; usually 40 MHz). For $J = 35$ to 64, only every other element is calculated exactly, from $J = 65$ to 128 every 4th element, and from $J = 129$ to 256 every 8th element is calculated from Eq. 2.36. The interpolation for in-between points is made with parabolic approximation individually for the real part of the numerator (NR), the imaginary part of the numerator (NI), the real part of the denominator (DR) and the imaginary part of the denominator (DI). These functions are interpolated individually before taking the complex quotient in Eq. 2.36 because NR, NI, DR and DI are individually smooth functions of frequency, but their quotient may not be (in fact it can be singular if DR and DI both go to zero at some frequency). At the points of actual calculation, the various complex G's in Eq. 2.36 are calculated in

lines 2500 to 2570, the latter $[(1/G_S) - \text{multiplied}]$ terms in the numerator and denominator are calculated in lines 3000 to 3050 (these lines are skipped if the parasitic impedance, $1/G_S$, is zero), while the rest of the numerator and denominator terms are calculated in lines 3100 to 3126. The resulting NR, NI, DR and DI results are stored in individual arrays for interpolation and actually carrying out the complex quotient to give V_O/i_p (the real and imaginary components of which are stored in arrays C and D). All of the above subroutines are executed as a part of the program at line 200. The program at line 300 (to 392) calculates the noise bandwidth, NB, from this frequency response data, and also converts the real and imaginary form of data into magnitude-phase form for display in processor arrays A and B (with hard-copy by calling line 700; see the lower right-hand portion of Fig. A.1). The program at line 400 uses the inverse Fourier transform (IFT) to convert the real and imaginary form of frequency domain data to the time domain. The IFT directly gives an unnormalized impulse response, but this is integrated to give the step response and then both are normalized by noting that the magnitude of the step at large time must equal the magnitude of V_O/I_i at $F = 0$ (called R_0). From the peak of the normalized impulse response and the Johnson noise calculated from the noise bandwidth, the minimum detectable current pulse is calculated. Line 800 displays this transient response data for hard copy (as shown in the upper left portion of Fig. A.1). The plotting program, lines 1000 to 1099 graphs individually the real and imaginary components of the denominator, DR and DI, along with the magnitude, $DM = [DR^2 + DI^2]^{1/2}$, for the frequency range 0 to 1.4 GHz. In this frequency range the numerator of Eq. 2.36 is more or less constant (dominated by g_m), so that DR and DI are the keys to the response. In particular, if both DR and DI approach zero at the same frequency, the amplifier will oscillate at that frequency. Figure A.1 shows the results from this program for the case with no parasitic source impedance ($1/G_S = 0$) with typical parameter values for a Mark IA preamp. Note that in this calculation, the GAASFET

input voltage noise is not considered ($e_1 = 0$ in Fig. 2.8), so that the output noise on N_0 values will be too low.

APPENDIX I. COMPUTER PROGRAM FOR 3-NODE (PARASITIC) MODEL OF MESFET PREAMP 1st STAGE (DPO TEK BASIC LANGUAGE)

```

PRECEDENCE 3-NODE GMS FET PREAMP CALCULATION (SHORTENED). 74-84
10101
10102 DPO TEL EN. IC 001-01
10103 REMARK P 3-NODE (PARASITIC) MESFET PREAMP CALCULATION
10104 PRINT "CAL"
10105 PICTURE
10106 LET EN=1 LET J=PO LET RO=J+1 LET J=RL LET EN=0
10107 PRINT "PARAMETERS FOR 3-NODE MESFET PREAMP CALCULATION RUN #":RO
10108 IF J=0 GOSUB 4000
10109 GOSUB 4100
10110 LET NF=(PF*PF*(GM*(1/RO)))
10111 LET CR=(NF+1*PO+1*FL+1/RI)
10112 LET NF=GM*(1/RF+NR)
10113 LET OF=OP*(1+FS*FL+RS*FS)/RO+1/RB+1/RL)/RI
10114 LET CF=OP*(1*PO+1*RL+1*RB+1/PI+GM)/RF
10115 LET FO=NR OR
10116 PRINT PRINT PRINT "NO. 1P FOR THIS CALCULATION WILL BE RO=":RO:""O
HMS "
10117 PRINT PRINT PRINT "PLEASE EXAMINE THE ABOVE QUANTITIES CAREFULLY.
IF ALL ARE OK, PRESS ANY KEY TO CONTINUE TO CHANGE ANY PARAMETERS, HIT
'PECLT' OR 'ETPL P' AND START OVER AFTER MAKING CHANGES."
10118 LET BC=10010R
10119 WAIT
10120 STOP
10121 PRINT PRINT "CALCULATION OF FREQUENCY RESPONSE HAS STARTED."
10122 LET FL=1 IF FS=0 LET FL=0 IF LS=0 LET FL=0
10123 LET C=0 LET D=0 LET SC=51 21FE LET HCF="HZ"
10124 LET SC=17 LET HCF=HCF
10125 LET CI=1 RI LET GO=1 RO LET GF=1/RF LET GB=1/RB
10126 DIMENSION U(272) DIMENSION UI(272) DIMENSION BR(272)
10127 DIMENSION BI(272)
10128 LET UF=0 LET UI=0 LET FF=0 LET BI=0 LET NA=0
10129 DIMENSION F(272) DIMENSION G(272) DIMENSION BK(272)
10130 LET C=0 LET BI=0 LET EN=0
10131 LET U=0 2831FE
10132 DATA 0.0,0.0,0.0,0.0,0.0,0.0
10133 READ F,GB,FS,TR,IN,OP,RO,F2,F3,FY
10134 GOSUB 7100
10135 LET J=1 589 FE
10136 REMARK H ACTUAL CALCULATION PROCEDURE AT 2000
10137 LET EN=1
10138 GOSUB 3000
10139 LET EN=0
10140 STOP
10141 REMARK P CALCULATE & DISPLAY GAIN-PHASE
10142 IF C=250=0 GOSUB 7000
10143 LET A=C/1000
10144 INTEGRATE H/B
10145 LET NG=510*(1/21)(256)
10146 LET U=OP*(1/256-201)(256)
10147 LET NF=OP*(1/256)
10148 LET F2=OP*(OP*(1/256), 7071100)-256)
10149 LET EN=1 LET F=0.0/0 LET EN=0
10150 LET TA=58 LET HA=589 LET TS=TA LET HB=HA
10151 LET F=HA LET F=5 GOSUB 7100
10152 GOSUB 7000 PRINT "MAGNITUDE U/I F3=":F3:"HZ"
10153 GOSUB 7200 PRINT "PHASE OF U/I P"
10154 STOP
10155 REMARK P CALCULATE (IFT) & DISPLAY IMPULSE AND STEP RESPONSE
10156 IF C=250=0 GOSUB 7000
10157 GOSUB 7100
10158 LET IFT=0 PA=PE
10159 INTEGRATE A PO LET NF=PO (1/510)
10160 LET U=510-1000 LET U=0-1000000
10161 LET F=0 LET U=0-1000000
10162 LET TA=58 LET HA=589 LET TS=TA LET HB=HA
10163 LET F=HA LET F=5 GOSUB 7100
10164 GOSUB 7000 PRINT "MAGNITUDE U/I F3=":F3:"HZ"
10165 GOSUB 7200 PRINT "PHASE OF U/I P"
10166 STOP
10167 REMARK P CALCULATE (IFT) & DISPLAY IMPULSE AND STEP RESPONSE
10168 IF C=250=0 GOSUB 7000
10169 GOSUB 7100
10170 LET IFT=0 PA=PE
10171 INTEGRATE A PO LET NF=PO (1/510)
10172 LET U=510-1000 LET U=0-1000000
10173 LET F=0 LET U=0-1000000
10174 LET TA=58 LET HA=589 LET TS=TA LET HB=HA
10175 LET F=HA LET F=5 GOSUB 7100
10176 GOSUB 7000 PRINT "MAGNITUDE U/I F3=":F3:"HZ"
10177 GOSUB 7200 PRINT "PHASE OF U/I P"
10178 STOP

```

```

700 REMARK P GRAPH & HARD COPY OF GAIN-PHASE
710 PRINT "C-L"
720 GOSUB 8000
730 PRINT "MAGNITUDE AND PHASE (0.5 DB/DIV) OF VO/IP. RF=";RF; ", RL=";
    PL;" LL=";LL11E9;"NHV, LS";LS11E9;"NHV"
740 GRAPH PA,PB
750 PRINT "RO=";RO;" F30E=";F311E-6;" MHZ, NOISE BN=";NB;"^C^N^C^L"
760 STOP

800 REMARK P GRAPH & HARD COPY IMPULSE AND STEP RESPONSE
810 PRINT "C-L"
820 GOSUB 8000
830 PRINT "IMPULSE AND STEP RESPONSE RF=";RF; ", RL=";PL;" LL=";LL11E9
    ;"NHV, LS=";LS11E-9;"NHV"
840 GRAPH PA,PB
850 PRINT "(U/Q)=";UP11E12," U/C, HQ=";HQ;" EL, RO=";RO," NB=";NB;"^C^N
    ^C^L"
860 STOP

900 REMARK R PRINTOUT OF CALC DATA AND PERFORMANCE PARAMETERS
905 PRINT "C-L"
910 GOSUB 8000
920 PRINT PRINT "PRINTOUT OF PPEAMP PARAMETERS AND CALC'D PERFORMANCE
    RESULTS"
930 PRINT "PPEAMP CIRCUIT ELEMENT VALUES"
940 GOSUB 4100
950 PRINT PRINT "PERFORMANCE RESULTS:" PRINT
960 PRINT "30E BWWIDTH, F3=";F311E-6," HZ"
970 PRINT "10% TO 90% RISETIME, TR=";TR;" S"
980 PRINT "DC TRANSIMPEDANCE, RO=";RO;" VOLTS/AMP (RO=";RO;" FROM DC C
    ALL)"
990 PRINT "NOISE BANDWIDTH, NB=";NB11E-6," MHZ"
1000 PRINT "JOHNSON NOISE, NI=";NI;" VOLTS"
1010 PRINT "PEAK IMPULSE RESPONSE, (U/Q)=";UP11E12," VOLTS COULOMB"
1020 PRINT "MINIMUM DETECTABLE CURRENT PULSE, HQ=";HQ;" ELECTRONS"
1030 STOP

1040 REMARK R PLOT-OUT OF DR-DI-DM FROM 0 TO 1.4GHZ  $V_A = \frac{NR + jNI}{DR + jDI}$ ;  $DM = \sqrt{Dk^2 + LI^2}$ 
1050 LET EN=1
1060 FOR I=300 TO 1000 STEP 100:PLOT 0.1,70:PLOT 1.1,770:NEXT I
1070 FOR I=70 TO 770 STEP 100:PLOT 0.300,1:PLOT 1.1000,1:NEXT I
1080 LET SS= 2+1E-5
1090 FOR I=0 TO 1.41 STEP SS:PLOT 0,(500+1+255),45:PRINT "A_"I NEXT I
1100 PLOT 0.340,55:PRINT "A_DM=0"
1110 PLOT 0.340,55:PRINT "A_DR=0"
1120 PLOT 0.340,55:PRINT "A_DI=0"
1130 PLOT 0.340,55:PRINT "A_FREQUENCY (GHZ)=J":PLOT 0.0,100:PRINT "A_"
1140 LET SI=PL 266
1150 LET EN=250 E0.0 IF BF>0 THEN LET EN=BN/BF
1160 PLOT 0.350,750:PRINT "A_1 DIV VERT =" ,100/BN
1170 LET IN=1.401E9/FE
1180 LET IF=270 5
1190 PLOT 0.300,800:PRINT EN+KF
1200 FOR I=0 TO IN
1210 LET K=BN/I+EN+KF GOSUB 1090
1220 PLOT 1.1,85+700 S,K NEXT I
1230 LET EN=250 E0.0 IF BF>0 THEN LET EN=BN/BF
1240 LET IF=270 5
1250 PLOT 0.300,810:PRINT EN+KF
1260 FOR I=0 TO IN
1270 LET I=BN/I+EN+KF GOSUB 1090
1280 PLOT 1.1,85+700 S,K NEXT I
1290 LET EN=250 E0.0 IF BF>0 THEN LET EN=BN/BF
1300 LET IF=270 5
1310 PLOT 0.300,820:PRINT EN+KF
1320 FOR I=0 TO IN
1330 LET K=BN/I+EN+KF GOSUB 1090
1340 PLOT 1.1,85+700 S,K NEXT I
1350 PLOT 0.0,750:PRINT "A_"
1360 LET EN=0:PRINT "RUNNING" :RU STOP
1370 IF I.700 GOTO 1093
1380 IF I.0 GOTO 1093
1390 RETURN
1400 LET EN=EN*10 LET K=(I+IF)/10+KF
1410 IF I.700 GOTO 1097
1420 IF I.0 GOTO 1097
1430 RETURN
1440 LET EN=EN*10 LET K=(I+IF)/10+KF
1450 RETURN
1460 STOP

```

THIS PLOT ROUTINE GIVES
 THE REAL FREQUENCY VALUES OF
 THE A (DR) AND IMAGINARY (DI)
 COMPONENTS OF THE DENOMINATOR
 OF EQ. 3, ALONG WITH THE
 MAGNITUDE OF THE DENOMINATOR (LI)

⇒ 2000 REMARK P ORGANIZING ROUTINE FOR FREQUENCY RESPONSE CALCULATION

2001 IF FF=1 PRINT "2000"

2010 FOR J=0 TO 34

FOR J=0 TO 34 (F.O. 34*FL WHERE FL IS THE STEPSIZE - 40MHz) EACH POINT IS CALCULATED, N INTERPOLATED

2020 GOSUB 6000

2030 GOSUB 6100

2040 NEXT J

2050 LET J=34 GOSUB 6000

2060 GOSUB 6100

2070 FOR J=36 TO 64 STEP 2

FOR J=35 TO 64 EVERY OTHER POINT IS CALCULATED, WHILE IN-BETWEEN POINTS ARE INTERPOLATED.

2080 GOSUB 6000

2090 GOSUB 6100

2100 LET I=J-3 GOSUB 6200

INTERPOLATION IS INDIVIDUAL FOR NR, NI, LA, DI (4 FUNCTIONS) AND -OR- LET DIVIDE IS CARRIED OUT AFTER INTERPOLATION.

2110 GOSUB 6300

2120 NEXT J

2130 LET J=64 GOSUB 6000

2140 GOSUB 6100

2150 FOR J=71 TO 138 STEP 4

FOR J=65 TO 128 EVERY 4th POINT IS

2160 GOSUB 6000

CALCULATED WITH IN-BETWEEN POINTS INTERPOLATED

2170 GOSUB 6100

2180 LET I=J-2 GOSUB 6400

2190 GOSUB 6300

2200 LET I=J-2 GOSUB 6200

2210 GOSUB 6300

2220 LET I=J-7 GOSUB 6200

2230 GOSUB 6300

2240 NEXT J

2250 LET J=138 GOSUB 6000

2260 GOSUB 6100

2270 FOR J=144 TO 272 STEP 8

FOR J=129 TO 255 EVERY 8th POINT IS

2280 GOSUB 6000

CALCULATED WITH IN-BETWEEN POINTS INTERPOLATED

2290 GOSUB 6100

2300 LET I=J-12 GOSUB 6500

2310 GOSUB 6300

2320 LET I=J-18 GOSUB 6400

2330 GOSUB 6300

2340 LET I=J-21 GOSUB 6200

2350 GOSUB 6300

2360 LET I=J-19 GOSUB 6200

2370 GOSUB 6300

2380 LET I=J-14 GOSUB 6400

2390 GOSUB 6300

2400 LET I=J-17 GOSUB 6200

2410 GOSUB 6300

2420 NEXT J

2430 REMARK P THIS COMPLETES THE CALCULATION OF THE 256 FREQUENCY PTS

2440 LET RO=C(356)

2450 IF FT=0 THEN LET J=255

2460 IF FT=0 GOSUB 7700

2470 RETURN

⇒ 2500 REMARK R CALCULATE COMPLEX G'S FOR GIVEN FREQUENCY

2501 IF FF=1 PRINT "2500"

2510 LET W=WM*J: IF W=0 LET N=001

2520 LET JI=HXCP: LET DR=RG: LET DI=-1/(HXCG) GOSUB 5200

2530 LET GG=HXCP: LET JG=M1: LET DR=1: LET DI=HXCP: GOSUB 5200

2540 LET GN=HXCP: LET GI=GN: LET JG=HXCP: LET JF=HXCP

2550 LET DR=RG+FL*1E-20: LET DI=HILS: GOSUB 5300

2560 LET GS=H0: LET JS=H1: HNC5: LET DI=H1: GOSUB 5200

2570 REMARK R LINES 2544-2546 FOR "LQ" FORM OF LOAD 2543 CHITS 'EM

2580 GOTO 2550

2590 LET DR=M3: LET DI=H1: HXCP: GOSUB 5200

2600 LET DI=M3: LET DI=H1: HXCP: GOSUB 5200

2610 LET GL=M3: GS: LET JI=H1: HNC5

2620 LET NR=0: LET NI=0: LET DR=0: LET DI=0

2630 RETURN

RE, IM (1/FL) VS FREQUENCY
COMPLETES RE AND IM

$$G_T = G_I + jJ_T$$

$$G_F = G_I + jJ_F$$

$$G_G = G_G + jJ_G$$

$$y_n = G_0 + jG_L$$

$$G_L = G_D + jJ_L \text{ etc.}$$

USED ONLY WHEN A LOAD WITH AN INDUCED ANGLE LQ BETWEEN DRAIN AND RL, LL IS CONSIDERED. LINE 2543 NORMALLY CAUSES THIS TO BE SKIPPED

```

=> 3000 REMARK P 00 IF CALCULATION PORTION REQUIRED FOR RS,LS>0
3001 IF FF=1 PRINT 3000
3010 LET HQ=CO+GG+GO LET HI=JO+JG+GI LET HQ=GF LET HI=JF GOSUB 5000
3012 LET TI=HI LET TI=HI LET HQ=GO LET HI=JO LET HQ=GG LET HI=JG GOSUB 5
000
3016 LET HQ=HQ+TI LET HI=HI+TI LET HQ=GS LET HI=JS GOSUB 5100
3020 LET HQ=HQ LET HI=HI LET HQ=GL+GI LET HI=JL+JI GOSUB 5000
3024 LET HQ=HQ LET HI=HI LET HQ=GL LET HI=JL LET HQ=GO+GG
3028 LET HI=JO+JG GOSUB 5000
3032 LET TI=HI LET TI=HI LET HQ=GG LET HI=JG LET HQ=GO LET HI=GI
3036 GOSUB 5000
3040 LET HQ=HQ+TI LET HI=HI+TI LET HQ=GS LET HI=JS GOSUB 5100
3044 LET HQ=GI LET HI=JI GOSUB 5000
3048 LET HQ=HQ+GO LET HI=HI+GI
3052 RETURN
=> 3100 REMARK P 00 IF CALCULATION-FINAL PART (PART REQ'D EVEN IF RS=LS=0) COMPLETE CALCULATION
3101 IF FF=1 PRINT 3100
3110 LET HQ=HQ+GF+GO LET HI=HI+JF+GI
3114 LET HQ=GO+GL LET HI=JO+JL LET HQ=GG+GI LET HI=JG+JI GOSUB 5000
3118 LET HQ=HQ+GO LET HI=HI+GI LET HQ=GF LET HI=JF
3122 LET HQ=GO+GL+GG+GI+GO LET HI=JO+JL+JG+JI+GI GOSUB 5000
3126 LET HQ=HQ+GO LET HI=HI+GI
3130 RETURN
=> 3200 REMARK P 00 OUTLINE TO CALCULATE (HR+JHI)/(OR+JOI)
3201 IF FF=1 PRINT 3200
3204 LET HQ=HR LET HI=HI LET HQ=OR LET HI=OI GOSUB 5100
3212 LET HQ=J+HR LET HI=J+HI LET HQ=OR LET HI=OI
3220 RETURN
=> 4000 REMARK P 00 PARAMETER DATA FOR MESFET PREAMP
4010 LET PS=2E4 LET FO=750 LET FF=5000 LET RG=10
4020 LET PI=3E5 LET PL=1000 LET PS=15
4030 LET CO=5E-13 LET CF=2E-14 LET CG=4E-13 LET CL=1E-12
4040 LET CP=3E-13 LET CS=0
4050 LET GM= 0.12 LET LL=2E-7 LET LS=0
4060 LET FE=4E7
4070 RETURN
=> 4100 PRINT "INPUT CIRCUIT PARAMETERS:"
4102 PRINT "RI=";RI;" OHMS  CF=CF;" CF;" PF."
4104 PRINT "FEEDBACK PARAMETERS:"
4106 PRINT "FI=";FI;" OHMS  CF=CF;" CF;" PF."
4108 PRINT "SOURCE PARASITIC PARAMETERS:"
4110 PRINT "PS=";PS;" OHMS  LS=";LS;" NANOHENRIES. CS=";CS;" PF."
4112 PRINT "LOAD PARAMETERS:"
4114 PRINT "RL=";RL;" OHMS  RG=";RG;" OHMS. LL=";LL;" NHY. CL=";CL;" PF."
4116 PRINT "MESFET PARAMETERS:"
4118 PRINT "GM=";GM;" MHOS. RG=";RG;" OHMS. CG=";CG;" PF. CO=";CO;" PF."
4120 RETURN
=> 5000 REMARK P 00 COMPLEX MULTIPLY SUBROUTINE. M=N*A
5002 LET HQ=HO*HO+HI*HI LET HI=HO*HI+HI*HO
5004 RETURN
=> 5100 REMARK P 00 COMPLEX DIVIDE SUBROUTINE. M=N/D
5102 LET HQ=HO*HO+HI*HI LET HQ=HO*HO+HI*HI LET HI=(HI*HO-HO*HI)/HQ
5104 RETURN
=> 5200 REMARK P 00 COMPLEX INVERSION SUBROUTINE. 1/D=M
5202 LET HQ=HO*HO+HI*HI LET HQ=HO*HO+HI*HI LET HI=-HI/HQ
5204 RETURN
=> 6000 REMARK P 00 SUBROUTINE SEQUENCER FOR EACH CALCULATED J VALUE
6001 IF FF=1 PRINT 6000
6010 GOSUB 3500
6015 LET HQ=0 LET HI=0 LET OR=0 LET OI=0
6020 IF FL=0 GOSUB 3000
6030 GOSUB 3100
6040 GOSUB 3200
6050 RETURN
=> 6100 REMARK P 00 DATA LOG SUBROUTINE FOR CALCULATED POINTS
6101 IF FF=1 PRINT 6100
6104 IF J<55 GOTO 6100
6106 IF J<55 GOTO 6100
6108 IF J<55 GOTO 6100
6110 LET C=J/55.00 LET C=J/55.00 LET C=J/55.00
6112 IF J<55 GOTO 6100
6114 IF J<55 GOTO 6100
6116 RETURN

```

A5

245

APPENDIX A.6

```

100 REMARK PR NOISE HISTOGRAM ANALYSIS
101 LET PB=0
102 HOLD B,B0;FP,DG
105 DISPLAY "NOISE HISTOGRAM. SET B VERT FOR <2.5 DIV PEAK-ZERO CENTER
      -AND PANEL STORE."
106 PRINT "AFTER SETTING UP INPUTS, ENTER ANY NUMBER"
110 INPUT QZ
120 PRINT "HOW MANY WAVEFORMS DO YOU WANT TO AVERAGE?"
125 INPUT NK
129 LET B=PB
130 GET B;0,SF
132 LET A=0
135 LET SA=SF/2
140 LET HAS=DUS
144 LET HC=102.4/SF
145 LET B=PB
146 LET WE=SB
150 REMARK RM LOOP
151 FOR K=1 TO NK
155 LET NG=0
156 STR B
157 FOR WJ=0 TO WE+.004 STEP .002
158 LET NG=NG+0
159 NEXT WJ
160 HOLD B
161 LET B=PB
162 LET B=B-MEA(B)
164 LET B=B+HC+256.02
170 FOR J=0 TO 510
172 LET A(B(J))=A(B(J))+1
178 NEXT J
180 NEXT K
181 LET HC=0:LET PA=A:STOP

200 REMARK PR RMS ANALYSIS OF NOISE HISTOGRAMS
202 LET N=0:LET N1=0:LET N2=0
204 FOR J=0 TO 511
206 LET S=A(J)
207 IF S=0 GOTO 216
208 LET N=N+S
210 LET DX=J-256
212 LET S=S*DX:LET N1=N1+S
214 LET N2=N2+S*DX
216 NEXT J
220 LET M1=N1/N:LET MS=(N2/N)-(M1*M1)
224 LET P1=SQR(MS)
226 LET CF=SA/51.2:LET M=M1*CF
228 LET PM=P1*CF
230 PRINT "TOTAL OF",N,"POINTS MEASURED."
232 PRINT "DISTRIBUTION CENTER (MEAN) IS AT",M,HAS,"(CENTER ZERO). ("
      ,M1,"ELEMENTS)."
234 PRINT "ROOT MEAN SQUARE DEVIATION IS",PM,HAS,". (THIS IS",P1,"ELE
      MENTS)."
240 STOP

```

APPENDIX A.7

```

300 REMARK PP GAUSSIAN FITTING TO NOISE HISTOGRAM
301 GOSUB 2200
302 LET IM=1
304 LET PB=LOG(D)
305 LET EM=0
307 LET CS=-2
308 HOLD D
310 HOLD ME,B,FP
311 LET SB=SA:LET HB=HAS
312 LABEL PB,"LOG OF HISTOGRAM"
314 LET PC=0:LET C1=0:LET C2=0
316 LET AR=ITR(0.3*PI)
318 LET AC=ITR(256*MI+.5)
320 FOR K=(AC-AP) TO AC+AR
322 LET C1=C1+1
324 LET C2=C2+B(K)
326 NEXT K
328 LET K0=.015+C2/C1
330 LET C3=0.5/(R1*PI)
332 FOR J=0 TO 511
334 LET DX=J-(256*MI)
336 LET C4=K0-DX*DX*C3
338 IF C4>C5 GOTO 348
340 LET C(J)=0
342 GOTO 350
348 LET C(J)=C4
350 NEXT J
352 PRINT "GAUSSIAN CALCULATED IN PC"
354 PRINT "LOG Z=K0-(X-M)2/(2*PI*CF)"
356 PRINT "K0=",K0,"EXP(K0)=",EXP(K0)
358 PRINT "FM, THE STANDARD DEVIATION, IS",R1*CF,HAS,"OF",R1,"ELEMENTS."
360 LET SC=SA:LET HC=HAS
362 LET PC=C
364 STOP

2200 REMARK PPR GAUSSIAN SMOOTHING FOR HISTOGRAMS
2202 LET PD=0:LET SD=SA:LET HD=HAS:LET VD=VAS
2204 FOR J=3 TO 508
2206 LET D(J)=(A(J-3)+2*A(J-2)+4*A(J-1)+5*A(J)+4*A(J+1)+2*A(J+2)+A(J+3))
      /19
2208 NEXT J
2210 LET PD=D
2212 RETURN

400 REMARK PP NOISE ANALYSIS IN FREQ DOMAIN
402 LET A=0
404 LET VE=SB
405 FOR J=0 TO JM
410 STR PB
411 FOR WJ=0 TO VE+.004 STEP .002:NEXT WJ:HOLD PB
412 LET B=PB:LET B=B-MEA(B)
415 FFT B,PC,PD
420 LET PA=A+SQR(C+C*D*D)
425 NEXT J
426 LET SA=SC:LET HA=HC:LET VA=VC
430 LET C=A/(JM+1)
435 LET TC=256:LET HC=SC/2:LET PC=C:LET TC=0:LET HC=0
436 HOLD PC
440 STOP

```


APPENDIX A.8

```

600 REMARK PR PROGRAM FOR 3DB BANDWIDTH OF C
610 LET C0=MAX(C)
620 LET F3=(SC/51.2)*(CRS(C(256))+.7071*C0)-256)
630 PRINT "3DB BANDWIDTH OF C (RELATIVE TO MAX) IS F3=";F3;HC$
640 STOP

1000 LET A0=A1:LET A1=0
1001 PRINT " ARRAY TO BE AVERAGED IS (A=1, B=2, C=3, D=4):"
1002 INPUT A1
1004 IF A1=1 THEN LET TUS="A"
1006 IF A1=2 THEN LET TUS="B"
1008 IF A1=3 THEN LET TUS="C"
1010 IF A1=4 THEN LET TUS="D"
1012 IF A1=0 THEN LET A1=A0
1020 PRINT "AVERAGE ROUTINE ON ARRAY ";TUS;": INPUT J START AND J FINAL"
1022 INPUT JS,JF
1024 LET AV=0:LET JW=JF-JS+1
1025 IF A1=1 GOTO 1030
1026 IF A1=2 GOTO 1040
1027 IF A1=3 GOTO 1050
1028 IF A1=4 GOTO 1060
1029 PRINT "INVALID ARRAY SELECTED (YOU GOOFED). ABORT.":STOP
1030 FOR J=JS TO JF
1032 LET AV=AV+A(J)
1034 NEXT J
1036 GOTO 1070
1040 FOR J=JS TO JF
1042 LET AV=AV+B(J)
1044 NEXT J
1046 GOTO 1070
1050 FOR J=JS TO JF
1052 LET AV=AV+C(J)
1054 NEXT J
1056 GOTO 1070
1060 FOR J=JS TO JF
1062 LET AV=AV+D(J)
1064 NEXT J
1070 LET AV=AV/JW
1072 PRINT "AVERAGE OF ";TUS;" FROM J=";JS;" TO ";JF;" IS AV=";AV
1074 STOP

1200 PRINT "ATTENUATE B BY FACTOR OF ";AF;" PER EL STARTING AT J="
1202 LET EM=1:LET MF=AF
1203 IF MF=0 THEN LET AF=0.98
1204 PRINT "ATTENUATE B BY FACTOR OF ";AF;" PER EL STARTING AT J="
1210 LET MF=1
1212 INPUT JS
1220 FOR J=JS TO 511
1230 LET B(J)=B(J)*MF:LET MF=MF*AF
1240 NEXT J:LET PB=B
1244 LET EM=0
1250 STOP

1300 REMARK RR PROGRAM TO CALCULATE NOISE BANDWIDTH OF MAG ARRAY IN C
1310 DIMENSION X(511)
1320 PRINT "NOISE BANDWIDTH OF C CALC. INPUT J1 (+ & - INTEGRATION LIM
      ITS)"
1330 INPUT J1
1340 LET C0=MAX(C)
1346 LET X=C*C
1350 INTEGRATE X,X
1360 LET NB=(X(256+J1)-X(256-J1))/(2*C0*C0)
1365 LET NB=NB*(C/51.2)
1370 PRINT "NOISE BANDWIDTH OF C CALC'D FROM J=";256-J1;" TO";256+J1;"
      IS"
1380 PRINT NB;" HZ"
1390 STOP

```

APPENDIX A.9

```

6900 PRINT " PROGRAM TO CALCULATE NOISE INTEGRAL OF DBM CURVES"
6902 PRINT "THIS IS THE STARTING POINT; PROCEEDING CLEARS ALL ARRAYS."
6904 PRINT "INPUT ANY NUMBER TO PROCEED:"
6906 INPUT K
6908 DIMENSION AF(50):LET AF=0
6910 DIMENSION AD(50):LET AD=0
6912 DIMENSION AP(50):LET AP=0
6914 DIMENSION IP(50):LET IP=0
6916 LET K=0
6918 PRINT "INITIALIZATION COMPLETE: INPUT NOISE CURVES STARTING WITH
        LOWEST FREQUENCY CURVE"
6920 GOTO 7000
6950 PRINT "FIRST POINT IN ARRAY: INPUT APPROPRIATE ZERO-FREQUENCY VALUE
6952 INPUT DB
6954 LET AF(0)=0:LET AD(0)=DB:LET AP(0)=10*((DB/10-3)/DF
6960 RETURN
7000 PRINT "INPUT NOISE BANDWIDTH FOR CURVE (FROM RESOLUTION):"
7002 INPUT DF
7004 PRINT "INPUT FREQUENCY/CM FOR CURVE (DISPERSION):"
7006 INPUT HD
7008 PRINT "BEGIN: INPUT OF HORIZONTAL POSITION(CM)-DBM POINT PAIRS"
7010 PRINT "HORIZONTAL POSITION FIRST, DBM LAST. USE CONTROL P TO STOP"
7012 IF K=0 GOSUB 6950
7020 INPUT HP,DB
7021 IF HP*HD<=AF(K) GOTO 7400:IF DB-AD(K)>30 GOTO 7400
7022 LET K=K+1
7024 LET AF(K)=HP*HD:LET AD(K)=DB
7026 IF DB-AD(K-1)>1 GOTO 7300
7028 IF AD(K-1)-DB>1 GOTO 7300
7030 GOTO 7200
7040 LET IP(K)=IP(K-1)+DP
7042 LET AP(K)=10*((.1*AD(K))-3)/DF
7048 GOTO 7020
7100 PRINT "NOISE INTEGRAL CALCULATION DATA AND RESULTS"
7102 PRINT
7104 PRINT "FREQ(HZ)  SIG(DBM)  NP(W/HZ)  INTG'D POWER  INTG'D
        VOLTAGE NOISE"
7105 LET K=-1
7106 LET K=K+1
7110 PRINT AF(K),AD(K),AP(K),IP(K),(SQ(50*IP(K)))
7111 IF K<5 GOTO 7106
7112 IF AF(K+1)>0 GOTO 7106
7120 STOP
7200 LET DP=((AF(K)-AF(K-1))/DF)*((10*((.05*(AD(K)+AD(K-1))-3))
7202 GOTO 7040
7300 LET DD=AD(K)-AD(K-1)
7302 LET DP=((AF(K)-AF(K-1))/DF)*((10*((.1*AD(K-1)-3))*(10*((.1*DD)-1))/
        (.23026*DD))
7304 GOTO 7040
7400 PRINT "BAD POINT ENTERED (FREQ NOT ABOVE PREVIOUS OR >30 DB CHANGE
        IN SIG) TRY AGAIN"
7402 GOTO 7020

```